Master's thesis

Trym Bærheim

Reversible Heat Effects in Electrodes Relevant for Lithium-Ion Batteries

Master's thesis in Mechanical Engineering
Supervisor: Odne Stokke Burheim
Co-supervisor: Astrid Fagertun Gunnarshaug
June 2021

NTNU
Norwegian University of Science and Technology
Faculty of Engineering
Department of Energy and Process Engineering

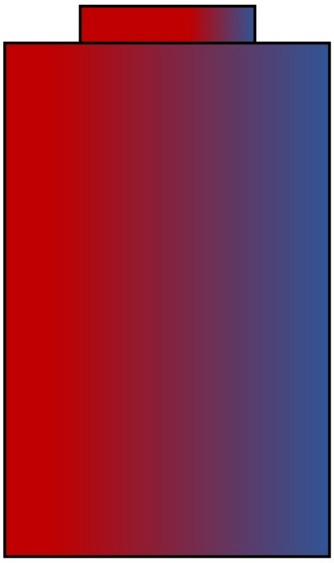

NTNU
Norwegian University of
Science and Technology

Trym Bærheim

Reversible Heat Effects in Electrodes Relevant for Lithium-Ion Batteries

Master's thesis in Mechanical Engineering
Supervisor: Odne Stokke Burheim
Co-supervisor: Astrid Fagertun Gunnarshaug
June 2021

Norwegian University of Science and Technology
Faculty of Engineering
Department of Energy and Process Engineering

NTNU
Kunnskap for en bedre verden

Preface

This Master's thesis constitutes the final part of a 5 year program in Mechanical Engineering at the Norwegian University of Science and Technology (NTNU). In the program, the thesis accounts for 30 ECTS. It was supervised by professor Odne Stokke Burheim, professor at the department of energy and process engineering (EPT), and Astrid Fagertun Gunnarshaug, a doctoral research fellow at the department of chemistry. The work intends to amplify the university's battery research, and also adds to the previous work done by Gunnarshaug and co-workers on this topic.

Acknowledgements

This thesis would not have been possible without the unceasing support from friends, family and my partner, and to them, I am forever grateful. Further, a special thanks must be given to Odne, for his enthusiastic introduction to the battery world, good discussions and contributions to my professional and personal development this past year. I would also like to thank Astrid for being an inexhaustible source of knowledge, fencing off my questions at any time of day. I am grateful to her not only for the academical help and support, but also for her ability to quickly solve practical problems. Finally, I would like to thank the entire battery group for the valuable knowledge-input, know-how, and discussions they have provided. A special thanks goes to Jake, Lena, Silje, Markus, Colin, Christian, Ingvild, Frode and Dan, who have all helped me out in different situations with this thesis.

Abstract

With the growing use of lithium-ion batteries for energy storage, an understanding of heat effects is becoming increasingly important to reduce aging and improve performance. Earlier research suggests that the reversible heat in these batteries is the sum of local effects that are many times larger than the total effect, but with opposite signs that make them cancel. In this thesis these local effects were explored for three different electrode materials and two different electrolytes relevant for lithium-ion batteries. Non-equilibrium theory was applied to describe the complicated interaction between transport of heat, mass and charge. Symmetric, thermoelectric cells were produced to isolate the local, reversible heat effects from other heat-generating phenomena in the batteries. An experiment was conducted where the voltage was measured when a temperature difference was applied to a symmetric cell at open circuit conditions (which quantifies the Seebeck voltage). This was then related to the reversible, local heat at the electrode (the Peltier heat) by use of Onsager's reciprocal relations. Peltier heats for Li_xFePO_4 were reported at different states of lithiation ($0.47 < x < 1$) and for two different electrolytes. Measurements were also made for $LiCoO_2$ and $LiMn_2O_4$ with the two different electrolytes, but due to high uncertainties it was difficult to report precise values. In general the reported values were *lower* and *more stable in time* than what has been suggested in earlier research. This implies that the local effects may be smaller than what was first anticipated. It also suggests that the influence on the Peltier heat of concentration gradients of different components in the electrolyte in this specific case are opposite in sign, and similar in magnitude, thereby cancelling the effect of one another at full Soret equilibrium (when there is no longer a change in concentration gradients in the electrolyte). Also, a high change in the local heat effect was seen when changing the electrolyte, indicating that this should be investigated further. It was also found that the local heat effect of the Li_xFePO_4 varies little with state of lithiation (or state of charge), which was expected due to the stable entropy change seen in these electrodes during charge/discharge.

Sammendrag

Med økende bruk av lithium-ione batterier for å lagre energi, blir det stadig viktigere å forstå interne varmeeffekter for å redusere aldring og bedre ytelsen til disse. Tidligere forskning indikerer at den reversible varmeeffketen i slike batterier er summen av lokale effekter som er mange ganger større enn den totale effekten, men nulles ut fordi de har motsatt fortegn. I denne masteroppgaven ble disse lokale effektene utforsket i tre ulike elektrodematerialer og med to ulike elektrolytter som var relevante for lithium-ione batterier. Ikke-likevekts termodynamikk ble brukt for å beskrive de kompliserte interaksjonene mellom transport av varme, masse og ladning i systemet. Symmetriske, termoelektriske celler ble laget for å isolere de lokale, reversible varmeeffektene fra andre varmegenererende prosesser i batteriene. Et eksperiment ble gjennomført hvor spenningen ble målt når en temperaturforskjell ble etablert i en celle med åpen krets (som kvantifiserer Seebeck-spenningen). Denne kunne deretter relateres til den reversible, lokale varmen på elektroden (Peltiervarmen) ved hjelp av Onsager's teori om gjensidig påvirkning. Peltiervarmen for Li_xFePO_4 ble rapportert ved ulike ladetilstander ($0.47 < x < 1$) og ved bruk av to ulike elektrolytter. Forsøk ble også utført med $LiCoO_2$ og $LiMn_2O_4$ elektroder med de to elektrolyttene, men på grunn av store usikkerheter knyttet til forsøkene var det vanskelig å rapportere gode verdier. Generelt var verdiene som ble funnet *lavere* og *mer stabile i tid* enn hva tidligere forskning viser. Dette kan indikere at de lokale effektene er mindre enn hva som først ble antatt. At verdiene er mer stabile i tid kan også bety at bidraget til den lokale varmen fra konsentrasjonsgradientene i elektrolytten nuller hverandre ut når en stasjonær tilstand oppnås (altså når konsentrasjonsgradientene ikke lenger endres). En relativt stor endring i verdiene ble observert når elektrolytten ble endret. Dette kan ha en viktig påvirkning på den lokale varmeeffekten, og burde undersøkes videre i fremtidig forskning. Det ble også observert, som forventet, at den lokale varmeffekten på Li_xFePO_4 elektrodene varierte lite med ladetilstand. Dette var forventet fordi denne elektroden har en svært stabil entropiendring, som endres lite under opp- og utladning.

Contents

Figures

Tables

Acronyms

emf electro-motive force. 14, 31, 79, 129

ANFIS adaptive neural fuzzy interface system. 129

ASGSMO adaptive swithcing gains sliding mode observer. 129

BI bi-linear interpolation. 129

BMSs Battery Management Systems. 19

CC coulomb counting. 61, 62, 127–129

CCCV Constant Current - Constant Voltage. 66

DEC diethyl carbonate. xiii, xv, xvi, 7, 11, 28, 29, 45, 46, 49, 57, 79, 87–89, 91, 93, 95, 99, 100, 135–137, 140, 142, 143, 145, 146, 151, 153–157

DMC dimethyl carbonate. xv, xvi, 11, 45, 46, 49, 57, 59, 78, 79, 87–89, 91, 95, 96, 99, 100, 135, 138, 141, 144, 151, 153, 154, 156

EC ethylene carbonate. xiii, xv, xvi, 7, 11, 28, 29, 45, 49, 57, 78, 79, 87–89, 91, 93, 95, 96, 99, 100, 135–138, 140–146, 151, 153–157

EIS electrochemical impedance spectroscopy. 129

EMC ethyl methyl carbonate. 7

GA genetic algorithm. 128, 129

IR impulse response. 129

KF kalman filter. 128, 129

LAM loss of active material. 10, 13

LCO Lithium Cobalt Oxide. xvi, 2, 3, 7, 9, 28, 32, 56, 58, 59, 71, 82, 83, 87, 89, 91–93, 95, 97, 99, 103, 135

LFP Lithium Iron Phosphates. xv, xvi, 3, 8, 9, 29, 32, 56, 58, 62, 64, 65, 71, 79, 87, 91–97, 99, 100, 103, 135, 155, 157

LIB lithium-ion battery. 1, 6, 7, 11, 12, 20, 22, 29, 116

LIBs lithium-ion batteries. 3, 5, 7, 8, 10, 15, 16, 19, 20, 26, 96, 97, 99, 101, 103

LLI loss of lithium inventory. 10–13

LMO Lithium Manganese Oxides. xv, xvi, 3, 9, 32, 56, 58, 79, 87, 89, 91, 92, 95, 97, 99, 135, 153

LNMO Lithium Nickel Manganese Oxides. 9

LTO Lithium Titanate. 8, 97

MARS multivibrate adaptive regression splines. 129

NCA Lithium Nickel Cobalt Aluminium Oxides. 9, 103

NMC Lithium Nickel Manganese Cobalt Oxides. 9, 103

NN neural network. 128, 129

OCV open-circuit voltage. 62, 65, 128, 129

PC propylene carbonate. 7, 28

PE polyethylene. 56

PET polyethylene terephthalate. 56

PIO proportional-integral observer. 129

SEI solid-electrolyte interface. 7, 11–13, 61, 63, 97, 102

SMO sliding mode observer. 128, 129

SoC state of charge. 1, 3, 11–13, 16, 19, 20, 27, 36, 39, 55, 56, 59–66, 92, 95, 96, 99, 100, 103, 127–129, 145, 146

SoCs states of charge. 3, 55, 62, 64, 66, 92, 103

SoH state of health. 13, 127

SPI solid permeable interface. 7, 11, 12

SPKF sigma point kalman filter. 128, 129

UPF unscented particle filter. 129

Chapter 1

Introduction and Motivation

1.1 Motivation

With the ever-growing electrification of the transportation sector, as well as the harvesting of more renewable energy sources that produce energy at a different time than the energy is consumed, the need for energy storage is rapidly increasing. The dominating commercialized, rechargeable battery technology today is the lithium-ion battery (LIB). This technology is being used in everything from phones and computers to electric cars and ferries. Batteries are constantly required to deliver more energy and power, while being compact and capable of charging as fast as possible. The automobile industry is working on reducing the battery weight, while still maintaining a high level of safety. In addition to this, battery lifetime is an important parameter for the growing electrification of society. A longer life improves both the economical and environmental advantage of using a battery. As the use of LIB technology is extended, the demand for a better understanding of performance and aging of these batteries is evident. Both aging and performance are highly affected by temperature, which is why proper models of the heat generation to achieve appropriate cooling is essential.

Heat effects have been studied for many years, and it is generally recognized that there are three contributors to heat generation and dissipation in batteries: (1) ohmic losses caused by the internal resistance in the battery cell; (2) heat generation caused by overpotential; and (3) reversible heat generated or absorbed due to the change in entropy of the battery system [1]. In this thesis, focus is given to the latter, and less studied, reversible heat. When the current density in a battery is high, the most important contribution to heat comes from ohmic resistances (Joule heat) and resistances to the electrode reactions (reflected by the overpotential) [2]. The reaction entropy, however, can act both as a source and a sink for heat, and is further dependent on state of charge and battery chemistry [2, 3]. Even though this effect is most pronounced at low current densities (constituting up to 88 % of the total heat effect in a $LiCoO_2$-graphite cell at C/8), it is still important at higher current densities, ranging from 5 to 17 % of the total heat at 1 C in batteries using $LiMn_2O_4$ and $LiCoO_2$ electrodes [3].

Even though thermal models have included the reversible heat effect since the beginning [4], attention has only recently been given to *local* heat effects that could possibly be quite large. Richter *et al.* indicated in [2] that the total reversible heat in the battery was caused by the sum of local heat effects at each electrode that are opposite in sign. They stipulated that the heating and cooling effects that exist locally at each electrode (at different physical locations in the cell) could be as much as 11 times higher than the total effect [2]. If this is the case, modelling the total heat effect may not be sufficient, because local temperatures could give rise to aging or reduced performance at the individual electrodes. Thus, quantifying these local effects may be important to achieve more precise battery models, which in turn could reduce aging and improve performance of the batteries through the implementation of better control and cooling systems.

1.2 Earlier Research

The heat generation or dissipation from entropy change can be attributed to the Peltier effect (heat generated or dissipated locally at each electrode) and the Dufour effect (heat transported by a concentration gradient in the electrolyte). It is thus interesting to quantify these effects to get a better understanding of what causes the reversible heat effect found in batteries. Gunnarshaug *et al.* showed in [5] that the total heat effect from entropy change can be expressed in terms of the Peltier heat at each electrode, because the Dufour effects give contributions to the local Peltier heats, and are thus included in these [5]. Focus is therefore put on the Peltier heats, but it shall be seen that the Dufour effect is also accounted for in the local heat effects.

In this thesis, the Peltier heat will be calculated from values of the Seebeck coefficient, which is the voltage that is created when a temperature difference is applied to a symmetric cell at open circuit conditions. The reason why the Peltier heat is not calculated directly comes from the nature of this phenomena. By definition the Peltier heat is the heat that must be added to an electrode|electrolyte interface to keep the temperature constant when a positive electric current is passing from left to right at *reversible conditions* [6]. Establishing this situation, with measurement techniques that do not interfere with the internal processes in the cell, is quite challenging. Luckily, the Onsager relations (explained in Section 2.5) say that the Peltier heat of one electrode is related to the Seebeck coefficient of a cell with two identical electrodes [6]. For a symmetric cell the Seebeck coefficient is [6]:

$$\epsilon(t) = \left(\frac{\Delta\varphi}{\Delta T}\right)_{j=0} \tag{1.1}$$

While the Peltier heat can be written in the following way thanks to the Onsager relations [6–8]:

$$\pi = -FT\epsilon(t) \tag{1.2}$$

Richter *et al.* were the first to obtain experimental results for the local reversible heat (Peltier heat) from the Seebeck coefficient for a Lithium Cobalt Oxide (LCO) electrode in [2]. The values were found to vary with time, with a minimum value of -45 ± 6 kJ/mol and a maximum value of 84 ± 9 kJ/mol. These large variations were attributed to heat transport caused by concentration gradients in the electrolyte (Dufour effects). Combining these values with the total entropy change found in literature, Richter *et al.* found that the heat effect on the graphite electrode in a LCO-graphite cell were equally large, and of opposite sign. The values reported there varied from -73 ± 9 kJ/mol to 56 ± 6 kJ/mol. This is substantial, considering that the total reversible heat effect caused by the entropy change in the LCO-graphite cell is only 11 kJ/mol [2]. These were the first indications that the local, reversible effects could be important enough to include in battery models.

The work done by Richter *et al.* was continued by Gunnarshaug *et al.* [6]. In [6] the Peltier heat of a $LiFePO_4$ (LFP) electrode near 0 % SoC was measured. It was found that the Peltier heat varied from 37 to 122 kJ/mol for the LFP, and from 19 to 104 kJ/mol for the graphite, depending on the concentration gradients in the electrolyte. Again it is apparent that both the Peltier heats and the Dufour effects are substantial.

Further, Gunnarshaug *et al.* used reported values for half-cell entropies in combination with reported Seebeck coefficients for lithium-metal electrodes from literature to estimate the Peltier heat of various electrode materials relevant for LIBs [5]. Based on these estimations, it would appear that the Peltier heat is affected both by state of charge and cell chemistry of the electrodes.

Recently, Spitthoff *et al.* also proposed how the local heat effects could be included in a thermal battery model, and showed how the influence of these effects lead to a quite significant heat generation in a battery stack [9].

1.3 Objective

This thesis is meant to expand the work of Gunnarshaug *et al.* [5, 6], Spitthoff *et al.* [9] and Richter *et al.* [2] which report possible large local reversible heat changes in lithium ion batteries, that are often overlooked in models.

Here, three different electrode materials will be explored ($LiFePO_4$ (LFP), $LiMn_2O_4$ (LMO) and $LiCoO_2$ (LCO)), as well as two different electrolytes consisting of a $LiPF_6$ salt in different carbonate solvents. In addition, one of the electrode materials (LFP) will be investigated at different states of lithiation (equivalent to different states of charge of the battery). The goal is to quantify the reversible heat effects that will be seen locally at these electrodes when charging or discharging a battery.

1.4 Organization of the Thesis

The thesis is organized in following manner. Chapter 2 first introduces the general function and components of LIBs. Then, the most common aging mechanisms are discussed, and it is shown how they are affected by temperature. Thereafter, heat effects in batteries are introduced, followed by an introduction to thermal battery models. It becomes clear that local effects are not accounted for, and non-equilibrium theory is introduced along with thermoelectric cells, which constitute a tool for calculating local heat effects. At the end of the theory, previous work applying non-equilibrium theory to calculate local heat effects in batteries are presented.

Following the theory, a description of the experimental system is given in Chapter 3, as well as a mathematical system description based on non-equilibrium theory. The equations derived in this chapter form the basis for the discussion.

In Chapter 4 the experimental method used to quantify the local heat effects is described.

Finally, in Chapter 5 the results obtained are presented and discussed, followed by a conclusion in Chapter 6 and proposed further work in Chapter 7.

Chapter 2

Theory

In this section relevant background theory will be studied. First, the general function and important components of lithium-ion batteries are explained, followed by an introduction to aging mechanisms that take place in the batteries. Thereafter, heat generation in batteries is discussed, and an introduction to existing thermal models in batteries is given. Non-equilibrium thermodynamics are then applied to account for complicated interactions between different transport phenomena. Ultimately, thermocells are introduced as a way of isolating local reversible heat effects from other mechanisms that generate heat in the battery, and earlier work related to this topic is presented.

2.1 Litium-Ion Batteries - Structure and Function

In order to understand aging and performance of a lithium-ion battery it is essential to understand how it is composed, and how it functions. Section 2.1.1 explains the general structure and the function of a LIB, while Section 2.1.2 goes into detail on some of the key components in the battery.

2.1.1 How a Lithium-Ion Battery Works

A lithium-ion battery consist of:

- The *anode*, storing Li-ions. During discharge Li-ions migrate from the anode to the cathode
- The *cathode*, storing Li-ions. During discharge Li-ions migrate to the cathode from the anode. The anode and cathode are with a common term referred to as *electrodes*. The electrodes are composed of several components (binder, conductive material, etc.), and the component that contributes to storing charge is often referred to as the *active material*.
- An inert *separator*, keeping the electrodes apart
- *Electrolyte*, allowing the movement of ions between the electrodes. The electrodes and the separator are porous, and the electrolyte fills these pores and facilitates ion-transport
- *Current collectors* at the electrodes. The current collectors are used to collect the free electrons at the electrodes.

A simple schematic of a lithium-ion pouch cell is shown in Figure 2.1.

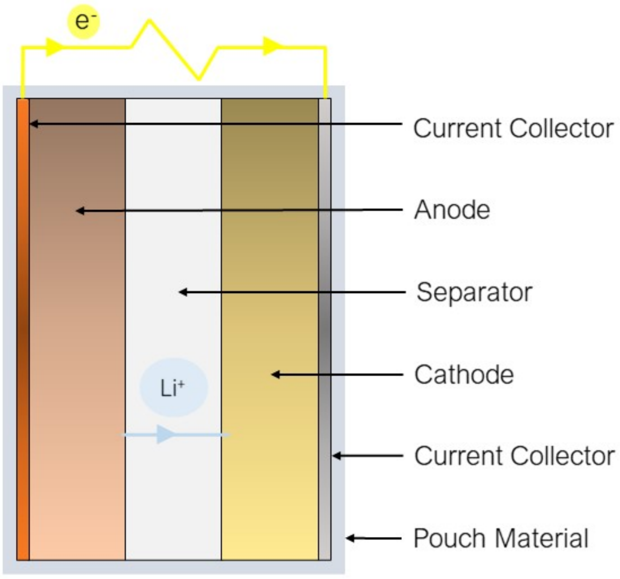

Figure 2.1: A schematic of a lithium-ion pouch cell during discharge. The flow of electrons is forced through an outer circuit, while the Li-ions pass from the anode to the cathode through the separator.

When the battery is discharging, the anode releases Li-ions which migrate through the electrolyte to the cathode, going through the separator. At the same time, electrons move from the anode to the cathode through an outer circuit creating electricity that can be exploited. When charging, the process is reversed.

It should be noted here that the "battery world" often refers to the electrodes by the same name (cathode and anode) also during charging, even though the oxidation occurs at what would then be called the cathode. The definition is based on the processes happening upon discharge - oxidation happens at the anode during discharge and reduction at the cathode [10]. In classical electrochemistry, the oxidation always occurs at the anode, so the electrodes switch names during charging. In this thesis the "battery-world" definition will be applied. For example, in a LIB with one lithium oxide intercalation electrode (like Li_xCoO_2 (LCO)) and one carbon-based intercalation electrode (Li_xC_6), the LCO electrode will be referred to as the cathode both during charging and discharging, while the carbon-based electrode will be referred to as the anode in both situations.

2.1.2 Important Lithium-Ion Battery Components

Electrolyte

The electrolyte conducts ions while being an insulator for electric charge [11]. At the same time it should not react with the reactants of a cell beyond transport of the ions [11]. An electrolyte can be either solid or liquid. In a solid electrolyte, the electrolyte in itself acts as a separator, whereas in a liquid electrolyte a separator is required to keep the electrodes from physical contact.

The electrolyte also determines the magnitude of the open circuit voltage of the cell, because it determines the limiting electrochemical potential $\tilde{\mu}$ at the two electrodes. In order to avoid a chemical reduction of the electrolyte at the anode, the highest state of energy at which the anode will give an electron should be lower than the lowest state of energy at which the electrolyte will take up an electron. Conversely, the lowest state of energy at which the cathode receives an electron should be higher than the highest state at which the electrolyte gives an electron to avoid oxidation of the electrolyte at the cathode [11]. This is what decides the stability window of the electrolyte, which determines the maximum voltage window the cell can operate in without reacting with the electrolyte. However, this voltage window can be expanded by the use of additives in the electrolyte [12]. By adding components that are more easily reduced by the anode and more easily oxidized by the cathode than the solvents in the electrolyte, it is possible to protect the solvents, even when the battery operates outside the stability window of the original electrolyte [12].

The electrolyte in a LIB commonly consists of one or more conducting salts, like $LiClO_4$, $LiAsF_6$, $LiBF_4$ and $LiPF_6$ dissolved in some solvent, like ethylene carbonate (EC), propylene carbonate (PC), diethyl carbonate (DEC) and ethyl methyl carbonate (EMC) [13]. Graphite, which is the most commonly used anode material for LIBs, has a catalyzing effect on the reduction of the electrolyte solvents [14]. Because of this, the formation of a passive film at the surface of the carbon anode is essential in order to protect the electrolyte from further reduction. Such a passive film is formed mainly during the first charge of the battery. This film is called the solid-electrolyte interface (SEI), and is created by a reduction of the electrolyte at the anode during charging [13]. A similar layer, sometimes referred to as the solid permeable interface (SPI) forms at the cathode due to oxidation of the elctrolyte [13]. The SEI and SPI layers prevent further decomposition of the electrolyte, while letting lithium-ions pass through. As shall be discussed in Section 2.2 the SEI-layer formation is an important contributor to battery aging, and is affected by temperature.

Electrodes

According to Goodenough there are seven quality factors that determine how well suited an insertion compound is to be used as an electrode material for a secondary battery. Here this is exemplified for LIBs even though Goodenough did it for secondary batteries in general. The quality factors are [11]:

1. Reversible insertion and extraction of Li-ions
2. High solid-solution range, meaning high capacity of the host structure to take up Li-ions, while weighing little in itself
3. An energy threshold for electron acceptance/donation matched to the electrolyte stability window
4. A small change in potential with concentration of Li-ions, to give a voltage as constant as possible with discharge
5. High bulk ionic conductivity to reduce joule losses in the electrodes and the electrolyte
6. High bulk electronic conductivity, also to reduce joule losses
7. Low resistance in the interfaces for both ionic and electronic transport

Based on these criteria, much work has been done to improve the performance of the electrodes. Nitta *et al.* name different strategies that have been applied to make better electrodes, like dimensional reduction, composite formation, doping, morphology control, coating and electrolyte modification [15]. As one example, the electric conductivity has been improved by introducing small particles conducting additives like carbon black in the electrodes [16]. Another example is improvements in the production techniques to find an optimal balance between porosity and compactness in order to achieve good ionic and electronic conductivity [17, 18].

Anode
The most common anode material in commercialized lithium-ion batteries is graphite [19], though also other materials have been used, such as Lithium Titanate (LTO), alloying metals (Ge, Si, Sn or P) and conversion metals (SnO_2 and SiO). Because primarily cathode materials are investigated in this thesis, further discussion of anode materials is deemed redundant. For an extensive overview over different anode materials, the reader is referred to Nitta *et al.* and the sources therein [15]. It should be retained, however, that in commercialized LIBs graphite is the most used material. Also, because the *cathode* is the main bottleneck in terms of energy density, graphite is likely to keep being used as anode in these batteries, as much more research is being done on improving the cathode materials than the anode materials (though some research indicates that Si-based anodes may be on the way [20–24]).

Cathode
There are several different types of cathode materials, like conversion materials and polyanion compounds, but the most commonly used are transition metal oxides [15]. To limit the scope of this text, only the transition metal oxides will be discussed here. It is common to distinguish between three types of such oxides based on the structure:

- *Olivine* structured materials , like LFP.

- *Layered metal oxides*, like LCO, NMC and NCA.
- *Spinel* structured materials, like LNMO and LMO.

The olivine lattice only allows 1D mobility of the ions, so the diffusion is slow. Also, the specific capacitance and the low potential vs Li/Li+ are not optimal. However, the structure gives high safety and cycle stability and a moderate price [19]. Lithium Iron Phosphates, $LiFePO_4$ (LFP) is an example of an olivine structured metal oxide. A disadvantage of LFP compared to other materials is that the average voltage is low ($\sim$ 3.45 V), and also that it suffers from high rates of self-discharge.

The layered metal oxides are structured so that the ions can move in 2D planes in the active material. These materials have high specific capacity, but moderate safety and a higher price. An example is LCO. Lithium Cobalt Oxide, $LiCoO_2$ (LCO) has attractively high theoretical specific capacity (274 mAh/g) and a high discharge voltage ($\sim$4.2-4.3 V vs Li/Li^+). However, only about half the capacity is available in commercialized LCO batteries because of the structural complexity and instability of $LiCoO_2$ and its deterioration at charging voltage over 4.2-4.3 V [25–27]. Using different metal-oxide coatings the discharge voltage has been increased up to 4.5-4.7 V in experiments, giving discharge capacities up to 180-190 mAh/g, but these have yet to be commercialized [28].

The spinel structured metal oxides allow for a full 3D ion-movement, which gives very high ionic diffusivity. The materials have fairly high capacity and moderate price [19]. An example is Lithium Manganese Oxides, $LiMn_2O_4$ (LMO) which exhibit excellent thermal and chemical stability, good price and low environmental impact[19]. Also the capacity retention has been reported to be quite good (>90 % after 400 cycles [29, 30]). Unfortunately the capacity is limited to around 120-130 mAh/g, which limits the possible energy density. In addition to this, the manganese dissolves at elevated temperatures, so operating temperature is limited [31].

Note that the examples given here are commonly used materials, but do not in any way constitute an exhaustive list. The mentioned cathode materials are the ones investigated in the experimental section of this thesis. One material of each type was chosen to potentially discuss the influence of the structure on local heat effects.

2.2 Battery Aging

This subsection presents the mayor aging mechanisms in lithium-ion batteries. It will become clear that temperature plays a central role in battery aging, which motivates the aim of this thesis - namely to quantify the local, reversible heat effects in LIBs.

2.2.1 Classification of Aging Mechanisms

Aging and degradation of batteries is complicated due to the interaction of different mechanisms that are affected both by the utilization and external environment of the battery [32]. The aging mechanisms can be either chemical or mechanical, and depend on the composition of the different battery components [32]. Nonetheless, it is common to separate three groups of degradation mechanisms [33]:

- **Loss of lithium inventory (LLI)**. These are mechanisms that in one way or another lead to less available Li-ions.
- **Loss of active material (LAM)**. These mechanisms reduce the active material that can be exploited.
- **Impedance increase due to reaction kinetics degradation**. Mechanisms that increase the resistance to transport of ions or electrons will give higher irreversible losses, and thus be a degradation mechanism of the battery.

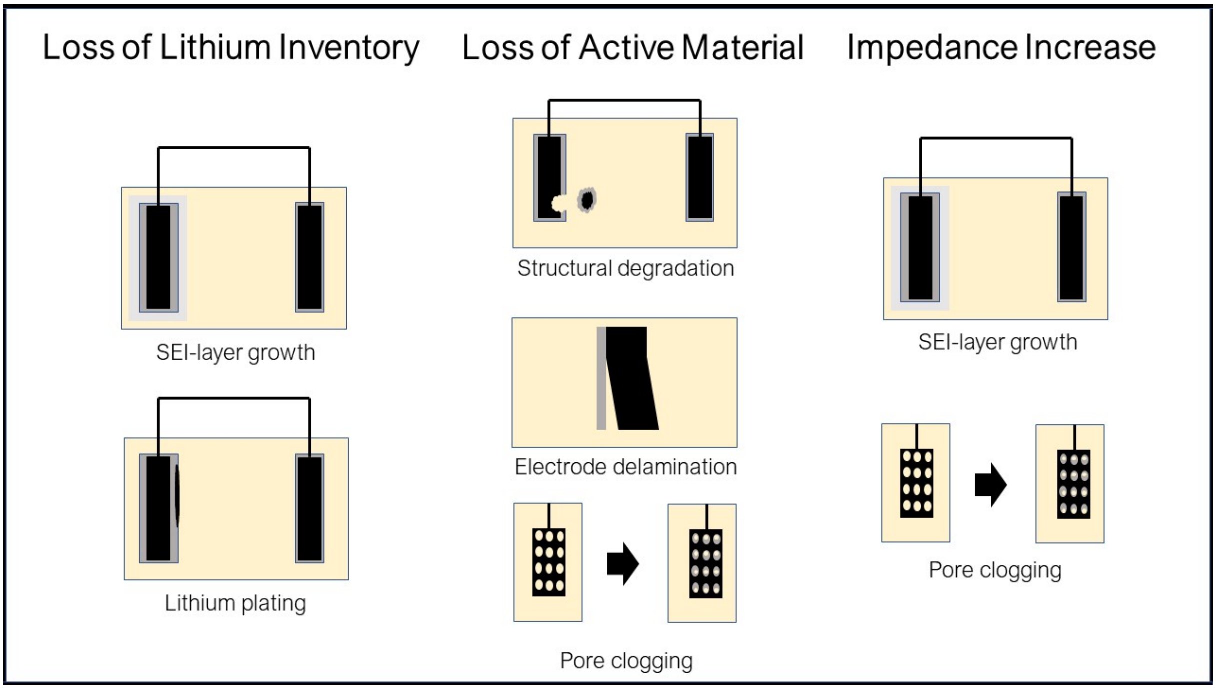

Figure 2.2: Illustration of some of the aging mechanisms in lithium-ion batteries.

2.2.2 Loss of Lithium Inventory

Loss of lithium inventory is mainly due to the formation of the SEI-layer, lithium plating and different lithium consumption rates at the two electrodes [34].

SEI-Layer Formation and Growth

As mentioned in Section 2.1.2 the solid-electrolyte interface (SEI)-layer is a passive layer that is formed mainly during the first charge cycle of the battery, and protects the electrolyte from being further reduced. Normally a process of various charge and discharge cycles at low C-rates called "formation" is carried out in order to establish a stable SEI-layer before the battery is put into use. The formation process typically consists of 3-5 full depth cycles around C/20 and 3-5 cycles at higher C-rates [35], although alternative procedures such as discharging in a smaller discharge window at high SoC could give shorter formation times while still maintaining the capacity [35].

The SEI-layer consists of several compounds which depend especially on the electrolyte composition. Malmgren *et al.* found that a full LIB-cell with carbonate based $LiPF_6$ electrolyte had a SEI-layer with several compounds containing C-O and P-F, as well as Li_2O [36]. An *et al.* state that a stable SEI-layer should contain stable and insoluble compounds such as Li_2CO_3 rather than metastable compounds such as ROLi or $ROCO_2Li$ (where R is a low-molecular weight alkyl group), which cause the SEI-layer to break up during cycling [37]. The same authors also state that the overall SEI-composition is over 50 % LiF and Li_2CO_3 [37].

The SEI-layer has an impact on capacity loss, self-discharge characteristics, cycle life, rate capability and safety [37]. Controlling the SEI-layer formation and growth is difficult because its composition, morphology and stability are affected by a variety of factors, like electrolyte composition, cell temperature, electrochemical conditions, and graphite morphology [37]. When the SEI-layer is formed during the first cycle, it generally consumes 10-20 % of the original capacity [37, 38]. After being formed, the SEI-layer prevents further decomposition reactions with salts and solvents in the electrolyte by shifting the surface potential of the anode to within the stability window of the electrolyte (increased resistance gives higher potential at the graphite surface) [37]. However, a continued decomposition does occur with time, giving a gradually thicker SEI-layer, which consumes Li-ions, solvents and salts, and increases the internal resistance of the cell. This gradual SEI-layer growth is due to electrolyte diffusion to the graphite surface and electron exposure to electrolyte [37]. This degradation also happens when the battery is not in use, and it has been shown that the capaciy loss during storage is accelerated at higher temperature and SoC [33, 39].

An *et al.* also mention that a "SEI-like" layer (sometimes called solid permeable interface (SPI)) forms on the cathode, especially at elevated voltages, where organic carbonates (like EC, DMC or DEC) in the electrolyte are oxidized by the cathode during charging or storage. This can be related to the oxidation potential of these molecules, which is around 4.7 V vs Li/Li^+ [37]. It should be noted that the oxidation potential of these substances is reduced with temperature, being only 4 V at 40 °C and 3.8 V at 60 °C [37]. Würsig *et al.* also report the formation of a passive film on different cathodes for certain electrolyte compositions, whereas other compositions give no such film [40]. This is in agreement with the theory that different molecules have different oxidation potentials, and underlines the importance of choosing the right electrolyte-composition to avoid unnecessary aging due to the formation and growth of these passive films. Research has mainly focused on how to limit SEI-layer growth as opposed to SPI because it has been shown that the SEI-layer on the anode grows more than the SPI-layer on the cathode [36].

The temperature-dependence of the reduction and oxidation potential for the different components in the electrolyte, as well as the temperature dependence during storage, are important motivators for finding the local temperatures in the battery. According to Campion *et al.*, elevated temperatures in electrolyte containing $LiPF_6$ leads to the creation of PF_5 which breaks down the SEI and frees up the graphite surface for further reduction of solvents [41].

Lithium-plating

Another mechanism that leads to loss of lithium inventory is lithium-plating, which is the deposition of metallic lithium on the graphite electrode [42]. This phenomena is typical during charging at high C-rates, high SoC and low temperatures [42]. When charging at low temperatures the kinetics in the battery are slow, and there is a competition between lithium-intercalation in the graphite, and plating on the surface of the graphite. The low temperature decreases the diffusion rate, and thus favors lithium-plating. If the SoC is high, there are few available sites in the graphite matrix, and diffusion rate is further reduced. At high C-rates the flow of Li-ions is higher. Therefore, the combination of these three factors (high C-rate, low temperature and high SoC) gives the highest Li-plating.

Earlier, it was believed that lithium plating was only a serious issue under harsh conditions, like high C-rates and at low temperatures. However, as pointed out by Yang *et al.*, recent studies have shown that lithium plating also occurs at milder cycling conditions in cells after extended cycling [43]. One possible explanation for this is the fact that continued SEI-layer growth leads to pore clogging that reduce the ionic kinetics at the anode and thus facilitates the lithium-plating [43]. Yang *et al.* show that SEI-layer formation is the main reason for capacity loss in early cycling ($<$ 1500 cycles), but that lithium-plating becomes the dominating capacity-fading factor as the SEI-growth gradually slows down [43]. Lithium-plating can also pose a safety threat, as the metallic lithium can form dendrites that penetrate the separator, causing a short circuit [43, 44].

Note that also this aging mechanism is dependent on temperature, but in this case cold temperatures is a problem. A battery must therefore operate in a balanced temperature range to avoid both Li-plating and SEI-layer growth.

Lithium Consumption Rates at the Electrodes

In an ideal lithium-ion battery, the same amount of Li-ions move back and forth between the two electrodes during charge and discharge, and there is no more "cyclable" lithium left in the anode after complete discharge, and no more lithium in the cathode after charge. In reality, there is always a limiting electrode, which is the electrode that is fully discharged at the end of discharge, and causes the cell to reach the end of discharge voltage [38]. According to Zhang and White, the limiting electrode changes throughout the cell-life [38]. In the first phase, the anode is the limiting electrode, which means that the anode is fully discharged, while the cathode is not fully intercalated with lithium because there is not enough lithium available after some has been consumed by the SEI-layer formation. In the second phase, the loss of active cathode material gradually balances the initial loss of lithium, though the anode is still the limiting electrode. In the third phase, the loss of active cathode material overcomes the initial loss, and the cathode becomes the limiting electrode, meaning that the anode becomes less and less discharged when the end of discharge voltage has been reached [38]. This difference in consumption rates at the electrodes lead to some cyclable lithium not being cycled, and is thus a mechanism for capacity loss.

2.2.3 Loss of Active Material

Loss of active material (LAM) is a secondary aging effect, and consists of structural damage and material loss due to metal dissolution, structural degradation, particle isolation and electrode delamination [33, 45]. The expansion and structural change of the electrodes during charge/discharge cause mechanical stresses that lead to gradually isolated active material [46]. An example of a mechanism that produces loss of active material is the clogging of the pores in the electrode structure caused by the gradual growth of the passive layer [39]. When the pores are clogged, less active material is accessible, and thus the capacity is reduced. Another example is that volume change of the carbon material during cycling causes partial degradation of the layers, which is repaired on the expense of available lithium [39]. Electrode delamination happens when the active material of the electrode is separated from the current collector and is therefore inaccessible to the flow of electrons.

2.2.4 Impedance Increase

In addition to the loss of lithium inventory and loss of active material, the increase in impedance leads to higher ohmic losses, and thus less exploitable power. The mechanisms that increase the impedance are largely already covered, including the formation and growth of passive layers on the electrodes, pore clogging, and conductivity losses in the electrolyte due to consumption of conducting salts [33]. It is mentioned here as a separate category of aging because the mechanisms that cause impedance increase have a dual effect on battery aging. The formation of the SEI-layer, for example, reduces the capacity of the battery both by increasing the impedance and thus increasing the ohmic losses, and by reducing the amount of lithium-ions available.

The impedance of the battery also increases during storage [33, 47]. Stroe *et al.* show that internal resistance increases non-linearly with time in a stored LFP-C battery, following a power-law function. The same authors showed that the resistance growth increases with storage temperature and state of charge [47]. The same qualitative results were found by Lamb and Pollet for LFP and NMC - the state of health (SoH) decreases more rapidly upon storage at higher temperatures and higher state of charge [33].

2.3 Heating and Cooling Effects in Lithium-Ion Batteries

The previous section (Section 2.2) highlighted how different aging mechanisms in the battery are affected by temperature, making it clear that a good heat regulation is essential to limit battery aging. In this section, the different contributions to heat generation and dissipation in a battery will be discussed. This will serve to illustrate which part of heat generation can be tied to reversible heat effects, which motivates the experiments carried out in this thesis. It is also relevant to have an understanding of heat generation and dissipation in batteries to understand why the applied experimental set-up was chosen to measure local, reversible heating and cooling effects.

When extracting useful work stored in a battery, chemical energy is converted to electrical through a conversion process. If the process is at equilibrium, the energy converted in the reaction can be given by the total enthalpy change, which in turn can be expressed in terms of reversible heat and reversible work, as done by Burheim [1]:

$$\Delta H = \Delta G + T\Delta S = W_{rev} - Q_{rev} \tag{2.1}$$

or in terms of molar quantities and rearranged to get the Gibb's free energy on the left hand side as [1]:

$$\Delta \overline{g} = \Delta \overline{h} - T\Delta \overline{s} = zF\Delta\varphi_{rev} \tag{2.2}$$

where:

G (or $\overline{g}$) : Gibb's (molar) free energy
H (or $\overline{h}$) : (Molar) enthalpy
S (or $\overline{s}$) : (Molar) entropy
T : Absolute temperature
W_{rev} : Reversible work
Q_{rev} : Reversible heat
$\Delta\varphi_{rev}$: Reversible potential or *emf*
z : Moles of electrons per mole of reactant
F : Faraday's constant

Equation 2.2 gives a relationship between the reversible potential and Gibbs free energy, and is known as Nernst's equation [1]. This is valid at equilibrium and isothermal conditions, so when no current is flowing through the cell. However, in any irreversible processes not occurring at equilibrium, losses will inevitably be a part of the equation, as well as other driving forces, which shall be explored in Section 2.5. The cell potential can then be expressed as the reversible potential minus the losses [1]:

$$\Delta\varphi_{cell} = \Delta\varphi_{rev} - rj - \eta \tag{2.3}$$

$\Delta\varphi_{cell}$: Potential in the cell when a given current is drawn
$\Delta\varphi_{rev}$: Reversible potential or *emf*
r : Resistance in the cell
j : Current density
η : Overpotential

By combining Equation 2.2 and Equation 2.3, the cell potential can be expressed as:

$$\Delta\varphi_{cell} = \frac{\Delta\overline{h}}{zF} - \frac{T\Delta\overline{s}}{zF} - rj - \eta \tag{2.4}$$

Here, $\Delta\overline{h}$ is the change in enthalpy, $\Delta\overline{s}$ the change in entropy, rj the ohmic losses and η the overpotential. This equation is a good starting point for understanding most processes affecting the potential, and thereby energy, delivered by the battery. The measurable heat generation in a battery is often given as the current multiplied by the dissipation terms in the potential equation, thus [33]:

$$q = \frac{T\Delta S}{F} j + rj^2 + \eta j \tag{2.5}$$

Where the convention used is that entropy change (ΔS) is taken for the full cell during charging, and a positive change in entropy contributes to heat the battery [10]. A brief introduction to the different terms in Equations 2.4 and 2.5 will be given.

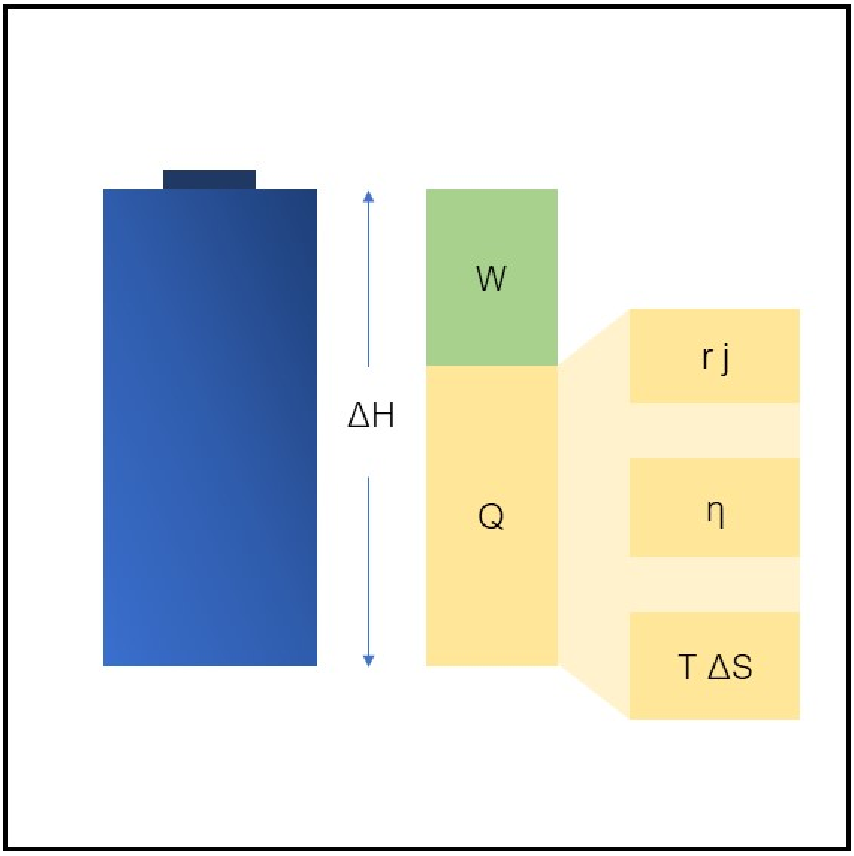

Figure 2.3: Illustration of the different heat terms in lithium-ion batteries and how they relate to the enthalpy (ΔH) and the available work (W).

2.3.1 Reaction Enthalpy ($\Delta\bar{h}$)

The first term on the right hand side of Equation 2.4 is the reaction enthalpy divided by a constant. Enthalpy is the sum of the internal energy and the product of pressure and volume of a system, $H = U + PV$ [48]. Bose show that if the pressure in a system is maintained constant, a small amount of added heat dQ will lead to a change in internal energy and volume, thus $dQ = dH$ at constant pressure (see [48]). Enthalpy can therefore be seen as a measurement of the heat in a system [48].

2.3.2 Entropy Change ($\Delta\bar{s}$)

The entropy of a system tells us something about the degree of randomness or disorder - higher entropy means more randomness [48]. In a system, one often contributes reversible heat to changes in entropy, and the term $T\Delta S$ gives information about reversible heat. Thus the second term on the right hand side of Equation 2.4 can be either a source or a sink, depending on the direction of the reaction. In lithium-ion batteries, the contribution from the entropy change to heat dissipation or generation varies greatly with chosen battery components (electrode material and electrolyte) and also throughout a charge cycle. This fact supports the theory that local changes in entropy are significant compared to the total entropy change in a cell, because the entropy change at each electrode has opposite sign, as shown by Gunnarshaug *et al.* in [6]. The total entropy change of the battery cell should be seen as the sum of contributions from different sub-systems (anode, cathode, electrolyte) that have different and varying changes in entropy. This can easily be understood by thinking about the electrodes during the discharge process. One of the electrodes gives electrons to the outer circuit, and lithium leaves the electrode structure, while the opposite happens on the other electrode. The oxidation/reduction of lithium causes a change in entropy that has opposite sign on the two electrodes. In addition to this, the lithiation/delithiation can cause structural changes that depend on the material and on the amount of lithium already present in the electrode. Therefore, the change in entropy is different depending on the material and state of charge. The structural changes may occur differently during lithiation and delithiation, which means that the change in entropy does not necessarily follow the same patter during charge and discharge, even for the same material. Thus, it is not possible to give the sign of entropy change based solely on whether the cell is charging or discharging, unless factor such as cell chemistry and state of charge are also accounted for. The entropy change could lead to net heating in some parts of the SoC-window, while leading to net cooling in other parts.

2.3.3 Ohmic Losses (rj)

Ohmic losses, or Joule losses, are caused by the friction the ions meet as they travel through the resistive electrolyte, and the electrons meet as they travel through a conducting material. The ohmic losses are calculated as the product of the current and the ohmic resistance (or current density and resistivity) [1]. The ohmic losses are always positive, meaning that they always contribute to heat generation.

2.3.4 Overpotential (η)

Overpotential is defined as the additional potential (beyond thermodynamic requirements) needed to drive a reaction at a certain rate [49]. It can also be seen as the departure from equilibrium potential that occurs when a Faradaic current passes through the cell, and is often therefore expressed as [49, 50]:

$$\eta = \Delta\varphi_{cell} - \Delta\varphi_{eq} \tag{2.6}$$

where:

$\Delta\varphi_{cell}$: Cell potential
$\Delta\varphi_{eq}$: Equilibrium potential

Where the equilibrium potential is the potential when equilibrium conditions are reached. Others chose to express the overpotential in terms of the reversible potential (which is taken at open circuit conditions), as done *i.e.* by Burheim [1]:

$$\eta = \Delta\varphi_{cell} - \Delta\varphi_{rev} - rj \tag{2.7}$$

where $\Delta\varphi_{rev}$ is the reversible potential. The reversible potential is defined through Nernst's equation (Equation 2.2).

When the overpotential is expressed by Equation 2.6, irreversible thermodynamic effects are not properly accounted for. The cell potential $\Delta\varphi_{cell}$ can differ from the equilibrium potential ($\Delta\varphi_{eq}$) even without a current passing through the cell, due to the effect of concentration gradients of neutral components in the electrolyte, or because of potential caused by a gradient in temperature. Therefore, Equation 2.6 is only valid if uniform temperature and concentration distribution is assumed in the electrolyte. The coupling of transport phenomena that cause potential gradients not accounted for by overpotential is discussed in Section 2.5. For the rest of this chapter, uniform distribution of neutral components, and uniform temperature is assumed.

Burheim and Ni *et al.* both separate between two types of overpotential (in addition to the ohmic losses) which are concentration overpotential (η_c) and reaction overpotential (η_r) [1, 51].

Concentration Overpotential (η_c)

The concentration overpotential is the overpotential due to an non-homogeneous distribution of species in the electrolyte, and is given by Burheim as [1]:

$$\eta_{\bar{c}} = \frac{\bar{R} \cdot T}{z \cdot F} \left| ln \frac{\bar{c}_{surf}}{\bar{c}_{bulk}} \right| \tag{2.8}$$

where:

$\bar{R}$: Universal gas constant
T : Absolute temperature
z : Amount of electrons per mole of reactants
F : Faraday's constant
$\bar{c}_{surf}$: Concentration of species at the electrode surface
$\bar{c}_{bulk}$: Concentration of species in the bulk

The concentration overpotential is caused by the resistance to the transport of reactant species to the point of reaction, and resistance to the transport of product species away from the cite of reaction [51]. These concentrations will be affected by the species' movement in the electrolyte. Fick's law of diffusion gives the relation between a rate of transport and the concentration gradient when only transport of mass is considered, as [1]:

$$J_i = D_i \frac{d\bar{c}_i}{dx} \tag{2.9}$$

where:

J_i : Transport rate (mass flux) of species i
D_i : Diffusion coefficient of species i
$\frac{d\bar{c}_i}{dx}$: Concentration gradient of species i

The mass flux is related to the current density by:

$$J_i = zFj \tag{2.10}$$

Combining Equations 2.9 and 2.10, the relation between the concentration gradient and current is given as:

$$\frac{d\bar{c}_i}{dx} = \frac{zFj}{D_i} \tag{2.11}$$

It becomes clear from Equation 2.11 and 2.8 that the concentration overpotential will be more pronounced at higher currents, and goes to zero as the current goes to zero. One can also deduce this from the reaction rate - as the current density increases, the reaction consuming reactant species and producing product species happens more frequently, and thus a higher concentration difference will establish between the bulk and the reaction cite. This equation does not, however, take into account the transient, non-equilibrium conditions, where coupling effects exist between mass transport, temperature and potential gradients. These coupling effects are explained in Section 2.5.

Reaction Overpotential (η_r)

The reaction overpotential [1] or activation overpotential [49, 51] is an overpotential that is required to provide the necessary activation energy to drive a reaction at the rate given by the current [49]. This is especially relevant at low currents where the kinetics are slow beacause more activation energy is required [49]. It can be described by the Butler-Volmer equation, which can be found in Appendix A.

2.4 Thermal Battery Models

A mayor motivation for investigating the local reversible heat effects in lithium-ion batteries is to gain deeper understanding of the heat generation and dissipation in order to make more precise battery models. This, in turn, will allow us to reduce battery aging, and improve performance and safety of the battery. Battery models are relevant to be applied in Battery Management Systems (BMSs), but also to design functional cooling systems and good algorithms for state of charge estimation. A few battery models will therefore be briefly revisited here, to get an idea of where these fields are today.

2.4.1 The Evolution of Thermal Battery Models

A common starting point when discussing battery models, is the model of an electrochemical system given by Sherfey and Brenner in 1958 [4]. Their equation can be written as done by Rao and Newman [52]:

$$-Q = It_d \sum_i \frac{T}{nF} f_i \Delta S_i + It_d \left(IR + \eta_a - \eta_c\right) \tag{2.12}$$

where f_i is the fraction of the total current I used for the reaction i, Q is the heat evolved in a time interval t_d, T is the temperature, n is the amount of electrons, F is Faraday's constant and ΔS_i is the entropy change of the reaction i. The first term on the right represents the reversible heat and the second term sums up the irreversible heats (ohmic losses and overpotentials at each electrode). This equation has been much used, and is the same one formulated in a simpler fashion by Lamb and Pollet in Equation 2.5.

A more extensive model was developed by Bernardi *et al.* [53]. They were the first to formulate a general energy balance for a battery system that included several electrochemical reactions, phase changes, mixing effects and joule heating [53]. Earlier models, like the one proposed by Sherfey and Brenner, had not included phase changes and mixing effects. The equation given by Bernardi *et al.* can be formulated as [52, 53]:

$$C_p \frac{dT}{dt} - \dot{Q} = -\sum_1 I_1 T \frac{d\Delta\varphi^{avg}_{ocv,1}}{dT} + \left(\sum_1 I_1 \Delta\varphi^{avg}_{ocv,1} - I\Delta\varphi\right) + \text{mixing} + \text{phase change} \tag{2.13}$$

where $C_p \frac{dT}{dt}$ is the accumulated heat in the cell, $\dot{Q}$ is the heat dissipated to the surroundings, $\Delta\varphi^{avg}_{ocv,1}$ is the average potential for reaction 1 measured at open circuit at average compositions, T is the temperature, I is the current and $\Delta\varphi$ is the cell potential. The mixing and phase-change terms can be found in [53].

Since Bernardi *et al.* proposed Equation 2.13 as a model, many authors have suggested different ways of modelling heat generation in batteries. Chen and Evans formulated three dimensional models based on the equation by Bernardi *et al.* for lithium-polymer batteries [54] and lithium-ion batteries [55]. Rao and Newman simplified the equation given by Bernardi *et al.* by neglecting phase change and mixing effects, and presented two ways of estimating heat generation in an insertion battery: a global energy balance, and a local heat generation method (see [52] for details). Pals and Newman formulated one-dimensional models for the thermal behaviour in lithium-polymer batteries both on cell level [56] and stack level [57]. Verbrugge modelled in three dimensions the temperature and current distribution in a battery module [58]. Gu and Wang made a coupled model that included both thermal and electrochemical effects [59], based on various theoretical and empirical equations like the Butler-Volmer equation, species conservation, charge conservation and an empirical equation for open circuit voltage from Doyle *et al.* [60]. Chen *et al.* developed a three-dimensional thermal model for LIBs considering convection and radiation on a cell stack and in a battery pack [61].

These are just some examples of important contributions to thermal models for lithium-ion batteries. Good overviews over work done in this field are given by various authors, such as Xia *et al.* [62], Liu *et al.* [63], Ramadesigan *et al.* [64], Bandhauer *et al.* [65] and Rao and Wang [66].

2.4.2 Models on Cell and Module Level

One way of classifying the models is by separating between models on cell and module level as done by Xia *et al.* [62].

Battery Models on Cell Level

The thermal behaviour in batteries are a complex interaction of several mechanisms, including mechanical, electrical, chemical and thermal, that all change with factors such as time, temperature, state of charge and cycling of the battery [62]. These interactions make it difficult to accurately quantify the heat generation in the cell, and there is still much ongoing research in this field.

As illustrated in the previous section, various mathematical approaches have been applied to understand the physics in a LIB system. Xia *et al.* classify the cell-level models as electro-thermal, electrochemical thermal, and thermal runaway (which aim to describe the thermal runway phenomena) [62]. They further differentiate on the dimensions of the models, which can be lumped-parameters, one-dimensional, two-dimensional, three-dimensional, or mixed-dimensional [62]. The reader is referred to [62] for examples of the different types of models.

In addition to accounting for the heat generation in the cell, it is important to have a thorough understanding of the heat transport. Factors such as thermal boundary conditions and thermophysical material properties (like density, thermal conductivity and heat capacity) are influential factors in this aspect. The difficulty lies in the highly anisotropic nature of the battery, where properties can vary by an order of magnitude in the in-plane direction compared to the cross-plane direction [62]. Large temperature gradients are bound to be present, giving further variation in temperature-dependent properties and complicating the modelling process.

It is normal to solve an equation for the thermal transport on the form [67]:

$$\rho C_p \frac{\partial T}{\partial t} = -\nabla \cdot \left(\underline{\underline{\kappa}} \nabla T \right) + Q_v \tag{2.14}$$

where ρ is the density of the domain material, C_p is the specific heat capacity $\underline{\underline{\kappa}}$ is the matrix of thermal conductivities and Q_v is the volumetric heat source. Solving this equation for the battery-specific conditions is a complex mathematical problem, which is usually done numerically [62].

Battery Models on Module Level

On module level, Xia *et al.* explore different cooling configurations, where factors such as coolant type, geometry of the cell and module, as well as cell characteristics must be taken into account [62].

The module level battery models are quite specific to the geometry, and are considered outside the scope of this text. Including local reversible effects (like the Peltier and Dufour effect which shall be explained in Section 2.5.2) is relevant for the models on module level, but only enters these models through the influence on the cell-level heat generation or dissipation.

2.4.3 Including the Peltier and Dufour Effects in Thermal Models

This thesis studies local reversible heat effects that have gone largely unaccounted for in literature. Spitthoff *et al.* proposed including terms for such effects in a thermal model, showing the influence of including them in a single cell and in a stack of 80 cells [9]. The latter case showed a substantial contribution to the change in temperature. They also point out that several authors have discussed these local, reversible phenomena [53, 56, 68–70], but that they are usually omitted in models. A common expression used for heat generation is [9]:

$$Q = I\left(\Delta_{tot}\varphi - \Delta_{tot}\varphi_{j=0} + T\frac{\Delta_{tot}\varphi_{j=0}}{dT} + M\overline{C_p}\frac{dT}{dt}\right) \tag{2.15}$$

Spitthoff *et al.* criticize this much-used expression, because it averages out the local heating and cooling effects, giving a less precise model (see [9] for details). Recent research indicates that the local heating and cooling from the Dufour and Peltier effects (see Section 2.5.2) may be substantial [2, 6, 9]. Including these effects in the models may therefore be critical to properly explaining the thermal behaviour of the batteries, especially in modules where several cells are stacked together.

2.5 Non-Equilibrium Thermodynamics Applied to Battery Systems

In order to properly study heat generation in batteries, the application of non-equilibrium thermodynamics has been proposed, because heat generation often takes place when the system is not at equilibrium. In a battery-cell, there are several transport processes happening simultaneously, and the interaction between these processes can best be described through non-equilibrium theory. In a LIB, there may be transport of heat, mass, and electric charge. There is an interaction between these factors that is not captured by equilibrium thermodynamics. For instance, mass transport occurs not only because of the presence of a concentration gradient, but also due to gradients in temperature and electric potential [8]. These so-called coupling effects will be briefly explained here. For a more thorough explanation, the reader is referred to literature regarding non-equilibrium thermodynamics, like [7] and [8]. An introduction to this field has also been given in Appendix B. In this section, the relevant equations are presented along with a short discussion of cross-transport phenomena that will be applied in the discussion in this thesis.

2.5.1 Non-Equilibrium Description of a Battery System

The starting point for the non-equilibrium description of a battery is the entropy production. It has been argued by Gunnarshaug *et al.* that a one-directional description can be applied to the system in this thesis (equivalent to the system used in [6]), so only transport in the x-direction is included here. For description of a full battery, where thermal insulation cannot be assumed, the three dimensional equation may have to be considered (this equation can be found in Appendix B). In the one-dimensional case the entropy production per unit volume and unit time can be written in terms of the fluxes and driving forces as [7]:

$$\Theta = \sum_{j=1}^{k} X_j \mathbf{J_j} \tag{2.16}$$

This equation will be applied to the system used in this thesis in Section 3.2. When the system has transport of mass, heat, and charge, Equation 2.16 would be written as:

$$\Theta = J'_q \frac{\partial}{\partial x}\left(\frac{1}{T}\right) - \sum_i J_i \frac{1}{T}\left(\frac{\partial \mu_{i,T}}{\partial x}\right) - j\frac{1}{T}\left(\frac{\partial \varphi}{\partial x}\right) \tag{2.17}$$

where J'_q is the measurable heat flux, $\frac{\partial}{\partial x}\left(\frac{1}{T}\right)$ is the thermal driving force, J_i is the mass flux of component i, $\left(\frac{\partial \mu_{i,T}}{\partial x}\right)$ is the chemical potential of component i, j is the current density, and $\frac{\partial \varphi}{\partial x}$ is the potential gradient. The reason behind using the measurable heat flux J'_q in stead of the actual heat flux J_q can be found in Appendix B.6.

To apply Equation 2.16, relations between the forces and fluxes must be expressed. Where equilibrium thermodynamics use Fick's law, Fourier's law and Ohm's law to describe the transport of respectively mass, heat and charge, non-equilibrium thermodynamics also take into account the conversion between different energy forms in the so-called coupling coefficients [8]. Any flux, J_i can be expressed as a linear, homogeneous function of the forces as [7]:

$$J_i = \sum_{j=1}^{k} L_{ij} X_j \tag{2.18}$$

where $i = 1, 2, ..., k$. Applying this to the classical laws of transport (Equations B.13 - B.15 in Appendix B) yields the following equations for a bulk system with transport in the x-direction only [8]:

$$\begin{aligned} J_q' &= L_{qq}\left(\frac{\partial}{\partial x}\frac{1}{T}\right) + L_{qm}\left(-\frac{1}{T}\frac{\partial \mu_T}{\partial x}\right) + L_{q\varphi}\left(-\frac{1}{T}\frac{\partial \phi}{\partial x}\right) \\ J_m &= L_{mq}\left(\frac{\partial}{\partial x}\frac{1}{T}\right) + L_{mm}\left(-\frac{1}{T}\frac{\partial \mu_T}{\partial x}\right) + L_{m\varphi}\left(-\frac{1}{T}\frac{\partial \phi}{\partial x}\right) \\ j &= L_{\varphi q}\left(\frac{\partial}{\partial x}\frac{1}{T}\right) + L_{\varphi m}\left(-\frac{1}{T}\frac{\partial \mu_T}{\partial x}\right) + L_{\varphi\varphi}\left(-\frac{1}{T}\frac{\partial \phi}{\partial x}\right) \end{aligned} \tag{2.19}$$

The vector equation 2.19 illustrates in one dimension, with mass flux of one component, the coupling between the different transport phenomena. The forces of transport include the thermal force ($\frac{\partial}{\partial x}\frac{1}{T}$), the chemical force ($-\frac{1}{T}\frac{\partial \mu_T}{\partial x}$) and the electrical force ($-\frac{1}{T}\frac{\partial \phi}{\partial x}$). The subscript T in μ_T indicates that the chemical potential should be taken at constant temperature. The coefficients (L_{ij}) are often referred to as phenomenological coefficients. The diagonal coefficients (L_{ii}) are called the main coefficients, and can be related to the thermal conductivity (λ), the mass diffusion coefficient (D), and the electrical conductivity (κ). The off-diagonal coefficients ($L_{ij}, i \neq j$) are the coupling coefficients. These express the interaction between the different transport processes, which have a relevant influence on the thermal behaviour of the battery. Notice particularly that the measurable heat flux (J_q') not only depends on the thermal gradient ($\frac{\partial}{\partial x}\frac{1}{T}$), but also on the gradient in chemical potential ($\frac{\partial \mu_T}{\partial x}$) and the electrical potential gradient ($\frac{\partial \varphi}{\partial x}$). A closer look shall now be taken on these cross-phenomena.

2.5.2 Interdependence of Transport Phenomena

The interdependence of the different transport phenomena, represented by the cross-coefficients ($L_{ij}, i \neq j$) in Equation 2.18, give rise to reciprocal transport effects. These effects have largely been ignored in battery models, even though recent research activity indicates that their influence may be substantial [2, 6, 9]. The mathematical description of these phenomena, as well as a further discussion of them can be found in Appendix B.4. A summary is given here.

The *Dufour Effect* is the transport of heat caused by a concentration gradient. The reciprocal effect, namely the transport of matter caused by a temperature gradient, is quite known, and often referred to as thermal diffusion or the *Soret effect*. Both these effects are small in gases and liquids [8]. In descriptions of homogeneous systems they can therefore often be neglected. This does not, however, apply to heterogeneous systems, where the coupling coefficients are large [8]. For a complete heat model in a full battery system the Dufour effect should be included.

Another such effect is the potential gradient that arises in a material due to a gradient in temperature. This effect can be quantified at open circuit conditions, and is referred to as the *Seebeck voltage*. The reciprocal effect is the *Peltier heat*, which is the reversible heat generated or dissipated locally at each electrode of a cell when current is flowing [9]. The Peltier effect is the main interest in this thesis, although the Dufour effect shall also be discussed. The total reversible heat of a cell is given by the entropy of the cell reaction ($\frac{T\Delta S}{F}j$ in Equation 2.5). Locally, at each electrode, the reversible heat effect is the Peltier heat [9]. The total contribution to the entropy of a cell can be found by summing up the contribution of the Peltier heats at each electrode (see Supplementary Material of [9]):

$$T\Delta S = \pi^{s,a} - \pi^{s,c} \tag{2.20}$$

Where ΔS is the total entropy change across the cell, $\pi^{s,a}$ is the Peltier heat at the anode and $\pi^{s,c}$ is the Peltier heat at the cathode. The opposite sign is because of the convention used, defining the Peltier heat as positive when the electrode acts as an anode in the traditional electrochemical sense [9]. It is not apparent from Equation 2.20 that the Dufour effect contributes to the change in entropy. However, as shall be shown in Section 3.2, and as shown by Spitthoff *et al.* in [9], the Dufour effect contributes by adding extra terms to the local Peltier heats ($\pi^{s,a}$ and $\pi^{s,c}$).

2.5.3 Finding the Peltier Heat from the Seebeck Coefficient

By definition it is intrinsically difficult to calculate the Peltier heat, seeing as it is the reversible heat generated or dissipated locally on one electrode when current is flowing. The difficulty lies in isolating it from the other heat dissipation terms (due to overpotential and ohmic losses) which are also dependent on the current (see Equation 2.5). Even though attempts to calculate the Peltier heat directly can be found in literature (see *i.e.* [71]), the errors are believed to be large in these measurements [5]. Gunnarshaug *et al.* argue that these calorimetric methods always give low estimates, because some of the heat always escapes to the surroundings because of the electrodes high conductivity [5]. Luckily, there is a way to circumvent this difficulty.

Lars Onsager derived a relation between the cross-coefficients ($L_{ij}, i \neq j$) based on the principle of microscopic reversibility (see i.e [7] for a derivation of the relations). In short, he stated for the coefficients in Equations 2.18 and 2.19 that [7]:

$$L_{ij} = L_{ji} \quad i \neq j \tag{2.21}$$

This means that the magnitude of influence between two cross-phenomena is reciprocal. This relationship essentially allows us to determine one coefficient from knowledge of the other. So instead of trying to measure the Peltier heat (local, reversible heat at the electrode when a current is flowing in the cell), it is possible to measure the Seebeck voltage (potential difference created by a temperature difference at open circuit conditions). For a symmetric cell with two equal electrodes, the Seebeck coefficient can be defined as [6]:

$$\epsilon(t) = \left(\frac{\Delta\varphi}{\Delta T}\right)_{j=0} \tag{2.22}$$

where $\Delta\varphi$ and ΔT are the potential and temperature differences across the cell respectively. The Onsager relation gives [6, 7]:

$$\pi(t) = -FT\epsilon(t) \tag{2.23}$$

Where F is Faraday's constant and T is the temperature. The time-dependency of these equations will be discussed further in Section 3.2.

Equations 2.22 and 2.23 form the foundation of the experimental work in this thesis. By measuring the potential difference in a symmetrical cell that is subject to a temperature difference while no current is flowing (a so-called thermocell), the Seebeck coefficient can be found. From the Seebeck coefficient, the Peltier heat of the electrode in question is simply found from Equation 2.23.

2.6 Thermoelectric Cells

A thermoelectric cell, or a thermocell, is an electrochemical cell were the two electrodes are at different temperatures [7]. In these cells, many of the trans-phenomena effects described in Section 2.5.2 are observed. The temperature difference through the cell causes an electromotive force (a potential), as a consequence of the Seebeck effect. If current is flowing through the cell, heat will be transported by the charge carriers (Peltier effect). The electrolyte in these cells is often a solution composed of two or more components, so concentration gradients are likely to form, which means that a Soret effect (or thermal diffusion) is also observed.

A thermocell can be used to convert heat to electricity, or vice versa, through the principles described Section 2.5.2 [72]. The thermocell also offers a way to study the heat preceding from these effects without studying the entire battery. By setting up a cell with a temperature difference but without current, the Soret and Seebeck effects can be measured, while other effects such as ohmic heating, overpotential and the Peltier effect are not present. The reciprocality between the Seebeck and Peltier effects given by Onsager's relation then allows a calculation of the Peltier heat based on the Seebeck coefficient. This is the principle used by Gunnarshaug *et al.* in [6], and is also the principle applied in this thesis to study local heating effects in LIBs. In fact, by looking at the voltage created by a temperature difference (the Seebeck voltage), the goal is to say something about the heat generated or absorbed reversibly when a current passes through a battery (Peltier heat).

The concept of thermoelectric cells is interesting, not only to understand heating effects in batteries, but also because these cells can be used to produce electric potential from heat, thus converting from a lower grade energy form to a higher one [72]. As much as 60 % of energy is believed to be lost worldwide, most of it as heat [73]. Finding a way to convert this low-grade energy back to useful higher-grade energy has been an ongoing effort in the scientific community for many years. Zhang and Zhao give an overview over the development of thermoelectric technology throughout history, where the newest technology is reported to have conversion efficiencies on the order of 15 - 20 % [73]. Thermoelectric materials are often environmental friendly, and give a way to convert heat to useful work, as well as a method for refrigeration. However, due to the low theoretical conversion efficiency and even lower achievable efficiencies, this technology still requires further development to see a wide commercialization [73]. The possible use of old batteries as thermoelectric cells to create useful electric energy from waste heat is seen as a secondary (and rather far-fetched) motivation for this thesis.

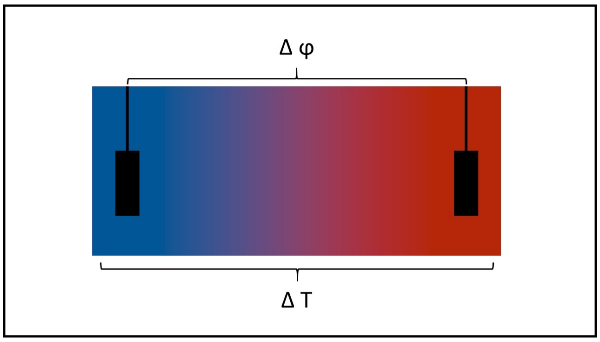

Figure 2.4: Illustration of how a thermoelectric cell (thermocell) works. A temperature difference between two identical electrodes causes a potential difference that can be exploited.

2.7 Previous Work on Single Electrode Peltier Heat

In this thesis, the aim is to quantify the local, reversible heat generation and dissipation on the electrodes of a battery, so that these effects can be considered in battery models and cooling systems. The local, reversible effects of interest are related to the entropy change of the cell. The reaction entropy can act both as a source and a sink for heat, and is further dependent on state of charge and battery chemistry [2, 3]. It can be shown that the heat generation or dissipation from entropy change in the cell can be attributed to the Peltier effect on each electrode through the equation (see Supplementary Material in [9]):

$$T\Delta S = \pi^{s,a} - \pi^{s,c} \tag{2.24}$$

where $\pi^{s,a}$ is the single electrode Peltier heat of the anode while $\pi^{s,c}$ is the single electrode Peltier heat of the cathode. It is thus interesting to quantify the Peltier effects to get a better understanding of the reversible heat found in batteries. It should be noted here that this equation is valid both for half-cells (where an electrode is paired with a Li-metal counter electrode) and full-cells (a normal battery cell). The terms from the transported entropy in the electrolyte (which shall be derived in Section 3.2) enter both Peltier heats in a way that makes them cancel for the total entropy difference, given that the same electrolyte is used in measurements of the individual electrode Peltier heats [5]. The terms from the electrolyte do, however, contribute to local heat effects, and cannot be omitted in a detailed thermal model [5]. Among these local effects is the Dufour effect, as shall be seen in the discussion of this thesis.

Even though the Peltier heat is a well established phenomena that has been much studied historically (see *i.e.* [74] or [75]), the local heat differences caused by this effect have long been omitted in models, and few values have been reported. In recent years, however, the phenomena has gotten attention in some research groups. Values have been reported for Seebeck coefficients using non-isothermal measurements on symmetric cells (thermocells). In addition to this, Gunnarshaug *et al.* showed in a recent review how earlier reported values of entropy change can be used to estimate the Peltier heat using Equation 2.24 [5]. These two approaches to measure and calculate the Peltier heat will be revisited in this section.

2.7.1 Peltier Heat from the Seebeck Coefficient in Symmetric Cells

Thanks to the historical interest in thermoelectric energy conversion, combined with the recent desire to achieve good thermal models of batteries, it is possible to find values in literature of the Peltier heat for single electrodes calculated from the Seebeck coefficient.

Kuzminskii *et al.* reported values for Seebeck coefficients in relation to the possible use of different materials in devices for direct thermoelectric energy conversion. Among the reported systems was a Li_xTiS_2 | $yLiBF_4$ in γ-BL | Li_xTiS_2 where the Seebeck coefficient was measured for a temperature difference of 60 K at different values of lithiation in the electrodes (0.6 < x (wt %) < 3.6, where x is from Li_xTiS_2) with varying composition of the electrolyte. With a 52:48 wt% $yLiBF_4$ to γ-BL the results showed a Seebeck coefficient varying from 0.65 mV/K to 4.65 mV/K when x was increased from 0.6 to 3.6, and a decrease from 4.65 mV/K to 1.29 mV/K when x was increased further from 3.6 to 5.3. The results also showed that with lower wt% of the lithium salt, the Seebeck coefficient decreased, from 4.65 mV/K at a 52:48 wt % composition to 3.06 mV/K at a 22:78 wt% composition [76].

Huang *et al.* reported Peltier heats for three different systems: (1) Li_xC_6 | $LiPF_6$ | $Li_{1-x}CoO_2$; (2) Li | $LiPF_6$ | $Li_{1-x}CoO_2$; and (3) Li | $LiPF_6$ | Li_xC_6. In these experiments the equilibrium voltage ($\Delta\varphi_{eq}$) was measured at different temperatures after a two hour rest. The reported values for the Seebeck coefficient ($\epsilon = \left(\frac{\partial \varphi}{\partial T}\right)_{j=0}$) was - 0.3086 ±0.010 mV/K for Li_xC_6 | $LiPF_6$ | $Li_{1-x}CoO_2$, - 0.0918 ±0.003 mV/K for Li | $LiPF_6$ | $Li_{1-x}CoO_2$, and 0.2151 ±0.004 mV/K for Li | $LiPF_6$ | Li_xC_6 [77]. Huang *et al.* also reported the value for a symmetric cell using metal lithium electrodes, giving $\epsilon = 1.17 \pm 0.03$ mV/K, leading to a Peltier heat of $q_r = -33.66$ kJ/mol at 298 K [77].

Hudak and Amatucci gave values for the initial Seebeck coefficient (t < 5 minutes) of symmetric thermoelectric cells using Li_xTiS_2, $Li_xV_2O_5$ and lithium metal electrodes in different electrolytes. The anions used were BF_4^- or PF_6^-, whereas PC or a mixture of EC and DEC were used as solvents. The results show that the Seebeck coefficient of both the intercalation electrodes varies in a non-linear, but similar, fashion with extent of lithiation ($0 < x < 0.8$). They show that the anion (BF_4^- vs PF_6^-) and the electrolyte concentration (0.1 M to 1 M) have a slight influence on the Seebeck coefficient, whereas no dependence on the solvent (EC:DEC vs PC) was found [78]. The reported values vary between roughly 0.4 mV/K and 1.3 mV/K depending on configuration, and the reader is referred to [78] for the complete results. The Seebeck coefficient for the lithium metal electrode was also reported here for a symmetric cell, giving values from roughly 0.95 mV/K to 1.25 mV/K when varying the anion salt, electrolyte solvent and electrolyte concentration [78].

Richter *et al.* used a similar set-up as the one used in the experiments in this thesis (which will be explained in Section 4.3) to measure the Seebeck coefficient for a symmetric cell with $LiCoO_2$ electrodes with a 1 M $LiPF_6$ in a 1:1 (v:v) of EC and DEC. They gave the first reports of two different, time-dependent phenomena with characteristic times of 4.5 and 21.3 hours. The reported Seebeck coefficient varied from - 2.8 mV/K at the initial state to 1.5 mV/K in the state characterized by partial Soret equilibrium [2]. This amounts to Peltier heats for the LCO electrode varying from - 45 kJ/mol to 84 kJ/mol just with the time dependence of the Seebeck coefficient. Richter *et al.* also used this data to calculate the Peltier heat of a carbon anode counterpart from full cell data, giving values from -73 kJ/mol to 56 kJ/mol. They concluded that the concentration gradients in the electrolyte could be quite large, and that the common assumption of uniform electrolyte in battery modeling is imprecise. Dufour and Peltier effects should be included when modeling thermal effects in batteries [2].

Black *et al.* report values of the Seebeck coefficient for symmetric thermocells of solid lithium metal and composite $Li_{3.5}Fe(CN)_6$ electrodes, as well as asymmetric cells combining these. All cells used 1 M $LiClO_4$ in a 1:1 solvent of EC:DEC. They used stepped and pulsed temperature gradients, where each step lasted 1000 seconds, and the Seebeck coefficient was reported as the average value of the last 500 seconds of each step [80]. The results showed Seebeck coefficients for the lithium metal around 1 mV/K, which also coincides with the results from Hudak and Amatucci in [78]. For the composite $Li_{3.5}Fe(CN)_6$ electrodes, the reported value was -0.6 mV/K. In the full cell measurements, however, the results indicated an unexpected synergy between the electrodes that caused the measured Seebeck coefficient to vary from the one expected from the measurements of each electrode in symmetric cells. When using isothermal pulsed changes in temperature, the reported Seebeck coefficient for the asymmetric cell was 4.3 ±0.4 mV/K, whereas only heating one electrode gave gave 0.7 ± 0.2 mV/K (when heating the Li-metal) and 3.9 ± 0.5 mV/K (when heating the $Li_{3.5}Fe(CN)_6$).

Gunnarshaug *et al.* reported the Seebeck coefficient of LFP ($LiFePO_4$) and graphite (Li_xC_6) electrodes in electrolyte of LiPF6 dissolved in EC:DEC (1:1 wt%) for initial, intermediate, and steady state when a temperature difference was applied across a symmetric thermocell, letting the measurements go for hours, up to days. For the LFP the average calculated values using a temperature difference from 2.4 K to 9.2 K was $\epsilon_0 = -1.3 \pm 0.4$ mV/K for t=0, $\epsilon_{int} = -0.9 \pm 0.3$ mV/K for the partial Soret equilibrium and $\epsilon_\infty = -4.3 \pm 0.6$ mV/K for full Soret equilibrium [6]. This gave a time-dependent Peltier heat with minimum value at partial Soret equilibrium of 26 kJ/mol, and a maximum value of 122 kJ/mol at full Soret equilibrium for the LFP [6]. The values reported for graphite varied in the same manner from 19 kJ/mol to 104 kJ/mol [6].

Gunnarshaug *et al.* also published in 2021 the first review paper concerning measurements of Seebeck coefficients and Peltier heats relevant to LIBs, indicating the recent interest in this topic [5]. In the review, most of the aforementioned research on Seebeck coefficients measured in symmetric, non-iosthermal cells was summarized [5]. In addition, they calculated the Peltier heat from the Seebeck coefficient in the experiments where this was not reported, following the method that will be shown in the next section (Section 2.7.2).

A summary of some of the reported Seebeck coefficients from measurements in symmetric non-isothermal cells have been given in Table 2.1. Notice that not all values have been included, and interested readers are referred to the complete overview in [5], or to the individual sources. The values are taken from [5] and the given individual sources. The error is given as two standard deviations as done in [5]. The sign convention used in this thesis has been applied to the values in the table, which means that the sign of some of the reported values have been changed (see Section 2.7.3). Most these authors have reported one value, unaware of the possible time-changing nature of the Seebeck coefficient reported by Richter *et al.* [2]. The time-frame for the reported values has therefore also been reported.

Table 2.1: Reported values of the Seebeck coefficient for some electrode materials using symmetric cells.

Electrode	x	Electrolyte	Timeframe	ΔT	ϵ [mV/K]	Source
Li_xTiS_2	0.6 (wt%)	$LiBF_4$ in γ-BL (52:48 wt%)	-	60 K	- 0.65[1]	[76]
	1.3 (wt%)				- 0.79	
	3.0 (wt%)				- 2.02	
	3.6 (wt%)				- 4.62	
	4.5 (wt%)				- 1.85	
	5.3 (wt%)				- 1.29	
	3.6 (wt%)	$LiBF_4$ in γ-BL (36:64 wt%)	-	60 K	-3.84	[76]
		$LiBF_4$ in γ-BL (22:78 wt%)			-3.06	
	0	1 M $LiPF_6$ in EC:DMC (1:1 v/v)	< 5 min	1 - 5 K	-0.49 ± 0.09	[78]
	0.2				-1.1 ± 0.8	
	0.4				-1.16 ± 0.12	
	0.6				-1.03 ± 0.08	
	0.8				-1.00 ± 0.12	
	0	1 M $LiBF_4$ in PC	< 5 min	1 - 5 K	-0.52 ± 0.09	[78]
	0.2				-1.0 ± 0.8	
	0.4				-0.96 ± 0.13	
	0.6				-0.96 ± 0.11	
	0.8				-0.92 ± 0.12	
$Li_xV_2O_5$	0	1 M $LiPF_6$ in EC:DMC (1:1 v/v)	< 5 min	1 - 5 K	-0.60 ± 0.12	[78]
	0.2				-0.98 ± 0.10	
	0.4				-1.06 ± 0.07	
	0.6				-1.0 ± 0.2	
	0.8				-0.88 ± 0.10	
$Li_{3.5}Fe(CN)_6$	-	1 M $LiClO_4$ in EC:DEC (1:1)	1000 sec	1 - 5 K	-0.57 ± 0.12	[79]
Li_xFePO_4	1	1 M $LiPF_6$ in EC:DEC (1:1 wt%)	< 15 min	2.4 - 9.2 K [2]	-1.3 ± 0.2	[6]
Li_xCoO_2	1	1 M $LiPF_6$ in EC:DEC (1:1 wt%)	N/A [3]	2.90 - 7.84 K [4]	-2.8 ± 0.3	[2]
Li	-	1 M $LiPF_6$ in EC:DMC (1:1 v/v)	2 h	0 - 25 K	-1.17 ± 0.06	[77]
	-	1 M $LiClO_4$ in EC:DEC (1:1)	1000 sec	1 - 5 K	-0.98 ± 0.06 1.00 ± 0.04	[79]
	-	1 M $LiBF_4$ in PC	< 5 min	1 - 5 K	-1.07 ± 0.06	[78]
	-	0.1 M $LiBF_4$ in PC	< 5 min	1 - 5 K	-0.96 ± 0.09	
	-	1 M $LiPF_6$ in PC	< 5 min	1 - 5 K	-1.24 ± 0.07	
	-	1 M $LiPF_6$ in EC:DMC (1:1 v/v)	< 5 min	1 - 5 K	-1.25 ± 0.12	

2.7.2 Peltier Heat from Full-Cell and Half-Cell Entropy Change

In battery literature it is common to apply the term "full-cell" when referring to a battery cell, whereas a "half-cell" is a cell where one of the electrodes has been replaced with a lithium metal electrode [5]. In addition to summarizing calculated Seebeck coefficients from non-isothermal symmetric cells, Gunnarshaug *et al.* calculate the Peltier heats from earlier entropy measurements of half-cells and

---

[1] Errors not reported

[2] Estimated internal temperature difference in the cell (see [6])

[3] The initial Seebeck coefficient was calculated from other points in the measurements, so not taken at the initial time (see [2])

[4] Estimated internal temperature difference in the cell (see [2])

full-cells [5]. By measuring the Seebeck coefficient, and thereby the Peltier heat, of one electrode, the Peltier heat of the other electrode may be calculated from data of half-cell and full-cell entropy measurements [5]. This will be applied here to stipulate values for the anode from the measured values of different cathode materials found in the experiments in this thesis. It is thus relevant to show how these calculations are carried out.

As stated by Gunnarshaug *et al.*, a common mistake in literature is to believe that the local heat effect on one electrode surface can be determined as the change in entropy of a half-cell using that same electrode [5]. Assuming that the totality of the entropy change in a half-cell comes from one electrode is not correct. The contribution from the lithium metal electrode is rather large (see *i.e.* the values reported by Hudak and Amatucci in [78] or Black *et al.* in [79] for the Seebeck coefficient of symmetric cells using lithium metal electrodes compared to the intercalation electrodes in the same papers). Therefore, assuming that the total entropy change comes from the electrode that is not lithium metal gives big errors in calculations.

In classical thermodynamics, the entropy change of an electrochemical cell is given as [5]:

$$\Delta S = nF\left(\frac{d\varphi}{dT}\right)_{j=0} \tag{2.25}$$

where n is the number of electrons involved in the reaction, F is Faraday's constant, $\left(\frac{d\varphi}{dT}\right)_{j=0}$ is the temperature dependence of the *emf* taken at open circuit conditions (the Seebeck coefficient). The reversible heat term (which is also found in Equation 2.5) is expressed as [5]:

$$q = \frac{T\Delta S}{nF}j \tag{2.26}$$

The entropy change of the full-cell battery has often been calculated using Equations 2.25 and 2.26. Different potentiometric methods have been applied, and the most common methods have been summarized by Zhang *et al.* in [81]. Combining potentiometric methods with Equation 2.25 gives one way of achieving the full-cell change in entropy. Another class of methods is by calorimetry: measuring the reversible heat and calculating the change in entropy from Equation 2.26. Such measurements and how they are used to calculate the entropy change can be found in [82, 83].

The procedure for calculating the Peltier heat of one electrode when measurements of the other have been made combines reported values for the change in entropy with Equation 2.24. Using Equations 2.25 or 2.26, the entropy change can be found either by measuring the Seebeck coefficient (temperature dependence of the *emf*) or by measuring the reversible heat. Once the entropy change has been quantified, one can calculate the Peltier heat of the missing electrode by applying Equation 2.24. Although few reports of the Peltier heat exist in literature, many authors have reported the entropy change of half-cells and full-cells. Gunnarshaug *et al.* exploited this fact in [5], and calculated the Peltier heat from earlier reports of entropy change in half-cells. Using the reported values of the Seebeck coefficient of pure lithium from Table 2.1, they were able to report values for the Peltier heat for a wide range of electrode materials and lithiation states (see [5] for the complete tables). Key values of Peltier heats calculated from half cell data that is relevant for the electrode materials studied in this thesis has been taken from [5], and plotted in Figure 2.5a - 2.5d.

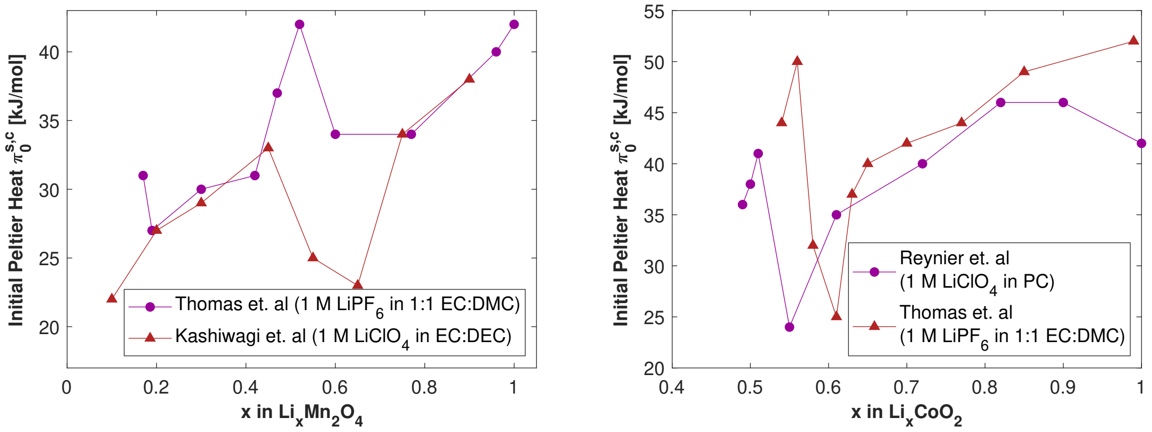

(a) Initial Peltier heat for LMO **(b)** Initial Peltier heat for LCO

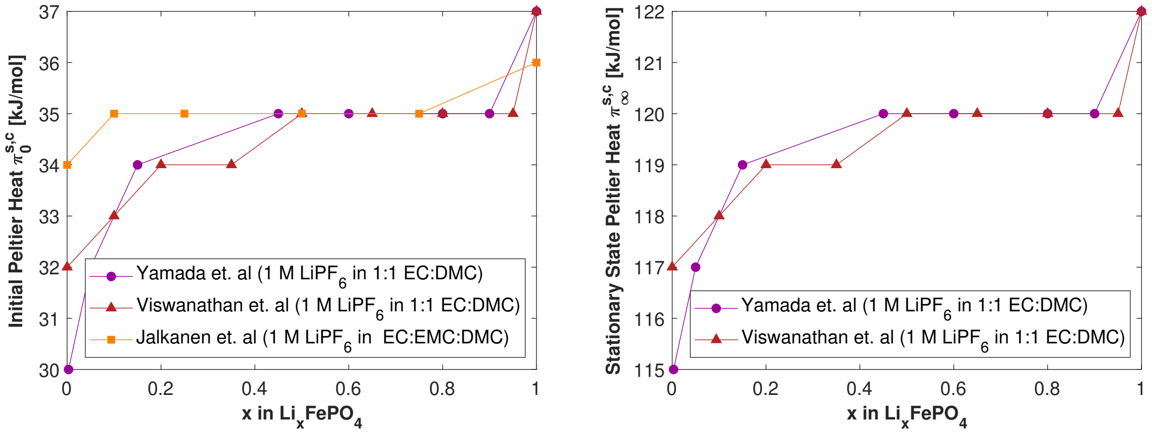

(c) Initial Peltier heat for LFP **(d)** Stationary State Peltier heat for LFP

Figure 2.5: Calculated values of the initial Peltier heat as a function of lithiation state based on reported half-cell entropy change by different authors in different electrolytes for (a) LMO; (b) LCO; and (c) LFP. (d) Shows the steady state Peltier heat for LFP calculated from values of the half-cell entropy change reported by different authors. All values are taken from [5]

The plots of the Peltier heat calculated from half-cell entropy measurements for the LFP, LMO and LCO electrodes shown in Figure 2.5 give some idea of the values that should be expected when calculating the Peltier heat from the Seebeck coefficient at different states of charge. The variations in the Peltier heat that are seen for LMO around $x = 0.5$ and LCO for $0.5 < x < 0.7$ are believed to be due to structural changes in the electrodes around these lithiation states [5]. As stated by Gunnarshaug *et al.*, more measurements of the peltier heat are needed to validate the data in these graphs [5].

In their review, Gunnarshaug *et al.* expressed the need for more detailed studies on the Dufour effect (heat flow caused by a concentration gradient) [5]. They proposed studying this phenomena by comparing initial to stationary values of the Seebeck coefficient. They also expressed the need for measured Peltier heats, as opposed to the estimated values found based on Equation 2.24 and the use of earlier reported values for entropy change. Measuring the Peltier heat (or Seebeck coefficient) would serve also to validate the values estimated in [5]. In addition, they stipulate that the Peltier heat undergoes large changes when the level of lithiation in the intercalation electrode changes (as also seen in the values in Table 2.1), and suggest that the Peltier heat should be measured for electrodes at different states of charge. The work in this thesis therefore aims to (1) report values of Seebeck coefficients for electrode materials, electrolytes, and lithiation states not reported before (2) report values for the steady state Seebeck coefficient by conducting experiments that have a long time-span in order to quantify the Dufour effect.

2.7.3 Clarifications of Terms and Conventions

Thermoelectric vs Thermogalvanic Seebeck Coefficients

The definition of the Seebeck coefficient for a metal-lithium electrode has caused some confusion in literature. Some have believed that using half-cells (an electrode coupled with a lithium-metal electrode) could give values for the Seebeck coefficient of the not-lithium electrode, because the Seebeck coefficient of the lithium metal electrode was close to zero [84]. This is not true. The mistake is believed to be because the value of the Seebeck coefficient measured in dry conditions was applied in stead of the value calculated with electrolyte, as pointed out by Black *et al.* [79]. While the dry value is reported around 0.01 mV/K [85], the wetted values is around 1 mV/K [77–79]. Both values are denoted $\epsilon = \left(\frac{\Delta\varphi}{\Delta T}\right)_{j=0}$, but the first is measured in a solid-state sample, whereas the second is taken across a cell with an electrolyte. In the first case, the (de)lithiation process will not take place, thus entropy change will be much smaller, seeing as much of the change in potential is attributed to this process [79]. When the term Seebeck coefficient is applied in this thesis, reference is made to the Seebeck coefficient taken across a cell with an electrolyte, unless otherwise specified.

Sign Convention

Much confusion may arise due to imprecise or unspecified sign conventions. As mentioned earlier, the battery community often refers to one electrode as cathode both during charge and discharge, even though the cathodic reaction (reduction) only happens on this electrode during discharge. The same goes for the electrode acting as anode during discharge. This terminology, although somewhat confusing, has also been applied in this thesis.

The sign of the Peltier heat changes if the electric current changes direction, thus it is essential that it is reported consistently [5]. In this thesis the reported values for the Peltier heat will be given for the electrodes as if an oxidation reaction were taking place on it, as done in [5]. This means that the reported values are valid for anodes during discharge and cathodes during charge, if the battery world definition of these terms are used. Consequently, when the values are combined, one of the values must change sign. If a traditional terminology were applied, the Peltier heats are reported for the electrodes when "acting as anodes".

The chosen sign convention allows for a better discussion of the local heat effects. From Nernst' Equation (Equation 2.2), one can see that the potential jump produced at the electrode and the Peltier heat have the same sign. When the electrode reaction contributes to work done, the potential jump and Peltier heat are positive. Positive Peltier heat thus means that there is a cooling effect. Looking at Equation 2.24, one can see that a positive entropy change across the cell (which contributes to the work done by the cell) will give a net positive Peltier heat, meaning that the cooling effect at the anode is higher than the heating at the cathode.

A discussion on the sign of reported values is given by Gunnarshaug *et al.* in [5]. In general, there is no agreement on convention in the values reported in literature, and the different sources use different conventions. Thus, care must be taken when comparing data from different sources.

Chapter 3

System Description

In this chapter the experimental set-up used to calculate the Peltier coefficients for the different materials and electrolytes used in this thesis is first described. Thereafter, the equations from non-equilibrium theory presented in the previous section are applied in order to find mathematical descriptions of the system, which will be used to obtain the results given in Chapter 5. The system description applies non-equilibrium thermodynamic theory from [7] and [8] in a similar manner as done by Gunnarshaug *et al.* in [6]. Seeing as the work in this thesis builds on the experiments done in [6] and use an identical experimental set-up, much of the system description will resemble the system description given there. However, because non-equilibrium thermodynamic theory is an unknown field to many, the essential derivations have still been included here.

3.1 Description of the System

The system to be described is the experimental set-up that was used to measure the potential in the thermocells at different ΔT. This potential was then used to calculate the Seebeck coefficient from the relations that will be derived in Section 3.2, based on the theory presented in the previous chapter. The Seebeck coefficients were then related to the Peltier heats using Equation 2.23.

This thesis was intended to expand the results found by Gunnarshaug *et al.* in [6] to other cell chemistries, different electrolyte compositions, and different SoCs. Consequently, the same experimental set-up used by Gunnarshaug *et al.* was applied in this thesis. For the convenience of the reader, the set-up is re-explained here.

3.1.1 The Thermoelectric Cell

A thermoelectric pouch cell with two identical electrodes and a stack of separators was assembled according to the procedure to be explained in Section 4.1. A schematic of the pouch cell cell is presented in Figure 3.1.

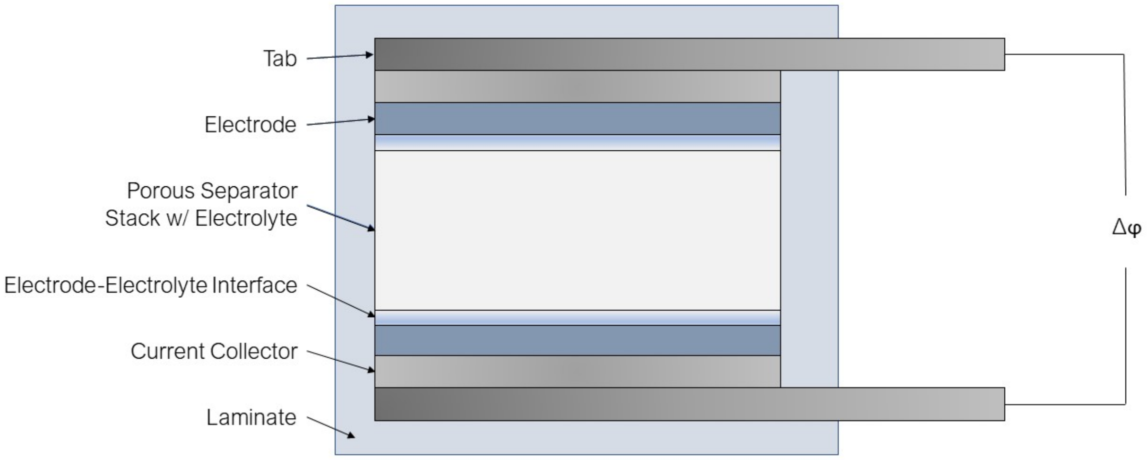

Figure 3.1: Schematic of the thermoelectric cell used in the experiments. This is only for illustrational purposes so the components are not to scale. The electrode-electrolyte interface is included as a separate component due to the derivations to be made in Section 3.2

The theoretical derivations of equations that will be done in Section 3.2 are based on this system. The notation used will be of importance, and is therefore presented in Figure 3.2. When subscripts are used for a variable at a certain location the first subscript represents in which subsystem the variable is taken, and the second subscript gives information about where in the subsystem it was taken. When subscripts are used for differences, the difference is usually taken across one subsection,

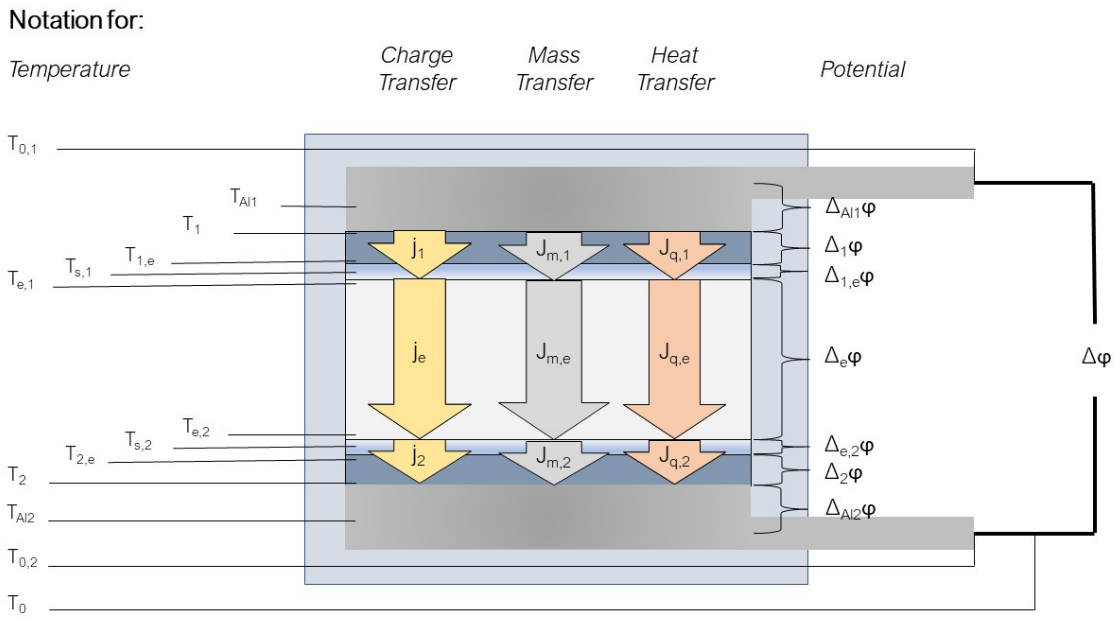

Figure 3.2: Notation used in the derivations in this thesis. For illustrational purposes only - the directions of the fluxes are not physical

and is therefore given with that subsection as a subscript. For example, $T_{1,e}$ is the temperature in the top electrode, taken close to the electrolyte, while $T_{1,Al1}$ is the temperature in the top electrode taken close to the current collector. The temperature difference $\Delta_1 T = (T_{1,e} - T_{1,Al1})$ is the difference across the top electrode. For simplicity, it is assumed that the tabs and the current collector are one component. In the actual cells, these are separate, which may give some inaccuracies in this model. It should also be noted that the electrode/electrolyte interface is included as an own component. Treating the surface as an autonomous thermodynamic system is consistent with the treatment given to surfaces by Kjelstrup and Bedeaux in *Non-Equilibrim Thermodynamics of Heterogenous Systems*. The validity of this assumption is not discussed here, but is given in [8].

3.1.2 Experimental Set-Up

The cell was inserted in a set-up intended to keep the two electrodes at different, but constant temperatures, while limiting the loss of heat to the surroundings as much as possible. This set-up is shown schematically in Figure 3.3, and explained in detail in Section 4.3. The temperature was measured on each side of the set-up using thermocouples. These were inserted between two copper plates to ensure good thermal contact. The copper plate closest to the cell was thin in order to measure the temperature as close to the surface of the cell as possible. Hot water was circled through the top part of the set-up and cold water through the bottom to ensure a constant temperature profile through the cell. In order to avoid additional convection effects due to lower density in the hot electrolyte compared to the cold electrolyte, the hot water was always circled through the top of the set-up. This is also the reason why the experiment was carried out horizontally in stead of vertically - to avoid unnecessary in-plane convection causing concentration gradients perpendicular to the plane between the electrodes.

When at steady state, a temperature gradient is established across the system. Because the different parts have different thermal conductivities, the gradient varies throughout the system. The temperature profile for the cell is established theoretically and validated through experiments in Section 4.4.

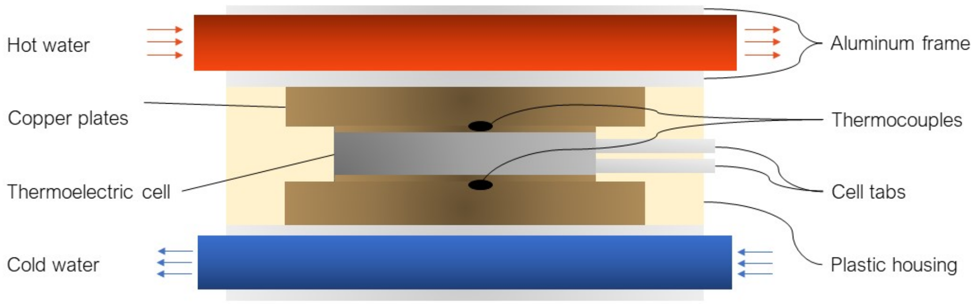

Figure 3.3: Schematic of the experimental set-up used to measure the potential when a temperature difference established in the cell

3.2 Mathematical System Description

The system is divided into five parts for the theoretical derivations: the two current collectors, tabs and electrode bulk phases (seen as one continuous component), the electrolyte bulk phase, and the two electrode-electrolyte interfaces. The notation used is described in Figure 3.2. The electrodes are identical, porous structures filled with electrolyte. The separator, which is a porous structure soaked in electrolyte, is not considered, as it is inert and only serves the function of maintaining the electrolyte in place and avoiding physical contact between the electrodes. Thus, the subsystem considered is the electrolyte bulk phase. When no transport takes place perpendicular to the axis connecting the electrodes, the system can be considered one-dimensional. If the cell were perfectly insulated on the sides, no heat would be lost in this direction. Even though the insulating material used has an air-gap for the tabs, the losses in this direction are likely to be small, so perfect insulation is assumed to simplify the equations.

3.2.1 The Total Potential

The experimental set-up shown in Figure 3.3 is used together with an Aguilent Data Aquisition Unit and the BenchVue software to determine the development of the total potential difference between the tabs when a temperature gradient establishes in the cell. From the total potential, the contributions from each subsystem must be found. The total potential can be expressed as the sum of the contributions:

$$\Delta\varphi = \Delta_1\varphi + \Delta_{1,e}\varphi + \Delta_e\varphi + \Delta_{e,2}\varphi + \Delta_2\varphi \tag{3.1}$$

Where the subscripts are: *1* - upper electrode, current collector and tab; *2* - lower electrode, current collector and tab; $1, e$ - upper electrode-electrolyte interface; $2, e$ - lower electrode-electrolyte interface; and e - electrolyte. Note that the current collectors and tabs are included in components 1 and 2.

Ideally, one would simply measure the potential across one sub-system at a time. However, a method has yet to be discovered that allows implementation of potential-measurement devices on different locations in the cell without affecting the behaviour. Thus, theoretical calculations of the contribution to the total potential will have to be found for each component. Note that the two electrode bulk phases are dictated by the same equations, and derivations are therefore only done for one side. The same goes for the electrode-electrolyte interfaces.

3.2.2 Equations for the Electrode Bulk

In the current collectors and tabs there is no flow of mass, only of charge and heat. It can be shown that this can also be approximated in the electrode bulk. If a temperature gradient were present across the electrode, one would have to differentiate between the electrodes at 0 % SoC and at other states of charge because the temperature gradient could give rise to a diffusion of lithium (Soret effect). At 0 % SoC the electrodes are fully lithiated, so the lithium has no vacancies to move to. At other states of charge, the lithium could potentially move to other vacancies if a driving force were present. However, it is assumed that the thermal conductivity of the electrodes are so much greater than that of the electrolyte that the temperature gradient in the electrodes can be ignored.

In addition to this, the potential difference between the electrodes used in the symmetric cell should be very low, because the cells were short-circuited before the experiments. Thus there should not be any driving forces causing lithium diffusion in the cells, and it is assumed that mass diffusion will not be present. Thus, the only transport would be of heat and charge, also in the electrodes, and it is possible to treat the electrodes, the current colletors and the tabs as one component.

By assuming that the transport happens in only one direction, Equation 2.16 for the entropy production in the system becomes:

$$\Theta = \sum_{j=1}^{k} X_j \mathbf{J_j} = J_q \frac{\partial (1/T)}{\partial x} - j \frac{1}{T} \frac{\partial \varphi}{\partial x} \tag{3.2}$$

The corresponding flux equations, with no mass transfer, can be found from Equation 2.19:

$$J_q = L_{qq} \left(\frac{\partial}{\partial x} \frac{1}{T} \right) + L_{q\varphi} \left(-\frac{1}{T} \frac{\partial \varphi}{\partial x} \right) \tag{3.3}$$

$$j = L_{\varphi q} \left(\frac{\partial}{\partial x} \frac{1}{T} \right) + L_{\varphi\varphi} \left(-\frac{1}{T} \frac{\partial \varphi}{\partial x} \right) \tag{3.4}$$

Note that Onsager's reciprocal relations apply, yielding equal cross-coefficients $L_{q\varphi} = L_{\varphi q}$. It is now possible to define the following in this system:

Peltier coefficient (π):

$$\pi \equiv \left(\frac{J_q}{j/F} \right)_{dT=0} = \frac{L_{q\varphi}}{L_{\varphi\varphi}} = T S^*_{e-} \tag{3.5}$$

Thermal conductivity (λ):

$$\lambda \equiv - \left(\frac{J_q}{\partial T / \partial x} \right)_{j=0} = \frac{1}{T^2} \left(L_{qq} - \frac{L^2_{q\varphi}}{L_{\varphi\varphi}} \right) \tag{3.6}$$

Resistivity (r):

$$r \equiv - \left(\frac{\partial \varphi / \partial x}{j} \right)_{dT=0} = \frac{T}{L_{qq}} \tag{3.7}$$

In these three expressions, the first equality gives the definition of the different coefficients, while the second equality shows them as inserted into Equations 3.3 and 3.4. The subscript e^- in S^* is used to indicate that the entropy is transported by electrons only in this sub-system.

In Equations 3.3 and 3.4, it is possible to eliminate the potential gradient from one of the equations. If the potential gradient is expressed using Equation 3.4, the elimination is done in the following way:

$$\left(-\frac{1}{T} \frac{\partial \varphi}{\partial x} \right) = \frac{1}{L_{\varphi\varphi}} \left(j - L_{q\varphi} \left(\frac{\partial}{\partial x} \frac{1}{T} \right) \right)$$

Inserting into Equation 3.3, and using the calculated partial derivative of the temperature, $\frac{\partial}{\partial x} \frac{1}{T} = -\frac{1}{T^2} \frac{\partial T}{\partial x}$, gives:

$$J_q = -\frac{L_{qq}}{T^2}\left(\frac{\partial T}{\partial x}\right) + \frac{L_{q\varphi}}{L_{\varphi\varphi}}\left(j + \frac{L_{q\varphi}}{T^2}\left(\frac{\partial T}{\partial x}\right)\right)$$

Which can be rearranged to express the temperature gradient as:

$$\frac{\partial T}{\partial x} = \left(J_q - \frac{L_{q\varphi}}{L_{\varphi\varphi}} j\right) \cdot \left[\frac{1}{T^2}\left(-L_{qq} + \frac{L_{q\varphi}^2}{L_{\varphi\varphi}}\right)\right]^{-1}$$

Replacing with equalities from Equations 3.5 - 3.7 yields:

$$\frac{\partial T}{\partial x} = \left(J_q - \frac{\pi j}{F}\right)\left(-\frac{1}{\lambda}\right) \tag{3.8}$$

In a similar fashion, one can find an expression for the potential gradient [6]:

$$\frac{\partial \varphi}{\partial x} = -\frac{\pi}{TF}\frac{\partial T}{\partial x} - rj \tag{3.9}$$

When measurements are made at open circuit, the current density is zero ($j = 0$), so the equations simplify to:

$$\frac{\partial T}{\partial x} = J_q\left(-\frac{1}{\lambda}\right) \tag{3.10}$$

$$\frac{\partial \varphi}{\partial x} = -\frac{\pi}{T}\frac{\partial T}{\partial x} \tag{3.11}$$

By integrating both sides of Equation 3.11 across the length of the electrodes, current collectors and tabs, the potential difference for the upper electrode system can be found as [6]:

$$\boxed{\Delta_1 \varphi = S_{e-}^* \Delta_1 T} \tag{3.12}$$

Where the transported entropy in this specific case has been expressed as $S^* = \pi/T$. The calculations on the bottom system is the same, and yields:

$$\boxed{\Delta_2 \varphi = S_{e-}^* \Delta_2 T} \tag{3.13}$$

Considering the Current Collectors, Tabs and Electrode Bulk as One Component

Note that the potential drop in the surface between the current collectors and tabs, as well as the surface between the current collector and electrode bulk have not been accounted for as interfaces. Considering the interface as a separate system is only relevant if the properties at the surface vary significantly from the properties in the bulk. Should the tabs and current collector be separated by electrolyte or an air pocket, the properties at the surface may vary from the properties in the bulk, and such a consideration would be relevant. However, if there is good contact between the current collector and tabs, they are of the same material and can be considered one bulk phase. Good contact should be achieved when the cells are sealed in vacuum. Regarding the electrode-current collector interface, good contact is guaranteed by the production method. The active material of the electrode is coated on to an aluminium backing as a slurry, and then dried. However, the electrode and the current collector are of different materials, so the interface could potentially be different from the bulk phases. The argument in this case is that the transported entropy of "good metals" is usually close to zero, and so the difference between the entropy transport in the metallic electrode material and the metal aluminum current collector is irrelevant [86]. Agar displays typical values for some metals (Pb, Cu, Ag, Pt and Bi), and they are mostly in the range 0.121 - 0.460 [J/mol K] with the exception of Bi which has a reported value of 7.11 [J/mol K] [1] [86]. The contribution to the Seebeck coefficient is given as $\frac{S^*_{e^-}}{F} = \frac{[0.121, 0.460]}{\cdot 96000} \approx 1 \cdot 10^{-5} - 5 \cdot 10^{-5} (V/K)$. If these values are compared to the Seebeck coefficients found by Gunnarshaug *et al.* in [6], which are on the order of 1 mV/K with an accuracy of 10^{-4} V, it becomes clear that the effect of the transported entropy in the metals can be ignored. Therefore, separating between the electrode bulk phase and the current collector is hardly necessary, and a separate treatment of the different components is deemed redundant.

3.2.3 Equations for the Electrode - Electrolyte Interfaces

The electrode-electrolyte interface is considered a surface following the convention used by Kjelstrup and Bedeaux in *Non-Equilibrium Thermodynamics of Heterogeneous Systems* [8]. Considering the surface as a separate thermodynamic system can be convenient if the properties vary significantly across it. By definition, a surface has a thickness that is small compared to adjacent bulk phases, and changes in parameters such as temperature or potential for a distance comparable to the surface thickness in the homogeneous regions are small [8]. While the variables in homogeneous phases are continuous, they are considered discrete at the surface. This is necessary, because the surface can act as a source or a sink of heat or potential due to the reactions happening on it, which causes discontinuities.

Even though a variety of reactions can take place on the electrode surface throughout the lifetime of a battery - *i.e.* electrolyte reduction during formation or dissolution of active material in the electrolyte during cycling - there is one dominating reaction in terms of frequency: the lithium reduction and oxidation. In order to achieve a completely accurate model, one would have to include all the possible reactions, but here focus is given to standard operation, and reactions that happen sporadically, or under very specific conditions, have therefore been omitted. The electrode reaction for the anode during discharge is lithium oxidation [6]:

$$Li \longrightarrow Li^+ + e^- \tag{3.14}$$

At the cathode the opposite reaction occurs, reducing the positively charged lithium-ions to neutral Li that intercalates into vacancies in the host structure. Upon charging, the situation is reversed, so that the reactions happen at opposite electrodes. These reactions cause the transport of mass and charge across the surface. One mole of Li-ions are produced at the anode and consumed at the cathode per Faraday of electric charge passing through the outer circuit during discharge. These changes, plus the transport in the electrolyte, give the change in composition close to each electrode [8]. By omitting transport along the surface, the entropy production at the surface can be written on the following form [6]:

---

[1] The values in [86] are given in [cal/mol K]. The conversion is done by multiplying the values with a factor 4.184 [J/cal].

$$\Theta^s = J_q'^i \Delta_{i,s}\left(\frac{1}{T}\right) + J_q'^o \Delta_{s,o}\left(\frac{1}{T}\right) - j\frac{1}{T^s}\left(\Delta_{i,o}\varphi + \frac{\Delta_n G^s}{F}\right) \tag{3.15}$$

The notation at the surface is given so that the first subscript represents where the quantity comes from, and the second subscript where it goes to. i is the bulk phase before the surface, o is the bulk phase after the surface, and s is the surface. For example, $\Delta_{i,s}T$ is the temperature change from the bulk phase before the surface (T^i), to the temperature at the surface (T^s).

Studying the right hand side of Equation 3.15, one can see that the entropy production on the surface is equal to the entropy transported by the heat flux from each of the adjacent bulk phases to or from the surface ($J_q'^i$ and $J_q'^o$), the entropy transported by charged particles ($\Delta_{i,o}\varphi$) and the neutral components ($\Delta_n G^s$). Notice the force $\left(\Delta_{i,o}\varphi + \frac{\Delta_n G^s}{F}\right)$. The reaction rate of the chemical reaction (r) is tied to the electric current density (j) through the relation $r = j/F$, which is why the term can be written as $j\frac{\Delta_n G^s}{TF}$ in stead of $r\frac{\Delta_n G^s}{T}$. Therefore, the entropy transported by charge and mass are interrelated, and combine to one effective force with two contributions: (1) the change in potential across the surface ($\Delta_{i,o}\varphi$), and (2) the Gibbs free energy of the neutral components ($\Delta_n G^s$). In this formulation by Gunnarshaug *et al.*, it is implicit that no mass transfer happens across the surface that is not tied to the chemical reaction.

When at equilibrium, and when the temperature is constant ($\Delta T = 0$), the excess entropy production is zero ($\Theta = 0$), leaving Nernst's equation:

$$\Delta_{i,o}\varphi = -\frac{\Delta_n G^s}{F} \tag{3.16}$$

Which is valid for *emf*-measurements where small currents are used [7].

Returning to the non-equilibrium situation, Equation 3.15 gives the corresponding flux-force relations [6]:

$$J_q'^i = J_{q_1}' = L_{q_1q_1}\left(\Delta_{i,s}\frac{1}{T}\right) + L_{q_1q_2}\left(\Delta_{s,o}\frac{1}{T}\right) - \frac{L_{q_1\varphi}}{T}\left(\Delta_{i,o}\varphi + \frac{\Delta_n G^s}{F}\right) \tag{3.17}$$

$$J_q'^o = J_{q_2}' = L_{q_2q_1}\left(\Delta_{i,s}\frac{1}{T}\right) + L_{q_2q_2}\left(\Delta_{s,o}\frac{1}{T}\right) - \frac{L_{q_2\varphi}}{T}\left(\Delta_{i,o}\varphi + \frac{\Delta_n G^s}{F}\right) \tag{3.18}$$

$$j = L_{\varphi q_1}\left(\Delta_{i,s}\frac{1}{T}\right) + L_{\varphi q_2}\left(\Delta_{s,o}\frac{1}{T}\right) - \frac{L_{\varphi\varphi}}{T}\left(\Delta_{i,o}\varphi + \frac{\Delta_n G^s}{F}\right) \tag{3.19}$$

The subscripts for the measurable heat fluxes have been given as J_{q_1}' and J_{q_2}' for simplicity. The Onsager's reciprocal relations ($L_{ij} = L_{ji}$) also hold for this equation. The following definitions are introduced [6]:

$$\pi^{i,o} = \left(\frac{J'^{i}_{q}}{j/F}\right)_{\Delta_{i,s}T=0} = \frac{L_{q_1\varphi}}{L_{\varphi\varphi}} \tag{3.20}$$

$$\pi^{o,i} = \left(\frac{J'^{o}_{q}}{j/F}\right)_{\Delta_{s,o}T=0} = \frac{L_{q_2\varphi}}{L_{\varphi\varphi}} \tag{3.21}$$

$$\lambda^{s,i} = \left(\frac{J'^{i}_{q}}{\Delta_{i,s}T}\right)_{j=0} = \frac{1}{(T^{i,o})^2}\left(L_{q_1q_1} - \frac{(L_{q_1\varphi})^2}{L_{\varphi\varphi}}\right) \tag{3.22}$$

$$\lambda^{s,o} = \left(\frac{J'^{o}_{q}}{\Delta_{s,o}T}\right)_{j=0} = \frac{1}{(T^{o,i})^2}\left(L_{q_2q_2} - \frac{(L_{q_2\varphi})^2}{L_{\varphi\varphi}}\right) \tag{3.23}$$

$$r^{s} = -\left(\frac{\Delta_{i,o}\varphi + \frac{\Delta_n G^s}{F}}{j}\right)_{\Delta_{i,s}T=\Delta_{s,o}T=0} = \frac{T^{s}}{L_{\varphi\varphi}} \tag{3.24}$$

To arrive at these equations it has been assumed no coupling across the interface ($L_{q_1q_2} - \frac{L_{1\varphi}L_{\varphi 2}}{L_{\varphi\varphi}} = 0$). The thermodynamic forces can then be expressed by using the Equations 3.17-3.19 and the definitions above, yielding:

$$\Delta_{i,s}T = -\frac{1}{\lambda^{s,i}}\left(J'^{i}_{q} - \frac{\pi^{i}}{F}j\right) \tag{3.25}$$

$$\Delta_{s,o}T = -\frac{1}{\lambda^{s,o}}\left(J'^{o}_{q} - \frac{\pi^{o}}{F}j\right) \tag{3.26}$$

$$\left(\Delta_{i,o}\varphi + \frac{\Delta_n G^s}{F}\right) = -\frac{\pi^{i}}{T^{i,o}F}\Delta_{i,s}T - \frac{\pi^{o}}{T^{o,i}F}\Delta_{s,o}T - r^{s}j \tag{3.27}$$

At open circuit ($j = 0$), these equations simplify. The expression for the potential drop across the surface becomes [6]:

$$\Delta_{i,o}\varphi = \frac{\pi^{i,o}}{T^{i,o}F}\left(T^{i,o} - T^{s,i}\right) + \frac{\pi^{o,i}}{T^{o,i}F}\left(T^{s,i} - T^{o,i}\right) - \frac{\Delta_n G^{i,s}}{F} \tag{3.28}$$

In [6], Gunnarshaug *et al.* simplify this further by claiming that the temperature drop from the electrode to the electrolyte (across the surface) is negligible. A similar argument is found in [87], where contact resistance between the active material and electrolyte is ignored based on (1) the particles in the electrolyte and the active material having similar thermal conductivities, and (2) the fact that the electrolyte fills the pores in the active material, so no air-gap exists between the layers. If there is no gap between the materials and their thermal conductivities are close to equal, the temperature gradient will be continuous across the surface, as long as no heat source or sink exists at the surface. As stated earlier, heat generated or absorbed by reactions taking place on the surface could cause a temperature difference. However, because of the relation between the reaction rate and current density ($r = j/F$), the reaction rate is negligible when the current density is close to zero. Thus, it is assumed that the temperature difference across the electrode-electrolyte interface is negligible with the experimental setup used (mathematically $T^{i,o} = T^{s,i} = T^{s,o} = T^{o,i}$), which leads to the simplified expression:

$$\Delta_{i,o}\varphi = -\frac{\Delta_n G^s}{F} \tag{3.29}$$

The reaction Gibb's free energy $\Delta_n G^s$ has contribution from the neutral components of the Li-intercalation-reaction only, which means that [6]:

$$\frac{\Delta_n G^s}{F} = \frac{1}{F}\left(-\mu^s_{Li,T^{s,i}}\right) \tag{3.30}$$

Where $\mu^s_{Li,T^{s,i}}$ is the chemical potential of lithium at the electrode surface taken at constant temperature. Because of the sign convention applied, the expressions used for the two electrodes will have opposite sign. By combining the potential difference for the two electrode-electrolyte interfaces (top and bottom) in one equation, one would get:

$$\Delta_{1,e}\varphi + \Delta_{e,2}\varphi = \frac{1}{F}\left((\mu^s_{\mathrm{Li,T^{s,1}}}) - (\mu^s_{\mathrm{Li,T^{s,2}}})\right) \tag{3.31}$$

Finally, the chemical potential is tied to the partial entropy through the Maxwell relation [6]:

$$S^s_j = \left(\frac{\partial S^s}{\partial N^s_j}\right)_{p,T,N_{i\neq j}} = -\left(\frac{\partial \mu^s_j}{\partial T}\right)_{p,N} \tag{3.32}$$

By combining Equations 3.31 and 3.32 and assuming that the temperature gradient is constant through the electrolyte and across the surface, the final expression for the contribution from the two electrode-electrolyte interfaces to the total potential can be written as:

$$\Delta_{1,e}\varphi + \Delta_{e,2}\varphi = \frac{1}{F} S^s_{\mathrm{Li}} \Delta T \tag{3.33}$$

Where ΔT is the temperature difference between the two surfaces, S^s_{Li} is the entropy of the lithium across the two surfaces. This is the contribution to the potential difference from both surfaces, considering the assumptions: (1) no current, (2) negligible temperature change across the surfaces, (3) no coupling of transport phenomena across the surfaces, and (4) no mass transfer across the surface except the one tied to the chemical reaction.

3.2.4 Equations for the Electrolyte

The electrolyte is the most complicated subsystem because there is coupled transport of mass, heat and charge. Two different electrolytes were used in the experiments:

1. A $LiPF_6$ salt in a solution of 1:1 wt % ethylene carbonate (EC) and diethyl carbonate (DEC)
2. A $LiFP_6$ salt in a solution of 1:1 volume % EC and dimethyl carbonate (DMC).

These electrolyte are both ternary electrolytes, as they have three components. The governing equations will therefore be the same, and their derivations are given below.

The Ternary Electrolyte

The chemical potential of the three components in the ternary electrolyte are interrelated by the Gibbs-Duhem relation [6]:

$$\left(\sum_{i=1}^{3} c_i d\mu_{i,T}\right)_{T,P} = 0 \tag{3.34}$$

Where c_i is the concentration of component i and $d\mu_{i,T}$ is the change in chemical potential of component i taken at constant temperature. This simplified Gibbs Duhem relation is valid at constant pressure and temperature. Even though the system in this thesis has a temperature difference, the relation is still valid because the gradients $(\frac{\partial \mu_j}{\partial x})$ are evaluated at constant temperature. The transition from $\frac{\partial}{\partial x}\left(\frac{\mu_j}{T}\right)$ to $\frac{1}{T}\frac{\partial}{\partial x}\mu_{j,T}$ gives an extra term, which is eliminated by using the measurable heat flux (J'_q) in stead of the absolute heat flux (J_q). The derivation can be found in Appendix B.6.

The Gibbs Duhem relation is used to eliminate the gradient of one component from the equation. This is done by choosing that component as the frame of reference. According to Kjelstrup and Bedeaux, any frame of reference can be chosen for transport if there is local equilibrium [8]. In the electrolyte the separator is considered inert, so its movement with respect to the chosen component does not have to be included in the equations. In [6], DEC is chosen as the frame of reference, and the same will be done here for the first electrolyte. This means that DMC is chosen for the second electrolyte to get the same equations. The entropy production can then be written as [6]:

$$\Theta = J'_q \frac{\partial}{\partial x}\left(\frac{1}{T}\right) - c_1(v_1 - v_3)\frac{1}{T}\left(\frac{\partial \mu_{1,T}}{\partial x}\right) - c_2(v_2 - v_3)\frac{1}{T}\left(\frac{\partial \mu_{2,T}}{\partial x}\right) - j\frac{1}{T}\left(\frac{\partial \varphi}{\partial x}\right) \tag{3.35}$$

Where v_i is the velocity of component i, defined as $v_i \equiv J_i/c_i$. The term $c_i(v_i - v_3)$ is therefore the flux of component i relative to component 3. We denote the relative fluxes as J_1 and J_2, whereas the third flux is eliminated from the equation (the third component has no flux relative to itself). The corresponding flux equations are [6]:

$$\frac{\partial}{\partial x}\left(\frac{1}{T}\right) = r_{qq}J'_q + r_{1q}J_1 + r_{2q}J_2 + r_{q\varphi}j \tag{3.36}$$

$$-\frac{1}{T}\left(\frac{\partial \mu_{1,T}}{\partial x}\right) = r_{1q}J'_q + r_{11}J_1 + r_{12}J_2 + r_{1\varphi}j \tag{3.37}$$

$$-\frac{1}{T}\left(\frac{\partial \mu_{2,T}}{\partial x}\right) = r_{2q}J'_q + r_{21}J_1 + r_{22}J_2 + r_{2\varphi}j \tag{3.38}$$

$$-\frac{1}{T}\left(\frac{\partial \varphi}{\partial x}\right) = r_{\varphi q}J'_q + r_{\varphi 1}J_1 + r_{\varphi 2}J_2 + r_{\varphi\varphi}j \tag{3.39}$$

The resistivity coefficients, r have been used, because the relations are here expressed with the forces on the right hand side and the fluxes on the left. By rewriting and introducing some essential coefficients, these relations can be rewritten as :

$$J'_q = -\lambda \frac{\partial T}{\partial x} + q_1^* \Big(J_1 - \frac{t_1}{F} j \Big) + q_2^* \Big(J_2 - \frac{t_2}{F} j \Big) + \frac{\pi}{F} j \tag{3.40}$$

$$J_1 = -D_{11} \frac{\partial c_1}{\partial x} - D_{12} \frac{\partial c_2}{\partial x} - c_1 D_{1T} \frac{\partial T}{\partial x} + \frac{t_1}{F} j \tag{3.41}$$

$$J_2 = -D_{21} \frac{\partial c_1}{\partial x} - D_{22} \frac{\partial c_2}{\partial x} - c_2 D_{2T} \frac{\partial T}{\partial x} + \frac{t_2}{F} j \tag{3.42}$$

$$F \frac{\partial \varphi}{\partial x} = -\frac{\pi}{T} \frac{\partial T}{\partial x} - b_1 \frac{\partial c_1}{\partial x} - b_2 \frac{\partial c_2}{\partial x} - F r j \tag{3.43}$$

Where λ is the thermal conductivity, q_i^* is the measurable heat of tranfer of component i, π is the Peltier coefficient, D_{ij} are the diffusion coefficients, D_{iT} are the thermal diffusion coefficients, c_i is the concentration of component i, t_i is the transport number of component i, b_{ij} are coefficients introduced for simplicity, r is the ohmic resistivity and F is Faradays's constant. The step-by-step derivation is given in Appendix D.1, following closely the derivation by Gunnarshaug *et al.* in [6]. The following definitions have been applied:

$$\lambda = \left(\frac{J'_q}{\partial T / \partial x} \right)_{j=J_1=J_2=0} \tag{3.44}$$

$$q_i^* = \left(\frac{J'_q}{J_i} \right)_{dT=j=J_{j \neq i}=0} \tag{3.45}$$

$$t_i = \left(\frac{J_i}{j/F} \right)_{dT=d\mu_{1,T}=d\mu_{2,T}=0} = \left(\frac{F \partial \varphi / \partial x}{\partial \mu_{1,T} / \partial x} \right)_{dT=j=0} \tag{3.46}$$

$$S^*_{Li^+} = \left(\frac{J'_q / T}{j/F} \right)_{dT=J_1=J_2=0} \tag{3.47}$$

$$\pi = \left(\frac{J'_q}{j/F} \right)_{dT=d\mu_{1,T}=d\mu_{2,T}=0} = -FT \left(\frac{\partial \varphi / \partial x}{\partial T / \partial x} \right)_{dc_1=dc_2=j=0} = t_1 q_1^* + t_2 q_2^* + T S^*_{Li^+} \tag{3.48}$$

$$D_{ij} = -\left(\frac{J_i}{\partial c_i / \partial x} \right)_{dT=dc_{j \neq i}=j=0} \tag{3.49}$$

$$D_{iT} = -\left(\frac{J_i}{c_i \partial T / \partial x} \right)_{dc_1=dc_2=j=0} \tag{3.50}$$

$$r = -\left(\frac{\partial \varphi / \partial x}{j} \right)_{dT=0, dc_1=dc_2=0} \tag{3.51}$$

$$b_i = t_1 a_{1i} + t_2 a_{2i} \tag{3.52}$$

The expressions for a_{ij} are found in Appendix D.1.

By integrating the potential across the thickness of the electrolyte, the expression for the potential difference is found as [6]:

$$F\Delta_{\mathrm{e}}\varphi = F\int_{d^1}^{d^e}\frac{\partial\varphi}{\partial x}dx = -S^*_{\mathrm{L^+}}\Delta_{\mathrm{e}}T - t_1 q_1^{*,\mathrm{e}}\ln\left(\frac{T_{1,e}}{T_{2,e}}\right) - t_2 q_2^{*,\mathrm{e}}\ln\left(\frac{T_{1,e}}{T_{2,e}}\right) - b_1\Delta_{\mathrm{e}}c_1 - b_2\Delta_{\mathrm{e}}c_2 \quad (3.53)$$

Using the simplification $\Delta ln(T) \approx \frac{1}{T}\Delta T$ when $\Delta T << T$, one arrives at the final expression for the potential difference contribution from the electrolyte:

$$\boxed{\frac{\Delta_e\varphi}{\Delta_e T} = -\frac{S^*_{Li^+}}{F} - \frac{t_1 q_1^*}{TF} - \frac{t_2 q_2^*}{TF} - \frac{1}{F}b_1\frac{\Delta_e c_1}{\Delta_e T} - \frac{1}{F}b_2\frac{\Delta_e c_2}{\Delta_e T}} \quad (3.54)$$

where $S^*_{Li^+}$ is the entropy transported by the lithium ions, t_i the transference coefficient of component i, q_i^* the heat of transfer of component i, $\Delta_e c_i$ the time-dependent concentration change of component i through the electrolyte, $\Delta_e T$ the temperature difference across the electrolyte, F Faraday's constant, T the absolute average temperature.

From Equation 3.54, one can observe that the potential difference across the electrolyte has contributions from: The transported entropy by the lithium ions ($\frac{S^*_{Li^+}}{F}$), the transported heat by mass flux of component i ($\frac{t_i q_i^*}{TF}$), and the concentration gradient of component i ($\frac{b_i}{F}\frac{\Delta_e c_i}{\Delta_e T}$). There is a time dependence of the last term, which shall be discussed in Section 3.2.6.

3.2.5 The Total Potential Difference

The total potential difference across the cell can now be found by summing up all the contributions. The equations are the same as the ones found by Gunnarshaug *et al.* in [6]. Summing up the contributions from the different terms, the general formula for the Seebeck coefficient can be written as:

$$\begin{aligned}\epsilon &= \left(\frac{\Delta_{tot}\varphi}{\Delta T}\right)_{j=0} \quad (3.55)\\ &= \frac{1}{F}\left(\frac{\Delta_1 T}{\Delta T}S^*_{e^-} + \frac{\Delta T}{\Delta T}S^s_{Li} + \frac{\Delta_2 T}{\Delta T}S^*_{e^-}\right)\\ &+ \frac{1}{F}\left(-S^*_{Li^+} - \frac{t_1 q_1^*}{T} - \frac{t_2 q_2^*}{T} - b_1\frac{\Delta_e c_1}{\Delta T} - b_2\frac{\Delta_e c_2}{\Delta T}\right)\end{aligned}$$

Where ΔT is the temperature difference across the electrolyte. Because of symmetry of the cell, and assuming that the transported entropy (S^*) changes little with temperature, the term $S^*_{e^-}$ is close to the same for the two electrodes, current collectors and tabs. Because the potential difference is measured on the outside of the cell, the temperature difference $\Delta_{Al1}T$ goes from the outside of the cell to the inside ($\Delta_{Al1}T = T_{Al1} - T_{0,1}$, see Figure 3.2). The same goes for the bottom electrode ($\Delta_{Al2}T = T_{0,2} - T_{Al2}$). Note that the temperature on the outside of the cell is assumed constant, so that $T_{0,1} = T_{0,2} = T_0$. Since the terms for the electrodes in Equation 3.55 ($\Delta_1 T$ and $\Delta_2 T$) also include the current collectors and tabs, these temperature differences are taken to the outside of the cell. Applying this to Equation 3.56 gives the following contribution from the electrodes, current collectors and tabs:

$$\frac{S^*_{e^-}}{\Delta T F}(\Delta_1 T + \Delta_2 T) = \frac{S^*_{e^-}}{F} \tag{3.56}$$

The Seebeck coefficient can then be expressed as:

$$\epsilon = \frac{1}{F}\left(S^s_{Li} - S^*_{e^-} - S^*_{Li^+} - \frac{t_1 q_1^*}{T} - \frac{t_2 q_2^*}{T} - b_1\frac{\Delta_e c_1}{\Delta T} - b_2\frac{\Delta_e c_2}{\Delta T}\right) \tag{3.57}$$

Where S^s_{Li} is the transported entropy of lithium through the two electrode surfaces, $S^*_{e^-}$ is the transported entropy by electrons, $S^*_{\mathrm{Li}^+}$ is the transported entropy by lithium ions, $t_i q_i$ is the contribution to the potential from mass transport by the temperature gradient and $b_i \Delta_e c_i$ is the contribution to the potential difference from the concentration gradient of component i.

3.2.6 Time-Dependence of the System

When a cell is exposed to a temperature gradient, the concentration gradients that build up in the cell cause changes to the electric potential [6, 86]. In the stationary state, there is a balance between the chemical and thermal force called Soret equilibrium [6]. Until this equilibrium situation is reached, different components in the battery electrolyte will move in the thermal field. This movement causes a time-dependent change in the measured potential that depends on the components in the electrolyte [6]. Because the Seebeck coefficient is the measured potential at open-circuit conditions when a temperature difference exists, it is directly dependent on these diffusion processes. The time-dependent mass diffusion of the different components are believed to happen on widely different time scales, according to the results given by Gunnarshaug *et al.* in [6] and Richter *et al.* in [2]. In this case, it can be assumed that the coupling between the two fluxes are so small that they can practically be ignored. The establishment of the two concentration gradients can then be treated separately. This means that the electrolyte can first be treated as a binary electrolyte consisting of $\mathrm{LiPF_6}$ and a carbonate solution of DEC/DMC and EC that establishes partial Soret equilibrium after a time t_1. Thereafter it can be treated as a new binary electrolyte consisting of EC and DEC/DMC that establishes a full equilibrium state after a time t_2, where $t_2 >> t_1$. In accordance with Gunnarshaug *et al.* it has been assumed that the $\mathrm{LiPF_6}$ salt causes the initial effect, whereas the slower process is the build-up of the gradient of EC in DMC/DEC [6].

The time-dependence of the Seebeck coefficient is seen in Equation 3.57, though it is not explicit. In order to see it more clearly, it is convenient to express the heat of transfer in the following way:

$$q_1^* = \left(\frac{J'_q}{J_1}\right)_{dT=j=0} = -T\left(\frac{\partial \mu_{1,T}/\partial x}{\partial T/\partial x}\right)_{j=J_1=0} \tag{3.58}$$

In other words: When the mass flux is zero (steady state), the contribution to the potential difference from the heat transported by mass ($\frac{t_1 q_1^*}{TF} = \frac{t_1}{TF}(-T\frac{\Delta\mu_{1,T}}{\Delta T}) = \frac{t_1 a_1}{F}\frac{\Delta c_1}{\Delta T}$) cancels against the potential difference created by the concentration gradient ($\frac{t_1 a_1}{F}\frac{\Delta c_1}{\Delta T}$). Thus, at stationary state only the transported entropy by Li-ions contributes to the potential difference (in the electrolyte).

With this information, it is possible to express the Seebeck coefficient at different time states. The use of a ternary electrolyte makes it natural to talk about three different states: (1) the initial state, where the electrolyte is still uniform and no concentration gradients are present; (2) an intermediate state where the fastest diffusion process has reached a partial equilibrium state; and (3) the stationary state, where all concentration gradients are established.

At initial time, when the electrolyte composition is uniform, the following expression is valid:

$$\epsilon_0 = \frac{1}{F}\left(S^s_{Li} - S^*_{e^-} - S^*_{Li^+} - \frac{t_1 q^*_1}{T} - \frac{t_2 q^*_2}{T}\right) \tag{3.59}$$

Thereafter, the fastest diffusion process reaches partial Soret equilibrium. This means that at time t_{int} the expression reduces to:

$$\epsilon_{int} = \frac{1}{F}\left(S^s_{Li} - S^*_{e^-} - S^*_{Li^+} - \frac{t_2 q^*_2}{T}\right) \tag{3.60}$$

Finally, when the last diffusion process reaches equilibrium, the Seebeck coefficient is:

$$\epsilon_\infty = \frac{1}{F}\left(S^s_{Li} - S^*_{e^-} - S^*_{Li^+}\right) \tag{3.61}$$

As we can see, the different contributions to the Seebeck coefficient can be calculated by achieving the values at different times in the process. At equilibrium the contribution from transported entropy is calculated. Thereafter the heat of transfer of the slowest component can be found at the first, partial Soret equilbrium. Finally, the contribution from the heat of transfer of component 1 is calculated from the initial Seebeck coefficient.

Time-Dependence at Other States of Charge

If the diffusion of lithium in the electrode were included, the Seebeck coefficient would have another time-dependent term. This time-dependency would come from the establishment of a concentration gradient within the electrodes due to the temperature difference across these. Numbers for the thermal diffusion of lithium in the electrodes (the Soret effect) have not been found in literature, and experiments would have to be carried out in order to establish whether or not these effects can be actually be ignored in a full cell. Because of the lack of data, it will be assumed here that the thermal lithium diffusion happens very fast compared to the thermal diffusion of components in the electrolyte, and that the effect of lithium diffusion can therefore be omitted. This is also reasonable by considering that the temperature change across the electrode is very small compared to the change across the electrolyte due to a much higher thermal conductivity (see Section 4.4).

3.2.7 The Peltier Coefficient from the Seebeck Measurement

The aim of this thesis is to quantify the local, reversible heat at the electrodes. With the equations for the Seebeck coefficient readily available, the Peltier coefficient can easily be expressed by applying Equation 2.23. In combination with the time-dependent Seebeck coefficient from Equations 3.59-3.61 a time-dependent Peltier coefficient can be expressed as:

$$\pi = -T\left(S^{s}_{Li} - S^{*}_{e^-} - S^{*}_{Li^+} - \frac{t_1 q^*_1}{T} - \frac{t_2 q^*_2}{T} - b_1\frac{\Delta_e c_1}{\Delta T} - b_2\frac{\Delta_e c_2}{\Delta T}\right) \tag{3.62}$$

3.3 Equation Summary - System Description

In the previous sections, it was shown how non-equilibrium thermodynamics can be applied to describe the processes taking place in the experimental system used in this thesis. Equations were derived that describe the contribution to the measured potential difference from each sub-system. This section summarizes these equations, which will be used in the experimental section of this thesis.

In the *electrodes, current collectors and tabs*, where only transport of heat and charge is present, the contributions to the potential were found to be:

$$\Delta_1\varphi = S^*_{e-}\Delta_1 T \tag{3.12}$$

$$\Delta_2\varphi = S^*_{e-}\Delta_2 T \tag{3.13}$$

The *electrode-electrolyte interfaces* were summed up to give one common contribution, related to the intercalation of lithium:

$$\Delta_{1,e}\varphi + \Delta_{e,2}\varphi = \frac{1}{F}S^s_{\mathrm{Li}}\Delta T \tag{3.33}$$

Finally the electrolyte, having transport of heat, mass and charge, gives the contribution:

$$\frac{\Delta_e\varphi}{\Delta_e T} = -\frac{S^*_{Li^+}}{F} - \frac{t_1 q^*_1}{TF} - \frac{t_2 q^*_2}{TF} - \frac{1}{F}b_1\frac{\Delta_e c_1}{\Delta_e T} - \frac{1}{F}b_2\frac{\Delta_e c_2}{\Delta_e T} \tag{3.54}$$

Summing up these, the total potential contribution is expressed directly as the Seebeck coefficient as:

$$\begin{aligned}\epsilon &= \left(\frac{\Delta_{tot}\varphi}{\Delta T}\right)_{j=0} \\ &= \frac{1}{F}\left(\frac{\Delta_1 T}{\Delta T}S^*_{e^-} + \frac{\Delta T}{\Delta T}S^s_{Li} + \frac{\Delta_2 T}{\Delta T}S^*_{e^-}\right) \\ &+ \frac{1}{F}\left(-S^*_{Li^+} - \frac{t_1 q^*_1}{T} - \frac{t_2 q^*_2}{T} - b_1\frac{\Delta_e c_1}{\Delta T} - b_2\frac{\Delta_e c_2}{\Delta T}\right)\end{aligned} \tag{3.57}$$

This is directly related to the Peltier heat through Equation 2.23, yielding:

$$\pi(t) = -FT\epsilon(t) = -T\left(S^s_{Li} - S^*_{e^-} - S^*_{Li^+} - \frac{t_1 q^*_1}{T} - \frac{t_2 q^*_2}{T} - b_1\frac{\Delta_e c_1}{\Delta T} - b_2\frac{\Delta_e c_2}{\Delta T}\right) \tag{3.62}$$

In addition to these relations, the time-dependence of the Seebeck coefficient (and thereby the Peltier heat) was expressed in an indirect manner by giving expressions for three separate situations:
(1) The initial state:

$$\epsilon_0 = \frac{1}{F}\left(S^s_{Li} - S^*_{e^-} - S^*_{Li^+} - \frac{t_1 q^*_1}{T} - \frac{t_2 q^*_2}{T}\right) \tag{3.59}$$

(2) The intermediate state, which occurs at partial Soret equilibrium caused by the fastest diffusion process:

$$\boxed{\epsilon_{int} = \frac{1}{F}\left(S^{s}_{Li} - S^{*}_{e^{-}} - S^{*}_{Li^{+}} - \frac{t_2 q^{*}_{2}}{T}\right)} \tag{3.60}$$

(3) The stationary equilibrium state:

$$\boxed{\epsilon_{\infty} = \frac{1}{F}\left(S^{s}_{Li} - S^{*}_{e^{-}} - S^{*}_{Li^{+}}\right)} \tag{3.61}$$

Chapter 4

Method and Calculations

In order to measure the Seebeck coefficients in different electrode materials, simple thermoelectric pouch cells with equal electrodes were made. These were then inserted into a structure meant to keep constant but different temperature at the two electrodes, while minimizing heat loss to the surroundings.

Some of the cells were charged, giving electrodes at different states of charge. The procedure at 0 % SoC was the simplest, because the electrodes could be assembled directly into a thermoelectric cell without first being charged. For the other states of charge, the general experimental procedure was as follows:

1. Two full cells with lithium metal oxide cathode and lithium metal anode were made
2. The cells were charged to the desired state of charge using the Arbin LBT 21084 Battery-Cycler, and left to rest till the voltage was relaxed
3. The cells were then introduced in a glovebox, where they were dissasembled and the electrodes were washed
4. From two full cells, one symmetric thermoelectric cell with lithium metal oxide as both electrodes was assembled
5. Experiments to determine the Seebeck coefficient for the given configuration (cathode material and SoC) were carried out

In this chapter, the content of each step above is detailed. In Section 4.1 the cell production method is described, which englobes both how to make the full cells for step 1 and the symmetric, thermoelectric cells for step 4. Section 4.1.2 describes the dissasembly and washing of electrodes (step 3). Section 4.2 describes how the charging was done, and discusses some of the difficulties encountered here (step 2). Section 4.3 describes the experimental set-up used to achieve the results that will be presented in Chapter 5 (step 5).

In addition to the measurements of the Seebeck coefficients, a temperature calibration test was carried out. This was done to validate the theoretical temperature calculations based on Fouriers law. The procedure for the temperature calibration experiments, as well as the production of the temperature calibration cell is detailed in Section 4.4.

4.1 Making the Cells

4.1.1 Assembling the Pouch-Cells

The thermoelectric pouch-cells used for the Seebeck-coefficient measurements were made using electrodes of Lithium Cobalt Oxide (LCO), Lithium Iron Phosphates (LFP) and Lithium Manganese Oxides (LMO). The LMO and LFP electrodes were delivered by Hohsen Corp. whereas the LCO electrodes were taken from Shenzhen Melasta Lithium-polymer cells, disassembled according to the procedure explained in Section 4.1.2. Thus, the LFP and LMO electrodes were unused, while the LCO electrodes came from pre-fabricated cells. The LCO electrodes taken from the Melasta cells were coated with active material on both sides of the current collector. In order to achieve electrical contact with the tabs, the active material had to be removed from one side of these electrodes. This was done by carefully scraping off the active material with a piece of tissue soaked in acetone. For the LMO and LFP electrodes this was not necessary as these electrodes were deliverd with active material coated on only one side of the current collector. This will be important for later discussion.

In order to measure the Seebeck coefficient at different SoC, a full cell consisting of one lithium metal anode, one electrode, a separator and electrolyte were first made. These were then charged to the desired SoC, and left to stabilize (minimum 48 hours). After this time, the cells were again disassembled, and two equal electrodes from two different full cells were put together to form a thermoelectric cell, consisting of two equal electrodes separated by 4 separators. The procedure used for making both the full cells and the thermoelectric cells is quite similar, and is described here. The charging procedure is described in further detail in Section 4.2.

The pouch cell was made from a 121 μm laminate consisting of 12 μm PET, 9 μm aluminum and 100 μm PE. This laminate melts when heat is applied, which gave a convenient method for sealing the cells. The laminate was cut into 4 x 8 cm pieces, and folded in half, so that the pouch measured approximately 4 x 4 cm. Two current-collector tabs were cut from a foil to approximately 0.4 x 4 cm. A 17 μm thick aluminum foil was used on both electrodes for the symmetric cells, while a 20 μm thick copper foil was used as tabs for the lithium-metal electrodes. The tabs were inserted into the pouch approximately 3 mm apart, and the first side was sealed by using a thermal bonding film (product TBF615 from 3M) and applying heat and pressure. Heat and pressure was applied for sealing using a Magneta Motor Audion Elektro 421MGMIDS-2 Sealmaster, sealing for 6 seconds at 630 W. After sealing the first side, the separators were introduced. The separators used were Whatman Glass Microfibre Filters GF/D (no 1823070, pore diameter of 2.7 µm). First, the separators were cut into circles of 20 mm diameter using a stamp. Then, for the thermocells, four separators were stacked and introduced into the open pouch while taking care to have one current-collector tab on the top of the stack, and one on the bottom. In the case of the full cells only one separator was used in stead of four. After introducing the separator(s) another side was sealed by applying heat and pressure, before introducing the half-complete cell into an argon-filled glove-box. Once inside the glove-box, the cells were completed by adding electrodes and electrolyte. The electrodes were pre-cut outside the glove-box to 18 mm diameter circles. When making the symmetric cells, one electrode was introduced on each side of the separator stack using ceramic tweezers, with the tabs on the outside in contact with the current collector. The same was done for the full-cells, but replacing one of the lithium-metal oxide electrodes with a lithium-metal electrode. After introducing the electrodes, all materials were left in the argon-filled glove-box for a minimum of 24 hours before electrolyte was introduced. Electrolyte was soaked into the separators using a 700 μl pipette for the symmetric cells, and a 300

μl pipette for the full cells. These quantities were chosen to get soaked separators that were not dripping. Two different electrolytes were used: (1) a $LiPF_6$ salt in a 1:1 wt % of ethylene carbonate (EC) and diethyl carbonate (DEC) solvent from Gotion (LP 40); and (2) a $LiPF_6$ salt in a 1:1 v/v of EC and dimethyl carbonate (DMC) solvent from Aldrich. (1) gives molar fractions of 0.055, 0.542 and 0.404 for the $LiPF_6$ salt, the EC and the DEC respectively[1]. (2) gives molar fractions of 0.036, 0.426[2] and 0.538[3] respectively for the salt, the EC and the DMC.

(a) Tabs and thermal bonding tape **(b)** Sealing first side **(c)** Introducing separator stack

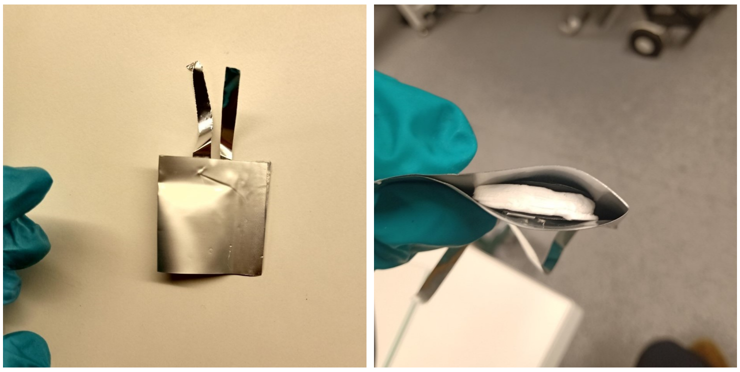

(d) Second side sealed **(e)** Electrodes introduced

Figure 4.1: Illustration of the cell assembly procedure for a symmetric cell. (a) The pouch film is folded, the thermal bonding tape and the tabs are put in position. (b) The first side is sealed and (c) the separator stack is introduced. (d) Shows the cell sealed on two sides, ready to be introduced in the glove-box. In (e) the electrodes have been introduced, and the cell is only missing electrolyte and the final seal.

---

[1] Values for the EC:DEC electrolyte taken from [6]

[2] For DMC, values of 1.071 g/mL and 90.078 g/mol were used for the density and molar mass respectively to find a value of 11.89 mol/L [88]

[3] For EC, values of 1.321 g/mL and 88.062 g/mol were used for the density and molar mass respectively, to find a value of 15.00 mol/L [88]

Finally, the cells were sealed using an Audion E Audionvac Vacuum-Sealer. The total sealing time was 34 seconds: 15 seconds to reach 1 bar vacuum, 15 seconds at vacuum to ensure no air left in the cell, and 4 seconds of sealing. After being sealed, the cells were left to rest for a few days before they were introduced into the experimental set-up. The procedure for producing the cells is shown with pictures in Figure 4.1.

The LCO-Electrodes

As opposed to the LFP and LMO electrodes, the LCO electrodes came from a commercialized cell. Therefore, they consisted of a current-collector coated with active material on both sides, with a tab of current-collector sticking out in one corner. Ideally, the electrodes used should only have one side coated with active material. Thus, a different treatment had to be given to these cells. In order to use these electrodes, two different methods were applied:

1. In the first method, the LCO-electrodes were cut so that the current-collector tab could be used to access the current-collector inside the electrodes. This current-collector tab was folded back, and put in contact with the tab that was already placed in the pouch-cell. The cut electrodes with the current-collector tab is pictured in Figure 4.2a. This method of folding back the current-collector tab essentially gives a structure consisting of: current collector - active material - current collector - active material - separator - active material - current collector - active material - current collector. This structure was used for the first cells assembled in this thesis. However, as shall be seen in the results, these cells gave quite noisy measurements, and this method is not recommended for future work.
2. The second treatment was to remove the active material from one side of the electrodes in order to access the current collector and give symmetric cells with the same structure as the ones made with other electrode materials. Acetone and a paper tissue was used to carefully remove the active material from one side. The acetone was added to the tissue by a pipette, and then the tissue was used to gently rub off the active material. This method worked quite well, although the side that was supposed to be intact seemed to be slightly damaged in the process. This, along with the fact that the LCO-electrodes were not in pristine conditions, make the results for the LCO-based symmetric cells hard to trust. An LCO-electrode where active material has been removed is shown in Figure 4.2b.

Electrodes that are not in pristine conditions should be investigated further, but the methods applied here did not yield good results as shall be seen in Chapter 5. A better method for removing the active material should therefore be sought if non-pristine electrodes are to be investigated.

(a) Method where the existing tab is used **(b)** Removing active material with acetone

Figure 4.2: Illustration of how the LCO electrodes were treated. (a) Shows a cell with three of the cut electrodes, where two of them have the current collector folded down from the top corner. This method does not take away the coating from one side. (b) Shows the electrode where parts of the active material has been removed with acetone.

4.1.2 Disassembling Cells and Washing Electrodes

Disassembly of cells was done in two situations: (1) after charging the cells to desired state of charge in order to measure Seebeck coefficients at different SoC, (2) in order to extract LCO electrodes from a commercialized cell to find the Seebeck coefficient for these electrodes. The LCO electrodes used in the experiments in this thesis were taken from commercial Lithium-polymer pouch cells from Shenzhen Melasta Battery Co. (model: SLPBB042126HD). These cells were disassembled in order to achieve the individual electrodes. The disassembly of the commercial cells was done by Christian Trandem and Colin Ringdalen MacDonald, but follows a similar procedure as the one described here.

The pouch-cells were disassembled in an argon-filled glove box, where the O_2 and H_2O levels were monitored and kept below 2 ppm (normally even < 0.1 ppm). Ceramic scissors were applied to cut open the pouch on one side, taking care not to damage the electrode(s). In the simple pouch-cells used to charge the electrodes to desired SoC, there was only one layer of electrodes, so opening one side of the pouch-cell gave direct access to these. In the case of the commercialized Melasta cells, a stack of electrodes was wrapped in a layer of current collector, which consequently needed to be removed before the electrodes could be accessed. The electrodes were then carefully extracted from the pouch using ceramic tweezers, and immediately washed. The washing procedure used was dependent on the electrode. For the cathode (lithium metal oxides), the electrode was washed for two minutes in DMC, and then left to dry in the argon filled glove-box for a minimum of 48 hours. For the anode (graphite), the electrode was left for ten seconds in DMC, dried for 1 minute and then left for another ten seconds in DMC. As with the cathode, the anodes were then left to dry for a minimum of 48 hours in the argon-filled glove-box. The drying was not done in an oven because the glove-box used did not have an oven installed, and it was not considered a good idea to extract the electrodes from the glove-box for the drying process immediately after having opened the cells.

When the electrodes that were taken for the SoC cells had been extracted, washed and dried, they could be inserted into symmetric cells, which were then filled with new electrolyte and left to rest. After taking out the electrodes to be used, the lithium-metal electrodes were taken out of the cells used for charging to assess their condition. Some dendrite growth was seen on the lithium metal used for the cells charged to higher states of charge. This should not influence significantly the achieved state of charge, as one charge cycle delithiates the cathode, and in essence only needs somewhere to deposit the lithium. This is discussed further in the next section.

4.2 Cell Charging

In order to execute thermoelectric experiments at different states of charge, it was necessary to charge the lithium oxide electrodes. Trying to disassemble a charged commercial cell with several layers of electrodes was considered to be too difficult without causing a short circuit. Thus, the applied method was to construct chargeable, one-layered cells, charge them to the desired SoC, disassemble them, and reassemble two lithium-oxide electrodes in a symmetric, thermoelectric cell (following the process explained in Section 4.1). To estimate the state of charge in the electrodes, coulomb counting (CC) was used. A single-layer pouch cell was constructed using two different strategies: (1) using a graphite electrode from a used, commercialized cell; and (2) using a pure lithium electrode. These strategies were chosen to avoid spending time on formation cycles, which was deemed irrelevant when considering the short lifetime of these cells (1 cycle before disassembly). The idea was that if a fresh graphite electrode was used, then the formation of SEI on the graphite electrode would consume considerable amounts of cyclable lithium, giving a less precise estimate of the remaining capacity in the lithium-oxide electrode. It was quickly discovered, however, that even when an old graphite electrode was used, the cells using a graphite gave very unstable and varying voltages, which were believed to be due to formation processes. The cells with lithium-metal as a counter-electrode, however, gave very good results. Thus, the lithium metal was chosen, and cells were produced only using Li-metal anodes. Even using the chosen method, some uncertainty exists concerning the estimated state of charge of the electrodes, mainly tied to the possible divergence between calculated capacity and actual capacity of the cells, but also related to possible loss of lithium (*i.e.* through the formation of passive layers on the electrodes).

4.2.1 Charging the Cells

In order to charge the cells, a set-up using a coin cell charger connected to an Arbin LBT21084MC Battery Cycler was used. The coin-cell charger was chosen because very small currents were required for the custom-made cells, preventing the use of a traditional pouch-cell charger. In order to charge pouch cells in a coin-cell charger, the tabs were inserted into the clamps separated by a piece of plastic (see Figure 4.3a). To hold the tabs in place, vinyl tape (Scotch Super 33+ from 3M) was used. The resistance of the set-up was tested by measuring the voltage at the tabs of the cell as close to the pouch as possible while current was flowing through. The results showed that the set-up gave acceptably low resistance, so that charging could be carried out as usual without accounting for a high outer resistance. The set up is pictured in Figure 4.3.

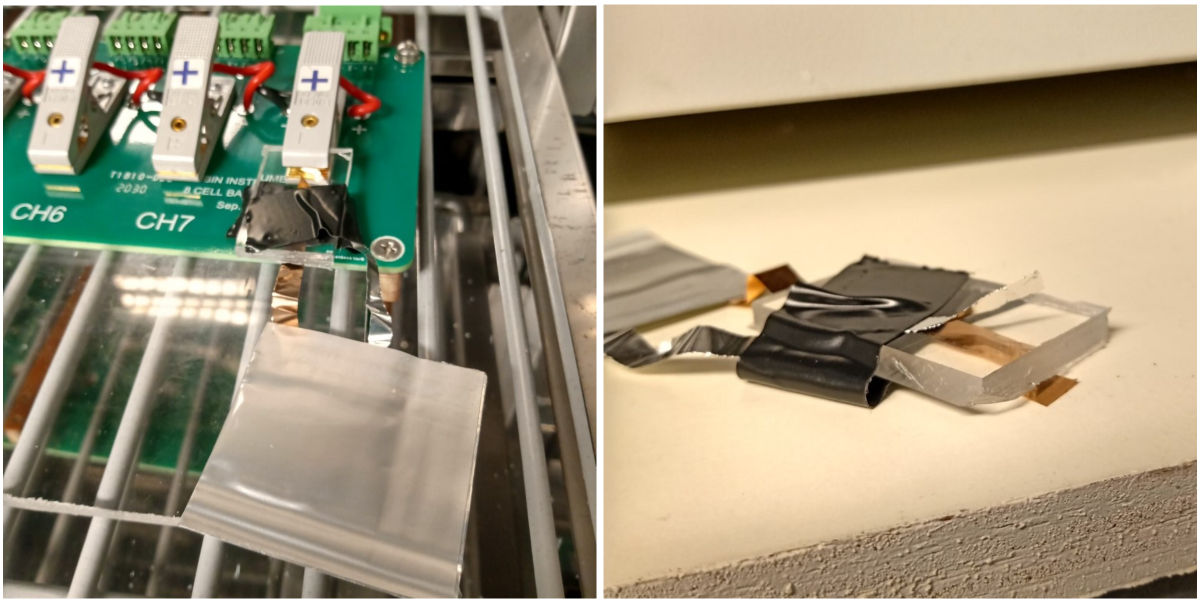

(a) Coin-cell charger with cell

(b) Plastic used to separate the tabs

Figure 4.3: Set-up used for charging the cells. (a) Pictures the coin-cell charger with an inserted pouch cell. A piece of transparent plastic is placed between the tabs to separate them. (b) Shows the piece of plastic with the pouch cell attached to it by vinyl tape.

Only the LFP cells were charged, because there was not enough time to charge the other cell chemistries. When charging the cells to states of charge lower than 100 %, constant current charging at C/20 was used until the desired SoC was reached, where the desired SoC was calculated based on the nominal capacity given by the manufacturer and using coulomb counting (See Section 4.2.2). For the cells charged to 100 % SoC, constant current charging at C/20 was used until a voltage of 3.75 V was reached. The voltage was then kept constant, letting the current be reduced until reaching C/40. After finishing the charging process, the cells were left to rest for a minimum of two days in order to get a relaxed open-circuit voltage. As pointed out by Huria *et al.*, the relaxation time for LFP is quite long when the state of charge is close to 0 or 100 % (>13 hours in their experiment) whereas intermediate SoCs have lower relaxation times [89]. This was also seen here when charging the cells.

4.2.2 Calculating the Nominal Capacity

The nominal capacity (Q) was used to calculate the state of charge using Equation C.1 (see Appendix C). The nominal capacity was calculated according to the equation:

$$Q = c \cdot A = c \cdot \pi \cdot \frac{D^2}{4} \tag{4.1}$$

where c is the capacity per area given by the manufacturer, A is the surface area of the electrode, π is 3.1415... and D is the diameter of the electrode. The capacity per area given by the manufacturer is $c = 1.5$ mAh/cm^2. The diameter is $D = 1.80 \pm 0.05$ cm if the precision of the electrode cutter is set to ±0.5 mm. The nominal capacity is then calculated as:

$$Q = \frac{\pi \cdot 1.5 \cdot 1.8^2}{4} = 3.8 \pm 0.2 mAh$$

Where the error is calculated from Gauss law of error propagation (see Appendix H). If the precision is assumed to be higher, the inaccuracy decreases. The results from the charging to 100 % SoC gave capacities in the range 3.5 to 3.7 mAh, indicating that the precision chosen here is good, but cannot alone account for the deviation from the theoretical capacity. It is believed that this deviation can be attributed mainly to the inaccuracy in the electrode cutter and the misalignment, as will be discussed in Section 4.2.5. In addition to this, the manufacturer did not state the upper cutoff-voltage. Using a higher voltage could potentially also give higher capacity. The chosen cutoff voltage will be discussed in Section 4.2.4.

4.2.3 Choosing an Anode Material

Normally when a cell is charged for the first time after being assembled, formation cycles are carried out. This is a series of charge/discharge cycles at low C-rates that lead to the formation of the SEI layer, mainly on the graphite electrode. By using lithium metal anodes, the SEI-layer formation should not be as significant, and should therefore give very limited capacity loss. In the experiments in this thesis, cells were assembled using both lithium-metal and graphite anodes.

When using graphite as the anode, the main problem was SEI-formation, which usually occurs in the first couple of cycles. Even though the graphite that was applied here came from a used cell, there is no guarantee that the SEI-layer was completely intact when cycling began. No study has been found that looks at how the SEI-layer is affected when the electrode is taken out of one cell and put into another. The voltage was highly unstable for the LFP-C cells, and this was believed to be due to SEI formation.

Using the graphite electrodes from a used commercialized cell also imposed another problem - the active material was coated on both sides of the current collector. In order to get electrical contact between the tab and the current collector, the active material was removed from one side by using acetone and scrubbing with a piece of tissue. Although the acetone should not have come into contact with the active material on the opposite side of the electrode, it is possible that the backside was mechanically damaged during the scrubbing, which could also have reduced the total capacity of the cell. However, this was deemed irrelevant because it was only the lithium oxide cathode (which was a new, unused material) that was transferred to the thermoelectric cells after being charged. So long as the graphite electrode had a higher capacity than the lithium oxide electrode, it should be possible to achieve a fully charged cathode ($LiMO_2$, where M is a metal).

The mayor problem with lithium-metal electrodes is the formation of dendrites due to lack of control in the lithium deposition. These dendrites could potentially cause a short-circuit in the cells by growing through the separator when using lithium-metal anodes. However, as only one charge cycle was carried out, and at quite low current, the risk was considered to be minimal. In any case, a short circuit would have become apparent before the cells were disassembled, and these electrodes would then be discarded. In Figure 4.4 one of the lithium-metal electrodes charged to 100 % SoC is pictured. Clear dendrite growth can be seen (black region).

Figure 4.4: Upon disassembly of the cells charged to higher states of charge, the Li-metal electrodes showed some black regions. These are believed to be due to dendrite growth, and would give some imprecision in the estimated state of charge for these cells.

Despite the dendrite growth at higher states of charge, the cells that used lithium metal as a counter anode showed much more stable voltages than the cells made with graphite from used, commercialized cells. Therefore, only the electrodes charged with the lithium metal as the counter electrode were used to make thermoelectric cells.

4.2.4 Cutoff Voltage

In literature, different values have been reported for the upper cutoff-voltage for LFP [90, 91], but usually they are in the range of 3.55 - 3.65 V for a LFP-C cell [89, 92–94]. The graphite anode usually has a potential around 0.1 V vs Li/Li+, so that the cutoff voltage for an LFP - lithium metal cell should be 0.1 V higher than the values given for LFP - graphite cells [95]. This amounts to an upper cutoff voltage around 3.65 - 3.75 V. The cells used were therefore charged to an upper cutoff voltage of 3.75 V, to ensure a close to 100 % SoC without triggering irreversible degradation mechanisms.

In a first version of the charge cycles, a cutoff voltage of 4.3 V was erroneously used for charging the LFP - Lithium-metal cells. This resulted in measured capacities slightly higher than the nominal capacity reported by the manufacturer (around 3.9 mAh). However, assuming a ±0.5 mm precision for the electrode cutter, these capacities were still within the limits of 3.8 ± 0.2 mAh. This also confirms the theory that the cutoff voltage used by the manufacturer may be slightly higher than the one applied here. Jin *et al.* reported that capacity fade was seen for a LFP-graphite cell at higher cut-off voltages (4.2 V compared to 3.6 V), but not for the initial cycles [96]. Thus, using a higher cutoff voltage in a one-cycle charge should not lead to significant capacity loss.

4.2.5 Uncertainties in the Achieved State of Charge

Some of the issues with accurately estimating the state of charge are discussed in Appendix C. Here, a simple Coulomb Counting (CC) method was applied, while the open-circuit voltage was used to validate the results. In the case of LFP, the curve showing voltage as a function of charge capacity has a large plateau around 3.4-3.5 V which makes precise validation of the SoC using OCV difficult. The reason why this simple method was still chosen to estimate the SoC, was because other factors were considered to have a bigger impact on the inaccuracy. First of all, pouch cells were assembled by hand, using round electrodes, which could lead to a mismatch between the top and the bottom electrode. Murray *et al.* showed that in assembly of three coin cells, misalignment lead to a 16 % lower capacity retention after 100 cycles for the worst aligned cell compared to the best aligned cell [97]. In the experiments in this thesis, the electrodes were inserted into the pouch cell by hand using tweezers, which was a very imprecise method. However, because coin cells are difficult to disassemble, using a pouch cell was deemed the best assembly method in order to later extract the electrodes from the cells. Also, seeing as the cells were only charged one time, with abundant lithium in the cell (using a lithium-metal anode), the capacity loss due to misalignment should not be too serious. This being said, it would undoubtedly be better to use a coin cell that allowed disassembly in order to get a better alignment between the electrodes, and this is recommended for future work.

A second factor giving lower accuracy in the SoC estimation was the rough edge made by the electrode cutter. When cutting the electrode material to the appropriate size, an electrode cutter with a 18 mm diameter was used. However, this cutting method could lead to both increased and decreased diameter due to a rough cutting edge. This is illustrated in Figure 4.5. The capacity of the electrode material was given by the manufacturer in mAh/cm^2, thus the total calculated capacity was influenced by the diameter of the electrodes. The nominal capacity was calculated using Equation 4.1. If the diameter is 1.80 cm originally, and decreases with 0.5 mm (= 0.05 cm) the nominal capacity decreases with 5.5 %. Thus, small variation on mm scale in electrode diameter would lead to large variations in the capacity.

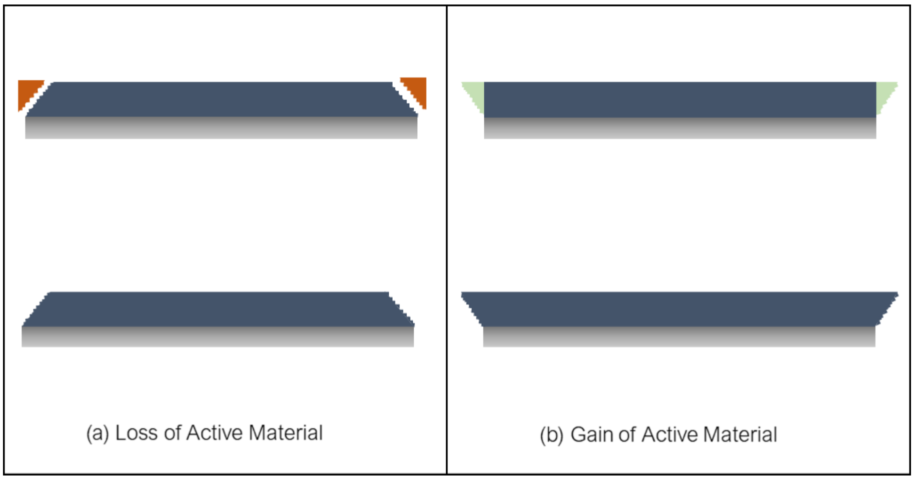
(a) Loss of Active Material

(b) Gain of Active Material

Figure 4.5: The effect of the electrode cutter precision on the state of charge. (a) Illustrates how a rough cut can lead to a lower capacity by giving loss of active material. (b) Illustrates how a rough cut can lead to a higher capacity by giving gain of active material.

4.2.6 Relation Between State of Charge and State of Lithiation

The state of charge is often closely related to the state of lithiation in the cell (*i.e.* x in $\mathrm{Li}_x\mathrm{FePO}_4$). If we assumed that the Coloumbic efficiency is 100 %, all the electrons in the cell contribute to the lithiation/delithiation process at the electrodes in a 1:1 ratio (1 mol $e^- = 1$ mol Li transported from one electrode to the other). This means that once an initial lithiation state is established, there is a direct relationship between the amount of electrons (or current) passing through the cell and the amount of intercalated lithium in the electrodes.

The Coloumbic efficiency (ratio between charge extracted from and charge inserted in the battery [98]) has been known to decrease with time as the battery is used, so the first assumption is not quite true. Nonetheless, for the one-cycle charge model applied in this thesis, the error should be small, unless significant formation processes are occurring.

The mayor error in our case lies in establishing the initial 0 % SoC and 100 % SoC. It has been assumed that the electrodes were delivered from the manufacturer at 0 % SoC, meaning for Li_xFePO4, $x = 1$. Further, it was assumed that the nominal capacity reported by the manufacturer was correct, and 100 % SoC was calculated based on this number. When charging the cells with a Constant Current - Constant Voltage (CCCV) profile, none of the cells reached the calculated nominal capacity of 3.8 mAh, even though a low current of C/40 was used as cut-off current in the constant voltage charging stage. This could indicate that the reported 100 % SoC by the manufacturer was not correct. However, it could also indicate that 100 % SoC was not reached, which could for example be due to a bad alignment or lost capacity during assembly or charging of the cell, or simply due to a lower cutoff voltage. In this thesis, the latter was assumed, and the reported states of charge are therefore calculated based on the nominal capacity reported by the manufacturer. By comparing this to the value achieved when charging the cells to maximum at CCCV, it is possible to estimate an error range for the reported states of charge. The lowest value achieved when charging the cells to their maximum state of charge was 3.5 mAh, which is 92 % of the nominal capcity reported by the manufacturer. This would increase the values reported for state of charge in this thesis by 9 %. The highest value found was 3.9 mAh for the cells charged to a high cutoff voltage of 4.3 V. This would amount to a decrease in the reported states of charge of 3 %. The error margin is therefore given as + 9 % and - 3 % of the given state of charge (thus for 13.33 % SoC the actual range is 12.93 % to 14.50 %).

4.3 Thermoelectric Potential Measurement Set-Up

The set-up for the thermoelectric potential measurements was similar to the one explained by Gunnarshaug *et al.* in [6] and is reproduced here in detail. A temperature difference was invoked in the cells, and the electric potential difference was measured. The temperature gradient was established by using two water-baths set to different temperatures. The middle temperature was always 25 °C, whereas the temperature differences applied were 5, 10, 15 and 20 °C.

The water was circled through two aluminum plates, holding together the rest of the set-up. Between the aluminum plates were four copper plates (two on each side) and the cell, with a thermocouple (RS pro K-type, 0.2 mm diameter) between the two copper plates on each side measuring the temperature. The copper plates and the cell were surrounded by a hard, insulating plastic to avoid unnecessary heat loss. The whole set-up was held in place by plastic screws and bolts going through the aluminum plates. The hot water was circled through the top layer of the set up in order to avoid convectional effects in the electrolyte. Copper was chosen as a heat-conductor to get an even distribution of heat across the cell. The frame used was illustrated in Figure 3.3, and the full set-up is illustrated in Figure 4.6, with the water baths, the frames and the cell.

4.3.1 Measuring the Thermoelectric Potential

The electrical potential was measured between the tabs in the cell by using an Aguilent 34970 A Data aquisition / Switch unit. Before starting the tests, the cells were short circuited for a minimum of 30 minutes, up to a few hours. Thereafter the potential was recorded without a temperature difference between the water baths (25 °C on both sides of the cell). This relaxation was left until a relatively stable potential was reached (in some cases the potential had not reached a stable value even after several days, so the experiments were carried out even though the potential was not at a stable value). After the relaxation, a temperature difference was established in the cell while the potential was recorded. The temperature difference was maintained for several days, until a relatively stable potential was reached. This was a balance between achieving stable values and the time spent on each experiment, and thus some tests were stopped before a stable value was reached in order to have time for other configurations. Afterwards, the temperature difference was set back to 0. The potential was measured both before, during and after applying the temperature difference. The time span for an experiment was typically one week, though both shorter and longer times were applied.

4.3.2 Temperature Notation

Three temperature differences, taken at three different places in the experimental set-up are referred to in this thesis. Therefore a quick clarification is in order. The Seebeck coefficient is reported as $\epsilon(t) = \left(\frac{\Delta\varphi}{\Delta T}\right)_{j=0}$. The temperature difference ΔT used to calculate the Seebeck coefficient is the internal temperature difference between the electrodes in the cell (*i.e.* $\Delta T = \Delta_{int}T$). This temperature is not measured, and must therefore be calculated as:

$$\Delta_{int}T = 0.55\Delta_{ext}T \tag{4.2}$$

Note that here the inner temperature has been assumed to constitute 55 % of the measured external temperature, based on the results from the calibration experiment (see Section 4.4). This assumption will also be discussed further in Section 5.2.6. The measured external temperature difference $\Delta_{ext}T$ is taken between two copper plates inside the set-up, and is not the same as the difference in water bath temperature $\Delta_{WB}T$ which is the one controlled in the experiments. The three temperature differences are illustrated in Figure 4.6.

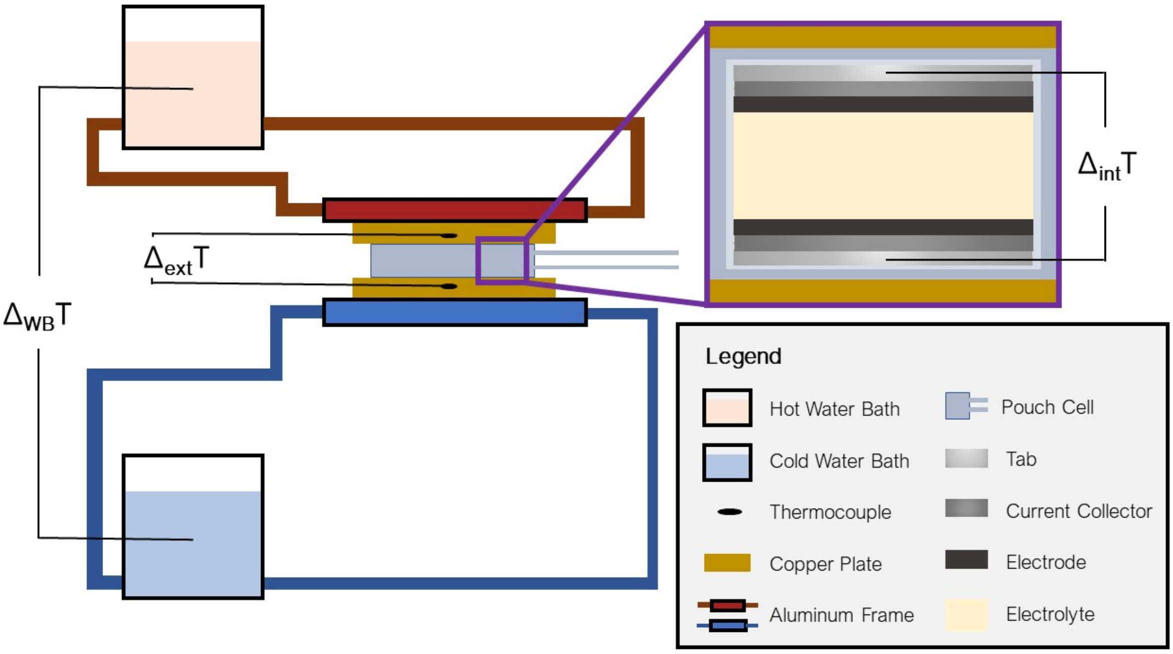

Figure 4.6: Illustration of the experimental set-up, as well as a clarification of the temperature differences used. $\Delta_{WB}T$ is controlled, $\Delta_{ext}T$ is measured, while $\Delta_{int}T$ or just ΔT is the calculated internal temperature difference in the cell required for the calculation of the Seebeck coefficient.

4.3.3 Issues with the Potential Measurement Set-Up

A couple of issues were observed when using the current test-set up, which affected the results obtained in this thesis. The first was that after a certain amount of time the water circulation was reduced, or stopped completely. This was found to be due to a clogging of the aluminum frames because of small debris-particles stacking up. This gave a very unstable temperature profile in some of the tests, as observed for instance in the results in Figure E.3d (Appendix E). In these tests, it was not possible to quantify the processes that relax over several days (thus the stationary state Seebeck coefficient could not be reported). Ideally, the water circulating through the close circuit in the water bath should be completely debris-free to avoid these kinds of issues. The instantaneous effect could still be reported in these cases.

A second issue will be discussed in Section 4.4, and relates to the difficulty of controlling the inner temperature in the cell. High contact resistance in different parts of the set-up lead to large losses in temperature difference. From the water bath temperature difference $\Delta_{WB}T$ to the internal cell ΔT, as much as 1/3 of the total temperature difference is believed to be lost due to contact resistance and possible losses in the tubes connecting the water baths to the frames. This loss is not of importance. What matters is having absolute control of the inner temperature difference to report accurate values. The highest insecurity in the current set up is believed to come from the non-uniformity of the pouch cells, which means that the contact resistance could vary from cell to cell. Therefore, the principal suggestion is using coin-cells in stead, giving a more consistent, if not necessarily lower, contact resistance.

4.4 Temperature Calibration of the Cell

As was illustrated in the experimental setup for the thermoelectric cells (Section 4.3), the temperature was only measured outside the cell during the experiments (see Figure 4.6). The temperature difference of interest, however, is the temperature difference inside the cell between the tabs, so across the system described in Figure 3.1. It was thus necessary to establish a temperature profile for the experimental set-up, in order to estimate the ratio between the measured temperature difference and the internal temperature difference in the cell. This was done by theoretical calculations, and the results were verified by an experimental temperature calibration in the lab.

4.4.1 Theoretical Calculations of Temperature Gradient

The theoretical calculations of the temperature gradient are based on Fourier's law. If the temperature is assumed uniformly distributed and no heat escapes through the sides of the cell, the heat flux can be seen as one-dimensional. In this case, the heat flux should be the same through each subsystem of the cell. Ignoring the coupling phenomena discussed in section 2.5 (assuming equilibrium), the heat flux per unit area can be found as:

$$J_q = \frac{\Delta T}{R_{tot}} \tag{4.3}$$

Where ΔT is the temperature difference across the system and R_{Tot} is the total thermal resistance in the system. The total resistance can be calculated as the sum of each individual resistance, as illustrated in Figure 4.7.

Because perfect thermal insulation is assumed on the side of the cell, the flux must be constant throughout the system. Thus, the contribution to the total temperature difference from each subsystem can be calculated from Fourier's Law for the subsystem:

$$\Delta T_i = J_q R_i \tag{4.4}$$

Where J_q is the total heat flux calculated from Equation 4.3 and R_i is the thermal resistance of the component i. The thermal resistances are calculated as:

$$R_i = \frac{\delta_i}{\kappa_i} \tag{4.5}$$

Where δ_i is the thickness of the component i and κ_i is the thermal conductivity of component i.

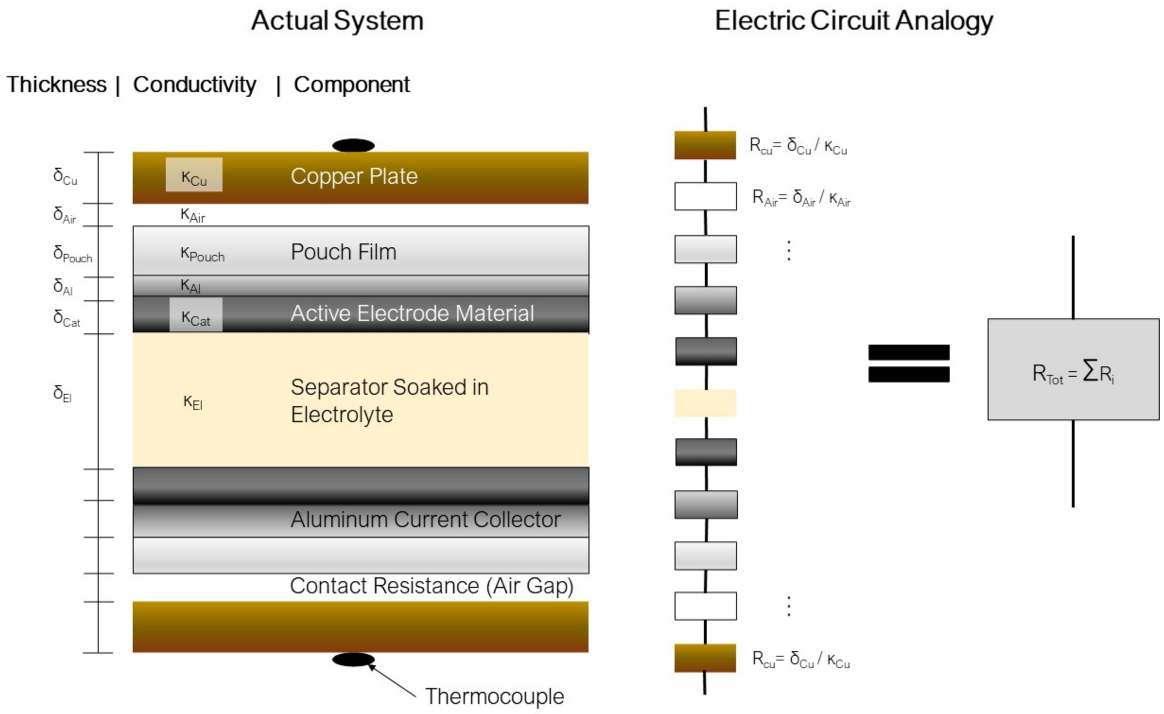

Figure 4.7: Illustration of how the individual resistances from each component are combined to find the total thermal resistance between the thermocouples

The relative temperature difference of each component in the system can now be calculated. The thermal conductivities of the LCO and LFP electrodes, as well as the separator stack were calculated based on data from [99], where they were reported for different materials soaked in electrolyte at 2.3 bar compaction pressure [4]. The value for $LiMn_2O_4$, as well as the aluminum foil and copper were taken from [100]. The value for air was taken from [101], while the value for the pouch material was taken from the data sheet provided by the manufacturer.

The thickness of each component was measured with a micrometer. This was done before assembly for all the components except the separator soaked in electrolyte. The thickness of this component was calculated by subtracting the thicknesses of the individual components from the total thickness of the cell. When the thickness of different cells was measured the results varied widely, from roughly 1.84 mm to 2.30 mm. For this reason, the error reported for the measured thickness of the stack of separators is large.

The results are presented in Table 4.1 and the temperature profile is represented graphically in Figure 4.8. Notice that because of symmetry of the cell, the relative contribution from the components that are equal on both sides have been summed up and reported as one component in stead of two in Table 4.1.

---

[4] In our case the compaction pressure was just 1 bar, so the values taken from [99] were extrapolated by assuming a linear relation from 4.6 bars to 1 bar, and using the compaction-pressure dependency reported in [99] from 4.6 bars to 2.3 bars.

Table 4.1: Relative contribution to the total temperature difference from each layer in the thermocell. Values for the thermal conductivities are taken from [2, 100, 101]. Values have been reported for each of the electrode materials applied in this thesis, and assuming an average air gap δ_{Air} from 0 to 100 μm

Component	**Conductivity [W/(m K)]**	**Thickness** [μm]	**Relative Contribution to** ΔT [%]					
			For LFP		For LMO		For LCO	
			x=0	x=100	x=0	x=100	x=0	x=100
Copper Plates	398	2000 ± 100	0	0	0	0	0	0
Contact Resistance (Air Gap)	0.026	$0<\delta_{Air}<100$	0	42	0	44	0	44
Pouch Film (PET-C8)	0.26	157 ± 2	12	6	12	6	12	8
Aluminum Current Collector	237	17 ± 1	0	0	0	0	0	0
Separator Stack (Whatman Filter 1823070)	0.18 ±0.2	1548 ± 144	84	48	86	48	85	48
$LiFePO_4$	0.32 ± 0.02	68 ± 2	4	2	-	-	-	-
$LiMn_2O_4$	0.91 ± 0.12	75 ± 2	-	-	2	0	-	-
$LiCoO_2$	0.97 ±0.09	92 ± 1	-	-	-	-	2	2

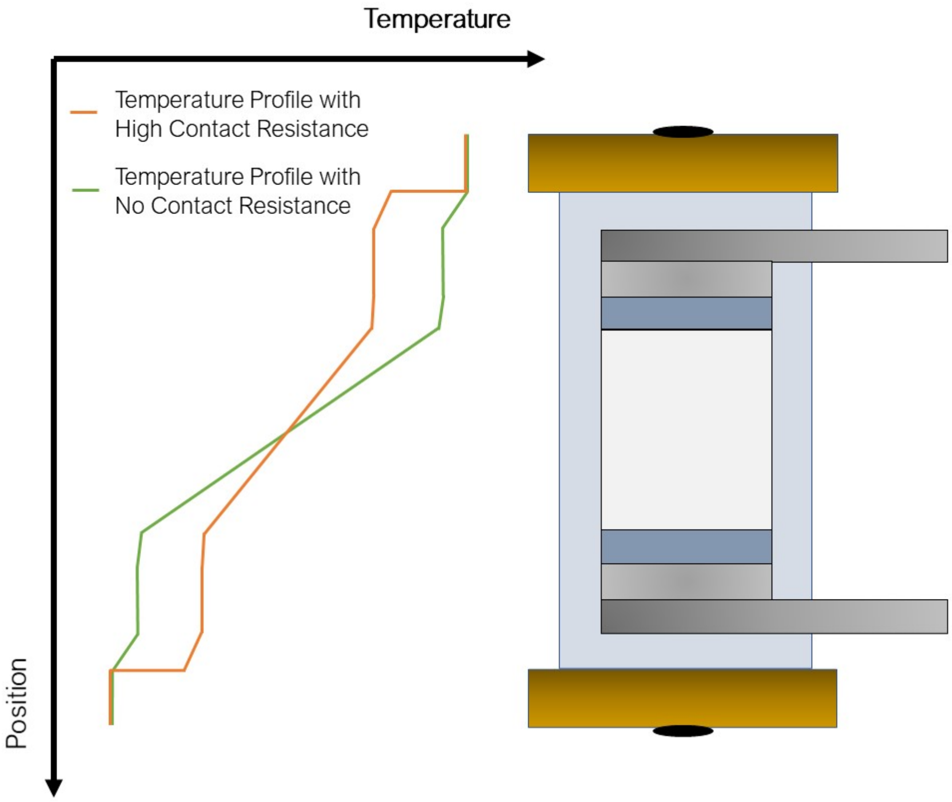

Figure 4.8: Illustration of the temperature profile through the cell based on the theoretical calculations with high and low contact resistance. The figure on the right illustrates the cell. It has been assumed stationary state, and that the conductivity is constant over the different components.

4.4.2 Temperature Calibration Experiment

In order to support the theoretical calculations of the temperature gradient in the cell, a temperature calibration cell was produced. The cell was made following the procedure explained in Section 4.1.1, but before sealing the second side of the cell, one thermocouple was introduced on the outside of each current collector (see illustration of placement in Figure 4.9). On the side where the thermocouples were introduced, thermal bonding tape (FastelFilm 16071) was used to seal the cell. The materials used are detailed in Section 4.1.1, and Hohsen $LiFePO_4$ electrodes were used for the calibration cell. After introducing electrolyte, the cells were taken directly to the calibration set-up. No rest was allowed to avoid having the thermocouples in the electrolyte for an extended period, as it was believed that this harsh environment could influence the functionality of the thermocouples.

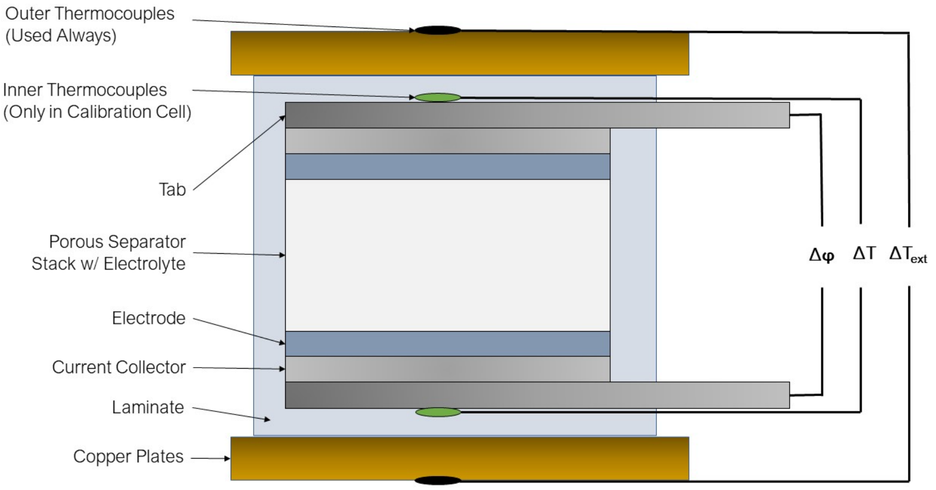

Figure 4.9: Illustration of the thermocouples' placement inside the cell made for the temperature calibration experiment. The outside thermocouples are the ones normally used for the temperature measurements

The temperature calibration experiment consisted of putting the cells with internal thermocouples in the thermoelectric set-up (illustrated in Figure 4.6 in Section 4.3) and setting the waterbaths to the same temperature, at 15, 25 and 35°. This was done to check that the thermocouples reported the same temperature. Following the calibration of the thermocouples, temperature gradients were established with a water bath Δ_{WB}T of 5, 10, 15 and 20 °C, and a mean temperature of 25 °C. The internal and external temperatures were measured. The temperature measured at each location is reported in Figure 4.10.

Further, the contribution of the measured internal temperature difference to the measured external temperature difference was calculated. This was done by taking the average temperature difference at each temperature step over the last four minutes (80 measurement points) for the in-

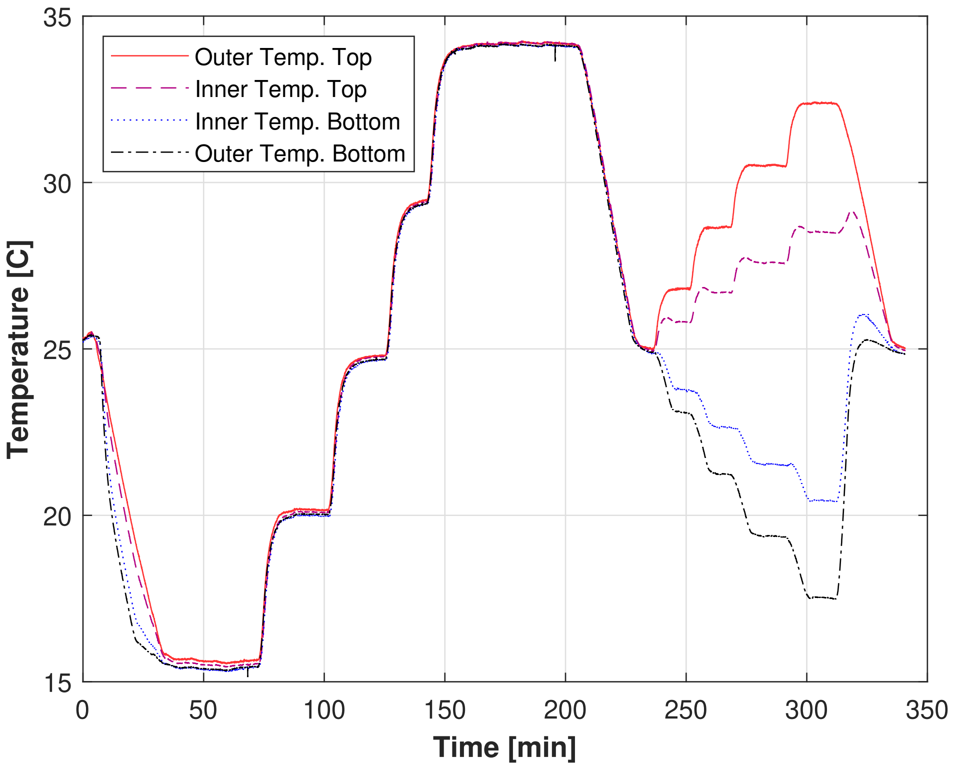

Figure 4.10: Measured temperatures at the different location indicated in Figure 4.9 during the calibration experiment

ternal and external temperature differences. Thereafter the ratio of internal to external temperature was calculated for each step. The resulting ratio $\Delta_{int}T/\Delta_{ext}T$ is given in Table 4.2. As can be seen, the internal temperature difference constitutes around 54.5 ± 0.5 % of the external temperature difference, indicating quite high contact resistance.

Table 4.2: Ratio of internal to external temperature in the calibration cell at different water bath temperatures. The error is reported as the standard deviation of the average.

Water Bath ΔT [K]	Externally Measured ΔT [K]	Internally Measured ΔT [K]	Internal to External ΔT Ratio ($\Delta_{int}T$ / $\Delta_{ext}T$) [%]
5	3.72 ± 0.02	2.04 ± 0.02	54.8 ± 0.9
10	7.41 ± 0.02	4.05 ± 0.02	54.7 ± 0.5
15	11.15 ± 0.01	6.07 ± 0.01	54.4 ± 0.2
20	14.87 ± 0.02	8.05 ± 0.02	54.1 ± 0.2

4.4.3 Discussion of the Temperature Profile and Airgap Measurements

Looking at the results from the calibration experiment (Table 4.2) it is apparent that the contact resistance between the pouch and the copper plates must be quite large. From the outer to the inner temperature measurements, roughly 45.5 % of the temperature difference is lost, leaving just 54.5 % of the measured temperature difference externally as the actual difference inside the cell. Noticeably, it was difficult to achieve proper sealing of the cell used for the temperature calibration experiment due to the inserted thermocouples. Therefore, it is not certain that vacuum existed inside this cell, which has several implications for the result. First of all, the applied values for the conductivities assumed an applied pressure difference of 1 bar, which gives some imprecision in these values. Secondly, faulty sealing could potentially lead to air trapped inside the calibration cell between the pouch and the thermocouple. This could lead to an additional resistance term in these cells that does not exist in the actual cells.

Assuming that there is no air gap internally in the cell so that the results from the calibration experiments are valid, it is possible to estimate the average air gap externally by comparing the experimental results to the results found theoretically in Table 4.1. By doing this, one finds that the average thickness of the air gap between the pouch and the copper plate has to be roughly 75 μm. This is substantial, and is a huge point of improvement for this method, as the reported internal temperature decides the magnitude of the Seebeck coefficient ($\epsilon = \left(\frac{\Delta\varphi}{\Delta T}\right)_{j=0}$).

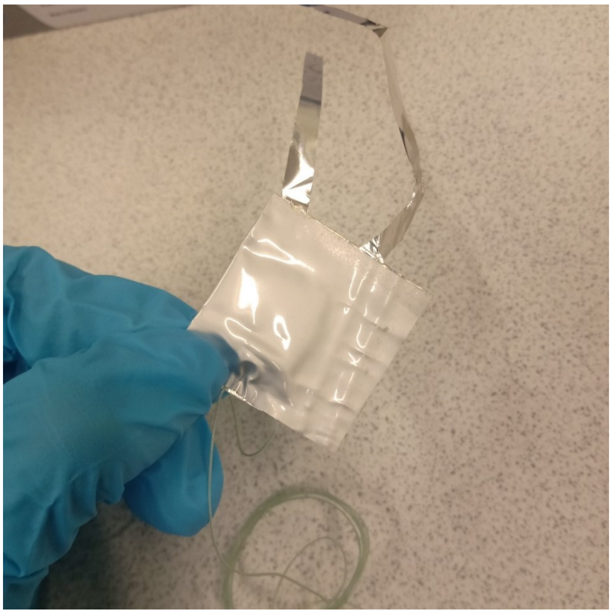

Figure 4.11: Picture of the temperature calibration cell used. The thermocouples were introduced in one side of the cell, and that side was sealed using thermal bonding film.

Chapter 5

Results and Discussion

In this chapter the results are presented, along with a discussion of these. First to be presented are the obtained potential curves as a function of time when a temperature difference was established in the cells. The expected form of these curves is discussed, and deviations are explained. Thereafter, the initial and stationary-state Seebeck coefficients are calculated from these curves for the different electrode-electrolyte combinations. Subsequently, these results are discussed and compared to values reported earlier in literature. Finally the Peltier heats are calculated, and the implications for batteries are discussed.

5.1 Time Evolution of the Potential

The Seebeck coefficient is reported as $\epsilon(t) = \left(\frac{\Delta\varphi}{\Delta T}\right)_{j=0}$, where the time-dependence comes from the variation of the potential, which was shown in Section 3.2 to be due to the concentration gradients establishing in the electrolyte. Before showing the calculated Seebeck coefficients, the plotted potential difference as a function of time when a temperature difference is established in the cell is presented. Because of the extensive volume of results, most of the plots are left in Appendix E. In this section the general form of the obtained graphs are presented and deviations from the expected form are discussed.

5.1.1 The Expected Evolution of the Potential

The cell potential of a symmetric cell using $LiFePO_4$ electrodes and an electrolyte with $LiPF_6$ salt in a 1:1 v/v EC:DMC solvent is shown in Figure 5.1. This illustrates the general behaviour observed in most of the cells. As can be observed, there is an immediate reaction to the temperature difference, where the potential decreases rapidly to a local minimum. Thereafter, a local maximum is achieved within one hour (at t = 9 hours in Figure 5.1b), before the the potential difference reaches a (relatively) steady value as $t \longrightarrow \infty$.

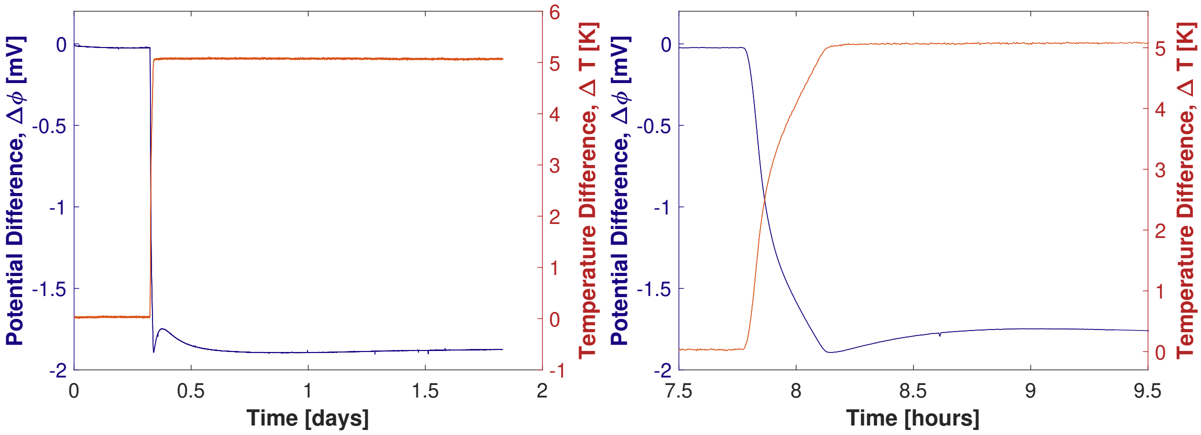

(a) Full test time **(b)** Zoom in on the initial effect of Figure 5.1a

Figure 5.1: Potential difference measured over a symmetric cell using $LiFePO_4$ electrodes and an electrolyte with $LiPF_6$ salt in a 1:1 v/v EC:DMC solvent. The temperature difference in the water baths was $\Delta_{WB}T = 15$ K. The plotted temperature difference is the calculated inner temperature difference between the electrodes. (a) Shows the measurement over two full days; and (b) shows the initial effect of changing the temperature.

This behaviour was observed for many of the cells (see *i.e.* Figures E.1a - E.1f and Figure E.3a-E.3c for LFP; Figures E.4d and E.5c for LMO; and Figures E.9 and E.10b - E.10c for Li_xFePO_4 with x = 0.87 and x = 0.67). This was the same general behaviour observed by Gunnarshaug *et al.* in [6], and Richter *et al.* in [2]. It is also the behaviour that is expected according to the equations derived based on non-equilibrium theory (see Equations 3.59-3.61).

When the electrolyte of a battery has more than one component, a Soret effect will be seen. This means that concentration gradients will be caused due to a temperature difference in the cell. These concentration gradients will in turn affect the potential when no current is flowing (the *emf*), giving a variation of the *emf* with time that is dependent on the concentration gradients [5]. Until Soret equilibrium is reached (mass fluxes in the electrolyte are zero), the variation in the *emf* can be quite large [6].

As can be seen in Figure 5.1, the potential quickly reacts to the change in temperature. After the initial change, the potential continues to a local maximum on a time scale varying from 30 minutes to 2 hours (in this case roughly 50 minutes). Thereafter, a slower process causes the potential to reach a stationary state value after 1-4 days. Diffusion-type processes will follow exponential curves, because concentration gradients change exponentially with time [2]. The existence of a local maximum value indicates that there are two dynamic processes competing with each other in the cells, which have opposite effects on the potential. The fastest process causes a decrease in the (negative) potential difference which gives us the maximum value around t = 9 h in Figure 5.1b. Thereafter the slower diffusion dominates, reducing the potential to a stationary state value as $t \longrightarrow \infty$. As explained by Gunnarshaug *et al.*, these two processes are superimposed on one another, and may have reciprocal influence on each other, even though one is faster than the other [6]. In [6], the fastest process is attributed to the lithium salt. The first maximum is then explained as the PF_6^- trying to establish equilibrium in an (average) carbonate-solvent [6]. Thereafter, the two carbonates separate to create a gradient of EC in DMC or DEC. In this second process, the salt may readjust, but this will happen much faster than the ongoing diffusion process. Further work is still required to establish which diffusion-process can be attributed to which change in potential. It will be assumed here that the fastest process is due to the lithium salt diffusion, as done by Gunnarshaug *et al.* [6].

5.1.2 Drift in Potential

Many of the cells did not reach a stationary state even when maintaining the temperature difference for several days. In some cases, the observed drift in potential was changing with time, making the stationary state Seebeck coefficient hard to calculate. This will be discussed further in Section 5.1.3.

In some of the cells, however, the drift was quite stable in time. In these cases it was possible to quantify the drift, and compensate for it in the results. This was done by using linear regression on the potential curves at the end of the relaxation phase (before the temperature difference was applied). After establishing the drift, the potential curve could be plotted by subtracting the slope of the drift curve from the potential. This is illustrated in Figure 5.2 for one of the cells with LFP electrodes. The same method was applied to calculate the steady state potential in other cases were a (relatively) stable drift was observed.

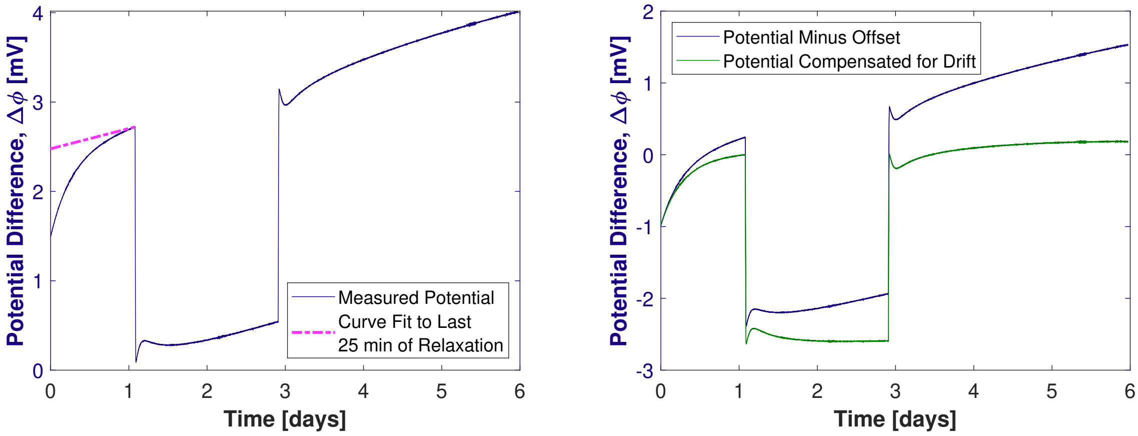

(a) Curve fit of final relaxation region

(b) Potential compensated for drift and offset

Figure 5.2: Illustration of how the potential curves were compensated for drift and offset. (a) Shows the original measured potential of a cell along with the curve fitted to the last 25 minutes of the relaxation. A clear drift in potential is still seen at the end of the relaxation time. (b) Illustrates the curve where the calculated drift has been subtracted from the original potential. The offset, calculated as the y-intersect of the estimated drift, has been subtracted from both the curves in (b).

5.1.3 Changing Drift in Potential

Several authors have reported a drift in potential that has not been properly explained (see *i.e.* [6] and [79]). The same was reported here for some of the cells. In some cases, it was possible to compensate this drift, as explained in Section 5.1.2. However, for some of the cells, the drift does not seem to be constant in time. An example can be seen by looking at Figure E.5c or E.1d. The drift in potential right before applying a temperature difference and the one at stationary state is not the same. This indicates either (1) that the cell does not get enough time to reach a stationary value; or (2) that if the deviation from a stationary state value comes from a drift, this drift is changing with time. When calculating the results for these cells, very high uncertainties had to be reported. The background for this has been illustrated in Figure 5.3. If the bias was compensated so that the stationary state value before putting on the temperature difference was constant, the value for stationary state when the temperature difference was on drifted. However, if the drift was compensated so that the stationary state value with a temperature difference was constant, the value at stationary state without a temperature difference drifted. Thus, the drift is changing with time. The problem with reporting values in these cases is that it is not possible to know *how* the drift changes with time. A linear variation would give very different results to an exponential variation.

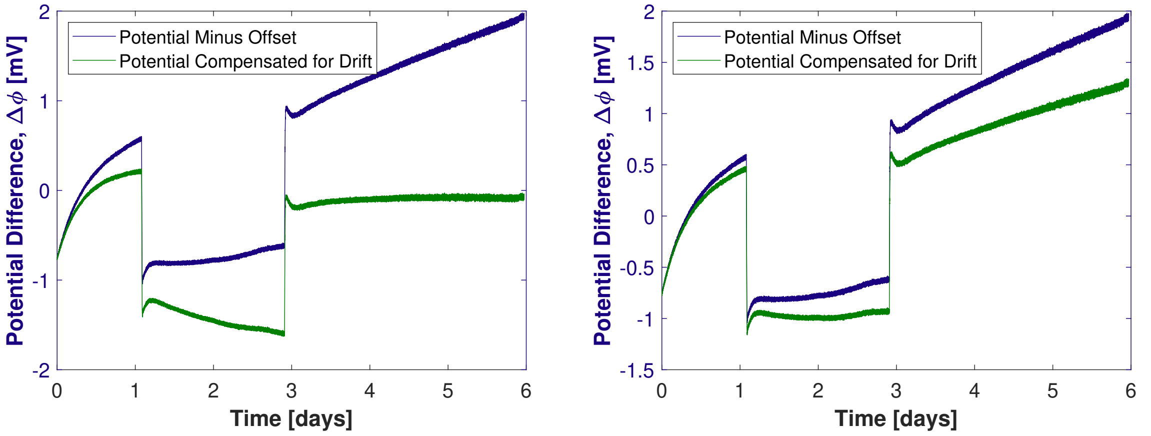

(a) Drift compensated to get good values at $\Delta T = 0$ **(b)** Drift compensated to get good values at $\Delta T \neq 0$

Figure 5.3: Illustration of how the drift changed with time in some of the cells, making it diffucult to calculate the Seebeck coefficient. (a) Illustrates the potential curve when compensating the drift so that the stationary state values are constant at $\Delta T = 0$. (b) Illustrates when the compensation is done so that the stationary state values are constant with an existing ΔT.

It is proposed to conduct longer-lasting experiments (more than one week) to clarify if the potential in the cells where drift was observed eventually reaches a stationary value. Gunnarshaug *et al.* [6] and Richter *et al.* [2] also observed a drift in potential that changed with time for some of their cells, yielding results with high errors. If an explanation behind the drift in potential could be found, it would be easier to prevent in experiments, which would contribute to improving the accuracy of the reported values.

5.1.4 Potential Variations Beyond Drift - Formation Processes

In addition to the drift, another phenomena made it difficult to achieve good numerical results for some of the cells. Observing for instance Figure E.7a and E.9a (also shown in Figure 5.4a and 5.4b), it becomes apparent that some process in these cells is taking place that cannot be explained by the theory presented here. There is a very prominent variation in potential that does not seem to have anything to do with the applied temperature difference. It is proposed here that this potential change is due to processes that take place in a battery shortly after being made, so-called formation processes. Normally the formation taking place in a cell includes processes such as establishing passive layers on the electrode surfaces and allowing the electrolyte to properly soak into all the components. All commercial batteries go through a procedure where these processes are allowed to happen before they are tested and finally sold to the consumer. Most of the cells in this experiment, however, were only allowed to rest for a few days after being made before being introduced in the experimental set-up. Thus, these formation processes could still be in play when the symmetric cell was introduced in the experimental set-up. This hypothesis could be verified by testing cells with the same configuration (electrolyte, state of lithiation and electrode material) that are allowed to rest different time periods before being introduced into the experimental set-up. There was unfortunately not enough time to conduct such a test.

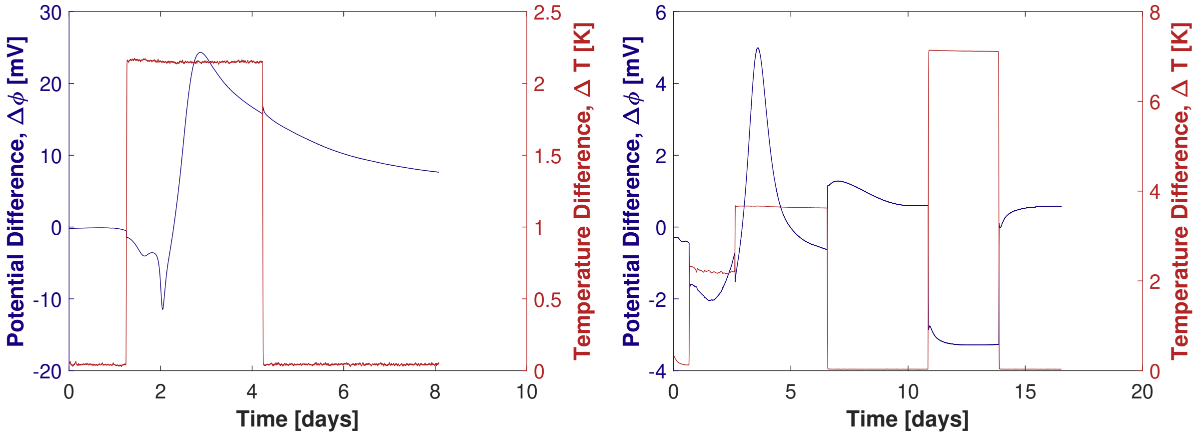

(a) Formation reactions in cell with $LiCoO_2$ electrodes **(b)** Formation reaction in cell with $Li_{0.87}FePO_4$ electrodes

Figure 5.4: Variation in the recorded potential that cannot be described by the reported theory. These variations are believed to be due to formation processes in the cells. (a) Shows a cell with $LiCoO_2$ electrodes and (b) shows a cell with $Li_{0.87}FePO_4$ electrodes.

These cells were not included in the measurements of the Seebeck coefficient, because the uncertainty was considered too big. For future experiments it is recommended that the cells are left to rest for a longer time period (some weeks) before being tested.

5.1.5 Cases where No Local Maximum was Observed

Another deviation from the expected behaviour was seen in cells which did not exhibit a local maximum after the initial drop in potential. This was observed for some of the LCO cells (see Figure E.6a, E.6d E.7d, E.8b and E.8c), and in measurements using the Li_xFePO_4 with $x = 0.47$ (Figure E.10d). For convenience of the reader, an illustration of this phenomena is given in Figure 5.5. These cells show an initial drop in potential, as usual, but do not thereafter exhibit the expected local maximum. In stead, the potential increases directly to a steady state value. It is believed that this observed behaviour is a deviation caused by different external factors, and not necessarily due to a deviation in the behaviour of the cells.

The first thing to be noted is that the results for the LCO electrodes varied widely in quality (see Appendix E.5 and E.6). Some measurement were very noisy (see *i.e.* Figures E.6b, E.7e and E.7f), some had extremely high drift in potential (Figures E.7b and E.7c), while others exhibited strange changes in potential that cannot readily be explained by the theory presented here (Figures E.6a and E.7a), which is believed to be due to formation processes in the cells. With such varying results, it is difficult to say something general about the behaviour of the cells, and more experiments should be conducted to see if a general trend can be established. Based on the results presented by Richter *et al.* for LCO electrodes, it is expected that they will follow the same general behaviour as found here for the other cells [2].

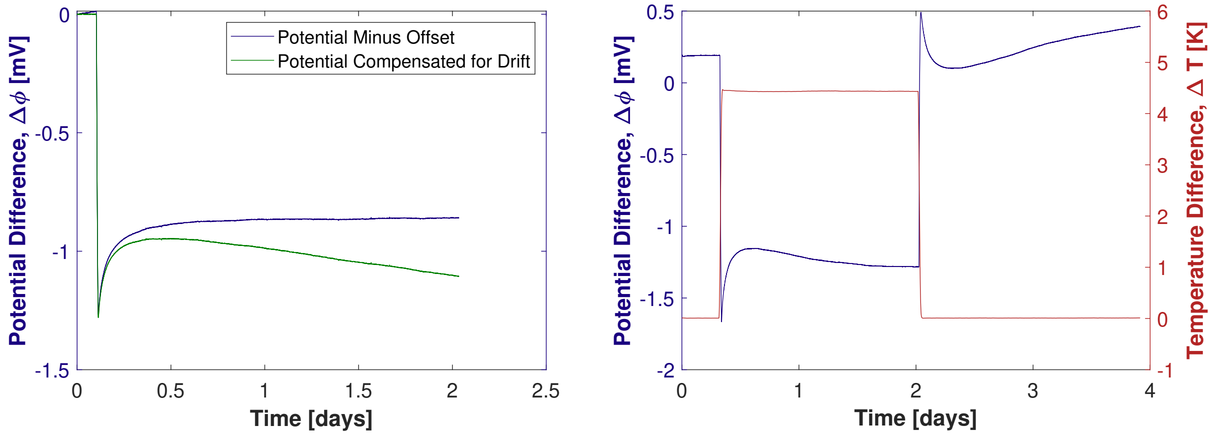

(a) No observed partial Soret equilibrium for $Li_{0.47}FePO_4$ **(b)** Observed Partial Soret equilibrium for $Li_{0.47}FePO_4$

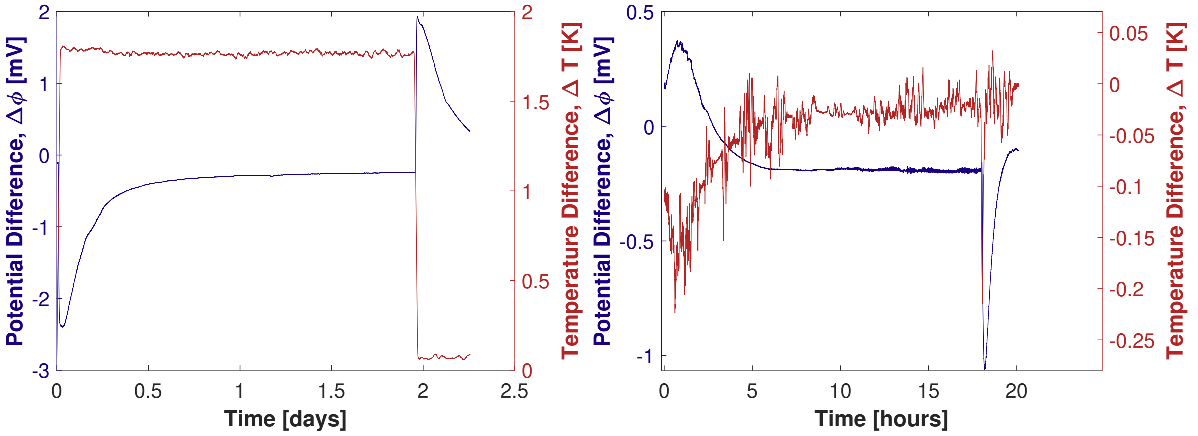

(c) No observed local Soret equilibrium for $LiCoO_4$ **(d)** Relaxation curve of the cell in (c)

Figure 5.5: Cases where partial Soret equilibrium was not observed, and possible explanations behind this. (a) Illustrates a cell with $Li_{0.47}FePO_4$ electrodes where local Soret equilibrium was not observed originally, and what the curve looks like if a linear drift in potential is subtracted from the original curve. (b) Shows a case where the local Soret equilibrium *is* observed with the same cell configuration as the cell in (a). (c) Shows a LCO cell where the local Soret effect is not observed. (d) Is the recorded relaxation curve of the cell in (c)

However, because the apparent lack of a local Soret equilibrium is observed in several cells, some explanation beyond saying that these are "bad results" is in order. In some of the cells, it is possible that the combination of drift and offset in potential mask the first peak that amounts to the local Soret equilibrium. This can be seen in by studying the potential measurements for the $Li_{0.47}FePO_4$ electrodes, given in Figures E.10d - E.10f in Appendix E.7, two of which are re-given in Figure 5.5a and 5.5b. These two measurements show similar, but slightly different behaviours.

The cell in Figure 5.5b exhibits the expected drop in potential followed by a local maximum before relaxing to a stationary value. The cell in Figure 5.5a does not display the expected local maximum, going straight from the initial minimum to a stationary state value. In this case, the cell that deviated from the expected behaviour displayed a slight drift in potential before the experiments started. If the drift is subtracted, a local maximum is observed, but the stationary state is not reached. This could indicate that the experiments were not conducted for a sufficient amount of time, and that the behaviour *does* coincide with the theory, but the cells need more time to reach a stationary state. It also indicates that the cells that exhibit a drift in potential yield imprecise results, even though it may seem like a stationary value is reached. It is not possible to know how this drift would change with time, which gives high uncertainties in the results, especially for the stationary state values.

For other cells, the explanation behind the lack of a local maximum value may lie in the relaxation curves. In the cell pictured in Figure 5.5c (also found in Appendix E.5, Figure E.6d), there was an abrupt change in temperature during the relaxation period that caused the cell potential to react. When the experiment was started, the cell was still reacting to the first change in temperature. This was not discovered at first because the temperature measurements had a lot of noise. However, by removing the general noise, it became clear that a temperature drop had taken place before starting the experiment. Observing Figure 5.5d it is clear that this temperature difference affects the potential, and the cell may still be reacting to this when the actual temperature difference is applied. Therefore the electrolyte in the cell cannot be assumed to have uniform distribution of components at the start of the experiment, affecting the results.

In conclusion, it is believed that in the cases where no local maximum in the potential is observed after the initial drop, it is due to poorly conducted experiments or a drifting potential. Nonetheless, more experiments must be conducted to confirm this, and to give an explanation to the drift in potential.

5.2 Calculated Seebeck Coefficients

Having studied the variations of the potential difference when establishing a temperature difference in the cell, the calculated Seebeck coefficients can now be presented and discussed. The Seebeck coefficients were calculated based on the measurements of the potential at different temperature differences. Because the potential difference changes with time, so does the Seebeck coefficient. Gunnarshaug *et al.* [5, 6] and Richter *et al.* [2] both calculate three values of the Seebeck coefficient, each value corresponding to a distinct time in the measurements. $\epsilon(t=0)=\epsilon_0$ is the initial state Seebeck coefficient, which should be taken at time $t=0$ when a temperature difference is applied to the cell. $\epsilon(t=int)=\epsilon_{int}$ is the Seebeck coefficient corresponding to the partial Soret equilibrium (when the fastest diffusion process approaches a first stationary state). $\epsilon(t\longrightarrow\infty)=\epsilon_\infty$ is the Seebeck coefficient for the final stationary state. In this thesis, focus has been given to the initial and stationary state values.

5.2.1 Initial Seebeck Coefficient (ϵ_0)

The initial value of the Seebeck coefficient is the immediate response of the system to a temperature difference. It should be measured when a temperature difference is present in the cell, but while the electrolyte is still homogeneous. Here, it was calculated based on the first minimum in potential seen as a response to putting on a temperature difference. Because the potential at $\Delta T=0$ should ideally be zero, any drift or offset in potential was subtracted before looking at the initial effect. In principle, the initial Seebeck Coefficient was thus calculated as :

$$\epsilon_0=\frac{\Delta\varphi_{\Delta T}(t=t_T)-\Delta\varphi_{\Delta T=0}(t=0)}{\Delta T} \tag{5.1}$$

Where $\Delta\varphi_{\Delta T}(t=t_T)$ was the potential measured right after the temperature difference was established (the minimum in Figure 5.1), $\Delta\varphi_{\Delta T=0}(t=0)$ was the offset in potential at the start and ΔT was the calculated internal temperature difference.

Two principle uncertainties exist when calculating this value. The first comes from the slow nature of establishing a temperature gradient between the electrodes. The temperature difference required time to establish (t_T), which meant that the diffusion processes got time to start before the initial effect could be properly quantified. Therefore, it must be assumed that the measured initial effect has some contribution from the concentration gradients (*i.e.* the electrolyte is not 100 % homogeneous). The second uncertainty comes from the cases where the original potential had a non-zero and changing value at the start of the experiment. This gave a rather high standard deviation for the bias ($\Delta\varphi_{\Delta T=0}(t=0)$) which propagated into the Seebeck coefficient. Thus the calculated Seebeck coefficient from the cases with an initial high bias accordingly has a high uncertainty in the reported values.

5.2.2 Seebeck Coefficient at Stationary State

The Seebeck coefficient at stationary state was simply taken as the potential divided by the temperature difference at the end of the experiments, when the potential reached a stationary state. In the cases where a drift was observed, the drift was subtracted from the potential before this value was calculated. Also in the case of the stationary state values, any offset from 0 at the start of the experiments was subtracted from the potential before the Seebeck coefficient was calculated.

The value of the stationary state potential used to calculate ϵ_{∞} was taken as the average value of the last 2 hours of the potential measurements. The error was reported as the standard deviation. In the cases were a high drift in potential was observed, the error was reported based on the drift, taken as the difference between the value corrected for drift and the value not corrected for drift.

5.2.3 Reporting the Seebeck Coefficient

It is easy to understand, by observing the varying nature of the measurements of the potential presented in Appendix E, that not all the results obtained in this thesis work were suited to report values of the Seebeck coefficients. To report properly the stationary state values, there should be little or no drift in potential as $t \longrightarrow \infty$, and also no drift at the start of the experiments. These conditions were achieved in a small minority of the cases, which made the stationary state values hard to report. For the initial values, an ideal case would require that the potential before applying the temperature difference was 0, and that this potential did not drift in the time before putting on the temperature difference. Also these conditions were absent from many of the results.

For the stationary state, a drift in potential makes it nearly impossible to report good values, because assumptions have to be made concerning the development of the drift. Will the potential eventually reach a stationary value? If so, how fast? Does the drift change when a temperature difference is applied? Because the nature of the drift observed here has not been further explained in literature or research, it is hard to know whether it is linear or exponential in nature. In fact, if it is caused by concentration gradients, it is more likely to be exponential than linear [2]. Thus, values for the stationary state were only reported in the cases where there was little or no drift before the experiments started.

When it comes to the initial values, the Seebeck coefficient quantifies the immediate response of the potential to a temperature difference. Even though this value should ideally be taken with homogeneous electrolyte composition, the error of finding this value when the composition is non-uniform should be small, given that the temperature difference establishes quickly. The contribution to the potential from a drifting bias right before and right after applying a temperature difference should be largely unaffected by this event (assuming that the processes causing the drift in potential are slow compared to establishing the temperature difference). In other words: any contribution to the potential present right before introducing a temperature difference should also be present (and largely unchanged) right after introducing the temperature difference. Therefore, it was easier to report the initial Seebeck coefficients than the stationary state ones, as a less stringent requirement is needed.

Even though it should be possible to determine the initial Seebeck coefficient with relative certainty even if the cells show a high drift in potential, high errors were reported here. This was done because the given method for establishing the temperature gradient was not very fast. In some cases, establishing the temperature difference could take up to 45 minutes! Because of this, the potential could change due to a drift or concentration effects while the temperature difference was establishing in the cell. For future experiments a faster method for establishing the temperature difference should therefore be sought.

The values found for initial and stationary state Seebeck coefficient for all the experiments were they could be reported (*i.e.* excluding results that were very noisy or had a very high drift in potential) are given in Appendix F (Table F.1). Based on the results from all the experiments, an average coefficient has been calculated for each configuration. These average values are summarized in in Table F.2 in Appendix F. These results have been left in the appendix to avoid confusion, because linear regression was chosen to report the values here. The linerar regression will be carried out in Section 5.2.5.

5.2.4 Reported Errors in the Seebeck Coefficient

The calculated errors for the Seebeck coefficients reported in Appendix F are the propagated errors from measurements of temperature and potential. In the cases where the drift in these measurements at stationary state was minimal, the errors were reported as the standard deviation of the measurements (corresponding to the noise in the measurements). In the cases where the potential (or temperature) drifted, the errors were reported based on the change in the value. For example, in the illustrated case in Figure 5.2 the potential compensated for drift and offset (green line in Figure 5.2b) changes from roughly -1 mV to 0 mV before the temperature difference is put on. The initial potential would then be reported as -0.5 ± 0.5 mV. This error would propagate to the reported Seebeck coefficient through Gauss law of error propagation, given in Appendix H.

When the average values of the Seebeck coefficients were calculated, the error was given as whichever was higher - the calculated standard error of the mean (see Appendix H) or as the standard deviation of the reported average.

5.2.5 Calculating the Seebeck Coefficient using Linear Regression

Some of the values reported here are based on experiments that did not yield very precise results, usually because of a high drift in potential. Looking at the errors in the reported values for average Seebeck coefficients in Table F.2 gives some idea of this imprecision. A better representation of this is found when the temperature difference is plotted against the potential difference for the individual experiments for each configuration. The Seebeck coefficient can then be found as the slope of the linear curve that best fits these points. This has been done for all the configurations in Appendix G. A selection of the results is presented in Figure 5.6.

Figure 5.6a presents the points taken to calculate the initial Seebeck coefficient for the $Li_{0.87}FePO_4$ electrodes with a 1 M $LiPF_6$ in 1:1 wt % EC:DEC electrolyte. Figure 5.6b represents the points taken to calculate the initial Seebeck coefficient for the $LiCoO_2$ with the same electrolyte. It immediately becomes clear that the estimated Seebeck coefficient cannot be accurately reported in the latter case, because there is a huge interval of possible correlations between the points. We also see that the value for the initial Seebeck coefficient found based on the slope of the regression line (-0.093 mV/K) differs greatly from the value reported based on the average of the experiments (from Table F.2 in Appendix F $\epsilon_0 = -0.58 \pm 0.47$ for LCO with EC:DMC). In the case of the $Li_{0.87}FePO_4$, on the other hand, the regression line gives a much better correlation between the points. In this case the reported value of -0.47 ± 0.19 mV/K taken from the regression line is in accordance with the calculated average of -0.46 ± 0.06 from Table F.2 (Appendix F). The same is true for the plots for LFP and LMO with EC:DEC solvent found in Figures 5.6c and 5.6d.

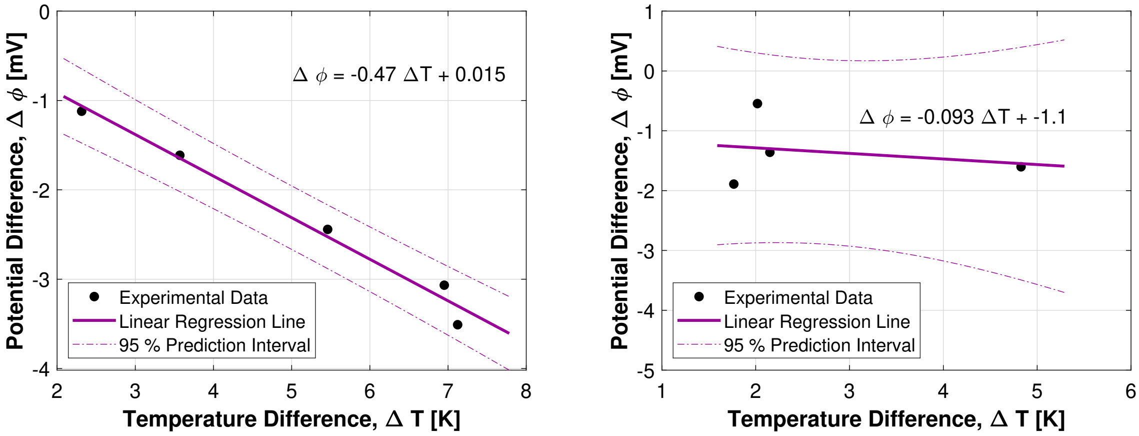

(a) Initial value, $Li_{0.87}FePO_4$ with EC:DEC solvent **(b)** Initial value, $LiCoO_2$ with EC:DEC solvent

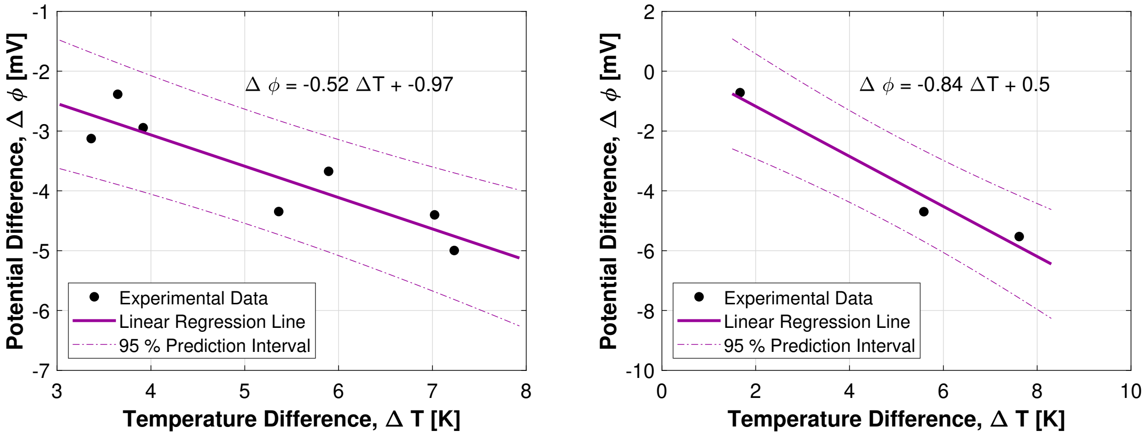

(c) Initial value, $LiFePO_4$ with EC:DEC solvent **(d)** Initial value, $LiMn_2O_4$ with EC:DEC solvent

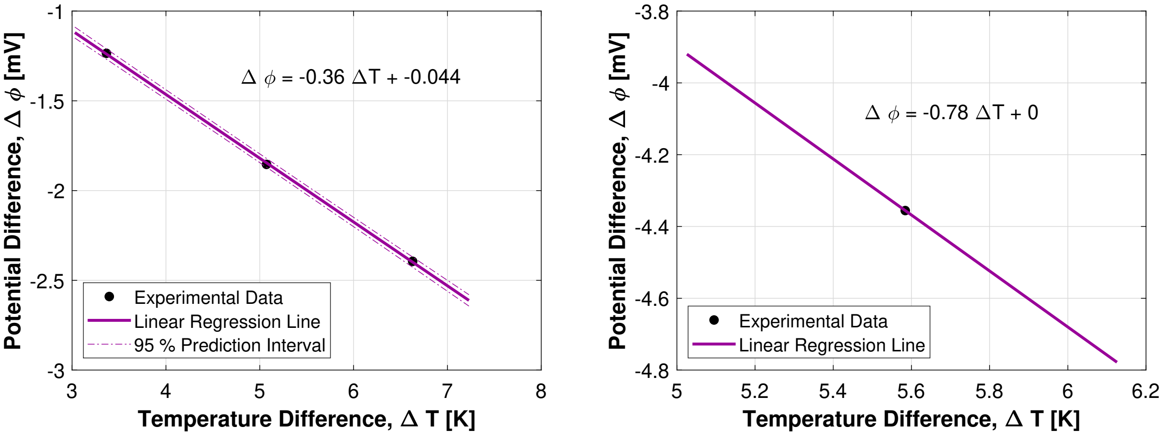

(e) Stationary state value, $LiFePO_4$ with EC:DMC solvent **(f)** Stationary state value, $LiMn_2O_4$ with EC:DEC solvent

Figure 5.6: Plots for different experiments of the internal temperature difference to the potential difference in the symmetric cells, along with the best-fit linear regression line to these points. (a)-(d) are taken at time t=0, so just after the temperature difference is applied.(e)-(f) show results at time $t \longrightarrow \infty$. The electrode and electrolyte solvent are stated under each graph.

In Figures 5.6e and 5.6f, one good and one bad case is illustrated for the steady state Seebeck coefficient. Figure 5.6e shows how a close-to-perfect correlation is found between the points for the stationary state value of the $LiFePO_4$ using a 1 M $LiPF_6$ salt in a solvent of EC:DMC. The reported value of -0.36 ± 0.03 mV/K is the same as the one calculated from the average of the points. As a contrast, Figure 5.6f shows how the stationary state Seebeck coefficient of the $LiMn_2O_4$ electrodes with an electrolyte using EC:DEC solvent has been calculated based only on one point, because the other experiments did not yield sufficiently stable values in stationary state. This value can be used as an indication, but more experiments must be conducted before a final value can be reported for this configuration.

The regression lines plotting potential difference to temperature difference for the other configurations can be found in Appendix G, and conclusions concerning the validity of the results will be drawn based on these curves. In cases where there is a high error in the average values, and little or no correlation exists between the points, no values were reported. This was true for the steady state values of LCO using EC:DEC solvent, the steady state value of LMO using EC:DEC solvent and the initial value of LMO using EC:DMC solvent. The average values for these configurations calculated in Table F.2 (Appendix F) have a high probability of being very imprecise, or directly wrong. Thus, more experiments are required to obtain better results in these cases. The values for the Seebeck coefficient found by using the regression-line method are reported in Table 5.1. The errors are reported as whichever was higher - the mean standard deviation from the regression line, or the average error of the calculated Seebeck coefficients for each individual experiment for each configuration.

Table 5.1: Reported Seebeck coefficients using a least square fit to all the experimental data for the different configurations in this thesis. The curve fits are shown in Appendix G

Electrode	Electrolyte	ϵ_0 [mV/K]	ϵ_∞[mV/K]
$LiFePO_4$	1 M $LiPF_6$ in 1:1 wt% EC:DEC	-0.52 ± 0.50	-0.63 ± 0.30
	1 M $LiPF_6$ in 1:1 v/v EC:DMC	-0.33 ± 0.03	-0.36 ± 0.03
$LiMn_2O_4$	1 M $LiPF_6$ in 1:1 wt% EC:DEC	-0.84 ± 0.84	**NR**
	1 M $LiPF_6$ in 1:1 v/v EC:DMC	**NR**	-0.41 ± 0.56
$LiCoO_2$	1 M $LiPF_6$ in 1:1 wt% EC:DEC	-0.09 ± 0.84	**NR**
	1 M $LiPF_6$ in 1:1 v/v EC:DMC	-0.22 ± 0.36	0.1 ± 0.5
$Li_{0.87}FePO_4$	1 M $LiPF_6$ in 1:1 wt% EC:DEC	-0.47 ± 0.19	-0.55 ± 0.37
$Li_{0.67}FePO_4$	1 M $LiPF_6$ in 1:1 wt% EC:DEC	-0.53 ± 0.29	-0.28 ± 0.56
$Li_{0.47}FePO_4$	1 M $LiPF_6$ in 1:1 wt% EC:DEC	-0.33 ± 0.10	-0.27 ± 0.10

NR-Not Reported

5.2.6 The Ratio of Internal to External Temperature

Richter *et al.* reported values for the ratio of internal to external temperatures to be $\Delta_{int}T/\Delta_{ext}T = 0.70 \pm 0.01$. The materials in the cells and the set-up used in [2] are quite similar to the materials and set-up used in this experiment. Therefore this discrepancy is surprising (here, the same ratio was reported as $\Delta_{int}T/\Delta_{ext}T = 0.55 \pm 0.01$). Three principle explanations are possible. The first, and the one that has been assumed by applying the value 0.55 ± 0.01 in stead of 0.70 ± 0.01 in this thesis, is that the average air gap in the set-up in this thesis is slightly thicker. As seen in Section 4.4, the contact resistance between the pouch and the copper plates is very sensitive to the thickness of this air gap. Therefore, anything from using different aluminum frames, to applying a different pouch material that "wrinkles" more could give a different value.

The second explanation is that there are differences from cell to cell that can give large variations in the internal temperature. This is the scariest explanation in terms of results, because it reduces drastically the precision with which the internal temperature difference can be reported. Using a water bath temperature difference of 20 K gave an external temperature difference of roughly 12 K. The internal temperature difference would then vary from 6.6 K to 8.4 K depending on which number was used. Assuming, based on the values from the experiments, that the initial potential drop at $\Delta_{WB}T = 20K$ is around - 4 mV, the initial Seebeck coefficient would change from - 0.48 mV/K (using $\Delta_{int}T = 0.70\Delta_{ext}T$) to -0.61 mV/K (using $\Delta_{int}T = 0.55\Delta_{ext}T$), amounting to a 27 % increase in reported values.

The third explanation lays in the difficulty encountered upon sealing the calibration cell with thermocouples inside, rendering possible an internal air gap in the cell. This explanation suggests that a higher ratio would be obtained for the actual cells compared to the calibration cell.

The sensitivity of the set-up to the air gap is unfortunate for the reported results. Comparing the external to internal temperature value reported by Richter *et al.* and the value reported here for a very similar set-up, a difference of 16 % is observed. If this discrepancy is due to variations in the average air gap from cell to cell, and not due to a difference between these two set-ups, or the materials applied, it would imply that the magnitude of the reported Seebeck coefficient could deviate as much as 30 % (as illustrated in the example above).

5.2.7 Discussion of the Reported Seebeck Coefficients

Though more experiments are required to confirm the values, it is interesting to comment on the preliminary results presented in Table 5.1.

Seebeck Coefficients with Different Electrolyte Composition

As a general trend, it would appear that both the initial and steady state Seebeck coefficients of all the electrodes are lower when using a 1:1 v/v EC:DEC solvent compared to using a 1:1 wt % EC:DMC. Even though the results for the LMO and LCO electrodes show high errors, making these results hard to trust, the same behaviour is also seen for the LFP.

The fact that the electrolyte influences not only the initial Seebeck coefficient (where the terms for heats of transfer of components, $\frac{t_i q_i^*}{T}$, are present) but also the steady state values, indicates that the electrolyte likely has an influence on the entropy transported by lithium-ions, (the term $S^*_{Li^+}$ in Equation 3.57). Curiously, this influence seems to be bigger than the influence on the heats of transfer, as the change is more prominent when changing the electrolyte than when comparing the initial to steady state values in the two cases. This indicates that the terms $\frac{t_i q_i^*}{T}$ are similar for the electrolytes containing DEC and DMC, whereas the entropy transported by lithium-ions, $S^*_{Li^+}$, varies significantly. It should be noted here that the electrolytes vary not only in which components they contain (one having DMC, the other DEC), but also in the molar fractions of the components. As was shown in Section 4.1, the molar fraction of the salt is 0.055 for the electrolyte containing DEC, while it is only 0.036 for the electrolyte with DMC. Hudak and Amatucci found that the anion used, and electrolyte concentration had an influence on the reported Seebeck coefficient, while changing the electrolyte solvent did not [78]. A decrease in the concentration of the salt decreased the values of the Seebeck coefficient [78]. This is in accordance with the observation made here, where the Seebeck coefficient decreases (in absolute value) with decreasing concentration of the salt. Thus it is possible that the lower molar fraction of the lithium salt in the EC:DMC electrolyte has a bigger influence than changing the solvent. The difference could for instance influence the cluster formation in the electrolyte. A lower molar fraction of anions and lithium-ions could give fewer and less bulky clusters, which could have a direct influence on the value of $S^*_{Li^+}$. However, these are just speculations at this point, and experiments would have to be conducted to confirm this.

Influence of Electrode Material

Unfortunately, the high errors in the results make it difficult to compare the different electrode materials. Taking the average gives different values than when using the linear regression, and with error limits the values for all the electrodes are within the bounds of one another. More experiments would be required to report values with lower error-bounds.

For LCO the correlation between the experiments is close to non-existent (see Figure 5.6b), and trying to generalize these results would therefore be of little value. For LMO and LFP with electrolyte using EC:DEC solvent, however, the linear regression curve gives a better fit to the data points (see Figures 5.6c and 5.6d). Looking at these curves, and the corresponding reported coefficients, LMO has a higher initial Seebeck coefficient than the LFP. This observation coincides qualitatively with the Peltier heats for these electrodes calculated from entropy data from literature in [5] (see also

Figure 2.5), where the corresponding Seebeck coefficient for LMO is higher than the coefficient for LFP.

Different States of Charge for LFP

For low states of charge, the LFP cells follow the expected behaviour based on the calculations made by Gunnarshaug *et al.* in [5] (and represented in Figure 2.5c). The Seebeck coefficients are stable around 0.5 mV/K for $0.67 < x < 1$ (where x is the lithiation state in Li_xFePO_4). However, it drops down to 0.33 mV/K for $x = 0.47$. Gunnarshaug *et al.* reported in [5] a slight decrease in the Peltier heat (and thus the Seebeck coefficient) when $x<0.5$ using data from Viswanathan *et al.* [3], though this change is more likely to be a gradual change that appears sudden due to rounding. Thus the drop in value for the Seebeck coefficient observed for the $Li_{0.53}FePO_4$ electrodes does not coincide with the expected behaviour. However, this could simply be because of the linear fit. The regression finds the best fit to the data points in a least square sense. Because only three datapoints were used for this plot, many fits are possible. If the standard deviation is increased slightly, it is possible to fit a curve giving an initial Seebeck coefficient of $\epsilon_0 = -0.45 \pm 0.17$. This has been illustrated in Figure 5.7, where the original regression curve is plotted along with the modified curve which gives values that are in better accordance with literature data.

More data points are required to make a conclusion concerning the trend, but the preliminary results presented here suggest, as expected, that the state of charge has little influence on the Peltier heat for LFP at low states of charge (high lithiation values). This is related to the structural changes (or rather lack thereof) present in these electrodes during charging. LFP has only two phases ($LiFePO_4$ and $FePO_4$), unlike *i.e.* LCO which forms a solid solution of $Li_{1-x}CoO_2$ during charge/discharge [102]. This gives LFP a very flat charge/discharge curve, compared to the sloping curve of LCO. This is also reflected in the entropy change, which is higher upon phase transitions. Thus, the Seebeck coefficient reported here shows stable values, as expected, when the LFP electrodes are tested at low states of charge.

No values were reported at higher states of charge due to lack of time, thus this is left for further work. It is expected that these values will show relative stability, with a slight decrease in absolute value towards 100 % SoC.

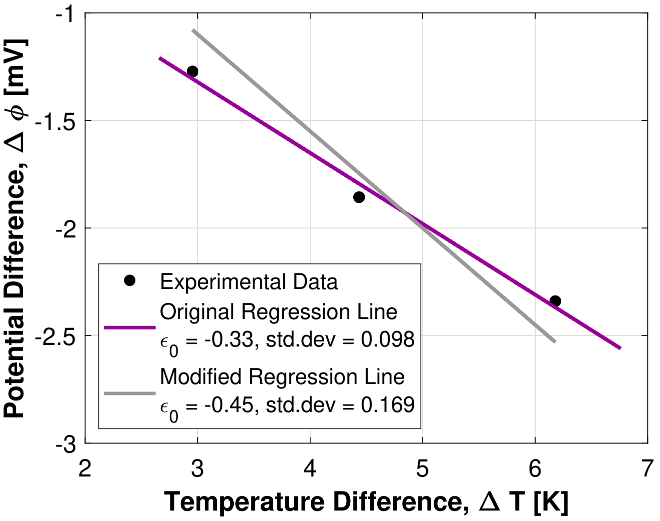

Figure 5.7: Illustration of how the regression line for the $Li_{0.47}FePO_4$ electrodes can be modified to fit with the expected behaviour from literature data. More data points are required to confirm the results.

Comparison with Values Reported Earlier

Comparing the values found here to the values reported in earlier research for a range of electrode materials in Table 2.1, one can see that the values achieved are of the same order of magnitude. The coefficients are in alignment with the reported value of 0.57 mV/K for $Li_{3.5}(CN)_6$ electrodes using a 1 M $LiClO_4$ in 1:1 EC:DEC electrolyte given by Black *et al.* [79]. They are also close to the values reported by Hudak and Amatucci for the Li_xTiS_2 electrodes at different lithiation states and with different electrolytes [78].

Nonetheless, the reported values both for LCO and LFP are much *lower* and *more stable in time* than the values proposed earlier by other authors. Gunnarshaug *et al.* reported an average initial Seebeck coefficient for LFP in a 1 M $LiPF_6$ 1:1 wt % EC:DEC electrolyte (corresponding to the one used here) of $\epsilon_0 = -1.3 \pm 0.2$, and a stationary state value of $\epsilon_\infty = -4.3 \pm 0.6$ [6]. For this electrolyte the values reported here were $\epsilon_0 = -0.52 \pm 0.50$ and $\epsilon_\infty = -0.63 \pm 0.30$. These values do not coincide. Even if it is assumed that the internal temperature difference is off by 16 % (using the value for $\Delta_{int}T/\Delta_{ext}T$ of 0.70 in stead of 0.55), the values reported here would *decrease*, giving even bigger differences.

The same is observed for LCO, where Richter *et al.* reported initial and stationary state Seebeck coefficients of $\epsilon_0 = -2.8 \pm 0.3$ and $\epsilon_\infty = -1.7 \pm 0.2$ respectively. Also in this case the same electrolyte ($LiPF_6$ salt in EC:DEC) was used. The values reported for LCO in this thesis, though subject to high errors, indicated Seebeck coefficients of $\epsilon_0 = -0.09 \pm 0.84$ and $\epsilon_\infty = +0.11 \pm 0.75$ based on the (rather poor) regression line, and $\epsilon_0 = -0.58 \pm 0.47$ and $\epsilon_\infty = -0.35 \pm 0.71$ based on the average value of the experiments. Either case gives much lower values than the ones reported by Richter *et al.*[2]. However, the electrodes used here were not in pristine condition, which could explain these discrepancies. Also, the general results for the LCO were not very good (see *i.e.* the low correlation found between the different experiments in Figure 5.6b).

In any case, the discrepancy remains for the reported values of LFP. One possibility that must be considered is that one (or several) of the reported values are wrong. This could be due to lack of control of the internal temperature (here calculated based on a calibration experiment that may be unrepresentative, and in [6] assumed to be equal to the one found by Richter *et al.* using a similar calibration experiment). It could also be due to the uncontrolled and thus-far unexplained drift in potential in combination with too short experiments, giving high uncertainty in the stationary state values. However, the magnitude of the discrepancies, and the fact that several experiments confirm the same values in all cases, suggest that other explanations may be necessary. The materials used for the electrolyte, the electrodes, the pouch and the separator in this thesis were the same as the materials used by Gunnarshaug *et al.* in [6]. The only difference in the production method was the fact that in [6] a piece of tape was used to hold the thermal bonding tape in place. In addition, these cells were left to rest for a longer time period before the experiments were conducted. These differences could potentially give a change of composition in the electrolyte, which would have an influence on the entropy transported by lithium-ions ($S^*_{Li^+}$ in Equation 3.57). Also, the wetted separator stack was 1.8 mm in [6], while it was measured to be roughly 1.5 mm in this thesis. This difference could indicate either a higher vacuum used when sealing the cells, or a thicker layer of separators. A higher vacuum could give increased tortuosity of the separator, which could influence the diffusion of components in the electrolyte.

The only way to confirm or discard any hypothesis regarding these discrepancies would be to conduct more experiments. Carefully controlling the drift in potential and (if possible) the internal temperature would yield more certain results. Studies should also be conducted where the influence of factors such as the separator tortuosity and the resting time post-production are monitored more meticulously.

5.3 Peltier Heats

After a long (but necessary) deviation, we finally find ourselves in position to calculate the Peltier heats of the electrode-electrolyte combinations explored in this thesis. Through Onsager's reciprocal relations, the Peltier heat is simply found from the Seebeck coefficient as:

$$\pi(t) = -FT\epsilon(t) \tag{2.23}$$

The mean temperature T of the experiments was maintained at 25 °C (298.15 K), and F is Faraday's constant, $F = 96485$ C/mol. Using this, the initial and steady state values of the Peltier heats can be calculated from the reported values of the Seebeck coefficient in Table 5.1. The results are presented in Table 5.2. The errors are given as the errors from the Seebeck coefficients, which are reflected in the Peltier heats through Gauss law of error propagation (see Appendix H).

Table 5.2: Reported Peltier heats, calculated from the Seebeck coefficients found experimentally

Electrode	**Electrolyte**	π_0 **[kJ/mol]**	π_∞**[kJ/mol]**
$LiFePO_4$	1 M $LiPF_6$ in 1:1 wt% EC:DEC	15 ± 14	18 ± 9
	1 M $LiPF_6$ in 1:1 v/v EC:DMC	9.5 ± 0.9	10 ± 1
$LiMn_2O_4$	1 M $LiPF_6$ in 1:1 wt% EC:DEC	24 ± 24	**NR**
	1 M $LiPF_6$ in 1:1 v/v EC:DMC	**NR**	12 ± 16
$LiCoO_2$	1 M $LiPF_6$ in 1:1 wt% EC:DEC	3 ± 24	**NR**
	1 M $LiPF_6$ in 1:1 v/v EC:DMC	6 ± 10	3 ± 14
$Li_{0.87}FePO_4$	1 M $LiPF_6$ in 1:1 wt% EC:DEC	14 ± 5	16 ± 11
$Li_{0.67}FePO_4$	1 M $LiPF_6$ in 1:1 wt% EC:DEC	15 ± 8	8 ± 16
$Li_{0.47}FePO_4$	1 M $LiPF_6$ in 1:1 wt% EC:DEC	9.5 ± 2.9	7.8 ± 2.9

NR-Not Reported

5.3.1 Implications for Batteries

The positive sign of the Peltier heat in Table 5.2 means that the electrode has a cooling effect when an oxidation reaction occurs on it (during charge). The errors in the reported values for LCO make it difficult to conclude on whether this electrode material will have a cooling or heating effect during discharge. For the other materials, even with high errors, a positive value is achieved. This means that a local *heating effect* is seen during *discharge* for electrodes of LFP and LMO (at 0 % state of charge). The values are reversed during charging, which means that a local cooling effect would be seen on these electrodes while charging. As expected, the effect is largely unchanged for LFP at different states of charge. The slightly lower value at $Li_0.47FePO_4$ is believed to be a deviation, though more measurements are required to confirm this.

The values of the Peltier heats found here suggest smaller local heat effects on these electrodes than stipulated by Gunnarshaug *et al.* in [5] and Richter *et al.* in [2], and also suggest that the variation with time is less significant than first anticipated. If the calculated values from Table 5.2 are used in combination with values of ΔS from literature, the Peltier heat of the anode can be calculated. The most commonly used anode material in modern LIBs is graphite (often denoted Li_xC_6). Using data from [3] the value of ΔS for a full cell consisting of LFP and graphite at 0 % SoC with a $LiPF_6$ salt in EC:DMC electrolyte is taken to be roughly $\Delta S = -60 \pm 15$ J/(mol K) (combining half-cell entropies for these cells from potentiometric measurements [3]). Using Equation 2.24 the Peltier heats for graphite can then be estimated. The value with the EC:DMC solvent is used, as this is the solvent used by Viswanathan *et al.* in [3]. The results yield $\pi^{s,a}_{0,C_6} = -8.4 \pm 4.5$ kJ/mol and $\pi^{s,a}_{\infty,C_6} = -7.9 \pm 4.6$ kJ/mol. The negative sign indicates that the Peltier effect at the graphite at 0 % state of charge *heats* the electrode when an oxidation occurs (during *discharge*). This is in direct contrast to the results reported by authors earlier [2, 6], indicating that at 0 % SoC the two electrodes both contribute to heating during discharge and cooling during charge. Large uncertainties exist in this estimate, however, both in the calculated values here, and in the estimates of the total cell entropy change calculated from half-cells in [3]. However, as the state of charge is increased, the total entropy change of the LFP-graphite cell estimated by Viswanathan *et al.* also increases rapidly to values that are much closer to 0 [3]. From roughly 5 % SoC till 100 % SoC the value of the total entropy is always $\Delta S > -20 \pm 15$ J/(mol K). Because the Peltier heat of the LFP has been found to be relatively constant with increasing SoC, the values for the graphite would then be on the order of $\pi^{s,a}_{0,C_6} > 3.5 \pm 4.5$ kJ/mol and $\pi^{s,a}_{\infty,C_6} > 4.0 \pm 4.6$ kJ/mol. These results indicate opposite effects on the two electrodes for most of the SoC-range, in accordance with what was reported by Gunnarshaug *et al.* [6] and Richter *et al.* [2], though on a much smaller scale.

Gunnarshaug *et al.* calculated the Peltier heat for graphite at different lithiation states from reported half-cell entropies of graphite, and using reported Seebeck coefficients for lithium-metal electrodes. The results of these calculations are presented in Figure 5.8, which was taken from [5] and reproduced with permission from the author. The reported values are given when the Li_xC_6 acts as anode (during discharge), which was also done for the electrode materials used in this thesis. In the figure, it is possible to observe the sharp increase in $\pi^{s,a}_0$ as the state of charge is increased from 0 % to 10 %. It is also possible to observe that these values are much larger in magnitude than the estimates found here for the Li_xC_6 based on half-cell entropy data from [3] and the experimental results for LFP. These discrepancies have a multitude of possible explanations, including the use imprecise values for the applied entropy change of the half-cells; imprecise values of the lithium-metal Seebeck coefficients used; and not taking into account the possibly high influence of the electrolyte composition on the entropy change. What becomes clear from the discrepancy, however, is that more research is required to establish higher accuracy in the reported values.

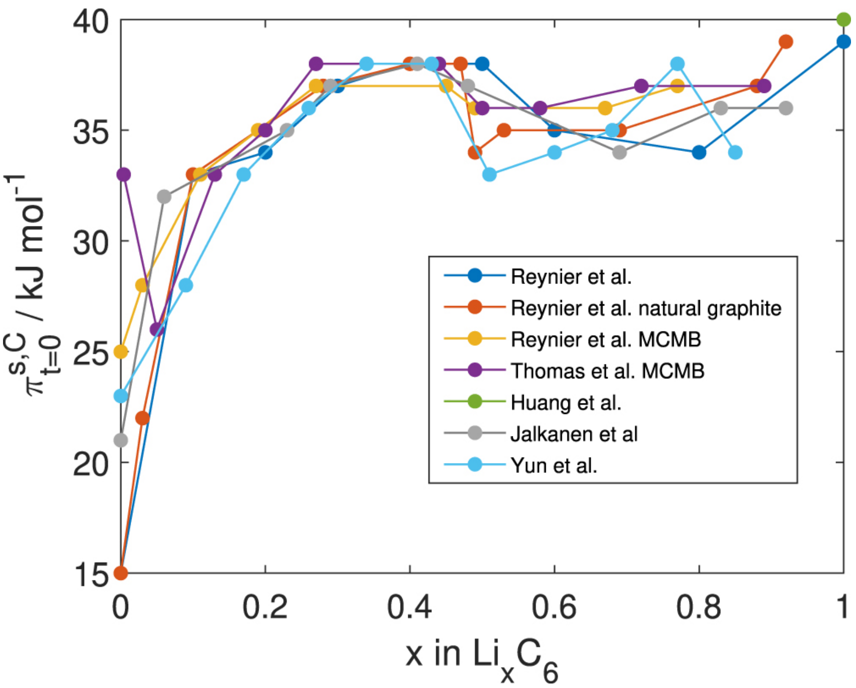

Figure 5.8: Initial Peltier heats for the graphite electrode at 298 K and different states of lithiation, calculated by Gunnarshaug *et al.* using different half-cell entropy data and reported Seebeck coefficients for lithium-metal (see [5] for sources). The figure was reproduced from [5] with permission.

Curiously, the values reported here for the local Peltier heats are reduced when a different electrolyte is used. If this turns out to be true also for the anode material, it could play an essential role in regulating the temperature in batteries. Imagine *i.e.* in an electric ferry or airplane, where the heat generated in the battery during charge is much more critical than during discharge, because the battery needs to be charged fast while it discharges much more slowly. In these cases it is desirable to choose an electrolyte that gives higher cooling effect during charging, even if it means more heat generation during discharge. Nonetheless, local effects explored here would also have to be taken into account. Even though a higher total cooling effect could be achieved, the local heating on the anode in the charging situation could have a detrimental effect on the battery, causing accelerated aging. As mentioned in the theory (see Section 2.2) the SEI-layer formation, which is one of the main aging mechanisms in modern LIBs, happens mainly on the graphite electrode. This mechanism is accelerated at higher temperatures. This means that even though an improved total cooling effect could be achieved by changing the electrolyte, the local heating at the graphite electrode could have a bigger influence on the battery aging. Viswanathan *et al.* studied the ratio of the reversible heat generation to total heat generation in different LIBs using an LTO anode, for different C-rates. They found that at C/8 the reversible heat of LCO was 700 % of the irreversible heat, whereas LFP and LMO were in the range 15 - 60 % [3]. At higher C-rates this ratio went down, but it was still 80 % for LCO at 1 C [3]. Balasundaram *et al.* also found the reversible heat in a LFP/graphite 18650 commercial cell during charging to be 27 %, 19 % and 9 % of the total heat generation at C-rates of 1 C, 2 C and 5C respectively [103]. This suggests that the reversible heat effect could be significant, even at relatively high C-rates. Thus the local heat effect at the anode in these batteries is even more significant (assuming that the total effect is the sum of two contributions with opposite sign), and the possibility of increased aging due to reversible heat is definitely present. Studies should be conducted where this is explored further. It is desirable to map out which electrolytes give minimal temperature rise at the anode, in order to reduce the possible aging. In fact, if overheating is not an issue it may even be favourable to choose an electrolyte that gives *lower* total cooling effect, simply because the local heating effect at the anode during charging would be reduced, which in turn could reduce aging. However, this would only be true if the risk of thermal runaway and other adverse effects were not present. It would also be necessary to compare this effect to the other heat generation terms in the battery (*i.e.* ohmic heat and heat due to overpotential).

Chapter 6

Conclusion

In this thesis, the local heat effects on electrodes relevant for lithium-ion batteries have been investigated. The Peltier heat is the local, reversible heat generated at one electrode when a current is flowing. This parameter is difficult to quantify because other heat generation terms (due to ohmic losses and overpotential) are also present when there is current passing through the cell. To isolate the Peltier effect, irreversible thermodynamic theory was applied. Specifically, transport equations were derived, showing a coupling of heat, mass and charge fluxes in the system. Onsager's reciprocal relations allow the Peltier heat to be calculated from the Seebeck coefficient (electrical potential created when a temperature difference is applied to an open-circuit cell). To do this, a symmetric, thermoelectric cell was made, consisting of two equal electrodes kept at different temperatures. The Seebeck coefficients (and thereby Peltier heats) were found to vary with time due to concentration gradients establishing in the cell. Values for the initial and stationary state Seebeck coefficients are reported for three different electrodes (LFP, LMO and LCO) and two different electrolytes (1 M $LiPF_6$ in 1:1 wt % EC:DEC and 1 M $LiPF_6$ in 1:1 v/v EC:DMC). For the LFP, values were also reported at three different states of lithiation ($x = 0.47$, 0.67 and 0.87 in Li_xFePO_4). The results can be found in Table 5.1 (Seebeck coefficients) and Table 5.2 (Peltier heats).

The results for LMO and LCO showed quite large errors, making it hard to draw any conclusion about the Seebeck coefficient (and thereby Peltier heat) for these. The indication is that the LMO has a higher Peltier heat than LFP, while LCO has lower values, though the high uncertainties make it hard to say.

For LFP at 0 % SoC using the 1 M $LiPF_6$ salt in EC:DEC, the reported values were -0.52 ± 0.50 mV/K and -0.63 ± 0.30 mV/K for the initial and steady state Seebeck coefficients respectively. When changing the electrolyte to the 1 M $LiPF_6$ in EC:DMC the reported values were reduced to -0.33 ± 0.03 mV/K and -0.36 ± 0.03 mV/K for the initial and steady state Seebeck coefficients respectively. This indicates that changing the electrolyte composition could potentially have a large influence on the Seebeck coefficients, and thereby the Peltier heats in LIBs. The difference is believed to be caused by a lower molar fraction of the anion salt, which would give less bulky clusters in the electrolyte, but more experiments are required to confirm this.

For the different states of lithiation of LFP ($x = 0.47, 0.67 \& 0.87$ in Li_xFePO_4), the results show, as expected, that the Seebeck coefficient (and thereby Peltier heat) changes little with SoC. This was expected due to the fact that the entropy of LFP changes little with SoC. For other electrodes, such as LCO where the entropy changes more gradually with state of lithiation, it is expected that the Peltier heat will vary more with SoC.

The reported values of the stationary state Peltier heat is close to the initial values, indicating that the two transport phenomena in the electrolytes used here give contributions to the transported heat that are similar in magnitude, and of opposite sign. The stationary state values of the Peltier heat were, however, difficult to report due to many of the cells having a high drift in potential. More experiments must therefore be conducted to confirm or discard this hypothesis.

In general, the values reported here for the Peltier heats were much *lower* and *stable in time* than what has been reported earlier. For LFP the EC:DEC solvent gave initial and stationary state Peltier heats of 15 ± 14 kJ/mol and 18 ± 9 kJ/mol respectively, while the EC:DMC solvent gave values of 9.5 ± 0.9 kJ/mol and 10 ± 1 kJ/mol for the initial and stationary state values respectively.

Combining the values reported here for LFP with the values given in literature for the total entropy change of a full cell, the Peltier heat of graphite at 0 % SoC was estimated to be -8.4 ± 4.5 kJ/mol and -7.9 ± 4.6 kJ/mol for the initial and stationary states respectively. However, at higher states of charge (SoC > 5 %) the values were on the order of 3.5 ± 4.5 kJ/mol and 4.0 ± 4.6 kJ/mol for the initial and stationary state Peltier heats respectively. These results indicate two important things: (1) The local reversible effect at the graphite electrode contributes to *heating* during discharge when the state of charge is low for the LFP-C cells; and (2) the reversible heat effect at the graphite electrode changes sign during the charge/discharge cycle, making it have a *cooling* effect during discharge for most of the SoC-window. Also, compared to values reported earlier, the heat effect calculated for the graphite electrode is much lower, and is also lower than the calculated values at the cathode. If more experiments confirm this, it could have an impact on the chosen cooling strategy for the cells.

Chapter 7

Further Work

Although batteries have been investigated for many years, we still do not fully understand the complicated interactions taking place, giving rise to different phenomena like heat generation and aging. This work adds to the work of various authors, like Gunnarshaug *et al.* [5, 6], Richter *et al.* [2], Hudak and Amatucci [78], Black *et al.* [79, 80] and Huang *et al.* [77], using the Seebeck coefficient to better explain the processes happening in lithium-ion batteries. However, much work is still required to quantify the local, reversible heat effects in LIBs. Some of the results found here are in direct contrast to the results indicated in earlier work, suggesting that the local heat effects may be much less significant than what was first anticipated. However, due to few reported values, this discrepancy has a large number of possible explanations. More experiments are required to confirm the values reported here.

One source of error for the reported values was the lack of control of the internal temperature difference. The calculations of the ratio between internal and external temperature difference were made based on some assumptions (*i.e.* assuming one-dimensional transport and stationary state), and should therefore be seen as estimates. As discussed in Section 5.2.6 this ratio also has some uncertainty due to the experimental set-up that gives quite high errors. This is one weakness of the current experimental method, because the internal temperature difference must be applied in the calculations. However, because of the sensitivity of the experiments, introducing thermocouples in the cells is not a good method for calibrating the temperature either. It is suggested for future studies to explore other methods that allow a better control of the internal temperature. This could be done by reducing the contact resistance between the cell and the thermocouples, for instance by using a coin cell in stead of a pouch cell (giving an even and smooth contact surface) or by using a cooling paste that guarantees good thermal contact. Recent investigations are also looking at the possibility of using optical fibers [104, 105] or thin-film sensors [106] to measure internal temperatures in batteries. Better control of the internal temperature is needed in order to report precise values. If the cell-to-cell variation in the ratio $\Delta_{int}T/\Delta_{ext}T$ is as much as 16 %, the influence on the precision of reported Seebeck coefficients could be as much as 30 % in the worst cases.

It would also be relevant to accomplish faster establishment of the temperature gradient in order to achieve more precise values for the initial Seebeck coefficient. The use of phase changing materials could be a possible solution to establish a temperature difference faster. Another possible solution would be to use separate water-baths for the relaxation and the temperature difference. Imagine a situation with three water baths - one at 25°C, one at 30°C and one at 20°C. The relaxation would be carried out connecting the 25°C water-bath to both the top and bottom aluminum frames. After the relaxation, the top frame could be connected to the hot water-bath, and the bottom to the cold one. This should ensure a faster establishment of the temperature difference in the set-up. Another factor that would ensure a faster establishment of the temperature difference in the cell would be to ensure good thermal contact between the components in the set-up. In the current set-up, 2/3 of the temperature difference was found to be lost from the water-baths to the inside of the cell. Better thermal contact would decrease this loss, but also ensure a faster establishment of the temperature gradient. By achieving a faster change in temperature across the cell, drifting potential would constitute a smaller uncertainty when determining the initial Seebeck coefficient. In addition, one would avoid the influence of other factors on the measured potential, such as the concentration gradients.

As proposed by Gunnarshaug *et al.*, a way of validating the values of the initial Seebeck coefficients ϵ_0 would be to accurately measure the heats of transfer of the components in the electrolyte (q_i^*). In combination with the transfer coefficients and the steady state values, the initial Seebeck coefficient could then be calculated from Equations 3.59-3.61. It is proposed as further work to do this, because the problem in rapidly establishing the temperature difference is then omitted. This could also be used as a way of validating the values found here.

It is also proposed as further work to conduct experiments that can yield higher precision in the stationary state values. This must be done by conducting fewer experiments with a longer time-span. It would give valuable information about the stationary state values for the Seebeck coefficient, which are as of now not reported in an orderly fashion for different electrode materials and lithiation states. In this thesis, attempts were made at reaching stationary state, but some of the cells exhibited a range of different behaviours, putting in doubt whether they would reach a stationary state ever, or keep drifting. Further studies with a longer time-scale could possibly give some answers regarding the drift in potential reported here.

The drift in potential seen here has also been reported by several authors [6, 78, 79]. This drift gives high uncertainties in the results, and eliminating it should be a priority in future experiments. It is believed that longer short-circuit and relaxation times (on the order of weeks) could help reduce the drift. It is also proposed to let the cells rest for a longer time period (weeks) after being made in order to ensure that formation processes are not present when the experiments are started. Establishing the source of the drift in potential would be useful in order to determine whether the deviation from the expected behaviour observed in some of the cells can be explained by the drift in potential, or needs to be investigated further.

Further experiments using pristine LCO is proposed, as opposed to the electrodes taken from commercial cells in this thesis. While experiments with commercialized, aged electrodes would be interesting, it is complicated because many commercial cells have active material coated on both sides of the current collector, making it hard to achieve good electrical contact without compromising the remaining active material. One proposal is to assemble full cells in a similar fashion as the one presented here, and then cycling these to achieve aged electrodes. Aging the electrodes before carrying out the experiments would be extremely relevant, both to investigate aged electrodes and to see the effect of the formation processes that happen in the first few cycles. However, transferring the aged electrodes to thermoelectric cells has its own set of challenges, including the unknown change of the SEI-layer in this process, and the influence of adding a new electrolyte to old electrodes.

The results found here indicate a rather substantial influence of changing the electrolyte. It is therefore proposed to conduct a more in-depth study of the electrolyte's influence on the Seebeck coefficient. Hudak and Amatucci did this to some extent in [78], but a deeper analysis looking at factors such as the amount of electrolyte, the molar fractions of the components, and the resting time between production and testing are needed.

The LFP cathodes that have been used for the SoC have a voltage plateau which makes it difficult to differentiate between different states of charge. The fact that the voltage does not change significantly with SoC is because the internal structural changes are small, thus it is expected that the transported entropy changes little with state of lithiation. Further experiments are required, both to confirm the values found for LFP, and to verify whether the Seebeck coefficient decreases as SoC approaches 100 %, as predicted by the calculations of the Seebeck coefficient from entropy data [5]. However, LIBs with an LFP cathode are not as widespread today, because other chemistries give higher energy and power densities. It would therefore be interesting and relevant to expand the work of this thesis to include other chemistries. For instance, LCO, NMC and NCA all have voltage-discharge curves that are much more affected by the state of charge, which would likely give a bigger difference in the Seebeck coefficient values at different states of charge.

Bibliography

[1] O. S. Burheim, *Engineering energy storage*. Academic press, 2017.

[2] F. Richter, A. Gunnarshaug, O. S. Burheim, P. J. Vie and S. Kjelstrup, ‘Single electrode entropy change for licoo2 electrodes,’ *ECS Transactions*, vol. 80, no. 10, p. 219, 2017.

[3] V. V. Viswanathan, D. Choi, D. Wang, W. Xu, S. Towne, R. E. Williford, J.-G. Zhang, J. Liu and Z. Yang, ‘Effect of entropy change of lithium intercalation in cathodes and anodes on li-ion battery thermal management,’ *Journal of Power Sources*, vol. 195, no. 11, pp. 3720–3729, 2010.

[4] J. Sherfey and A. Brenner, ‘Electrochemical calorimetry,’ *Journal of the Electrochemical Society*, vol. 105, no. 11, p. 665, 1958.

[5] A. F. Gunnarshaug, P. J. S. Vie and S. Kjelstrup, ‘Reversible heat effects in cells relevant for lithium-ion batteries,’ *Journal of The Electrochemical Society*, 2021.

[6] A. F. Gunnarshaug, S. Kjelstrup, D. Bedeaux, F. Richter and O. S. Burheim, ‘The reversible heat effects at lithium iron phosphate-and graphite electrodes,’ *Electrochimica Acta*, vol. 337, p. 135 567, 2020.

[7] K. S. Førland, T. Førland and S. Kjelstrup, *Irreversible Thermodynamics: Theory and Applications*. Tapir Academic Press, 2001.

[8] S. Kjelstrup and D. Bedeaux, *Non-equilibrium thermodynamics of heterogeneous systems*. World Scientific, 2008, vol. 16.

[9] L. Spitthoff, A. F. Gunnarshaug, D. Bedeaux, O. Burheim and S. Kjelstrup, ‘Peltier effects in lithium-ion battery modeling,’ *The Journal of Chemical Physics*, vol. 154, no. 11, p. 114 705, 2021.

[10] L. Spitthoff, E. S. Øyre, H. I. Muri, M. Wahl, A. F. Gunnarshaug, B. G. Pollet, J. J. Lamb and O. S. Burheim, ‘Thermal management of lithium-ion batteries,’ in *Micro-Optics and Energy*, Springer, 2020, pp. 183–194.

[11] J. B. Goodenough, ‘Design considerations,’ *Solid State Ionics*, vol. 69, no. 3-4, pp. 184–198, 1994.

[12] M. Li, J. Lu, Z. Chen and K. Amine, ‘30 years of lithium-ion batteries,’ *Advanced Materials*, vol. 30, no. 33, p. 1 800 561, 2018.

[13] A. M. Haregewoin, A. S. Wotango and B.-J. Hwang, ‘Electrolyte additives for lithium ion battery electrodes: Progress and perspectives,’ *Energy & Environmental Science*, vol. 9, no. 6, pp. 1955–1988, 2016.

[14] S. Zhang, K. Xu and T. Jow, 'Eis study on the formation of solid electrolyte interface in li-ion battery,' *Electrochimica acta*, vol. 51, no. 8-9, pp. 1636–1640, 2006.

[15] N. Nitta, F. Wu, J. T. Lee and G. Yushin, 'Li-ion battery materials: Present and future,' *Materials today*, vol. 18, no. 5, pp. 252–264, 2015.

[16] L. Fransson, T. Eriksson, K. Edström, T. Gustafsson and J. O. Thomas, 'Influence of carbon black and binder on li-ion batteries,' *Journal of power sources*, vol. 101, no. 1, pp. 1–9, 2001.

[17] J. Newman, 'Optimization of porosity and thickness of a battery electrode by means of a reaction-zone model,' *Journal of the Electrochemical Society*, vol. 142, no. 1, p. 97, 1995.

[18] V. Ramadesigan, R. N. Methekar, F. Latinwo, R. D. Braatz and V. R. Subramanian, 'Optimal porosity distribution for minimized ohmic drop across a porous electrode,' *Journal of The Electrochemical Society*, vol. 157, no. 12, A1328, 2010.

[19] P. Kurzweil and J. Garche, 'Overview of batteries for future automobiles,' in *Lead-acid batteries for future automobiles*, Elsevier, 2017, pp. 27–96.

[20] B. Jiang, S. Zeng, H. Wang, D. Liu, J. Qian, Y. Cao, H. Yang and X. Ai, 'Dual core–shell structured si@ sio x@ c nanocomposite synthesized via a one-step pyrolysis method as a highly stable anode material for lithium-ion batteries,' *ACS applied materials & interfaces*, vol. 8, no. 46, pp. 31 611–31 616, 2016.

[21] H. J. Kwon, J.-Y. Hwang, H.-J. Shin, M.-G. Jeong, K. Y. Chung, Y.-K. Sun and H.-G. Jung, 'Nano/microstructured silicon–carbon hybrid composite particles fabricated with corn starch biowaste as anode materials for li-ion batteries,' *Nano letters*, vol. 20, no. 1, pp. 625–635, 2019.

[22] A. A. Ensafi, M. M. Abarghoui and B. Rezaei, 'Metal (ni and bi) coated porous silicon nanostructure, high-performance anode materials for lithium ion batteries with high capacity and stability,' *Journal of Alloys and Compounds*, vol. 712, pp. 233–240, 2017.

[23] C. K. Chan, H. Peng, G. Liu, K. McIlwrath, X. F. Zhang, R. A. Huggins and Y. Cui, 'High-performance lithium battery anodes using silicon nanowires,' *Nature nanotechnology*, vol. 3, no. 1, pp. 31–35, 2008.

[24] J. Li, J. Wang, J. Yang, X. Ma and S. Lu, 'Scalable synthesis of a novel structured graphite/silicon/pyrolyzed-carbon composite as anode material for high-performance lithium-ion batteries,' *Journal of alloys and compounds*, vol. 688, pp. 1072–1079, 2016.

[25] T. Tian, T.-W. Zhang, Y.-C. Yin, Y.-H. Tan, Y.-H. Song, L.-L. Lu and H.-B. Yao, 'Blow-spinning enabled precise doping and coating for improving high-voltage lithium cobalt oxide cathode performance,' *Nano Letters*, vol. 20, no. 1, pp. 677–685, 2019.

[26] X. Wang, X. Wang and Y. Lu, 'Realizing high voltage lithium cobalt oxide in lithium-ion batteries,' *Industrial & Engineering Chemistry Research*, vol. 58, no. 24, pp. 10 119–10 139, 2019.

[27] J. Mosa and M. Aparicio, 'Lithium intercalation materials for battery prepared by sol-gel method,' in *Handbook of Sol-Gel Science and Technology*, A. J. L. Klein M. Aparicio, Ed., Springer, Cham, 2018. DOI: `https://doi.org/10.1007/978-3-319-32101-1_108`.

[28] V. Zhuravlev, A. V. Shikhovtseva, L. V. Ermakova, E. Evshchik, E. A. Sherstobitova, D. V. Novikov, O. V. Bushkova and Y. A. Dobrovolsky, 'Solution combustion synthesis of lithium cobalt oxide–cathode material for lithium-ion batteries,' *Int. J. Electrochem. Sci*, vol. 14, pp. 2965–2983, 2019.

[29] Q. Xia, S. Sun, J. Xu, F. Zan, J. Yue, Q. Zhang, L. Gu and H. Xia, 'Self-standing 3d cathodes for all-solid-state thin film lithium batteries with improved interface kinetics,' *Small*, vol. 14, no. 52, p. 1 804 149, 2018.

[30] Z. Cai, Y. Ma, X. Huang, X. Yan, Z. Yu, S. Zhang, G. Song, Y. Xu, C. Wen and W. Yang, 'High electrochemical stability al-doped spinel limn2o4 cathode material for li-ion batteries,' *Journal of Energy Storage*, vol. 27, p. 101 036, 2020.

[31] D. Andre, S.-J. Kim, P. Lamp, S. F. Lux, F. Maglia, O. Paschos and B. Stiaszny, 'Future generations of cathode materials: An automotive industry perspective,' *Journal of Materials Chemistry A*, vol. 3, no. 13, pp. 6709–6732, 2015.

[32] A. Barré, B. Deguilhem, S. Grolleau, M. Gérard, F. Suard and D. Riu, 'A review on lithium-ion battery ageing mechanisms and estimations for automotive applications,' *Journal of Power Sources*, vol. 241, pp. 680–689, 2013.

[33] J. J. Lamb and B. G. Pollet, 'Micro-optics and energy,' 2020.

[34] M. Dubarry, N. Qin and P. Brooker, 'Calendar aging of commercial li-ion cells of different chemistries–a review,' *Current Opinion in Electrochemistry*, vol. 9, pp. 106–113, 2018.

[35] S. J. An, J. Li, Z. Du, C. Daniel and D. L. Wood III, 'Fast formation cycling for lithium ion batteries,' *Journal of Power Sources*, vol. 342, pp. 846–852, 2017.

[36] S. Malmgren, K. Ciosek, M. Hahlin, T. Gustafsson, M. Gorgoi, H. Rensmo and K. Edström, 'Comparing anode and cathode electrode/electrolyte interface composition and morphology using soft and hard x-ray photoelectron spectroscopy,' *Electrochimica Acta*, vol. 97, pp. 23–32, 2013.

[37] S. J. An, J. Li, C. Daniel, D. Mohanty, S. Nagpure and D. L. Wood III, 'The state of understanding of the lithium-ion-battery graphite solid electrolyte interphase (sei) and its relationship to formation cycling,' *Carbon*, vol. 105, pp. 52–76, 2016.

[38] Q. Zhang and R. E. White, 'Capacity fade analysis of a lithium ion cell,' *Journal of Power Sources*, vol. 179, no. 2, pp. 793–798, 2008.

[39] M. Broussely, P. Biensan, F. Bonhomme, P. Blanchard, S. Herreyre, K. Nechev and R. Staniewicz, 'Main aging mechanisms in li ion batteries,' *Journal of power sources*, vol. 146, no. 1-2, pp. 90–96, 2005.

[40] A. Würsig, H. Buqa, M. Holzapfel, F. Krumeich and P. Novák, 'Film formation at positive electrodes in lithium-ion batteries,' *Electrochemical and Solid State Letters*, vol. 8, no. 1, A34, 2004.

[41] C. L. Campion, W. Li and B. L. Lucht, 'Thermal decomposition of lipf6-based electrolytes for lithium-ion batteries,' *Journal of The Electrochemical Society*, vol. 152, no. 12, A2327, 2005.

[42] M. Petzl and M. A. Danzer, 'Nondestructive detection, characterization, and quantification of lithium plating in commercial lithium-ion batteries,' *Journal of Power Sources*, vol. 254, pp. 80–87, 2014.

[43] X.-G. Yang, Y. Leng, G. Zhang, S. Ge and C.-Y. Wang, 'Modeling of lithium plating induced aging of lithium-ion batteries: Transition from linear to nonlinear aging,' *Journal of Power Sources*, vol. 360, pp. 28–40, 2017.

[44] W. Wu, R. Ma, J. Liu, M. Liu, W. Wang and Q. Wang, 'Impact of low temperature and charge profile on the aging of lithium-ion battery: Non-invasive and post-mortem analysis,' *International Journal of Heat and Mass Transfer*, vol. 170, p. 121 024, 2021.

[45] E. Sarasketa-Zabala, F. Aguesse, I. Villarreal, L. Rodriguez-Martinez, C. M. López and P. Kubiak, 'Understanding lithium inventory loss and sudden performance fade in cylindrical cells during cycling with deep-discharge steps,' *The Journal of Physical Chemistry C*, vol. 119, no. 2, pp. 896–906, 2015.

[46] Y. Zhang, R. Xiong, H. He, X. Qu and M. Pecht, 'State of charge-dependent aging mechanisms in graphite/li (nicoal) o2 cells: Capacity loss modeling and remaining useful life prediction,' *Applied Energy*, vol. 255, p. 113 818, 2019.

[47] D.-I. Stroe, M. Swierczynski, R. Teodorescu *et al.*, 'A comprehensive study on the degradation of lithium-ion batteries during calendar ageing: The internal resistance increase,' in *2016 IEEE Energy Conversion Congress and Exposition (ECCE)*, IEEE, 2016, pp. 1–7.

[48] S. Bose, *High temperature coatings*. Butterworth-Heinemann, 2017.

[49] J. B. Allen and R. F. Larry, *Electrochemical methods fundamentals and applications*. John Wiley & Sons, 2001.

[50] G. Evmenenko, R. E. Warburton, H. Yildirim, J. P. Greeley, M. K. Chan, D. B. Buchholz, P. Fenter, M. J. Bedzyk and T. T. Fister, 'Understanding the role of overpotentials in lithium ion conversion reactions: Visualizing the interface,' *ACS nano*, vol. 13, no. 7, pp. 7825–7832, 2019.

[51] M. Ni, M. K. Leung and D. Y. Leung, 'A modeling study on concentration overpotentials of a reversible solid oxide fuel cell,' *Journal of Power Sources*, vol. 163, no. 1, pp. 460–466, 2006.

[52] L. Rao and J. Newman, 'Heat-generation rate and general energy balance for insertion battery systems,' *Journal of the Electrochemical Society*, vol. 144, no. 8, p. 2697, 1997.

[53] D. Bernardi, E. Pawlikowski and J. Newman, 'A general energy balance for battery systems,' *Journal of the electrochemical society*, vol. 132, no. 1, p. 5, 1985.

[54] Y. Chen and J. W. Evans, 'Heat transfer phenomena in lithium/polymer-electrolyte batteries for electric vehicle application,' *Journal of the Electrochemical Society*, vol. 140, no. 7, p. 1833, 1993.

[55] Y. Chen and J. W. Evans, 'Thermal analysis of lithium-ion batteries,' *Journal of the Electrochemical Society*, vol. 143, no. 9, p. 2708, 1996.

[56] C. R. Pals and J. Newman, 'Thermal modeling of the lithium/polymer battery: I. discharge behavior of a single cell,' *Journal of the Electrochemical Society*, vol. 142, no. 10, p. 3274, 1995.

[57] C. R. Pals and J. Newman, 'Thermal modeling of the lithium/polymer battery: Ii. temperature profiles in a cell stack,' *Journal of the Electrochemical Society*, vol. 142, no. 10, p. 3282, 1995.

[58] M. W. Verbrugge, 'Three-dimensionai temperature and current distribution in a battery module,' *AIChE Journal*, vol. 41, no. 6, pp. 1550–1562, 1995.

[59] W. Gu and C. Wang, 'Thermal-electrochemical modeling of battery systems,' *Journal of The Electrochemical Society*, vol. 147, no. 8, p. 2910, 2000.

[60] M. Doyle, J. Newman, A. S. Gozdz, C. N. Schmutz and J.-M. Tarascon, 'Comparison of modeling predictions with experimental data from plastic lithium ion cells,' *Journal of the Electrochemical Society*, vol. 143, no. 6, p. 1890, 1996.

[61] S. Chen, C. Wan and Y. Wang, 'Thermal analysis of lithium-ion batteries,' *Journal of power sources*, vol. 140, no. 1, pp. 111–124, 2005.

[62] G. Xia, L. Cao and G. Bi, 'A review on battery thermal management in electric vehicle application,' *Journal of power sources*, vol. 367, pp. 90–105, 2017.

[63] H. Liu, Z. Wei, W. He and J. Zhao, 'Thermal issues about li-ion batteries and recent progress in battery thermal management systems: A review,' *Energy conversion and management*, vol. 150, pp. 304–330, 2017.

[64] V. Ramadesigan, P. W. Northrop, S. De, S. Santhanagopalan, R. D. Braatz and V. R. Subramanian, 'Modeling and simulation of lithium-ion batteries from a systems engineering perspective,' *Journal of the electrochemical society*, vol. 159, no. 3, R31, 2012.

[65] T. M. Bandhauer, S. Garimella and T. F. Fuller, 'A critical review of thermal issues in lithium-ion batteries,' *Journal of the Electrochemical Society*, vol. 158, no. 3, R1, 2011.

[66] Z. Rao and S. Wang, 'A review of power battery thermal energy management,' *Renewable and Sustainable Energy Reviews*, vol. 15, no. 9, pp. 4554–4571, 2011.

[67] M. Guo, G.-H. Kim and R. E. White, 'A three-dimensional multi-physics model for a li-ion battery,' *Journal of Power Sources*, vol. 240, pp. 80–94, 2013.

[68] M. Doyle, T. F. Fuller and J. Newman, 'Modeling of galvanostatic charge and discharge of the lithium/polymer/insertion cell,' *Journal of the Electrochemical society*, vol. 140, no. 6, p. 1526, 1993.

[69] K. E. Thomas and J. Newman, 'Heats of mixing and of entropy in porous insertion electrodes,' *Journal of power sources*, vol. 119, pp. 844–849, 2003.

[70] J. Newman, K. E. Thomas, H. Hafezi and D. R. Wheeler, 'Modeling of lithium-ion batteries,' *Journal of power sources*, vol. 119, pp. 838–843, 2003.

[71] M. J. Schmid, K. R. Bickel, P. Novák and R. Schuster, 'Microcalorimetric measurements of the solvent contribution to the entropy changes upon electrochemical lithium bulk deposition,' *Angewandte Chemie International Edition*, vol. 52, no. 50, pp. 13 233–13 237, 2013.

[72] W. Kobayashi, A. Kinoshita and Y. Moritomo, 'Seebeck effect in a battery-type thermocell,' *Applied Physics Letters*, vol. 107, no. 7, p. 073 906, 2015.

[73] X. Zhang and L.-D. Zhao, 'Thermoelectric materials: Energy conversion between heat and electricity,' *Journal of Materiomics*, vol. 1, no. 2, pp. 92–105, 2015.

[74] Q. Xu, S. Kjelstrup and B. Hafskjold, 'Estimation of single electrode heats,' *Electrochimica acta*, vol. 43, no. 18, pp. 2597–2603, 1998.

[75] J. Sherfey, 'Calorimetric determination of half-cell entropy changes,' *Journal of the Electrochemical Society*, vol. 110, no. 3, p. 213, 1963.

[76] Y. Kuzminskii, V. Zasukha and G. Kuzminskaya, 'Thermoelectric effects in electrochemical systems. nonconventional thermogalvanic cells,' *Journal of power sources*, vol. 52, no. 2, pp. 231–242, 1994.

[77] Q. Huang, M. Yan and Z. Jiang, 'Thermal study on single electrodes in lithium-ion battery,' *Journal of Power Sources*, vol. 156, no. 2, pp. 541–546, 2006.

[78] N. S. Hudak and G. G. Amatucci, 'Energy harvesting and storage with lithium-ion thermogalvanic cells,' *Journal of The Electrochemical Society*, vol. 158, no. 5, A572, 2011.

[79] J. J. Black, J. B. Harper and L. Aldous, 'Temperature effect upon the thermoelectrochemical potential generated between lithium metal and lithium ion intercalation electrodes in symmetric and asymmetric battery arrangements,' *Electrochemistry Communications*, vol. 86, pp. 153–156, 2018.

[80] J. J. Black, T. Murphy, R. Atkin, A. Dolan and L. Aldous, 'The thermoelectrochemistry of lithium–glyme solvate ionic liquids: Towards waste heat harvesting,' *Physical Chemistry Chemical Physics*, vol. 18, no. 30, pp. 20 768–20 777, 2016.

[81] X.-F. Zhang, Y. Zhao, Y. Patel, T. Zhang, W.-M. Liu, M. Chen, G. J. Offer and Y. Yan, 'Potentiometric measurement of entropy change for lithium batteries,' *Physical Chemistry Chemical Physics*, vol. 19, no. 15, pp. 9833–9842, 2017.

[82] K. Onda, H. Kameyama, T. Hanamoto and K. Ito, 'Experimental study on heat generation behavior of small lithium-ion secondary batteries,' *Journal of the Electrochemical Society*, vol. 150, no. 3, A285, 2003.

[83] K. Takano, Y. Saito, K. Kanari, K. Nozaki, K. Kato, A. Negishi and T. Kato, 'Entropy change in lithium ion cells on charge and discharge,' *Journal of Applied Electrochemistry*, vol. 32, no. 3, pp. 251–258, 2002.

[84] R. L. Magnússon, W. Kobayashi, M. Takachi and Y. Moritomo, 'Temperature effect on redox voltage in li x co [fe (cn) 6] y,' *AIP advances*, vol. 7, no. 4, p. 045 002, 2017.

[85] V. Surla, M. Tung, W. Xu, D. Andruczyk, M. Neumann, D. Ruzic and D. Mansfield, 'Seebeck coefficient measurements of lithium isotopes,' *Journal of nuclear materials*, vol. 415, no. 1, pp. 18–22, 2011.

[86] J. Agar, 'Thermogalvanic cells in advances in electrochemistry and electrochemical engineering,' *P. Delahay, Interscience Publ., New York*, pp. 31–109, 1963.

[87] M. Mastali, E. Foreman, A. Modjtahedi, E. Samadani, A. Amirfazli, S. Farhad, R. A. Fraser and M. Fowler, 'Electrochemical-thermal modeling and experimental validation of commercial graphite/lifepo4 pouch lithium-ion batteries,' *International Journal of Thermal Sciences*, vol. 129, pp. 218–230, 2018.

[88] G. H. Aylward and T. J. V. Findlay, *SI chemical data, 7th Edition*. New York, Wiley, 2013.

[89] T. Huria, G. Ludovici and G. Lutzemberger, ‘State of charge estimation of high power lithium iron phosphate cells,’ *Journal of Power Sources*, vol. 249, pp. 92–102, 2014.

[90] V. Srinivasan and J. Newman, ‘Discharge model for the lithium iron-phosphate electrode,’ *Journal of the Electrochemical Society*, vol. 151, no. 10, A1517, 2004.

[91] L. Saw, K. Somasundaram, Y. Ye and A. Tay, ‘Electro-thermal analysis of lithium iron phosphate battery for electric vehicles,’ *Journal of Power Sources*, vol. 249, pp. 231–238, 2014.

[92] F. Baronti, W. Zamboni, N. Femia, R. Roncella and R. Saletti, ‘Experimental analysis of open-circuit voltage hysteresis in lithium-iron-phosphate batteries,’ in *IECON 2013-39th Annual Conference of the IEEE Industrial Electronics Society*, IEEE, 2013, pp. 6728–6733.

[93] M. Ouyang, Z. Chu, L. Lu, J. Li, X. Han, X. Feng and G. Liu, ‘Low temperature aging mechanism identification and lithium deposition in a large format lithium iron phosphate battery for different charge profiles,’ *Journal of Power Sources*, vol. 286, pp. 309–320, 2015.

[94] M. Dubarry, C. Truchot and B. Y. Liaw, ‘Cell degradation in commercial lifepo4 cells with high-power and high-energy designs,’ *Journal of Power Sources*, vol. 258, pp. 408–419, 2014.

[95] M. Winter, J. O. Besenhard, M. E. Spahr and P. Novak, ‘Insertion electrode materials for rechargeable lithium batteries,’ *Advanced materials*, vol. 10, no. 10, pp. 725–763, 1998.

[96] H.-F. Jin, Z. Liu, Y.-M. Teng, J.-k. Gao and Y. Zhao, ‘A comparison study of capacity degradation mechanism of lifepo4-based lithium ion cells,’ *Journal of Power Sources*, vol. 189, no. 1, pp. 445–448, 2009.

[97] V. Murray, D. S. Hall and J. Dahn, ‘A guide to full coin cell making for academic researchers,’ *Journal of The Electrochemical Society*, vol. 166, no. 2, A329, 2019.

[98] A. Smith, J. Burns and J. Dahn, ‘A high precision study of the coulombic efficiency of li-ion batteries,’ *Electrochemical and Solid State Letters*, vol. 13, no. 12, A177, 2010.

[99] F. Richter, S. Kjelstrup, P. J. Vie and O. S. Burheim, ‘Thermal conductivity and internal temperature profiles of li-ion secondary batteries,’ *Journal of Power Sources*, vol. 359, pp. 592–600, 2017.

[100] L. Wei, Z. Lu, F. Cao, L. Zhang, X. Yang, X. Yu and L. Jin, ‘A comprehensive study on thermal conductivity of the lithium-ion battery,’ *International Journal of Energy Research*, vol. 44, no. 12, pp. 9466–9478, 2020.

[101] E. W. Lemmon and R. T. Jacobsen, ‘Viscosity and thermal conductivity equations for nitrogen, oxygen, argon, and air,’ *International journal of thermophysics*, vol. 25, no. 1, pp. 21–69, 2004.

[102] J. L. Allen, T. R. Jow and J. Wolfenstine, ‘Kinetic study of the electrochemical fepo4 to lifepo4 phase transition,’ *Chemistry of materials*, vol. 19, no. 8, pp. 2108–2111, 2007.

[103] M. Balasundaram, V. Ramar, C. Yap, L. Li, A. A. Tay and P. Balaya, ‘Heat loss distribution: Impedance and thermal loss analyses in lifepo4/graphite 18650 electrochemical cell,’ *Journal of Power Sources*, vol. 328, pp. 413–421, 2016.

[104] M. Nascimento, S. Novais, M. S. Ding, M. S. Ferreira, S. Koch, S. Passerini and J. L. Pinto, ‘Internal strain and temperature discrimination with optical fiber hybrid sensors in li-ion batteries,’ *Journal of Power Sources*, vol. 410, pp. 1–9, 2019.

[105] S. Novais, M. Nascimento, L. Grande, M. F. Domingues, P. Antunes, N. Alberto, C. Leitão, R. Oliveira, S. Koch, G. T. Kim *et al.*, 'Internal and external temperature monitoring of a li-ion battery with fiber bragg grating sensors,' *Sensors*, vol. 16, no. 9, p. 1394, 2016.

[106] S. Zhu, J. Han, H.-Y. An, T.-S. Pan, Y.-M. Wei, W.-L. Song, H.-S. Chen and D. Fang, 'A novel embedded method for in-situ measuring internal multi-point temperatures of lithium ion batteries,' *Journal of Power Sources*, vol. 456, p. 227 981, 2020.

[107] M. Rahman and M. Saghir, 'Thermodiffusion or soret effect: Historical review,' *International Journal of Heat and Mass Transfer*, vol. 73, pp. 693–705, 2014.

[108] F. Gesmundo, 'The evaluation of the thermodynamic factor for the diffusion of cations in pure oxides and in solid solutions of the (a, b) o type,' *Journal of Physics and Chemistry of Solids*, vol. 44, no. 8, pp. 819–831, 1983.

[109] J. P. Rivera-Barrera, N. Muñoz-Galeano and H. O. Sarmiento-Maldonado, 'Soc estimation for lithium-ion batteries: Review and future challenges,' *Electronics*, vol. 6, no. 4, p. 102, 2017.

[110] Z. Li, J. Huang, B. Y. Liaw and J. Zhang, 'On state-of-charge determination for lithium-ion batteries,' *Journal of Power Sources*, vol. 348, pp. 281–301, 2017.

[111] M. A. Hannan, M. H. Lipu, A. Hussain and A. Mohamed, 'A review of lithium-ion battery state of charge estimation and management system in electric vehicle applications: Challenges and recommendations,' *Renewable and Sustainable Energy Reviews*, vol. 78, pp. 834–854, 2017.

[112] K. S. Ng, C.-S. Moo, Y.-P. Chen and Y.-C. Hsieh, 'Enhanced coulomb counting method for estimating state-of-charge and state-of-health of lithium-ion batteries,' *Applied energy*, vol. 86, no. 9, pp. 1506–1511, 2009.

[113] F. Pei, K. Zhao, Y. Luo and X. Huang, 'Battery variable current-discharge resistance characteristics and state of charge estimation of electric vehicle,' in *2006 6th World Congress on Intelligent Control and Automation*, IEEE, vol. 2, 2006, pp. 8314–8318.

[114] S. Piller, M. Perrin and A. Jossen, 'Methods for state-of-charge determination and their applications,' *Journal of power sources*, vol. 96, no. 1, pp. 113–120, 2001.

[115] R. Xiong, J. Cao, Q. Yu, H. He and F. Sun, 'Critical review on the battery state of charge estimation methods for electric vehicles,' *Ieee Access*, vol. 6, pp. 1832–1843, 2017.

Appendix A

The Relation Between Current and Overpotential

Allen and Larry use the current-overpotential equation to discuss the difference between the reaction overpotential and concentration overpotential. The equation is given as [49]:

$$i = i_0 \left[\frac{C_{O,surf}(0,t)}{C_{O,bulk}} e^{-\alpha \cdot f \cdot \eta} - \frac{C_{R,surf}(0,t)}{C_{R,bulk}} e^{(1-\alpha) \cdot f \cdot \eta} \right] \tag{A.1}$$

Here, C is the concentration of the oxidized (O) and reduced (R) species at the bulk and surface, $f = F/RT$ (F: Faradays constant, R: The universal gas constant, T: Temperature), $\eta = E - E_{eq}$ is the total overpotential, i_0 is the exchange current or equilibrium current, and α is the reaction symmetry coefficient.

The current-overpotential equation (Equation A.1) gives information about the behavior of the cell current at different overpotentials. Note that the first term on the right hand side is the cathodic component current while the second term is the anodic component current. With this in mind, it becomes apparent that at large positive overpotentials the anodic current dominates, as the other exponential term goes to zero. Similarly, at large negative overpotentials the cathodic current dominates and the influence of the anodic current is negligable. When departing from the equilibrium potential, E_{eq}, the behavior of the current is dominated by the exponential terms in Equation A.1, and thus the current changes rapidly to begin with [49]. However, when large overpotential values are reached, the current stagnates, because the mass transfer becomes limiting for the reaction. Mathematically, this moderation comes through the terms $\frac{C_{surf}}{C_{bulk}}$, balancing the exponential terms [49].

Simplifications of the Current-Overpotential Equation
Equation A.1 can be simplified under certain conditions.

(1) Small Concentration Gradients
One example is if the concentration gradients are small. If the solution is stirred or the currents are kept so low that the surface concentrations do not differ significantly from the bulk concentrations, the simplification $\frac{C_{surf}}{C_{bulk}} \approx 1$ can be applied. Equation A.1 then becomes the Butler-Volmer equation [49]:

$$i = i_0 \left[e^{-\alpha \cdot f \cdot \eta} - e^{(1-\alpha) \cdot f \cdot \eta} \right] \tag{A.2}$$

This equation is, as stated by Allen and Larry, a good approximation to the current-overpotential equation (A.1) when currents are kept low enough to avoid significant influence of the concentration gradients. This is when the current is about 10 % of the smallest limiting current at either of the electrodes, which gives a ratio of concentration of species at the electrode surface to concentration of species in the bulk equal to 1 ± 0.1 [49]. In these cases, the overpotential is only due to the reaction rate. It can therefore be said that the Butler-Volmer equation essentially describes the reaction overpotential.

(2) Small Changes in Potential Close to E_{eq}

Another possible simplification of Equation A.1 is very close to the equilibrium potential, where the exponential term in the equation is small. For small values of x, it is possible to use the simplification $e^x \approx 1 + x$, so that the equation becomes:

$$i = i_0 \cdot f \cdot \eta \tag{A.3}$$

This shows that close to the equilibrium potential, and for small changes in potential, there is a linear relationship between the current and the overpotential.

(3) Large Overpotential Values

A further simplification of the Butler-Volmer equation can be made at large overpotential values (positive or negative), where one of the terms in Equation A.2 becomes negligible. For large negative overpotential values one would get [49]:

$$i = i_0 \cdot e^{-\alpha \cdot f \cdot \eta} \tag{A.4}$$

which can be rewritten as the famous Tafel equation:

$$\eta = a + b \cdot log(i) \tag{A.5}$$

with

$$a = \frac{2.3 \cdot R \cdot T}{\alpha \cdot F} log(i_0)$$

$$b = \frac{-2.3 \cdot R \cdot T}{\alpha \cdot F}$$

where the factor 2.3 comes from the conversion from natural to ten-based logarithm. This holds when the back reaction (the reaction from product to reactants) stands for less than 1 % of the current [49]. This means that if a reduction reaction is considered, the overpotential values should be so that:

$$\frac{e^{(1-\alpha) \cdot f \cdot \eta}}{e^{-\alpha \cdot f \cdot \eta}} = e^{f \cdot \eta} < 0.01 \tag{A.6}$$

At 25 degrees Celsius this amounts to an overpotential higher than 118 mV [49]. So if the overpotential is higher than 118 mV at 25 degrees Celsius it is reasonable to use the Tafel equation as an approximation for the reaction overpotential.

Appendix B

Fundamental Principles of Non-Equilibrium Thermodynamics

As many readers may be new to the field of non-equilibrium thermodynamics, a short introduction to the field is given here. The interested reader is referred to classical literature in the field, like [7] and [8].

B.1 The Starting Point: Internal Energy

To understand the reversible heating effects in a battery one looks at changes in entropy, thus the term $T\Delta S$ in Equation 2.4. In order to develop expressions for the entropy, it is possible to start by finding a relationship between entropy and internal energy.

The change in internal energy of a closed system is often given as [7]:

$$dU = dq + dw \tag{B.1}$$

which, when given in terms of state variables can be expressed as [7]:

$$dU = TdS - pdV \tag{B.2}$$

If the system is open, one must also account for the amount of matter in the system. Consider a system with several components, where n_i is the amount of component i. The change in internal energy is then [7]:

$$dU = TdS - pdV + \Sigma_i \mu_i dn_i \tag{B.3}$$

where

$$\mu_i = (\partial U / \partial n_i)_{S,V,n_{j \neq i}} \tag{B.4}$$

is the chemical potential of component i [7]. If electric work is also included, the equation becomes [7]:

$$dU = TdS - pdV + \Sigma_i \mu_i dn_i + dw_{el} \tag{B.5}$$

Rearranging Equation B.5 gives:

$$TdS = dU + pdV - \Sigma_i \mu_i dn_i - dw_{el} \tag{B.6}$$

Equation B.6 is the starting point for the derivations of equations in *Irreversible Thermodynamics - Theory and Applications* by Førland *et al.* [7]. Here, the full derivations are not included, as they can be found in [7].

B.2 Entropy Production for an Adiabatic System

Førland *et al.* exemplify the entropy production in a continuous adiabatic system by gradually building up the equations from a discontinuous case with just heat transfer, to the continuous case with transfer of heat, mass and electric charge [7]. Here, the discrete case with three transport processes is considered first, as this is the situation in a electrochemical cell, and is easier to picture. Thereafter, the continuous case with a membrane is considered, as this is relevant to understand the processes in a lithium-ion battery. For the full derivation, the reader is referred to [7].

B.2.1 Entropy Production in a Discontinuous System

Imagine two separate sub-systems (*i.e.* the electrodes in a galvanic cell) that are united by a junction (like a porous separator with electrolyte or an ion-bridge), where small amounts of heat, mass and charge can pass. It is first assumed that the junction has more or less a stationary state, so entropy does not change across the junction. The entropy change of the system is then the sum of the changes in entropy in each subsystem. When considering a small change in temperature, the governing equation for the entropy change is found to be [7]:

$$dS = \Delta\left(\frac{1}{T}\right)dq_1 - \frac{1}{T}\sum_i \Delta\mu_{i,T} dn_i - \frac{1}{T}\Delta\phi dQ \tag{B.7}$$

where:

dq_1 : Heat removed from subsystem 1
$\Delta\mu_{i,T}$: Variation in chemical potential of component i with changes in composition and pressure
n_i : Amount of component i
T : Absolute temperature
$\Delta\phi dQ$: Electric work (potential × transferred charge)

The first term on the right hand side is the entropy change due to the transport of heat from one subsystem to another. The second term comes from the transport of species with concentration gradients and the third term from the electric work carried out by the system. These three contributions to the change in entropy will also be found as the complexity of the system increases.

B.2.2 Entropy Production in a Continuous System

In Equation B.7, the entropy production for an electrochemical cell where a constant state is assumed across the junction is presented. Taking this a step further, a continuous system is to be considered by looking at a membrane separating two mixtures. By splitting the membrane into small subsystems, it is possible to arrive at the following equation for entropy production per unit volume and unit time, when considering forces and fluxes in the x-direction only [7]:

$$\Theta = \frac{\partial}{\partial x}\left(\frac{\partial S}{\partial t}\right) = \frac{\partial (1/T)}{\partial x}\left(\frac{\partial q}{\partial t}\right) - \frac{1}{T}\sum_i \left(\frac{\partial \mu_{i,T}}{\partial x}\right)\left(\frac{\partial n_i}{\partial t}\right) - \frac{1}{T}\left(\frac{\partial \phi}{\partial x}\right)\left(\frac{\partial Q}{\partial t}\right) \tag{B.8}$$

This equation is more commonly expressed in terms of the fluxes and driving forces as [7]:

$$\Theta = \sum_{j=1}^{k} X_j \mathbf{J_j} \tag{B.9}$$

or as the dissipation function by multiplying both sides by temperature [7]:

$$T\Theta = \sum_{j=1}^{k} X_j \mathbf{J_j} \tag{B.10}$$

Where the forces (X_j) and fluxes (J_j) for heat, mass and charge are given in Table B.1. Note that the fluxes and forces in Equation B.9 and B.10 are not the same, because there is a factor $1/T$ difference.

Table B.1: Fluxes and driving forces in the dissipation and entropy functions (Equations B.10 and B.9)

Variable	**Driving Force ($T\Theta$)**	**Flux ($T\Theta$)**	**Driving Force (Θ)**	**Flux Θ**
Heat	$X_q = -\frac{dlnT}{dx}$	$J'_q = \frac{dq}{dt}$	$X_s = -\frac{dlnT}{dx}$	$J_S = \frac{1}{T}\frac{dq}{dt}$
Mass	$X_i = -\frac{d\mu_{i,T}}{dx}$	$J_i = \frac{dn_i}{dt}$	$X_i = -\frac{1}{T}\frac{d\mu_i}{dx}$	$J_i = \frac{dn_i}{dt}$
Charge	$X_j = -\frac{d\phi}{dx}$	$j = \frac{dQ}{dt}$	$X_j = -\frac{1}{T}\frac{d\phi}{dx}$	$j = \frac{dQ}{dt}$

Notice also that the measurable heat flux (J'_q) is applied in stead of the actual heat flux (J_q). This simplifies the equations, and gives a more practical term to work with. The derivation of the change from J_q to J'_q is given in Section B.6.

In three dimensions the differentials are given as the gradients, so the entropy production per unit volume and unit time is [7]:

$$\Theta = -\nabla lnT\mathbf{J_s} - \Sigma_i \frac{1}{T}\nabla\mu_{\mathbf{i,T}}\mathbf{J_i} - \frac{1}{T}\nabla\phi\mathbf{j} \tag{B.11}$$

Similarly, the dissipation function becomes [7]:

$$T\Theta = -\nabla lnT\mathbf{J'_q} - \Sigma_i \nabla\mu_{\mathbf{i,T}}\mathbf{J_i} - \nabla\phi\mathbf{j} \tag{B.12}$$

To arrive at these equations (B.8 - B.12), the following assumptions were made by Førland *et al.* [7]:

- Uniform temperature, pressure and composition in each mixture
- No macroscopic changes in kinetic energy
- No transport of bulk solution through the membrane
- The system consists of subsystems of non-changing volume with fixed limits. All change in volume happens in the mixtures

- Because the steps are small compared to the size of a subsystem, the intensive variables are assumed to be constant in each subsystem
- No accumulation of charge anywhere in the system

Equation B.12 can be used by assuming local equilibrium. The system is divided into several subsystems, and the intensive variables are considered constant during transfer from one subsystem to the next, even though the values then changes as a result of the change in composition. Note that the dissipation function consists of three terms: heat, mass and electric charge, which are the same variables present in the much simpler Equation B.7.

B.3 Flux Equations and Coupling Coefficients

In equilibrium thermodynamics, we have expressions for transport of heat, mass and electric charge in terms of fluxes given by Fourier's law, Fick's law and Ohm's law, respectively. These laws are given below [8].

Fourier's law:

$$J_q = -\lambda \frac{dT}{dx} \tag{B.13}$$

Fick's law:

$$J_m = -D \frac{dc}{dx} \tag{B.14}$$

Ohm's law:

$$j = -\kappa \frac{d\phi}{dx} \tag{B.15}$$

These laws describe pure energy degradation, but do not take into account the conversion between different energy forms [8]. This is captured by so-called coupling coefficients, which give a more accurate description of transport phenomena. Any flux, J_i, can be expressed as a linear, homogeneous function of the forces as [7]:

$$J_i = \sum_{j=1}^{k} L_{ij} X_j \tag{B.16}$$

where $i = 1, 2, ..., k$. Applying this to the classical laws of transport (Equations B.13 - B.15) yields the following equations for a bulk system with transport in the x-direction only [8]:

$$\begin{aligned}
J_q' = J_1 &= L_{11}\left(\frac{\partial}{\partial x}\frac{1}{T}\right) + L_{12}\left(-\frac{1}{T}\frac{\partial \mu_T}{\partial x}\right) + L_{13}\left(-\frac{1}{T}\frac{\partial \phi}{\partial x}\right) \\
J_m = J_2 &= L_{21}\left(\frac{\partial}{\partial x}\frac{1}{T}\right) + L_{22}\left(-\frac{1}{T}\frac{\partial \mu_T}{\partial x}\right) + L_{23}\left(-\frac{1}{T}\frac{\partial \phi}{\partial x}\right) \\
j = J_3 &= L_{31}\left(\frac{\partial}{\partial x}\frac{1}{T}\right) + L_{32}\left(-\frac{1}{T}\frac{\partial \mu_T}{\partial x}\right) + L_{33}\left(-\frac{1}{T}\frac{\partial \phi}{\partial x}\right)
\end{aligned} \tag{B.17}$$

The vector equation B.17 illustrates in one dimension the coupling between the different transport phenomena. The forces of transport include the thermal force ($\frac{d}{dx}\frac{1}{T}$), the chemical force ($-\frac{1}{T}\frac{d\mu_T}{dx}$) and the electrical force ($-\frac{1}{T}\frac{d\phi}{dx}$). The subscript T indicates that the chemical potential should be taken at constant temperature. The coefficients (L_{ij}) are often referred to as phenomenological coefficients. The diagonal coefficients (L_{ii}) are called the main coefficients, and can be related to the thermal conductivity (λ), the mass diffusion coefficient (D), and the electrical conductivity (κ). The off-diagonal coefficients ($L_{ij}, i \neq j$) are the coupling coefficients. These express the interaction between the different transport processes. A system of a similar form can be used to describe the situation in a battery, as a battery cell also has transport of charge, mass, and heat.

B.3.1 The Phenomenological Coefficients

The coefficients L_{ij} are often referred to as phenomenological coefficients. There are some restrictions on these coefficients that can be useful when they are to be calculated. The simplifications are presented here, and proof can be found by interested readers in [7]. Onsager has shown that there is a reciprocal relation between the cross-coefficients ($L_{ij}, i \neq j$) for independent forces and fluxes, so that [8, 107]:

$$L_{ji} = L_{ij} \tag{B.18}$$

The proof for Onsager's relation and discussions around it can be found in [7, 8, 107], and is considered beyond the scope of this text. The relation essentially expresses that the magnitude of influence between two cross-phenomena is reciprocal.

In an irreversible process, the entropy increases, so the dissipation function must have a positive value ($T\Theta > 0$). This means that the main coefficients, L_{ii} must have a positive value (see [7] for proof):

$$L_{ii} > 0 \quad | \quad (i = 1, 2, 3, ...) \tag{B.19}$$

In a system of independent forces and fluxes, it is always possible to reduce the system to include only two fluxes and forces by setting all other forces to zero. The coefficients for that force-flux pair must then be so that [7]:

$$L_{ii}L_{jj} \geq L_{ij}^2 \tag{B.20}$$

A third restriction on the coefficients comes from dimensional considerations, and is known as the Curie principle: If the system is isotropic, there may not be any coupling between scalar and vector quantities. As a result of this principle the cross coefficients must be zero if some fluxes and forces are scalars while others are vectors [7]. These restrictions on the phenomenological coefficients will help reduce the number of unknowns when describing a physical system, like a battery.

B.3.2 Approximation in Steady State Systems

In steady state, the composition and gradients in the system do not change with time. For such systems, it is possible to express the driving forces as a difference across the system instead of as a gradient [7]. The system is then treated similarly to the discontinuous system in Section B.2. The heat dissipation equation for a system in steady state is [7]:

$$TdS = -\Delta lnTdq - \sum_i \Delta\mu_{i,T} dn_i - \Delta\phi dQ \tag{B.21}$$

In the steady-state case, it is convenient to give the fluxes over the whole cross-section (as opposed to giving it over unit area) because the cross section may not be constant between the reservoirs. The same flux symbols are applied for heat and mass (J'_q and J_m), although they are now taken over the whole cross section, not per unit area. The symbol I is used for current as opposed to the symbol j used for current density. Dissipated energy per unit time for the total system is then [7]:

$$\frac{TdS}{dt} = -\Delta lnTJ'_q - \sum_i \Delta\mu_{i,T} J_i - \Delta\phi I \tag{B.22}$$

The flux equations for the steady state system are given as [7]:

$$J_j = -\overline{L_{jq}}\Delta lnT - \sum_{i=1}^{k} \overline{L_{ji}}\Delta\mu_{i,T} - \overline{L_{j\phi}}\Delta\phi \qquad (j = q, 1, 2, ..., k, \phi) \tag{B.23}$$

where J'_q is the measurable heat flux, $J_1, ..., J_k$ are the mass fluxes of the components, and J_ϕ is the current I. Note that the average values of the coefficients $\overline{L_{ij}}$ over the whole cross-section are applied. Onsager's reciprocal relations (Equation B.18) are assumed to be valid also for the average coefficients, as assumed by Førland *et al.* [7].

B.4 Interdependence of Fluxes - Coupling Effects

The interdependence of the different transport phenomena, represented by the cross-coefficients ($L_{ij}, i \neq j$) in Equation B.16, give rise to reciprocal transport effects. Some of these are known and well studied, while others have been given less attention. The different phenomena will be explained briefly here, as they will be important for the discussion on local heating effects in batteries.

B.4.1 The Dufour and Soret Effects

The flux of heat caused by a concentration gradient is called the Dufour effect. The Dufour coefficient is given as the relationship between the transported heat flux and the concentration gradient with zero temperature gradient [8]:

$$D_D = -\left(\frac{J'_q}{\partial c_i/\partial x}\right)_{dT = dc_{j\neq i} = j = 0} \tag{B.24}$$

The reciprocal effect is a flux of matter caused by a temperature gradient, and is called thermal diffusion, or the Soret effect [7]. In a stationary state the flux of the moving component J_i is zero, and the Soret coefficient can be determined as the ratio between the concentration gradient and the temperature gradient [8]:

$$s_T = -\left(\frac{\partial c_i/\partial x}{c_i \partial T/\partial x}\right)_{J_i=0} \tag{B.25}$$

It should also be noted that at stationary state, one can describe the system in terms of total differences in stead of gradients, giving [7]:

$$s_T = -\left(\frac{\Delta c_m}{c_m \Delta T}\right) \tag{B.26}$$

It is now relevant to introduce the concept of *heat of transfer* (q_i^*), which is defined as the transferred heat that is coupled to the transport of component i when there is no temperature gradient. In other words, it is the amount of heat that is transferred with a charge carrier (like an ion or an electron). It is defined by Kjelstrup and Bedeaux as [8]:

$$q_i^* = \left(\frac{J_q}{J_i}\right)_{dT=J_{j\neq i}=j=0} \tag{B.27}$$

Both the Soret coefficient and the Dufour coefficient can be related to this quantity. According to Førland *et al.* [7]:

$$s_T = \frac{q_m^*}{RT^2} \tag{B.28}$$

whereas Kjelstrup and Bedeaux write [8]:

$$s_T = \frac{q_m^*}{c_m T}\left(\frac{\partial \mu_{m,T}}{\partial c_m}\right)^{-1} \tag{B.29}$$

The expression given by Førland *et al.* is valid only for an ideal, binary mixture. In this special case, the thermodynamic factor, which is related to the activity and concentration of the species, is unity [108]. Equation B.29 is a more general equation, valid also in multi-component systems.

The Soret and Dufour effects are small in gases and liquids [8]. In descriptions of homogeneous systems they can therefore often be neglected. This does not, however, apply to heterogeneous systems, where the coupling coefficients are large [8]. For a complete heat model in a full battery system the Dufour effect should be included.

B.4.2 The Seebeck and Peltier Effects

The voltage that can be measured in a material due to a temperature difference is known as the Seebeck voltage. The German physicist Thomas Johann Seebeck discovered this phenomena in 1821 because a magnetic field was created when two parallel strips of materials with different temperatures were joined together at both ends. This magnetic field is created by the current flowing through the materials. If one end is disconnected, current no longer flows, but a voltage can be measured across the open circuit. This voltage across a junction with a temperature difference is called the Seebeck voltage, and is given as:

$$V = \epsilon \cdot \Delta T \tag{B.30}$$

where ϵ is the Seebeck coefficient, and depends on the type of material at the junction.

Jean-Charles-Athanase Peltier discovered in 1834 that if a current passes through a single junction like the one described by Seebeck, the heat created is not consistent with what is predicted as ohmic heating. He did not, however, see the connection to Seebeck's experiments. This connection was made by William Thomson (later Lord Kelvin) in 1855. He discovered that the Peltier heat Q_p at a junction is proportional to the junction current through the relationship:

$$Q_p = \pi \cdot I \tag{B.31}$$

where π is the Peltier coefficient. He also discovered that the Peltier coefficient is related to the Seebeck coefficient by:

$$\pi = -\epsilon \cdot T \tag{B.32}$$

where T is the temperature at the junction.

This relationship is quite important, because it means that the Peltier coefficient can be determined by finding the Seebeck coefficient, or visa versa. This will be exploited in the experiments in this thesis, as the Peltier heat is difficult to isolate from other effects such as ohmic losses and overpotential, which are closely tied to the current flowing in the cell.

In a situation where there is a current, the Peltier effect gives a contribution to transferred heat. In the equation describing heat transfer in a battery (Equation 2.4), this contribution enters as a part of the entropy term (TdS). It is possible to arrive at Equation B.31 from the dissipation or entropy production equation (Equations B.12 or B.11) by looking at a situation where there is only transfer of charge and heat between two reservoirs. No mass transfer gives no flux of mass $J_m = 0$ and also no concentration gradient $\frac{\partial \mu_T}{\partial x} = 0$. The governing flux equations would then be [7]:

$$J_q = -\overline{L_{11}} \Delta lnT - \overline{L_{12}} \Delta \phi \tag{B.33}$$

$$I = -\overline{L_{21}} \Delta lnT - \overline{L_{22}} \Delta \phi \tag{B.34}$$

Considering a situation with no temperature difference between the reservoirs the term $\Delta lnT = 0$, so:

$$J_q = -\overline{L_{12}} \Delta \phi \tag{B.35}$$

$$I = -\overline{L_{22}} \Delta \phi \tag{B.36}$$

which means that when $\Delta T = 0$, the Peltier coefficient at the temperature of the reservoirs is [7]:

$$\left(\frac{J_q}{I}\right)_{\Delta T=0} = \frac{\overline{L_{12}}}{\overline{L_{22}}} = \pi_T \tag{B.37}$$

This expresses the same as Equation B.31, with $\left(J_q\right)_{dT=J_m=d\mu_T=0} = Q_p$.

The Peltier heat is a reversible effect. If the current is very small, it is possible to assume no joule losses, and so heat is transferred reversibly. In this case, and when there is no mass transport ($J_m = 0$) the entropy transferred per Faraday of charge by the charge carrier can be expressed as [8]:

$$S^* = \frac{\pi_T}{T} = \frac{1}{T}\frac{\overline{L_{12}}}{\overline{L_{22}}} \tag{B.38}$$

S^* is the transported entropy, and expresses the amount of transferred entropy per Faraday of charge.

Using Equations B.34 and B.38 along with the simplification $\Delta lnT \approx \frac{1}{T}\Delta T$ (which can be applied when the changes in temperature are small compared to the average temperature), one can arrive at the following expression [7]:

$$\Delta\phi = -S^*\Delta T - \frac{I}{\overline{L_{22}}} \tag{B.39}$$

When the current is negligible the relation between the thermoelectric power and the Peltier effect is found [7]:

$$\left(\frac{\Delta\phi}{\Delta T}\right)_{j=0} = -S^* = -\frac{\pi_T}{T} \tag{B.40}$$

Note that S^* is assumed constant over small changes in temperature. It has also been assumed here that there is only transport of charge and temperature (as is the case in metals). Note also that the transported entropy (S^*) here is given for the transfer of 1 Faraday of charge, while others give it as the transfer of 1 Coulomb of charge. The difference is a factor F, known as Faraday's constant, which is roughly $1F \approx 96500$ C/mol of electrons [7]. The expression would the become:

$$\left(\frac{\Delta\phi}{\Delta T}\right)_{j=0} = -S^* = -\frac{\pi_T}{FT} \tag{B.41}$$

It is easy to confuse the transported entropy (S^*) with the Seebeck coefficient (ϵ). By definition, the potential difference over the temperature difference when no current is flowing is the Seebeck coefficient:

$$\epsilon \equiv \left(\frac{\Delta\phi}{\Delta T}\right)_{j=0} \tag{B.42}$$

In the special case where only the transported entropy from the electrons ($S^*_{e^-}$) contributes to the potential difference, the Seebeck coefficient is exactly equal to the transported entropy. However, as will be shown in Section 3.2, other contributions to the coefficient are usually present (such as heat of transfer and concentration gradients). This shall be discussed in further detail in Section 3.2.6.

B.4.3 The Thomson Effect

In addition to discovering the Peltier effect, William Thomson saw that heat power (Q_τ) is absorbed or generated along the length of a material rod if a temperature difference exists and current is flowing through the rod. The magnitude of this power is proportional to the flow of current and the temperature gradient. This came to be known as the *Thomson effect* [107].

In a system where the temperature difference is small compared to the absolute temperatures of the reservoirs, the Peltier heat suffices to explain the transferred entropy according to Equation B.41. However, at large temperature differences, the changes with temperature in the entropy per faraday charge ($\frac{\delta S^*}{\delta T}$) must be accounted for. The quantity S^* changes with temperature, which gives rise to a heat exchange with the surroundings when electric charge is passed through a system where the temperature changes [7].

The Thomson coefficient is most easily explained through a simple example. Imagine an electric conductor where the temperature gradually changes from a temperature T_1 to a temperature T_2 over a distance l. The entropy that enters at 1 will be different than the entropy that exits at 2 because of the temperature difference. The change in S^* must be counteracted by the surroundings in order to keep the temperature gradient undisturbed [7]:

$$S^*_{T_2} - S^*_{T_1} = \frac{\partial S^*}{\partial T} \Delta T \tag{B.43}$$

The Thomson heat taken from the surroundings to counteract the change in entropy is then [7]:

$$Q_\tau = T \frac{\partial S^*}{\partial T} \Delta T \tag{B.44}$$

The heat absorbed over a temperature difference of unity, $\Delta T = 1$, is known as the Thomson coefficient [7]:

$$\tau = T \frac{\partial S^*}{\partial T} \tag{B.45}$$

Both the Thomson effect and Peltier heat are reversible - they change sign when the current is reversed. It should be noted that the Thomson effect is small, and often neglected in experiments [107].

B.4.4 Experimentally Independent Forces and Fluxes

When looking at the local entropy production in a system with transport of mass, heat and charge in the x-direction, the governing equation can be written as [7]:

$$\frac{\partial}{\partial x}(dS) = \frac{\partial}{\partial x}\left(\frac{\partial S}{\partial q}\right) dq + \sum_i \frac{\partial}{\partial x}\left(\frac{\partial S}{\partial n_i}\right) dn_i + \frac{\partial}{\partial x}\left(\frac{\partial S}{\partial Q}\right) dQ \tag{B.46}$$

This equation applies when changes over a small distance dx is considered in a cell of unit cross-section, and the quantities transferred are small so that changes in intensive variables are negligible [7]. Due to the coupling between different transport phenomena, it would be difficult to quantify the contribution from each term in Equation B.46 in a full system. However, because the contribution of the effects are added together, each term can be obtained independently of the other components by tweaking the experimental set-up [7]. The first term on the right hand side of Equation B.46, $\frac{d}{dx}\left(\frac{\delta S}{\delta q}\right) dq$, is the transported entropy by heat transfer. By setting up an experiment where all $dn_i = 0$ and $dQ = 0$, or where $\frac{\partial \mu_{i,T}}{\partial x} = 0$ and $\frac{\partial \phi}{\partial x} = 0$ the transported entropy due to heat transfer can be calculated from [7]:

$$\frac{\partial}{\partial x}\left(\frac{\partial S}{\partial q}\right) = \frac{\partial (1/T)}{\partial x} = -\frac{1}{T}\frac{\partial lnT}{\partial x} = \frac{1}{T} X_q \tag{B.47}$$

In a similar fashion, one can set up an experiment where $dq = 0$ and all $dn_i = 0$, or where $\frac{\partial lnT}{\partial x} = 0$ and $\frac{\partial \mu_{i,T}}{\partial x} = 0$ to find the transported entropy by charge transfer as [7]:

$$\frac{\partial}{\partial x}\left(\frac{\partial S}{\partial Q}\right)=\frac{1}{T}\frac{\partial}{\partial x}\left(\frac{\partial w_{el}}{\partial Q}\right)=-\frac{1}{T}\frac{\partial \phi}{\partial x}=\frac{1}{T}X_j \tag{B.48}$$

When it comes to the terms containing n_i, one must take into consideration that there is an interrelation between the different chemical potentials. When setting $dq=0$, $dn_{j\neq i}=0$ and $dQ=0$, or $\frac{\partial lnT}{\partial x}=0,\mu_{j\neq i,T}=0$ and $\frac{\partial \phi}{\partial x}=0$, Equation B.46 yields [7]:

$$\frac{\partial}{\partial x}\left(\frac{\delta S}{\delta n_i}\right)=-\frac{1}{T}\frac{\partial \mu_{i,T}}{\partial x}=\frac{1}{T}X_i \tag{B.49}$$

This equation can be applied for each *independent* change in chemical potential. However, the chemical potentials are interrelated by the Gibbs-Duhem equation [7]:

$$\sum_i x_i d\mu_{i,T}=0 \quad (p,T=constant) \tag{B.50}$$

where x_i is the mole fraction of component i and $\mu_{i,T}$ is the chemical potential of component i at temperature T. This means that when the temperature and pressure are constant, all but one μ_i can be varied independently. By choosing one of the components as a frame of reference, all changes are referred to that frame, and the n-1 forces X_i are all independent.

The time derivative of Equation B.46 gives the corresponding fluxes. Because only n-1 material fluxes are considered, certain conditions will give interdependent fluxes. However, Førland *et al.* state that because the forces are independent, it can be shown that the Onsager reciprocal relations (Equation B.18) still hold, even for interdependent fluxes [7].

B.5 Transported Entropy (S^*) and Heat of Transfer (q^*)

The term transported entropy will be used in this thesis, and is denoted S^*. The transported entropy is best explained as done by Agar in [86]. Imagine a solution of uniform composition divided into two sections by a reference plane. One mole of a particular component i is moved from one section to the other by diffusion or migration. The following assumptions are made by Agar: (1) The net amount of other components crossing the reference plane is zero; (2) the pressure is kept constant; and (3) the temperature is kept constant. (1) and (2) can be satisfied by acting on the components with suitable forces and moving the reference plane compared to the container [86]. (3) May require a transfer of heat to or from the system [86]. Because the temperature and pressure are constant, the change of entropy in one region must be exactly equal to the change in the other region with opposite sign, giving a net zero change in entropy for the system. If the process is carried out reversibly, the net heat transfer to the surroundings is zero. Even though the net heat transfer to the surroundings is zero, it is still possible that heat is taken up in one part of the system and given away in another part.

The partial molar entropy of the transported species i, s_i, would in an ideal case be subtracted from the first subsystem and added to the next subsystem when one mole of component i moves across the reference plane. However, there is no reason why the transfer of one mole of component i should cause the change in entropy to be exactly s_i. Agar concludes that the migration of one mole of component i across a reference plane causes the entropy in the subsystem to increase with a certain amount, called the *transported entropy* (S_i^*). However, unless the transported entropy S_i^* is exactly equal to the partial molar entropy of the transported component s_i, a heat has to be given to the surroundings by the second subsystem, and taken from the surroundings by the first subsystem. This heat ($Q_i^* = T\left(S_i^* - s_i\right)$) is the heat of transport (or heat of transfer) [86]. Notice that in the ideal case where $S_i^* = s_i$, no heat is transferred with the components ($q^* = 0$). In this paper the definition of heat of transfer used by Førland *et al.* and Kjelstrup and Bedeaux is applied. The heat of transport is defined as [7, 8]:

$$q_i^* \equiv \left(\frac{J'_q}{J_i}\right)_{dT=J_{j\neq i}=j=0} \tag{B.51}$$

B.6 The Measurable Heat Flux

The total heat flux J_q is often hard to quantify, because it includes heat transported in form of enthalpy of the components. Therefore, the measurable heat flux is often used instead. The measurable heat flux is defined as [8]:

$$J'_q = J_q - \sum_{i=1}^{n} H_j J_j \tag{B.52}$$

Where J_q is the total heat flux, H_j is the enthalpy of component j and J_j is the mass flux of component j.

The equations given in Section 2.5 and 3.2 have applied the measurable heat flux (J'_q) directly, by replacing the chemical potential $\frac{\partial \mu}{\partial x}$ with the chemical potential at constant temperature $\frac{\partial \mu_T}{\partial x}$. It will now be illustrated why this can be done. By derivating the chemical driving force, one gets:

$$\begin{aligned} \frac{\partial}{\partial x}\frac{\mu_j}{T} &= \frac{\partial}{\partial x}\left(\frac{\mu_j}{T}\right)_T + \frac{\partial}{\partial T}\left(\frac{\mu_j}{T}\right)\frac{\partial T}{\partial x} \\ &= \frac{1}{T}\frac{\partial}{\partial x}\left(\mu_{j,T}\right) + \left(\frac{1}{T}\frac{\partial \mu_j}{\partial T} - \frac{\mu_j}{T^2}\right)\frac{\partial T}{\partial x} \end{aligned} \tag{B.53}$$

Using the fact that $\frac{\partial \mu_i}{\partial T} = -S_i$ one arrives at:

$$\begin{aligned} \frac{\partial}{\partial x}\frac{\mu_j}{T} &= \frac{1}{T}\frac{\partial}{\partial x}\left(\mu_{j,T}\right) + \frac{1}{T^2}\left(TS_j - \mu_j\right)\frac{\partial T}{\partial x} \\ &= \frac{1}{T}\frac{\partial}{\partial x}\left(\mu_{j,T}\right) + H_j\frac{\partial}{\partial x}\frac{1}{T} \end{aligned} \tag{B.54}$$

Thus, replacing $\frac{\partial}{\partial x}\frac{\mu_j}{T}$ with $\frac{\partial}{\partial x}\frac{\mu_{j,T}}{T}$ gives an extra term containing the enthalpy (H_j). This term cancels with the extra term that arises from using the measurable heat flux (J'_q) in stead of the actual heat flux (J_q).

Appendix C

State of Charge Estimation

The state of charge (SoC) of a battery represents the available battery capacity, and is used to avoid over-discharge or over-charge as well as regulating the operation so that the battery aging is reduced [109]. Different studies have shown, for example, that the operating window in terms of SoC influences the battery aging [33]. Discharging a battery from 80 % - 20 % SoC gives reduced aging compared to using the battery in a full 0 % - 100 % window [33]. Also, storing the battery at a higher state of charge has shown to give a faster reduction in the battery's state of health [33]. Thus knowing the state of charge of the battery is important. It is included here because the state of charge will be estimated in the experimental section of this thesis.

Estimating the state of charge, or remaining capacity in a battery, is actually not as straightforward as one would think. First of all, a true state of charge should be defined at thermodynamic equilibrium, which is difficult to achieve during operation because it would require the battery to rest during use [110]. However, even if we only seek a simple descriptor of available energy or capacity, this is expected to be a function of numerous factors which in themselves are influenced by various thermal, electrical and chemical fields and gradients [110]. To top it all off, these factors are coupled, making the precise estimation of available energy a challenging combination of mathematical models, empirical correlations, measurements and statistics. To date, research is still being done in this field, and a universally applicable model has yet to be found.

C.0.1 Coulomb Counting

One mayor method for estimating state of charge is coulomb counting (CC), or Ah-counting [109, 110]. This method is used by the majority of the battery technology industry, and the state of charge is estimated as [110]:

$$SoC(t) = SoC_0 - \frac{1}{Q_{rated}} \int_0^t \eta i d\tau \qquad \text{(C.1)}$$

where

SoC_0: Initial SoC
Q_{rated}: Rated capacity
i: Charging/Discharging current. Convention: $i < 0$ for charging
η: Coulombic efficiency

Using coulomb counting as a method for estimating state of charge has several challenges, including: (1) uncertainty and errors in the determination of the initial state of charge (SoC_0), (2) accumulative errors due to imprecision in measurements of time, current and coulombic efficiency, (3) the use of rated capacity (Q_{rated}), which is often determined rather arbitrarily by manufacturers, (4) systematic errors in the tests [110]. In order to improve accuracy, the research community is constantly striving to achieve better precision in measurements, correct possible sources of error, and find precise correlations between SoC and other state parameters like open-circuit voltage (OCV), mechanical stresses or the electrochemical impedance in a certain frequency range in order to cross-check the values [110]. Coulomb counting is the most commonly used method to estimate SoC in practical applications, seeing as both current and time can be measured conveniently during use [110].

C.0.2 Improving the Accuracy of the Coulomb-Counting Method

Because of the problems mentioned in the previous section concerning coulomb counting, different strategies have been investigated and tested to improve the accuracy. Two groups can be distinguished, namely (1) cross-checking calibration methods and (2) regression models and algorithms.

Calibration

Several other state parameters in the battery can be used to cross-check the state of charge found by coulomb counting, including measurements of open-circuit voltage, internal resistance, impedance and surface tension [110, 111]. These methods can also be used independently for SoC-estimation. It is important to point out that the relationship between the different parameters and SoC is not always straightforward, and they all have different issues, as explained by Li *et al.* [110]. A shared issue for OCV, mechanical stresses and impedance is that they all require equilibrium conditions to give reliable readings, which is often hard to come by in practical applications.

Regression Methods, Models and Algorithms

In addition to the measurable quantities used for SoC-estimations, great effort has been put into making different methods, models and algorithms for this purpose. Most regression methods consist of two main building blocks [110]:

1. A battery model, which gives the relationship between SoC and different measurable quantities
2. An algorithm, which is used to incorporate the different sources and decide their importance in the estimation

When it comes to the battery models, it is common to use multi-physics models. The main issue with these is trying to accurately understand and model the coupling between different parameters, while still achieving manageable computing times.

In terms of algorithms, examples include kalman filter (KF), sigma point kalman filter (SPKF), neural network (NN), genetic algorithm (GA) and sliding mode observer (SMO). These help the regression methods handle systems of higher order, that are non-linear and include noise in the data-set [110].

C.0.3 Comments on State of Charge Estimation

In this section some of the problems tied to the estimation of state of charge have been addressed, with focus on coulomb counting as the main method. It should be noted that even though this is the predominant method, there are other ways to estimate state of charge without CC. There can be found examples in literature using properties of the electrolyte, impedance changes, open circuit voltage, internal resistance, voltage measurements and physics-based models [112–114]. Hannan *et al.* separate the SoC-estimation methods in five categories:

- *Conventional*, including OCV, *emf*, CC, EIS, resistance and model based
- *Adaptive filter algorithms*, like KF, UPF and SPKF
- *Learning algorithms*, like NN, ANFIS and GA
- *Non-linear observers*, like SMO, ASGSMO and PIO
- *Others*, like MARS, BI and IR

For a complete discussion of state of charge estimations and the different challenges tied to it, the reader is referred to the various existing reviews and sources therein [110–112, 114, 115].

Appendix D

System Equations

D.1 The Ternary Electrolyte

By starting with the entropy production and the corresponding flux equations for the ternary electrolyte:

$$\sigma = J_q' \frac{\partial}{\partial x}\left(\frac{1}{T}\right) - c_1(v_1 - v_3)\frac{1}{T}\left(\frac{\partial \mu_{1,T}}{\partial x}\right) - c_2(v_2 - v_3)\frac{1}{T}\left(\frac{\partial \mu_{2,T}}{\partial x}\right) - j\frac{1}{T}\left(\frac{\partial \phi}{\partial x}\right) \tag{D.1}$$

$$\frac{\partial}{\partial x}\left(\frac{1}{T}\right) = r_{qq}J_q' + r_{q1}J_1 + r_{q2}J_2 + r_{q\phi}j \tag{D.2}$$

$$-\frac{1}{T}\left(\frac{\partial \mu_{1,T}}{\partial x}\right) = r_{1q}J_q' + r_{11}J_1 + r_{12}J_2 + r_{1\phi}j \tag{D.3}$$

$$-\frac{1}{T}\left(\frac{\partial \mu_{2,T}}{\partial x}\right) = r_{2q}J_q' + r_{21}J_1 + r_{22}J_2 + r_{2\phi}j \tag{D.4}$$

$$-\frac{1}{T}\left(\frac{\partial \phi}{\partial x}\right) = r_{\phi q}J_q' + r_{\phi 1}J_1 + r_{\phi 2}J_2 + r_{\phi\phi}j \tag{D.5}$$

The Onsager's reciprocal relations are valid, so that:

$$\begin{aligned} &r_{q1} = r_{1q} && r_{q2} = r_{2q} && r_{q\phi} = r_{\phi q} \\ &r_{12} = r_{21} && r_{1\phi} = r_{\phi 1} && r_{2\phi} = r_{\phi 2} \end{aligned} \tag{D.6}$$

The following definitions are introduced

$$R_{ij} = r_{ij} - \frac{r_{iq}r_{qj}}{r_{qq}} \tag{D.7}$$

$$q_1^* = \left(\frac{J_q'}{J_1}\right)_{dT=J_2=j=0} = -\frac{r_{q1}}{r_{qq}} \tag{D.8}$$

$$q_2^* = \left(\frac{J'_q}{J_2} \right)_{dT=J_1=j=0} = -\frac{r_{q2}}{r_{qq}} \tag{D.9}$$

$$\lambda = \left(\frac{J'_q}{\partial T / \partial x} \right)_{j=J_1=J_2=0} = \frac{1}{r_{qq} T^2} \tag{D.10}$$

$$L_{11} = \frac{R_{22}}{R_{11}R_{22} - R_{12}R_{21}} \qquad L_{22} = \frac{R_{11}}{R_{11}R_{22} - R_{12}R_{21}} \qquad L_{12} = L_{21} = -\frac{R_{12}}{R_{11}R_{22} - R_{12}R_{21}} \tag{D.11}$$

$$R_{11} = \frac{L_{22}}{L_{11}L_{22} - L_{12}L_{21}} \qquad R_{22} = \frac{L_{11}}{L_{11}L_{22} - L_{12}L_{21}} \qquad R_{12} = R_{21} = -\frac{L_{12}}{L_{11}L_{22} - L_{12}L_{21}} \tag{D.12}$$

Which allows us to express the heat and mass fluxes as:

$$J'_q = -\lambda \frac{\partial T}{\partial x} + q_1^* J_1 + q_2^* J_2 - \frac{r_{q\phi}}{r_{qq}} j \tag{D.13}$$

$$J_1 = -\frac{L_{11}}{T} \left(\frac{\partial \mu_{1,T}}{\partial x} + \frac{q_1^*}{T} \frac{\partial T}{\partial x} \right) - \frac{L_{12}}{T} \left(\frac{\partial \mu_{2,T}}{\partial x} + \frac{q_2^*}{T} \frac{\partial T}{\partial x} \right) - \left(R_{1\phi} L_{11} + R_{2\phi} L_{12} \right) j \tag{D.14}$$

$$J_2 = -\frac{L_{12}}{T} \left(\frac{\partial \mu_{1,T}}{\partial x} + \frac{q_1^*}{T} \frac{\partial T}{\partial x} \right) - \frac{L_{22}}{T} \left(\frac{\partial \mu_{2,T}}{\partial x} + \frac{q_2^*}{T} \frac{\partial T}{\partial x} \right) - \left(R_{1\phi} L_{12} + R_{2\phi} L_{22} \right) j \tag{D.15}$$

The chemical potential is now rewritten as [6]:

$$\frac{\partial \mu_{i,T}}{\partial x} = \sum_j \Gamma_{ij} \frac{RT}{c_j} \frac{\partial c_j}{\partial x} \tag{D.16}$$

where Γ_{ij} is the thermodyamic factor, defined as [6]:

$$\Gamma_{ij} = \left(\frac{\partial \mu_{i,T}}{\partial c_j} \right)_{c_{i \neq j}} \frac{c_j}{RT} \tag{D.17}$$

Because the chemical potentials are related by the Gibbs-Duhem relation, it can be shown that the gradients can be expressed as a linear combination of the concentration gradients as [6]:

$$\frac{\partial \mu_{1,T}}{\partial x} = \left(\Gamma_{11} - \Gamma_{13} \frac{\left(\Gamma_{31} + \frac{c_1}{c_3} \Gamma_{11} + \frac{c_2}{c_3} \Gamma_{21} \right)}{\left(\Gamma_{33} + \frac{c_1}{c_3} \Gamma_{13} + \frac{c_2}{c_3} \Gamma_{23} \right)} \right) \frac{RT}{c_1} \frac{\partial c_1}{\partial x} + \left(\Gamma_{12} - \Gamma_{13} \frac{\left(\Gamma_{32} + \frac{c_1}{c_3} \Gamma_{12} + \frac{c_2}{c_3} \Gamma_{22} \right)}{\left(\Gamma_{33} + \frac{c_1}{c_3} \Gamma_{13} + \frac{c_2}{c_3} \Gamma_{23} \right)} \right) \frac{RT}{c_2} \frac{\partial c_2}{\partial x}$$

$$\frac{\partial \mu_{2,T}}{\partial x} = \left(\Gamma_{21} - \Gamma_{23} \frac{\left(\Gamma_{31} + \frac{c_1}{C_3} \Gamma_{11} + \frac{c_2}{c_3} \Gamma_{21} \right)}{\left(\Gamma_{33} + \frac{c_1}{c_3} \Gamma_{13} + \frac{c_2}{c_3} \Gamma_{23} \right)} \right) \frac{RT}{c_1} \frac{\partial c_1}{\partial x} + \left(\Gamma_{22} - \Gamma_{23} \frac{\left(\Gamma_{32} + \frac{c_1}{c_3} \Gamma_{12} + \frac{c_2}{c_3} \Gamma_{22} \right)}{\left(\Gamma_{33} + \frac{c_1}{C_3} \Gamma_{13} + \frac{c_2}{c_3} \Gamma_{23} \right)} \right) \frac{RT}{c_2} \frac{\partial c_2}{\partial x}$$

Which is simply expressed as [6]:

$$\frac{\partial \mu_{1,T}}{\partial x} = a_{11} \frac{\partial c_1}{\partial x} + a_{12} \frac{\partial c_2}{\partial x} \tag{D.18}$$

$$\frac{\partial \mu_{2,T}}{\partial x} = a_{21} \frac{\partial c_1}{\partial x} + a_{22} \frac{\partial c_2}{\partial x} \tag{D.19}$$

To further simplify the equations, the following definitions are given [6]:

$$t_1 = \left(\frac{J_1}{j/F}\right)_{dT=d\mu_{1,T}=d\mu_{2,T}=0} = \left(\frac{F\partial\phi/\partial x}{\partial\mu_{1,T}/\partial x}\right)_{dT=j=0} = -F\left(R_{1\phi}L_{11} + R_{2\phi}L_{12}\right) \tag{D.20}$$

$$t_2 = \left(\frac{J_2}{j/F}\right)_{dT=d\mu_{1,T}=d\mu_{2,T}=0} = \left(\frac{F\partial\phi/\partial x}{\partial\mu_{2,T}/\partial x}\right)_{dT=j=0} = -F\left(R_{1\phi}L_{12} + R_{2\phi}L_{22}\right) \tag{D.21}$$

$$q_1^* = \left(\frac{J'_q}{J_1}\right)_{\Delta T=J_2=j=0} = -T\left(\frac{\partial\mu_{1,T}/\partial x}{\partial T/\partial x}\right)_{j=J_1=J_2=0} \tag{D.22}$$

$$q_2^* = \left(\frac{J'_q}{J_2}\right)_{\Delta T=J_1=j=0} = -T\left(\frac{\partial\mu_{2,T}/\partial x}{\partial T/\partial x}\right)_{j=J_1=J_2=0} \tag{D.23}$$

$$S_{Li^+}^* = \left(\frac{J'_q/T}{j/F}\right)_{dT=J_1=J_2=0} = -F\frac{r_{q\phi}}{r_{qq}T} \tag{D.24}$$

$$\pi = \left(\frac{J'_q}{j/F}\right)_{dT=d\mu_{1,T}=d\mu_{2,T}=0} = -FT\left(\frac{\partial\phi/\partial x}{\partial T/\partial x}\right)_{dc_1=dc_2=j=0} = t_1q_1^* + t_2q_2^* + TS_{Li^+}^* \tag{D.25}$$

$$\tag{D.26}$$

Diffusion coefficients (D_{ij}), thermal diffusion coefficients ($D_{i,T}$) and ohmic resistivity are defined [6]:

$$\begin{aligned}
D_{11} &= -\left(\tfrac{J_1}{\partial c_1/\partial x}\right)_{dT=0,dc_2=0,j=0} = \tfrac{1}{T}\left(L_{11}a_{11} + L_{12}a_{21}\right)\\
D_{12} &= -\left(\tfrac{J_1}{\partial c_2/\partial x}\right)_{dT=0,dc_1=0,j=0} = \tfrac{1}{T}\left(L_{11}a_{12} + L_{12}a_{22}\right)\\
D_{21} &= -\left(\tfrac{J_2}{\partial c_1/\partial x}\right)_{dT=0,dc_2=0,j=0} = \tfrac{1}{T}\left(L_{12}a_{11} + L_{22}a_{21}\right)\\
D_{22} &= -\left(\tfrac{J_2}{\partial c_2/\partial x}\right)_{dT=0,dc_1=0,j=0} = \tfrac{1}{T}\left(L_{12}a_{12} + L_{22}a_{22}\right)\\
D_{1T} &= -\left(\tfrac{J_1}{c_1\partial T/\partial x}\right)_{dc_1=dc_2=0,j=0} = \tfrac{L_{11}q_1^*+L_{12}q_2^*}{c_1T^2}\\
D_{2T} &= -\left(\tfrac{J_2}{c_2\partial T/\partial x}\right)_{dc_1=dc_2=0,j-0} = \tfrac{L_{12}q_1^*+L_{22}q_2^*}{c_2T^2}\\
r &= -\left(\tfrac{\partial\varphi/\partial x}{j}\right)_{dT=0,dc_1=dc_2=0} = T\left(R_{1\varphi}\tfrac{t_1}{F} + R_{2\varphi}\tfrac{t_2}{F} - R_{\phi\varphi}\right)\\
&= -T\left(R_{1\varphi}^2L_{11} + 2R_{1\varphi}R_{2\varphi}L_{12} + R_{2\varphi}^2L_{22} + R_{\varphi\varphi}\right)
\end{aligned} \tag{D.27}$$

Finally, expressions for the flux-force relations can be written on the form [6]:

$$\begin{aligned}
J'_q &= -\lambda\tfrac{\partial T}{\partial x} + q_1^*\left(J_1 - \tfrac{t_1}{F}j\right) + q_2^*\left(J_2 - \tfrac{t_2}{F}j\right) + \tfrac{\pi}{F}j\\
J_1 &= -D_{11}\tfrac{\partial c_1}{\partial x} - D_{12}\tfrac{\partial c_2}{\partial x} - c_1D_{1T}\tfrac{\partial T}{\partial x} + \tfrac{t_1}{F}j\\
J_2 &= -D_{21}\tfrac{\partial c_1}{\partial x} - D_{22}\tfrac{\partial c_2}{\partial x} - c_2D_{2T}\tfrac{\partial T}{\partial x} + \tfrac{t_2}{F}j\\
F\tfrac{\partial\phi}{\partial x} &= -\tfrac{\pi}{T}\tfrac{\partial T}{\partial x} - \left(t_1a_{11} + t_2a_{21}\right)\tfrac{\partial c_1}{\partial x} - \left(t_1a_{12} + t_2a_{22}\right)\tfrac{\partial c_2}{\partial x} - Frj
\end{aligned} \tag{D.28}$$

By integrating the potential across the thickness of the electrolyte, the expression for the potential difference is found as [6]:

$$F\Delta_{\mathrm{e}}\phi = F\int_{d^1}^{d^e}\frac{\partial\phi}{\partial x}dx = -S^*_{\mathrm{L}^+}\Delta_{\mathrm{e}}T - t_1 q_1^{*,\mathrm{e}}\ln\left(\frac{T(d^{\mathrm{e}})}{T(d^1)}\right) - t_2 q_2^{*,\mathrm{e}}\ln\left(\frac{T(d^{\mathrm{e}})}{T(d^1)}\right) - b_1\Delta_{\mathrm{e}}c_1 - b_2\Delta_{\mathrm{e}}c_2 \tag{D.29}$$

Using the simplification $\Delta ln(T) \approx \frac{1}{T}\Delta T$ when $\Delta T << T$, one arrives at the final expression for the potential difference contribution from the electrolyte:

$$\frac{\Delta\phi_e}{\Delta T_e} = -\frac{S^*_{Li^+}}{F} - \frac{t_1 q_1^*}{TF} - \frac{t_2 q_2^*}{TF} - \frac{1}{F}b_1\frac{\Delta_e c_1}{\Delta_e T} - \frac{1}{F}b_2\frac{\Delta_e c_2}{\Delta_e T} \tag{D.30}$$

where $S{*}_{Li^+}$ is the entropy transported by the lithium ions, t_i the transference coefficient of component i, q_i^* the heat of transfer of component i, $\Delta_e c_i$ the time-dependent concentration change of component i through the electrolyte, $\Delta_e T$ the temperature difference across the electrolyte, F Faraday's constant, T the absolute average temperature, and the coefficients b_i are simply given as:

$$b_i = (t_1 a_{1i} + t_2 a_{2i}) \tag{D.31}$$

Appendix E

Potential Measurements

Only some of the results were included in Section 5.1 to highlight specific findings. Here, the rest of the measured electric potential and temperature differences for the different cells are given. The results are given in the following order:

- LFP with the $LiPF_6$ in EC:DEC electrolyte
- LFP with the $LiPF_6$ in EC:DMC electrolyte
- LMO with the $LiPF_6$ in EC:DEC electrolyte
- LMO with the $LiPF_6$ in EC:DMC electrolyte
- LCO with the $LiPF_6$ in EC:DEC electrolyte
- LCO with the $LiPF_6$ in EC:DMC electrolyte
- LFP with the $LiPF_6$ in EC:DEC electrolyte at different states of charge

E.1 $LiFePO_4$ with $LiPF_6$ in EC:DEC

Figures E.1 and E.2 give the plots of potential difference for the $LiFePO_4$ using an electrolyte with 1 M $LiPF_6$ salt in EC:DEC (1:1 wt %) solvent for different temperature differences. Notice that several cells with the same composition were tested under the same conditions to verify results. They were not plotted in the same graph because there was some variation in the measured external temperature difference (see *i.e.* Figure E.1a and E.1b where the temperature difference is slightly higher in the latter case).

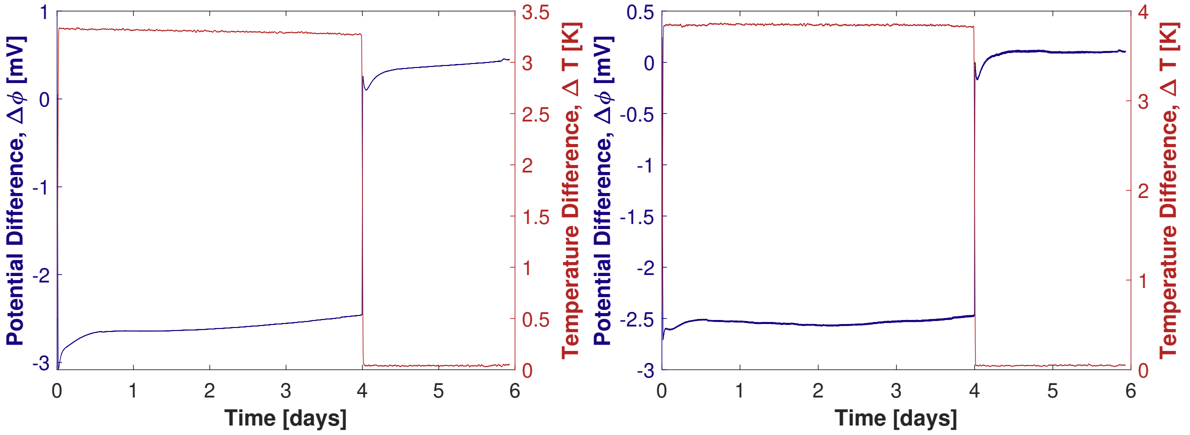

(a) Cell 1, $\Delta_{WB}T = 10$ K **(b)** Cell 2, $\Delta_{WB}T = 10$ K

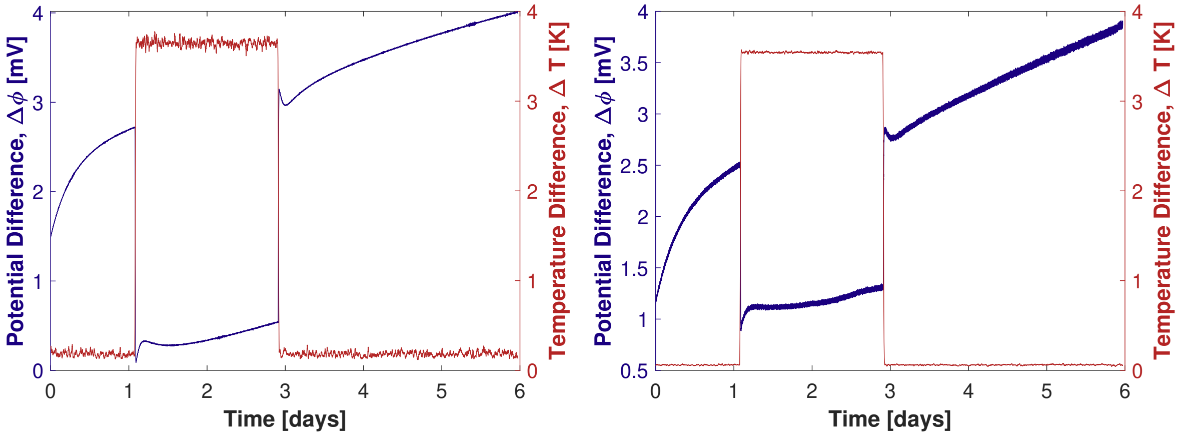

(c) Cell 3, $\Delta_{WB}T = 10$ K **(d)** Cell 4, $\Delta_{WB}T = 10$ K

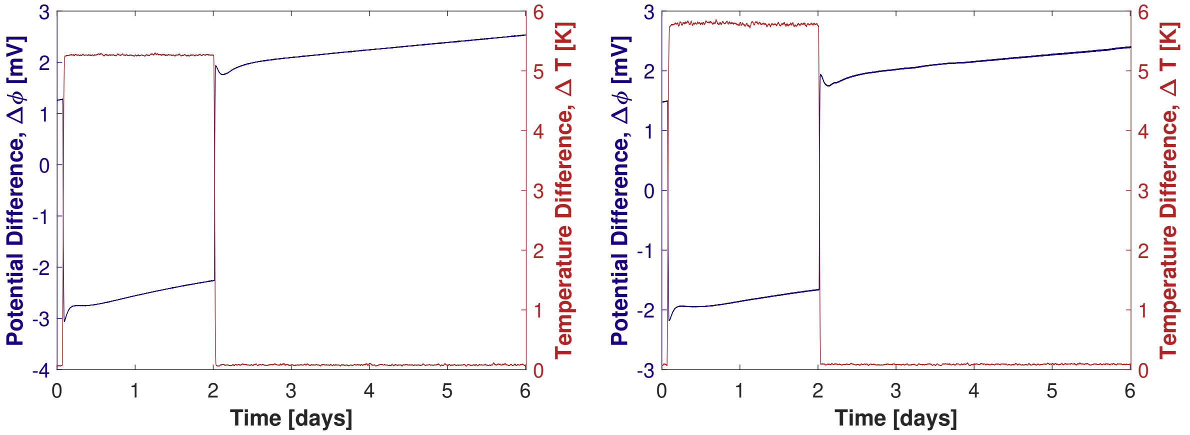

(e) Cell 3, $\Delta_{WB}T = 15$ K **(f)** Cell 4, $\Delta_{WB}T = 15$ K

Figure E.1: Potential measurements for symmetric cells using **LFP** electrodes with an electrolyte consisting of a $LiPF_6$ salt in 1:1 wt % **EC:DEC**. The different plots are from different experiments and with different water bath temperatures $\Delta_{WB}T$. The plotted temperature is the estimated internal temperature difference in the cell.

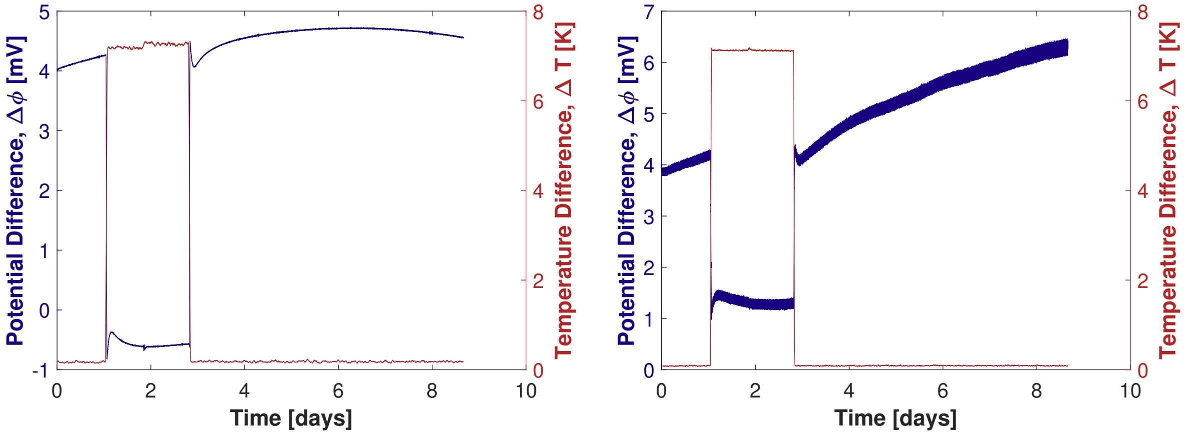

(a) Cell 3, $\Delta_{WB}T = 20$ K

(b) Cell 4, $\Delta_{WB}T = 20$ K

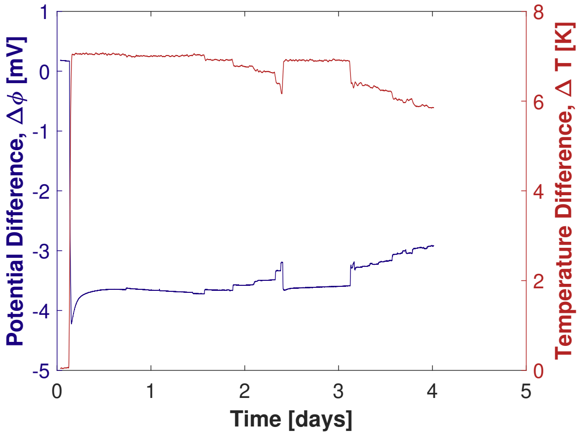

(c) Cell 5, $\Delta_{WB}T = 20$ K

Figure E.2: Potential measurements for symmetric cells using **LFP** electrodes with an electrolyte consisting of a $LiPF_6$ salt in 1:1 wt % **EC:DEC**. The different plots are from different experiments and with different water bath temperatures $\Delta_{WB}T$. The plotted temperature is the estimated internal temperature difference in the cell.

E.2 $LiFePO_4$ with $LiPF_6$ in EC:DMC

Figure E.3 gives the plots of potential difference for the $LiFePO_4$ using an electrolyte with 1 M $LiPF_6$ salt in EC:DMC (1:1 v:V) solvent for different temperature differences.

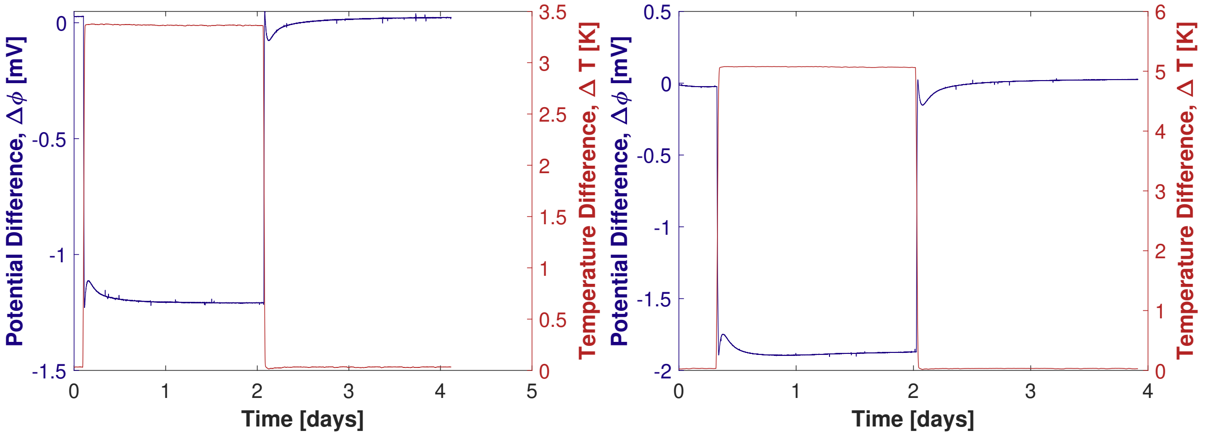

(a) Cell 1, $\Delta_{WB}T = 10$ K **(b)** Cell 1, $\Delta_{WB}T = 15$ K

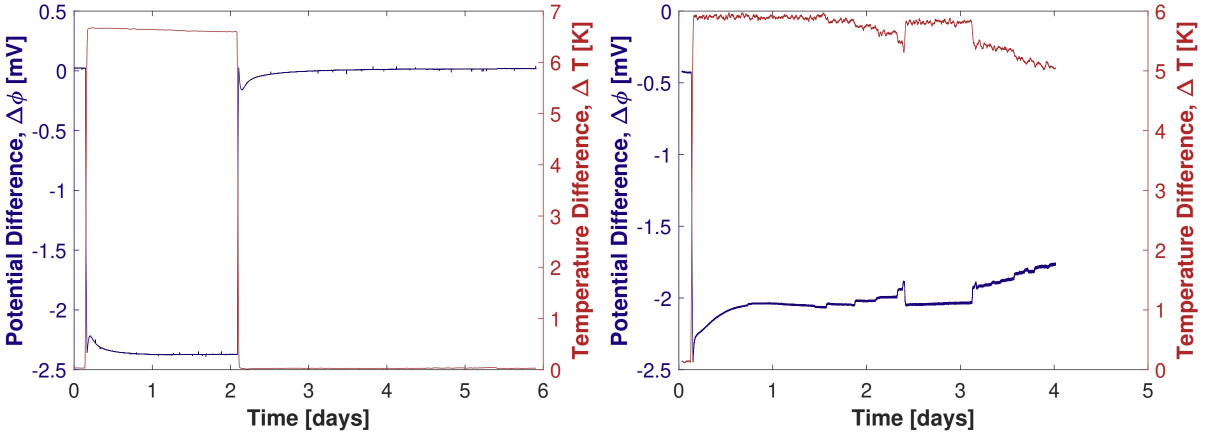

(c) Cell 1, $\Delta_{WB}T = 20$ K **(d)** Cell 1, $\Delta_{WB}T = 20$ K

Figure E.3: Potential measurements for symmetric cells using **LFP** electrodes with an electrolyte consisting of a $LiPF_6$ salt in 1:1 v:v **EC:DMC**. The different plots are from different experiments and with different water bath temperatures $\Delta_{WB}T$. The plotted temperature is the estimated internal temperature difference in the cell.

E.3 $LiMn_2O_4$ with $LiPF_6$ in EC:DEC

Figure E.4 gives the plots of potential difference for the $LiMn_2O_4$ using an electrolyte with 1 M $LiPF_6$ salt in EC:DEC (1:1 wt %) solvent for different temperature differences.

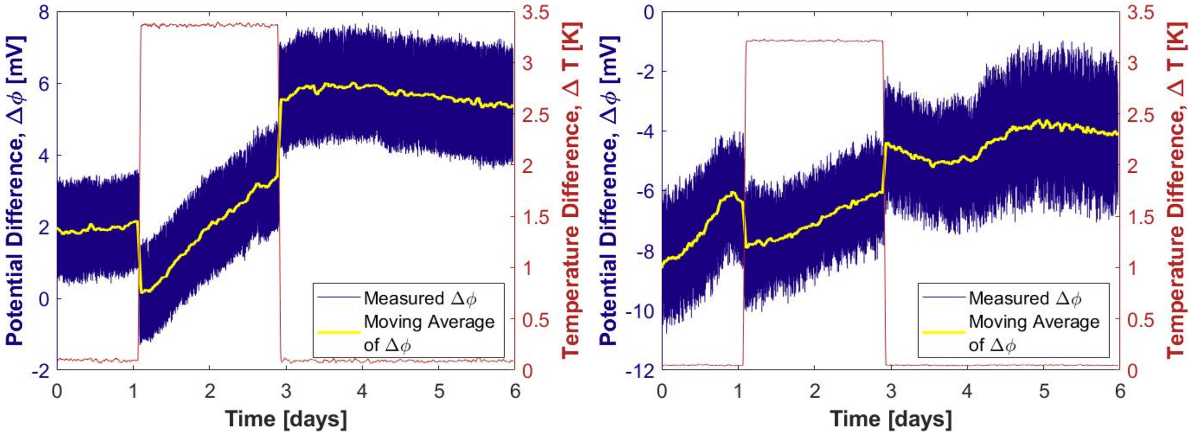

(a) Cell 1, $\Delta_{WB}T = 10$ K

(b) Cell 2, $\Delta_{WB}T = 10$ K

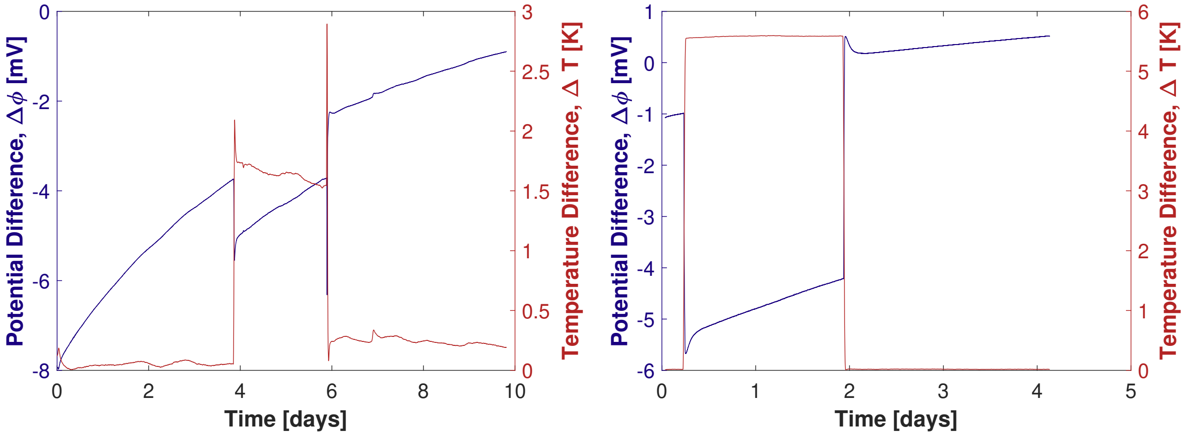

(c) Cell 3, $\Delta_{WB}T = 10$ K

(d) Cell 3, $\Delta_{WB}T = 15$ K

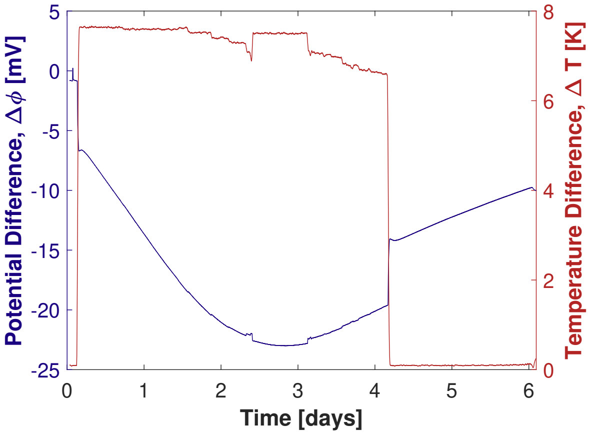

(e) Cell 3, $\Delta_{WB}T = 20$ K

Figure E.4: Potential measurements for symmetric cells using **LMO** electrodes with an electrolyte consisting of a LiPF$_6$ salt in 1:1 wt % **EC:DEC**. The different plots are from different experiments and with different water bath temperatures $\Delta_{WB}T$. The plotted temperature is the estimated internal temperature difference in the cell.

E.4 $LiMn_2O_4$ with $LiPF_6$ in EC:DMC

Figure E.5 gives the plots of potential difference for the $LiMn_2O_4$ using an electrolyte with 1 M $LiPF_6$ salt in EC:DMC (1:1 v/v) solvent for different temperature differences.

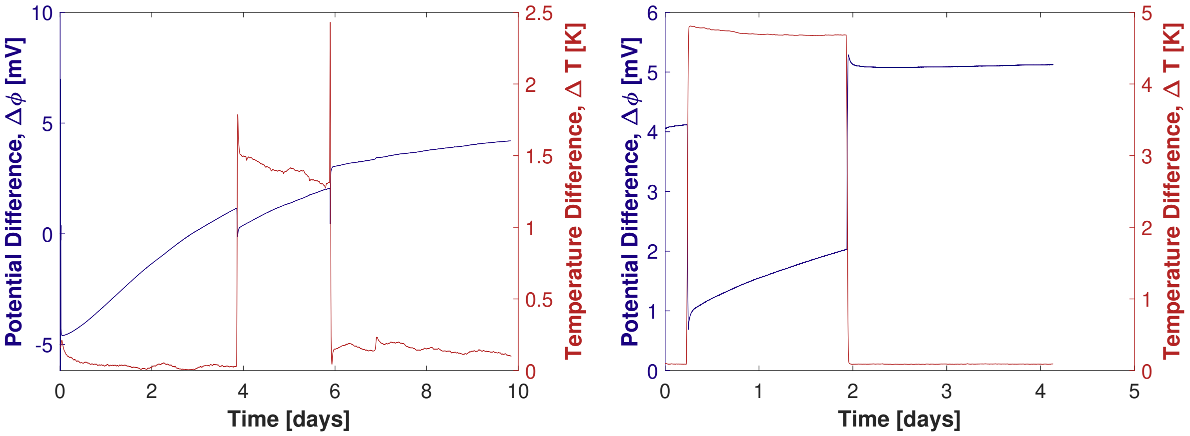

(a) Cell 1, $\Delta_{WB}T = 10$ K

(b) Cell 1, $\Delta_{WB}T = 15$ K

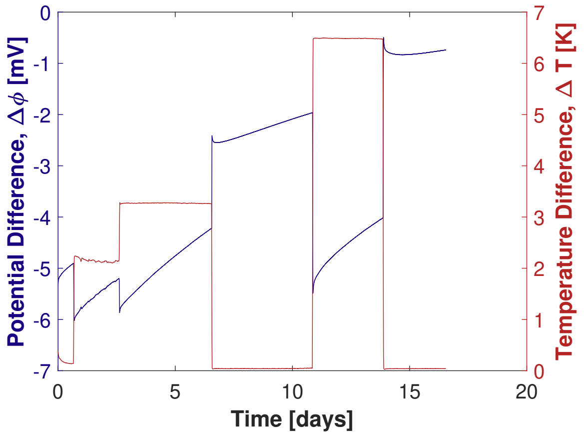

(c) Cell 1, various $\Delta_{WB}T$

Figure E.5: Potential measurements for symmetric cells using **LMO** electrodes with an electrolyte consisting of a $LiPF_6$ salt in 1:1 v/v **EC:DMC**. The different plots are from different experiments and with different water bath temperatures $\Delta_{WB}T$. The plotted temperature is the estimated internal temperature difference in the cell.

E.5 $LiCoO_2$ with $LiPF_6$ in EC:DEC

Figures E.6 and E.7 give the plots of potential difference for the $LiCoO_2$ using an electrolyte with 1 M $LiPF_6$ salt in EC:DEC (1:1 wt %) solvent for different temperature differences.

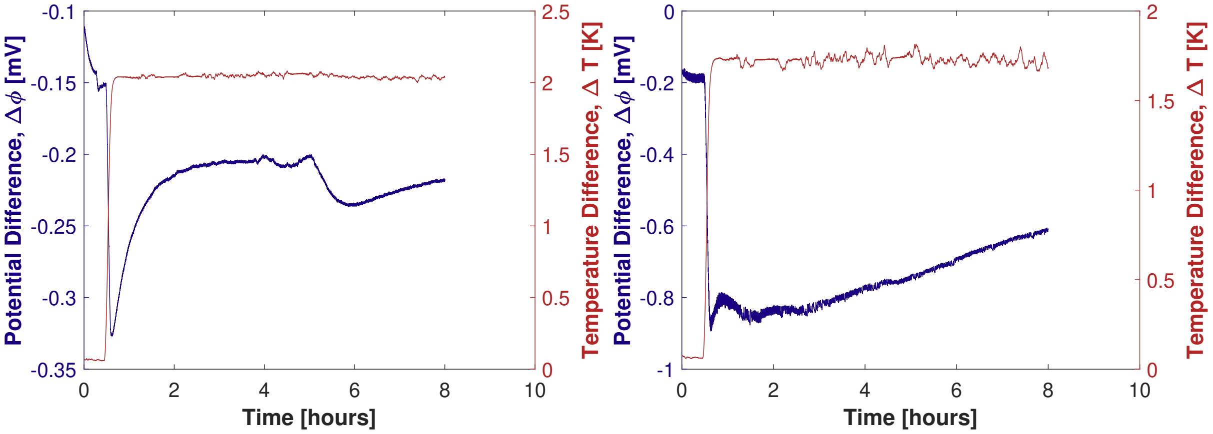

(a) Cell 1, $\Delta_{WB}T = 5$ K **(b)** Cell 2, $\Delta_{WB}T = 5$ K

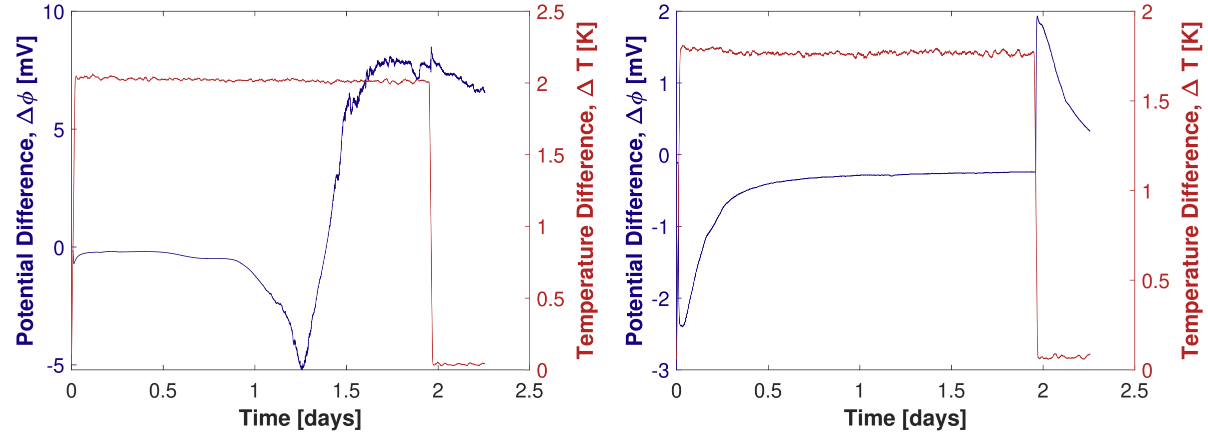

(c) Cell 1, $\Delta_{WB}T = 5$ **(d)** Cell 2, $\Delta_{WB}T = 5$ K

Figure E.6: Potential measurements for symmetric cells using **LCO** electrodes with an electrolyte consisting of a $LiPF_6$ salt in 1:1 wt % **EC:DEC**. The different plots are from different experiments and with different water bath temperatures $\Delta_{WB}T$. The plotted temperature is the estimated internal temperature difference in the cell.

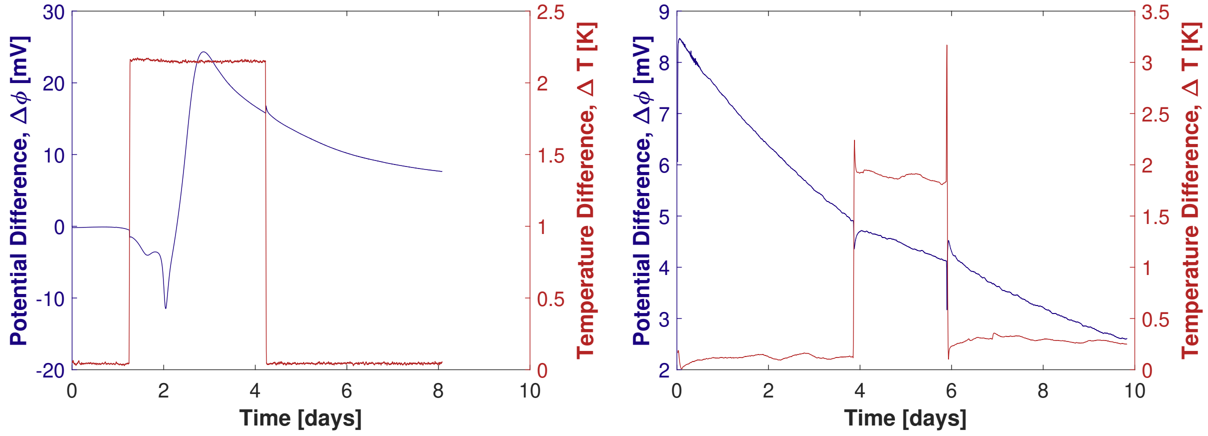

(a) Cell 3, $\Delta_{WB}T = 5$ K

(b) Cell 4, $\Delta_{WB}T = 10$ K

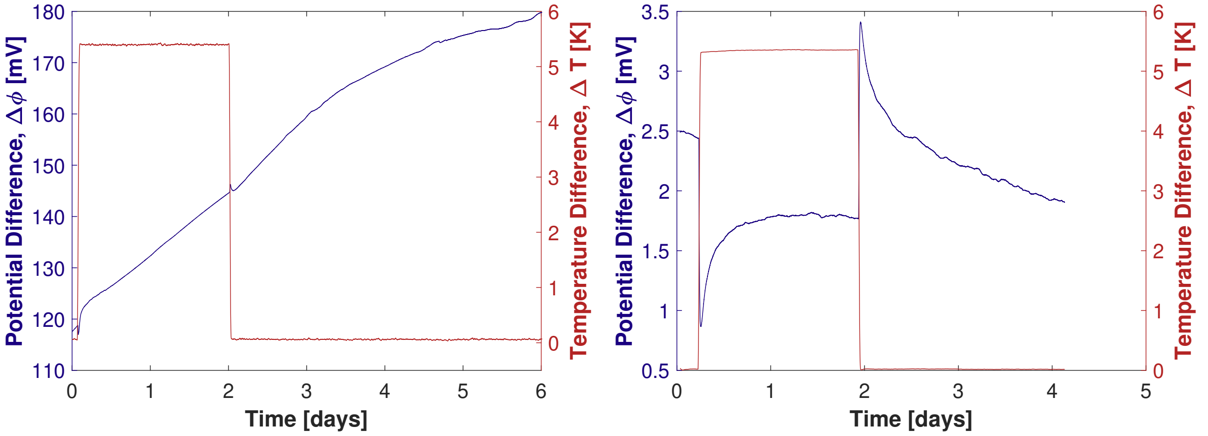

(c) Cell 5, $\Delta_{WB}T = 15$

(d) Cell 4, $\Delta_{WB}T = 15$ K

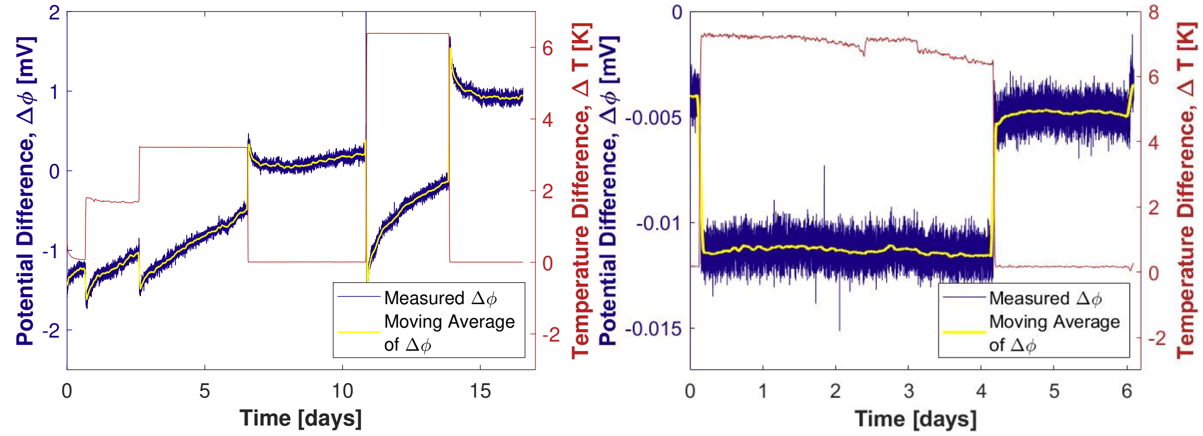

(e) Cell 4, various $\Delta_{WB}T$

(f) Cell 6, $\Delta_{WB}T = 15$ K

Figure E.7: Potential measurements for symmetric cells using **LCO** electrodes with an electrolyte consisting of a $LiPF_6$ salt in 1:1 wt % **EC:DEC**. The different plots are from different experiments and with different water bath temperatures $\Delta_{WB}T$. The plotted temperature is the estimated internal temperature difference in the cell.

E.6 $LiCoO_2$ with $LiPF_6$ in EC:DMC

Figure E.8 gives the plots of potential difference for the $LiCoO_2$ using an electrolyte with 1 M $LiPF_6$ salt in EC:DMC (1:1 v/v) solvent for different temperature differences.

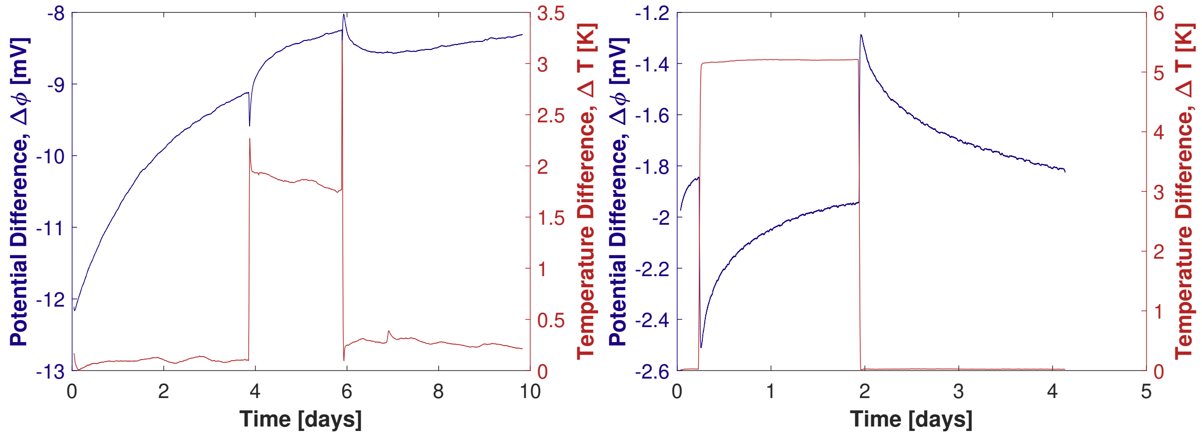

(a) Cell 1, $\Delta_{WB}T = 10$ K

(b) Cell 2, $\Delta_{WB}T = 15$ K

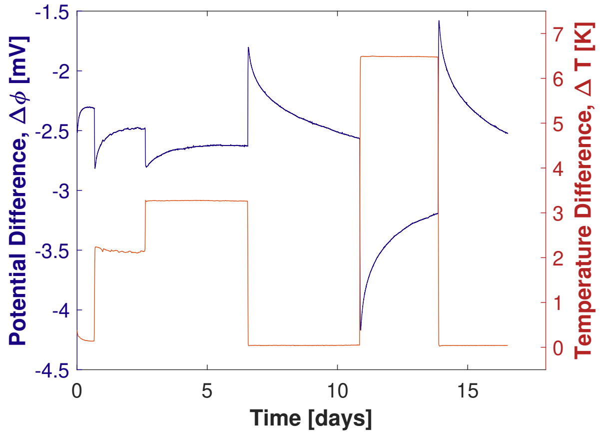

(c) Cell 2, various $\Delta_{WB}T$

Figure E.8: Potential measurements for symmetric cells using **LCO** electrodes with an electrolyte consisting of a $LiPF_6$ salt in 1:1 v/v **EC:DMC**. The different plots are from different experiments and with different water bath temperatures $\Delta_{WB}T$. The plotted temperature is the estimated internal temperature difference in the cell.

E.7 $\mathrm{Li}_x\mathrm{FePO}_4$ with LiPF_6 in EC:DEC for Varying x

Figures E.9 and E.10 give the plots of potential difference for the $\mathrm{Li}_x\mathrm{FePO}_4$ using an electrolyte with 1 M LiPF_6 salt in EC:DEC (1:1 wt %) solvent for different temperature differences and different lithiation states (x). The values are reported at different states of charge, and it is assumed that the relation between state of charge and lithiation is more or less linear, meaning that 100 % SoC is equivalent to $x = 0$, 50 % SoC gives $x = 0.5$ and 0 % SoC gives $x = 1$.

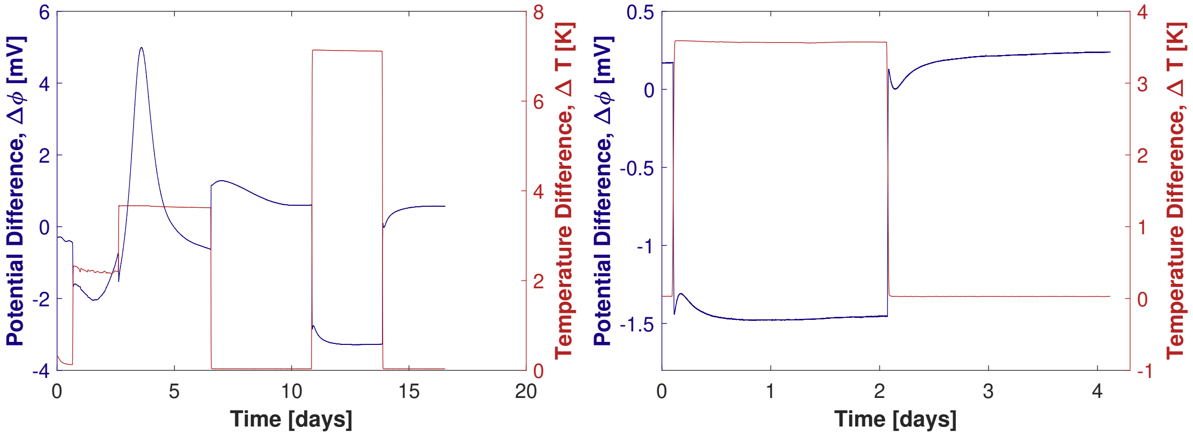

(a) $\mathrm{Li}_x\mathrm{FePO}_4$ with x = 0.87 and varying $\Delta_{WB}T$

(b) $\mathrm{Li}_x\mathrm{FePO}_4$ with x = 0.87 and $\Delta_{WB}T = 10$ K

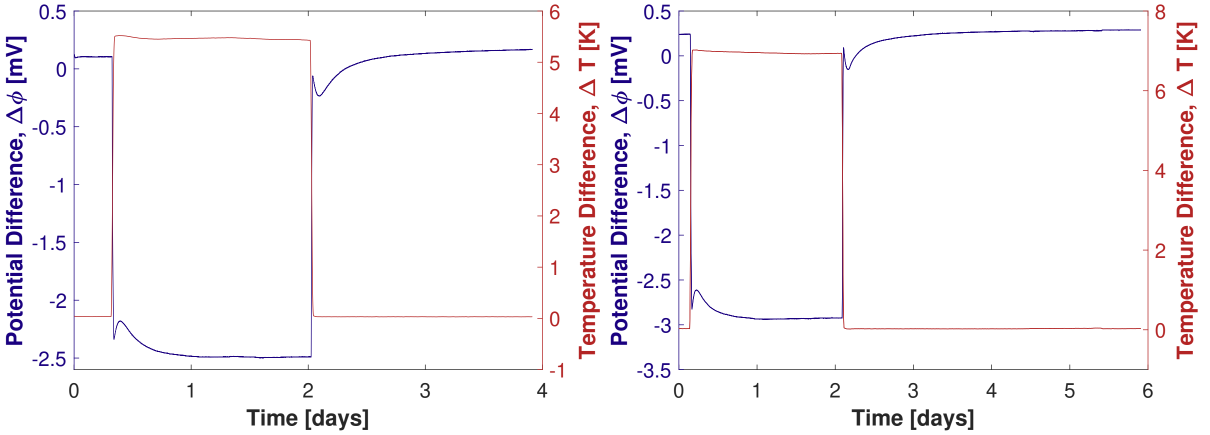

(c) $\mathrm{Li}_x\mathrm{FePO}_4$ with x = 0.87 and $\Delta_{WB}T = 15$ K

(d) $\mathrm{Li}_x\mathrm{FePO}_4$ with x = 0.87 and $\Delta_{WB}T = 20$ K

Figure E.9: Potential measurements for symmetric cells using $\mathbf{Li}_x\mathbf{FePO}_4$ electrodes with an electrolyte consisting of a LiPF_6 salt in 1:1 wt % **EC:DEC**. The lithiation state is x = 0.87 (13.33 % SoC). The different plots are from different experiments and with different water bath temperatures $\Delta_{WB}T$. The plotted temperature is the estimated internal temperature difference in the cell.

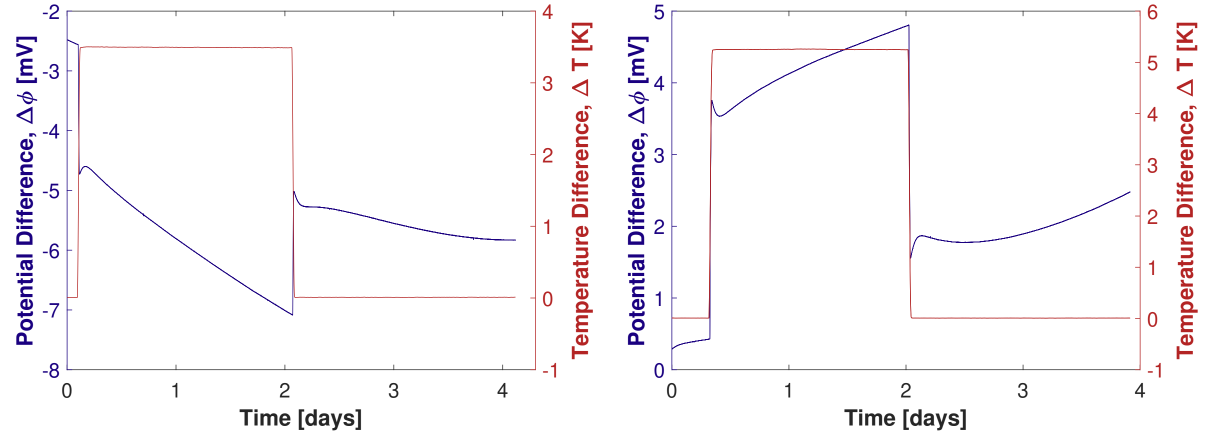

(a) $\mathrm{Li}_x\mathrm{FePO}_4$ with $x = 0.67$ and $\Delta_{WB}T = 10$ K **(b)** $\mathrm{Li}_x\mathrm{FePO}_4$ with $x = 0.67$ and $\Delta_{WB}T = 15$ K

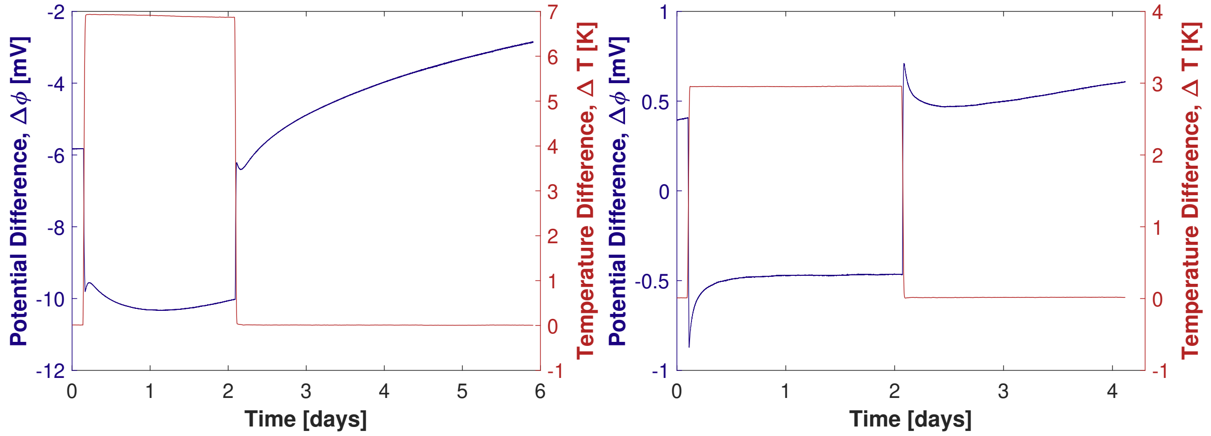

(c) $\mathrm{Li}_x\mathrm{FePO}_4$ with $x = 0.67$ and $\Delta_{WB}T = 20$ K **(d)** $\mathrm{Li}_x\mathrm{FePO}_4$ with $x = 0.47$ and $\Delta_{WB}T = 10$ K

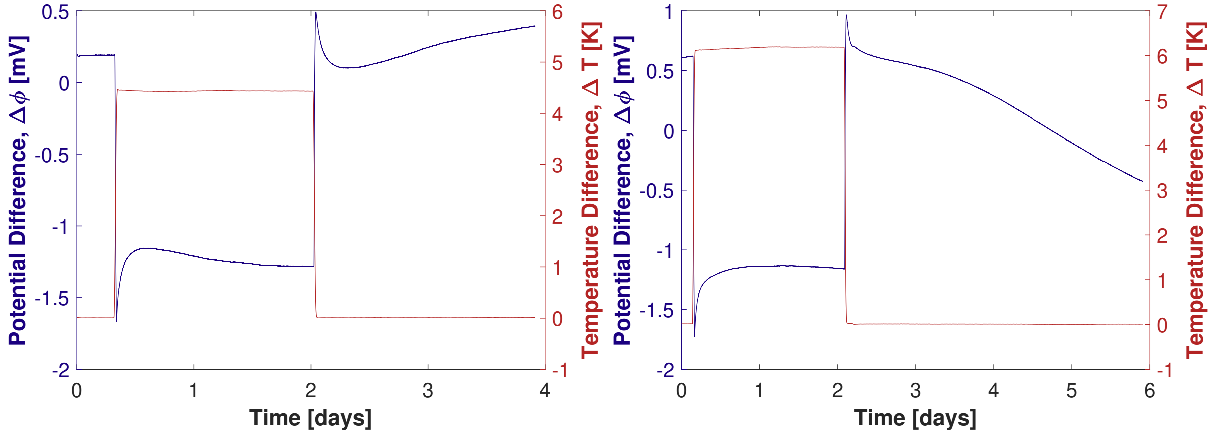

(e) $\mathrm{Li}_x\mathrm{FePO}_4$ with $x = 0.47$ and $\Delta_{WB}T = 15$ K **(f)** $\mathrm{Li}_x\mathrm{FePO}_4$ with $x = 0.47$ and $\Delta_{WB}T = 20$ K

Figure E.10: Potential measurements for symmetric cells using $\mathbf{Li}_x\mathbf{FePO}_4$ electrodes with an electrolyte consisting of a LiPF_6 salt in 1:1 wt % **EC:DEC**. The lithiation state is (a)-(c) x = 0.67 (33.33 % SoC) and (d)-(f) x = 0.47 (53.33 % SoC). The different plots are from different experiments and with different water bath temperatures $\Delta_{WB}T$. The plotted temperature is the estimated internal temperature difference in the cell.

E.8 Measurement Noise

The measurements of the temperature showed some noise, which affects the accuracy of the measurements. However, the noise in the graphs makes them harder to read. Therefore this noise was removed by plotting a moving mean value of the temperature difference, calculating each point as the mean value of the neighbouring 100 points. This has been illustrated in Figure E.11 where the left figure (Figure E.11a) displays the measured temperature difference, and the right figure (Figure E.11b) displays the temperature difference where the noise has been removed. Small variations in temperature around the mean temperature will not be accounted for in these figures.

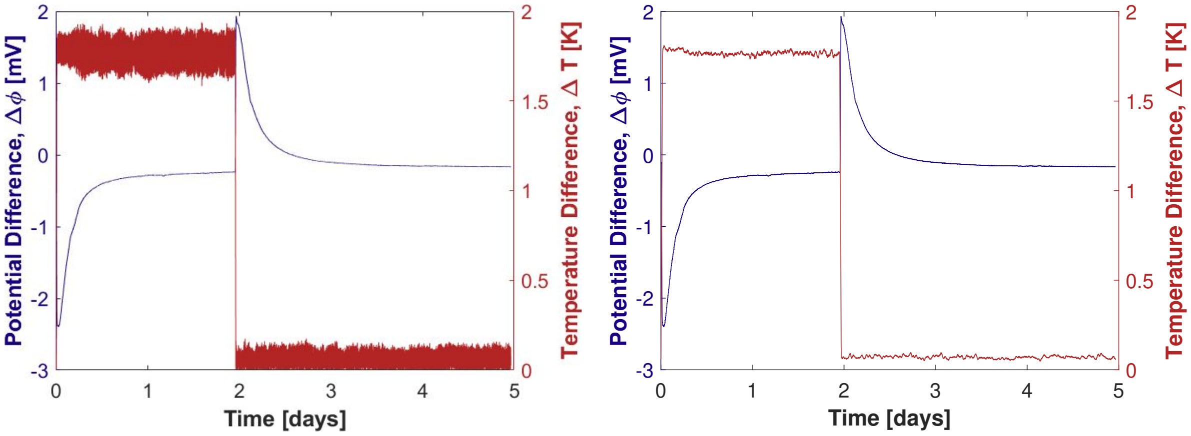

(a) With noise

(b) Without noise

Figure E.11: Illustration of how the measurement noise was removed from the temperature difference in some of the cells. (a) Illustrates a cell with measurement noise in the temperature difference while (b) illustrates the same temperature difference where a moving mean has been calculated for the temperature, using 100 points around each value to give the mean

Appendix F

Seebeck Coefficients for All Cells

Figure F.1 shows the Seebeck coefficient calculated for each individual experiment in this thesis, sorted by configuration of the symmetric cells used.

Table F.1: Reported Seebeck coefficient for the different configurations in this thesis. The figure makes reference to which potential measurements were used to calculate the values. High errors are usually caused by variations in temperature or potential with time.

Electrode	**Electrolyte**	**Cell**	ΔT **[K]**	ϵ_0 **[mV/K]**	ϵ_∞**[mV/K]**	**Figure** ($\Delta\varphi/\Delta T$)
$LiFePO_4$	1 M LiPF6 in EC:DEC		3.36 ± 0.01	-0.93 ± 0.05	-0.75 ± 0.04	E.1a
			3.65 ± 0.03	-0.65 ± 0.15	-0.64 ± 0.15	E.1c
			3.92 ± 0.01	-0.75 ± 0.02	-0.69 ± 0.02	E.1b
			5.36 ± 0.01	-0.81 ± 0.04	-0.75 ± 0.05	E.1e
			5.89 ± 0.02	-0.62 ± 0.07	-0.63 ± 0.07	E.1f
			7.02 ± 0.02	-0.63 ± 0.13	**NR**	E.2c
			7.23 ± 0.06	-0.69 ± 0.32	$-0,67 \pm 0.05$	E.2a
$LiFePO_4$	1 M LiPF6 in EC:DMC		3.36 ± 0.01	-0.37 ± 0.01	-0.37 ± 0.01	E.3a
			5.07 ± 0.01	-0.37 ± 0.01	-0.37 ± 0.01	E.3b
			6.63 ± 0.02	-0.36 ± 0.06	-0.36 ± 0.06	E.3c
$LiMn_2O_4$	1 M LiPF6 in EC:DEC		1.67 ± 0.03	-0.43 ± 0.85	**NR**	E.4c
			5.58 ± 0.01	-0.84 ± 0.03	-0.78 ± 0.18	E.4d
			7.62 ± 0.03	-0.73 ± 0.27	**NR**	E.4e
$LiMn_2O_4$	1 M LiPF6 in EC:DMC		1.43 ± 0.04	-0.44 ± 0.86	**NR**	E.5a
			2.14 ± 0.03	**NR**	-0.42 ± 0.31	E.5c
			2.23 ± 0.01	-0.50 ± 0.06	**NR**	E.5c
			3.27 ± 0.01	**NR**	-0.37 ± 0.46	E.5c
			4.70 ± 0.03	-0.73 ± 0.04	-0.55 ± 0.20	E.5b
			6.49 ± 0.01	-0.54 ± 0.13	-0.38 ± 0.22	E.5c
$LiCoO_2$	1 M LiPF6 in EC:DEC		1.77 ± 0.01	-1.07 ± 0.42	-0.57 ± 0.50	E.6d
			2.02 ± 0.01	-0.27 ± 0.01	**NR**	E.6c
			2.15 ± 0.01	-0.63 ± 0.06	**NR**	E.7a
			4.8 ± 0.5	-0.33 ± 0.83	-0.14 ± 0.09	E.7d
$LiCoO_2$	1 M LiPF6 in EC:DMC		1.88 ± 0.03	-0.25 ± 0.20	**NR**	E.8a
			1.93 ± 0.03	-0.25 ± 0.03	-0.08 ± 0.08	E.8c
			2.03 ± 0.01	-0.24 ± 0.03	**NR**	E.8c
			3.48 ± 0.01	**NR**	-0.09 ± 0.08	E.8c
			5.20 ± 0.01	-0.14 ± 0.02	-0.26 ± 0.25	E.8b
			6.90 ± 0.01	-0.27 ± 0.05	-0.14 ± 0.06	E.8c
$Li_{0.87}FePO_4$	1 M LiPF6 in EC:DEC		2.31 ± 0.01	-0.48 ± 0.08	**NR**	E.9a
			3.57 ± 0.01	-0.45 ± 0.01	-0.47 ± 0.01	E.9b
			5.46 ± 0.01	-0.44 ± 0.03	-0.48 ± 0.03	E.9c
			6.95 ± 0.02	-0.44 ± 0.06	-0.46 ± 0.06	E.9d
			7.12 ± 0.01	-0.49 ± 0.06	-0.54 ± 0.04	E.9a
$Li_{0.67}FePO_4$	1 M LiPF6 in EC:DEC		3.49 ± 0.01	-0.62 ± 0.02	-0.93 ± 0.34	E.10a
			5.25 ± 0.01	-0.64 ± 0.01	-0.61 ± 0.17	E.10b
			6.90 ± 0.02	-0.58 ± 0.08	-0.61 ± 0.21	E.10c
$Li_{0.47}FePO_4$	1 M LiPF6 in EC:DEC		2.95 ± 0.01	-0.43 ± 0.01	-0.33 ± 0.05	E.10d
			4.43 ± 0.01	-0.42 ± 0.01	-0.33 ± 0.01	E.10e
			6.18 ± 0.02	-0.38 ± 0.04	-0.30 ± 0.04	E.10f

NR - Not Reported, usually due to unstable measurements.

Table F.2: Reported average Seebeck coefficients for the different configurations in this thesis, calculated as the average of the values from all the experiments, reported in Table F.1.

Electrode	**Electrolyte**	ϵ_0 **[mV/K]**	ϵ_∞**[mV/K]**
$LiFePO_4$	1 M $LiPF_6$ in 1:1 wt% EC:DEC	-0.73 ± 0.15	-0.69 ± 0.08
	1 M $LiPF_6$ in 1:1 v/v EC:DMC	-0.37 ± 0.03	-0.36 ± 0.03
$LiMn_2O_4$	1 M $LiPF_6$ in 1:1 wt% EC:DEC	-0.67 ± 0.51	-0.78 ± 0.18
	1 M $LiPF_6$ in 1:1 v/v EC:DMC	-0.55 ± 0.44	-0.43 ± 0.31
$LiCoO_2$	1 M $LiPF_6$ in 1:1 wt% EC:DEC	-0.58 ± 0.47	-0.35 ± 0.71
	1 M $LiPF_6$ in 1:1 v/v EC:DMC	-0.19 ± 0.09	-0.14 ± 0.14
$Li_{0.87}FePO_4$	1 M $LiPF_6$ in 1:1 wt% EC:DEC	-0.46 ± 0.06	-0.49 ± 0.06
$Li_{0.67}FePO_4$	1 M $LiPF_6$ in 1:1 wt% EC:DEC	-0.61 ± 0.05	-0.72 ± 0.25
$Li_{0.47}FePO_4$	1 M $LiPF_6$ in 1:1 wt% EC:DEC	-0.41 ± 0.03	-0.32 ± 0.04

Appendix G

Determining the Seebeck Coefficient from Linear Regression

Based on several data points from different experiments, it was in many cases possible to fit a curve using linear regression. Because the Seebeck coefficient reports the relation between the potential and the change in temperature, the slope of a linear curve gives the Seebeck coefficient. The curves were plotted for initial and steady state values for the different configurations in this thesis. It should be noted that the points where no inherent relation was found are plotted without a curve (this applies to the initial value for LMO with EC:DMC solvent). In these cases, more experiments must be conducted to say something general about the Seebeck coefficients. In the case of LMO with the EC:DEC solvent, only one experiment gave results for the steady state seebeck coefficient, which means that drawing a conclusion about the coefficient would be far-fetched.

G.1 Initial Seebeck Coefficients from Linear Regression

Figures G.1 and the initial Seebeck coefficients for the different configurations have been reported using linear regression of the data points from experiments.

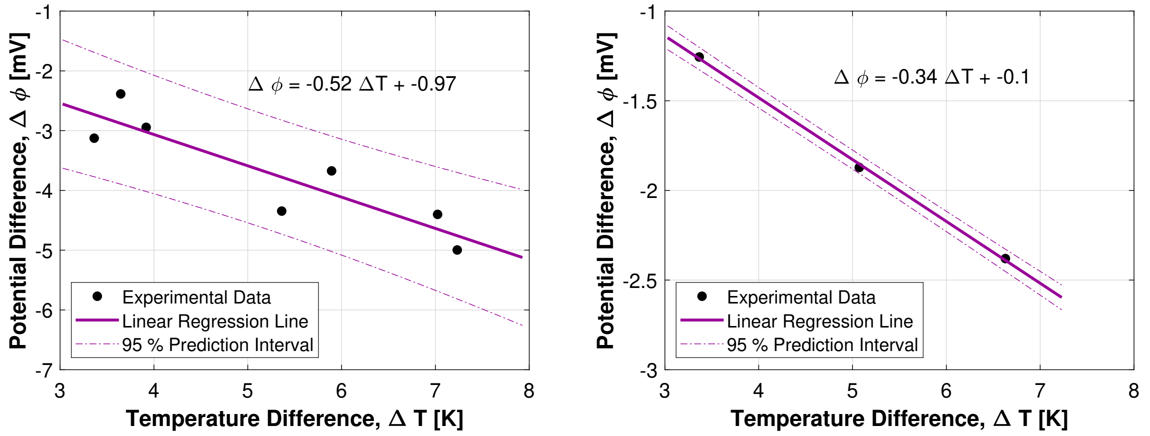

(a) $LiFePO_4$ with EC:DEC solvent

(b) $LiFePO_4$ with EC:DMC solvent

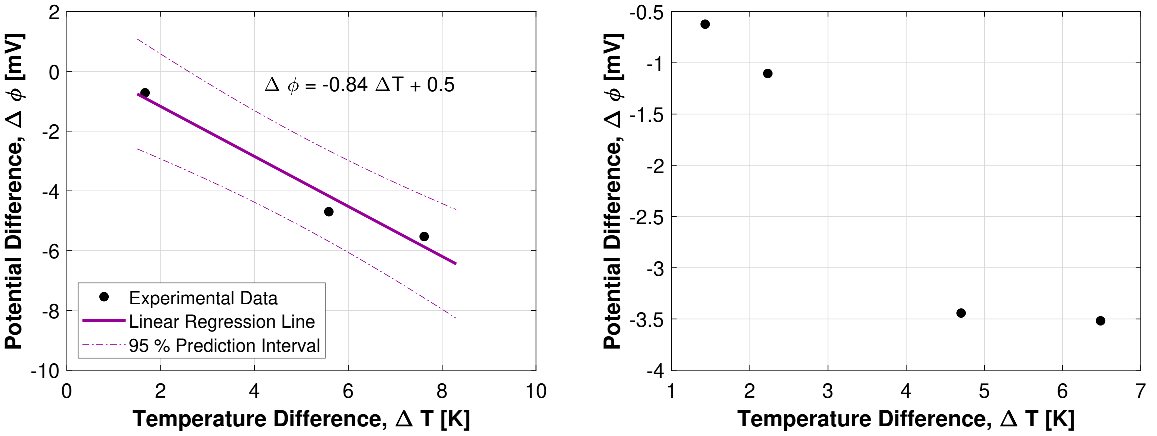

(c) $LiMn_2O_4$ with EC:DEC solvent

(d) $LiMn_2O_4$ with EC:DMC solvent

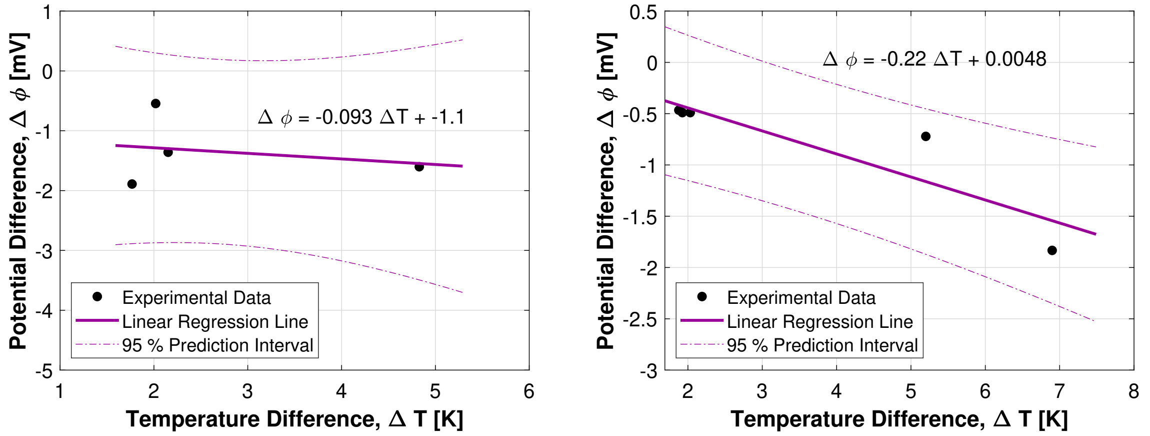

(e) $LiCoO_2$ with EC:DEC solvent

(f) $LiCoO_2$ with EC:DMC solvent

Figure G.1: Plots for different experiments of the internal temperature difference to the potential difference in the symmetric cells at time t=0, so just after the temperature difference is applied. This is used to deduce the Seebeck coefficient as the slope of the curve. The subfigures are for different configurations, as indicated below each figure. In (d) and (e) no best-fit linear regression line was found for the data.

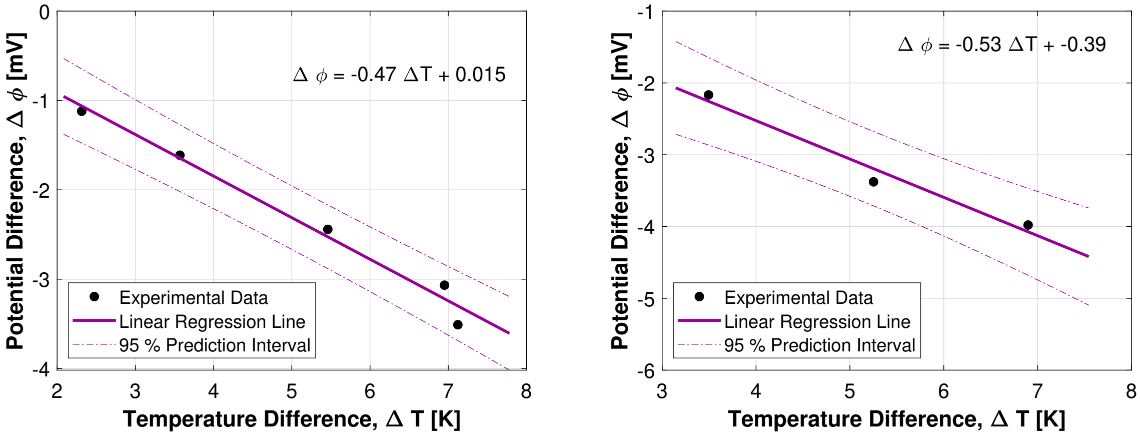

(a) $Li_{0.87}FePO_4$ electrodes

(b) $Li_{0.67}FePO_4$ electrodes

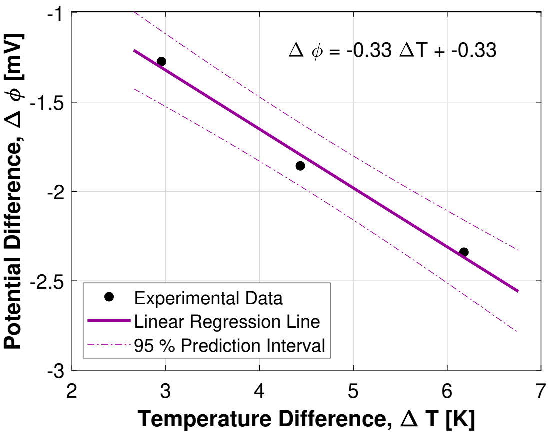

(c) $Li_{0.47}FePO_4$ electrodes

Figure G.2: Plots for different experiments of the internal temperature difference to the potential difference in the symmetric cells at time t=0, so just after the temperature difference is applied. This is used to deduce the Seebeck coefficient as the slope of the curve. The subfigures are for different lithiation states of the LFP electrode, as indicated below each figure. All cells used a 1 M $LiPF_6$ electrolyte in 1:1 wt % EC:DEC solvent.

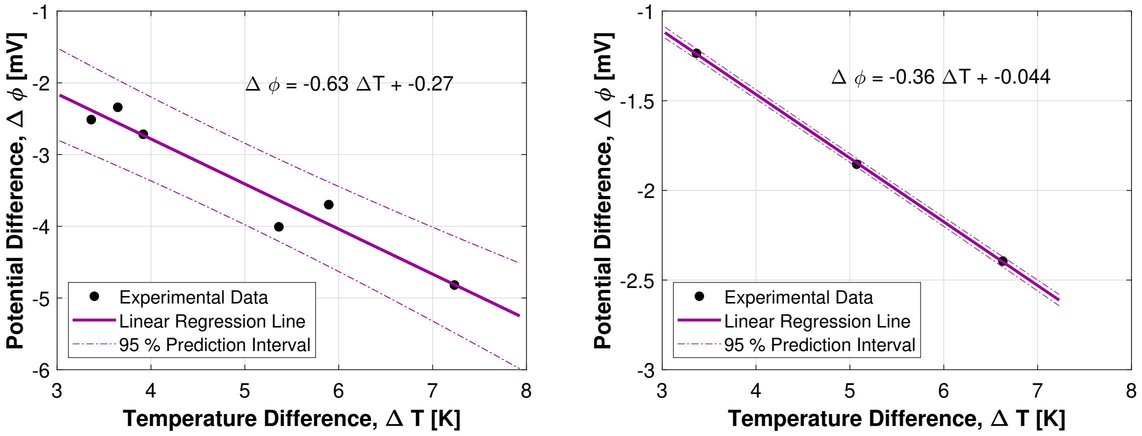

(a) $LiFePO_4$ with EC:DEC solvent

(b) $LiFePO_4$ with EC:DMC solvent

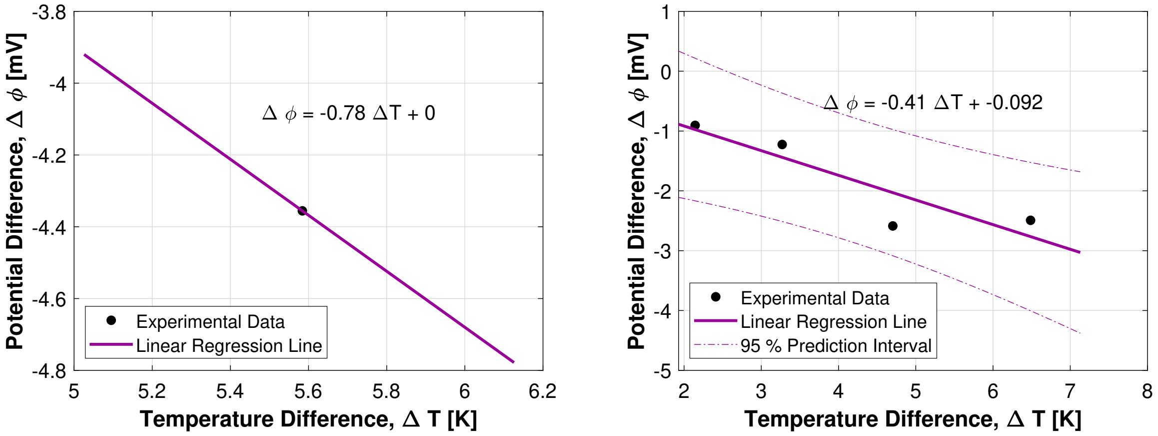

(c) $LiMn_2O_4$ with EC:DEC solvent

(d) $LiMn_2O_4$ with EC:DMC solvent

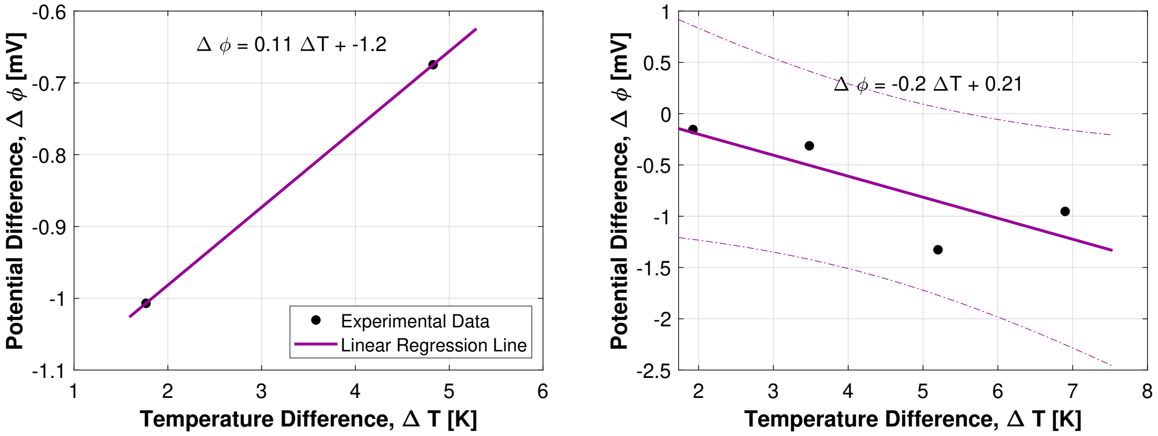

(e) $LiCoO_2$ with EC:DEC solvent

(f) $LiCoO_2$ with EC:DMC solvent

Figure G.3: Plots for different experiments of the internal temperature difference to the potential difference in the symmetric cells as $t \longrightarrow \infty$, so when a stationary state establishes in the cell. This is used to deduce the Seebeck coefficient as the slope of the curve. The subfigures are for different configurations, as indicated below each figure.

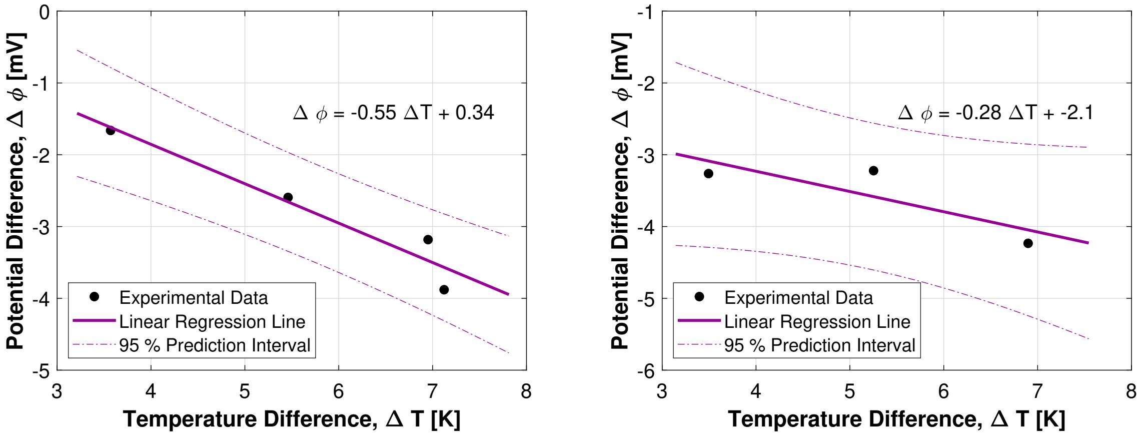

(a) $Li_{0.87}FePO_4$ electrodes **(b)** $Li_{0.67}FePO_4$ electrodes

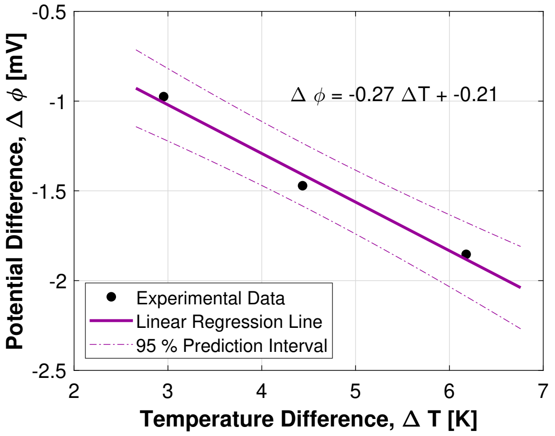

(c) $Li_{0.47}FePO_4$ electrodes

Figure G.4: Plots for different experiments of the internal temperature difference to the potential difference in the symmetric cells as $t \longrightarrow \infty$, so when a stationary state establishes in the cell. This is used to deduce the Seebeck coefficient as the slope of the curve. The subfigures are for different lithiation states of the LFP electrode, as indicated below each figure. All cells in this figure used a 1 M $LiPF_6$ electrolyte in 1:1 wt % EC:DEC solvent.

Appendix H

Error Calculations

The standard deviations of the measurements were calculated based on the readings, following the law:

$$s = \sqrt{\frac{\sum_i^N (x_i - \overline{x})^2}{N-1}} \tag{H.1}$$

This essentially means that the reported values for *i.e.* the potential at stationary state was taken as an average of several points, and the standard deviation reported according to the formula above.

It was assumed that the temperature and potential measurements were independent, so that the error in the Seebeck coefficient could be reported using Gauss law of error propagation, given by:

$$e = \sqrt{\left(\frac{\partial f}{\partial x_1}\right)^2 \cdot s_{x_1}^2 + \left(\frac{\partial f}{\partial x_2}\right)^2 \cdot s_{x_2}^2 + \ldots} \tag{H.2}$$

When the average Seebeck coefficient was calculated, the error was taken as the standard error of the mean, using the squared sum of the individual variances as the standard deviation of the mean. The standard error of the average Seebeck coefficient was then reported as:

$$\sigma_{\overline{x}} = \frac{s_{\overline{x}}}{\sqrt{n}} \tag{H.3}$$

Where n was the number of experiments and $s_{\overline{x}} = \sqrt{\sum_i^n s_{x_i}^2}$ the standard deviation of the mean.

Appendix I

Risk Assessment

ID	41228	**Status**	**Dato**
Risikoområde	Risikovurdering: Helse, miljø og sikkerhet (HMS)	Opprettet	02.02.2021
Opprettet av	Trym Bærheim	Vurdering startet	02.02.2021
Ansvarlig	Trym Bærheim	Tiltak besluttet	
		Avsluttet	

Risikovurdering:

Trym Bærheim NEW Master's Project - Half-Cell Entropy Measurements

Gyldig i perioden:
2/2/2021 - 8/2/2021

Sted:
VATL - C071.5

Mål / hensikt
Better understanding of local effects in the battery in order to make more precise complete models at a later state. Here we study the peltier heat for a half-cell at different SOC and for different chemistries.

Bakgrunn
[Ingen registreringer]

Beskrivelse og avgrensninger

Forutsetninger, antakelser og forenklinger
[Ingen registreringer]

Vedlegg
[Ingen registreringer]

Referanser
[Ingen registreringer]

Oppsummering, resultat og endelig vurdering

I oppsummeringen presenteres en oversikt over farer og uønskede hendelser, samt resultat for det enkelte konsekvensområdet.

Farekilde: **Opening Cell, Glove Box**

Uønsket hendelse: **Puncture Glove in Glove-Box**

Konsekvensområde:	Helse	Risiko før tiltak:	🟢	Risiko etter tiltak:	⚪
	Materielle verdier	Risiko før tiltak:	🟢	Risiko etter tiltak:	⚪

Uønsket hendelse: **Short Circuit**

Konsekvensområde:	Helse	Risiko før tiltak:	🟢	Risiko etter tiltak:	⚪

Farekilde: **Making Half-Cells**

Uønsket hendelse: **Short Circuit**

Konsekvensområde:	Helse	Risiko før tiltak:	🟢	Risiko etter tiltak:	⚪

Uønsket hendelse: **Puncture Glove in Glove-Box**

Konsekvensområde:	Helse	Risiko før tiltak:	🟢	Risiko etter tiltak:	⚪
	Materielle verdier	Risiko før tiltak:	🟢	Risiko etter tiltak:	⚪

Uønsket hendelse: **Cut**

Konsekvensområde:	Helse	Risiko før tiltak:	🟢	Risiko etter tiltak:	⚪

Farekilde: **Cycling Cells in Arbin Battery Cycler**

Uønsket hendelse: **Electric Shock**

Konsekvensområde:	Helse	Risiko før tiltak:	🟢	Risiko etter tiltak:	⚪

Uønsket hendelse: **Catching Fire**

Konsekvensområde:	Helse	Risiko før tiltak:	🟢	Risiko etter tiltak:	⚪
	Materielle verdier	Risiko før tiltak:	🟢	Risiko etter tiltak:	⚪

Endelig vurdering

Involverte enheter og personer

En risikovurdering kan gjelde for en, eller flere enheter i organisasjonen. Denne oversikten presenterer involverte enheter og personell for gjeldende risikovurdering.

Enhet /-er risikovurderingen omfatter

- Institutt for energi- og prosessteknikk

Deltakere

Astrid Fagertun Gunnarshaug

Lena Spitthoff

Morten Grønli

Odne Stokke Burheim

Lesere

[Ingen registreringer]

Andre involverte/interessenter

[Ingen registreringer]

Følgende akseptkriterier er besluttet for risikoområdet Risikovurdering: Helse, miljø og sikkerhet (HMS):

Helse

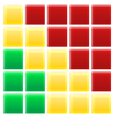

Materielle verdier

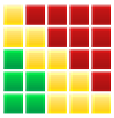

Omdømme

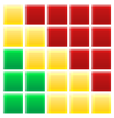

Ytre miljø

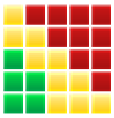

Oversikt over eksisterende, relevante tiltak som er hensyntatt i risikovurderingen

I tabellen under presenteres eksisterende tiltak som er hensyntatt ved vurdering av sannsynlighet og konsekvens for aktuelle uønskede hendelser.

Farekilde	Uønsket hendelse	Tiltak hensyntatt ved vurdering
Opening Cell, Glove Box	Puncture Glove in Glove-Box	Fireproof Box
	Puncture Glove in Glove-Box	Gloves
	Puncture Glove in Glove-Box	Fume Hood
	Puncture Glove in Glove-Box	Fireproof Box
	Puncture Glove in Glove-Box	Gloves
	Puncture Glove in Glove-Box	Fume Hood
	Short Circuit	Fireproof Box
	Short Circuit	Gloves
	Short Circuit	Ceramic Tools
	Short Circuit	Fireproof Box
	Short Circuit	Gloves
	Short Circuit	Ceramic Tools
Making Half-Cells	Short Circuit	Fireproof Box
	Short Circuit	Gloves
	Short Circuit	Fireproof Box
	Short Circuit	Gloves
	Puncture Glove in Glove-Box	Gloves
	Puncture Glove in Glove-Box	Ceramic Tools
	Puncture Glove in Glove-Box	Gloves
	Puncture Glove in Glove-Box	Ceramic Tools
	Cut	Gloves
	Cut	Gloves
Cycling Cells in Arbin Battery Cycler	Electric Shock	Gloves
	Electric Shock	Gloves
	Catching Fire	Fireproof Box
	Catching Fire	Fireproof Box

Eksisterende og relevante tiltak med beskrivelse:

Fireproof Box

[Ingen registreringer]

Gloves

[Ingen registreringer]

Ceramic Tools

[Ingen registreringer]

Fume Hood

[Ingen registreringer]

Goggles

[Ingen registreringer]

Lab Coat

[Ingen registreringer]

Risikoanalyse med vurdering av sannsynlighet og konsekvens

I denne delen av rapporten presenteres detaljer dokumentasjon av de farer, uønskede hendelser og årsaker som er vurdert. Innledningsvis oppsummeres farer med tilhørende uønskede hendelser som er tatt med i vurderingen.

Følgende farer og uønskede hendelser er vurdert i denne risikovurderingen:

- **Opening Cell, Glove Box**
    - Puncture Glove in Glove-Box
    - Short Circuit
- **Making Half-Cells**
    - Short Circuit
    - Puncture Glove in Glove-Box
    - Cut
- **Cycling Cells in Arbin Battery Cycler**
    - Electric Shock
    - Catching Fire

Detaljert oversikt over farekilder og uønskede hendelser:

Farekilde: Opening Cell, Glove Box

Cells are disassembled in order to get the wanted electrodes for the half-cells

Uønsket hendelse: Puncture Glove in Glove-Box

Årsak: Sharp edges on cell

Sannsynlighet for hendelsen (felles for alle konsekvensområder): **Lite sannsynlig (2)**

Kommentar:

Gloves are constructed of a tough material, and the cell-edges are not that sharp.

Konsekvensområde: Helse

Risiko:

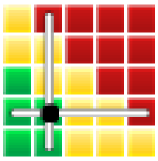

Vurdert konsekvens: **Middels (2)**

Kommentar: One would notice that the glove was punctured and would therefore be able to stop working immediately. Should one continue work, the risk of getting electrocuted would be existing. Also if any dangerous fumes from the electrolyte pass into the room, this could have a negative effect on health, but the fume hood should prevent any severe consequence, especially because the quantities are so low.

Konsekvensområde: Materielle verdier

Risiko:

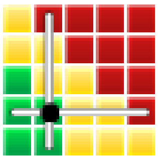

Vurdert konsekvens: **Middels (2)**

Kommentar: Would need to replace the glove in the glove box before continuing work

Uønsket hendelse: Short Circuit

If a cathode comes into contact with the anode they will short-circuit

Årsak: Contact between electrodes

Sannsynlighet for hendelsen (felles for alle konsekvensområder): **Sannsynlig (3)**

Kommentar:

Handling inside glove-box is difficult, and the anode and cathode could come into contact by mistake.

Konsekvensområde: Helse

Vurdert konsekvens: **Liten (1)**

Kommentar: The cells will be fully discharged, so little current would be available to pass from the anode to the cathode. Also we are working inside the glove-box

Risiko:

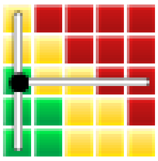

Farekilde: Making Half-Cells

Uønsket hendelse: Short Circuit

Årsak: Contact between electrodes

Sannsynlighet for hendelsen (felles for alle konsekvensområder): **Sannsynlig (3)**

Kommentar:

Handling inside the glove-box is difficult, and contact could be made without wanting to.

Konsekvensområde: Helse

Vurdert konsekvens: **Liten (1)**

Kommentar: The half cells are composed of electrodes of equal state, and the same material, so the potential difference would only be due to slight local differences. Thus, the current should be very close to zero.

Risiko:

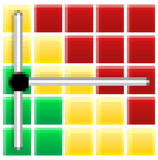

Uønsket hendelse: Puncture Glove in Glove-Box

Årsak: Sharp edges on cell

Sannsynlighet for hendelsen (felles for alle konsekvensområder): **Lite sannsynlig (2)**

Kommentar:

Edges not very sharp, and gloves made of tough material.

Konsekvensområde: Helse

Vurdert konsekvens: **Liten (1)**

Kommentar: Low voltage difference between electrodes, so severe electrocution is not probable. Should any electrolyte leak out it would be small amounts, and is not likely to have severe effects on health.

Risiko:

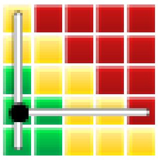

Konsekvensområde: Materielle verdier

Vurdert konsekvens: **Middels (2)**

Kommentar: Would have to buy new glove before work could be continued in the glove-box.

Risiko:

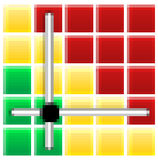

Uønsket hendelse: Cut

Sannsynlighet for hendelsen (felles for alle konsekvensområder): **Lite sannsynlig (2)**

Kommentar:

Would be wearing gloves. Also the edges are usually not that sharp

Konsekvensområde: Helse

Risiko:

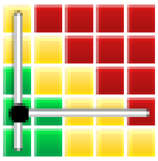

Vurdert konsekvens: **Liten (1)**

Kommentar: A cut would likely be in a finger or similar

Farekilde: Cycling Cells in Arbin Battery Cycler

Want to achive desired SOC for the measurements by cycling in the Arbin Battery Cycler

Uønsket hendelse: Electric Shock

Årsak: Contact with both electrodes upon rigging set-up

Sannsynlighet for hendelsen (felles for alle konsekvensområder): **Lite sannsynlig (2)**

Kommentar:

[Ingen registreringer]

Konsekvensområde: Helse

Risiko:

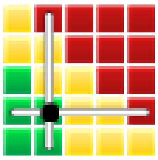

Vurdert konsekvens: **Middels (2)**

Kommentar: A severe electric shock could cause cardiac arrest. In our case the voltages are quite low, so it would probably not go to these extremes.

Uønsket hendelse: Catching Fire

Årsak: Thermal Runaway

Årsak: Malfunctioning Machine

Sannsynlighet for hendelsen (felles for alle konsekvensområder): **Lite sannsynlig (2)**

Kommentar:

[Ingen registreringer]

Konsekvensområde: Helse

Risiko:

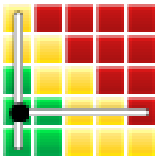

Vurdert konsekvens: **Liten (1)**

Kommentar: If the building catches on fire, it could cause injuries, but it is not likely that the building catches on fire.

Konsekvensområde: Materielle verdier

Risiko:

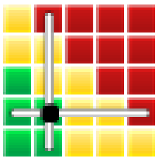

Vurdert konsekvens: **Middels (2)**

Kommentar: The box where the cycling is done is fire-proof and should therefore protect material values even if the cell catches fire.

Oversikt over besluttede risikoreduserende tiltak:

Under presenteres en oversikt over risikoreduserende tiltak som skal bidra til å reduseres sannsynlighet og/eller konsekvens for uønskede hendelser.

Detaljert oversikt over besluttede risikoreduserende tiltak med beskrivelse:

Detaljert oversikt over vurdert risiko for hver farekilde/uønsket hendelse før og etter besluttede tiltak

Trym Bærheim

Reversible Heat Effects in Electrodes Relevant for Lithium-Ion Batteries

NTNU
Norwegian University of
Science and Technology